SYNCHRONIZED MULTI-MATERIAL BIOPRINTING OF HETERO-CELLULAR

MODELS TO STUDY DRUG EFFICACY IN CO-CULTURE

Thesis

Submitted to the Faculty

of

Drexel University

by

Jessica Elizabeth Snyder

in partial fulfillment of the

requirements for the degree

of

Doctor of Philosophy

July 2014

UMI Number: 3633495

UMI
Dissertation Publishing

UMI 3633495

ProQuest

www.manaraa.com

Office of Graduate Studies
Dissertation/Thesis Approval Form

This form is for use by all doctoral and master's students with a dissertation/thesis requirement. Please print clearly as the library will bind a copy of this form with each copy of the dissertation/thesis. All doctoral dissertations must conform to university format requirements, which is the responsibility of the student and supervising professor. Students should obtain a copy of the Thesis Manual located on the library website.

Dissertation/Thesis Title: SYNCHRONIZED MULTI-MATERIAL

BIOPRINTING OF HETERO-CEUULUAR MODELS

TO STUDY DRUG EFFICACY IN CO-CULTURE

Author: JESSICA ELIZABETH SNYDER

This dissertation/thesis is hereby accepted and approved.

Signatures:

Examining Committee

    Chair

    Members

Academic Advisor

Department Head

DREXEL UNIVERSITY
Office of
Graduate Studies

D-5

REPORT OF PH.D. FINAL ORAL DEFENSE FORM

This form must be filed with the Office of Graduate Studies by the Dissertation Defense Chair (not the student) **within 48 hours of the oral defense.** In the case of disagreement within the Defense Committee, the Chair should consult with the Office of Graduate Studies. The deadline is typically the first day of final exams during the term in which the student plans to graduate. *Please check with the Office of Graduate Studies for exact term deadline.*

We have examined _Jessica Elizabeth Snyder_

Student ID _10683432_ who is pursuing the Ph.D. degree.

The results of the final dissertation defense on _06/09/2014_ ☑ WERE or ☐ WERE NOT

satisfactory. (MM/DD/YYYY) (Select One)

Each committee member must sign this form to show either agreement with or dissent from the overall result.

	Signature	Print Name
Chair		WEI SUN
Member		E. Çağlan Kumbur
Member		BINIL STARLY
Member		HONGLU WU
Member		Jack ZHOU
Member		
Member		

We dissent from the report:

Member		
Member		
Member		

Authorizations/Signatures

		Date	
Chair		Date	6/9/2014
Supervising Professor (if not the Chair)		Date	
Co-Supervising Professor (if applicable)		Date	
Department Graduate Advisor		Date	6/9/2014
Office of Graduate Studies		Date	6/11/2014

Office of Graduate Studies 3141 Chestnut Street Randell 240 Philadelphia, PA 19104
Tel: 215.895.0366 Fax: 215.895.0495 Email: ogsstaff@drexel.edu Web: www.drexel.edu/graduatestudies

(Last Updated 3/13/2014)

DEDICATIONS

Dear Mary Snyder, Matthew Snyder, Randolph Snyder, and Timothy Snyder, I share this accomplishment, like I have my struggles and you have your loving support, with you. My family.

ACKNOWLEDGEMENTS

TABLE OF CONTENTS

LIST OF TABLES

LIST OF FIGURES

ABSTRACT

**Synchronized Multi-material Bioprinting of Hetero-cellular Models to Study
Drug Efficacy in Co-culture**

Jessica Elizabeth Snyder
Wei Sun, Ph.D.

Bottom-up tissue engineering pursues automated process control over human tissue fabrication using the fundamental cellular, soluble, and architectural components as the working material. Key technology for methodological progress of bottom-up tissue engineering includes advanced biofabrication techniques to assemble viable biological material in 3-dimensional space and microfluidic devices to control timing and sequence of environmental stimulation. The presented research's objective is the development of design, characterization and fabrication approaches which integrate physiologically relevant microfluidic techniques and hetero-cellular architecture for cell-laden models by leveraging combinations of the biofabrication techniques; including precision extrusion deposition, multi-nozzle cell printing, replica molding, and a novel synchronized multi-material bioprinting system. This research focuses on the development of a synchronized multi-material bioprinter for the fabrication of 3D hetero-cellular models. The specific research objectives are: (1) combine multi-nozzle deposition system with a microlfuidic platform for controlled cell seeding in a microfluidic device for a hetero-cellular in vitro model for drug testing, (2) to define a 3D printing and replica molding processes to fabricate microfluidic and scaffold environments with control of the macro-scale (10^{-3}-10^{-1} m) patterning of channels/structural elements and micro-scale (10^{-4}-10^{-3} m) channel cross-section of internal features, (3) to develop and characterize an integrated synchronized multi-material bioprinter system to produce nano-liter droplets and 10^{-4}-10^{-3} m diameter filaments with a heterogeneous packaging resolution of 10^{-5}-10^{-3} m, and (4) to apply the synchronized multi-material bioprinter system to produce hetero-cellular models to study radioprotective drug efficacy in co-culture and

metabolism rates in simulated weightlessness environments. The presented biofabrication methods are applied to fabricate a hetero-cellular liver model to study drug efficacy of the pro-drug amifostine to shield liver from radiation genetic damage and pharmacokinetic up-take in model microgravity.

CHAPTER 1: INTRODUCTION

1.1   Bio-inspired micro-devices for tissue engineering

Tissue engineered in vitro models are reverse engineered from mature functional tissue's fundamental elements, architecture and the physical stimulation acting in the environment. The fidelity of an in vitro model is evaluated by biochemical and physiological self-organization processes; which are strongly correlated in vivo to signaling and contact between cell types. Methods to improve in vitro model fidelity include co-culture conditions and greater biomimetic complexity. Model complexity is limited by biomanufacturing capability to assemble multiple cell types in macro/micro-scale architecture within a bioreactor system.

Biomimetic benchmarks of an engineered in vitro tissue include defining the functional entities of mature functional tissue, heterogenous assembly of the defined entities, and a porous network for mass transfer of nutrients and removal of waste. Physiological intelligence enables individual cells to behave collectively as agregates for tissue-level function both in vivo and in vitro. The stability of parenchymal cells, support role of non-parenchymal cell types and physical/chemical processes within a target tissue and between tissues are key facets of a tissue microenvirnment. Histological characterization of tissues, similar to a blueprint, defines the micro-scale packaging of cell types, porous space and strutural matrix as well as and the macro-scale architecture of the tissue in relation to neighboing organism's other tissues. High diffusivity of oxygen and other water soluble metabolites through an in vitro model correlate to viable cells and minimize cell death (Ling et al., 2007; Y. S. Song et al., 2009). A successful extra cellular matrix material mimics mass transfer characteristics, including porosity and polarity, to allow for adequate for nutrient/soluble factor exchange. Physical processes including cell's anchoring substrate stiffness, mechano-stimulation by strain in an elastic matrix, shear stress due to fluid flow, electrical current in piezoelectic tissues (such as bone), and pressure from hydrostatic fluid column or 3-dimensional culture.

Each application of an in vitro model has a target sensitivity and acceptable tolerance based on the nature of the study and manufacturing limitations. Prototyping a specific in vitro design within a defined tolerance is critical to evaluating performance in an iterative design cycle. Key technology for methodological progress in microfluidic devices for drug discovery includes microfabrication techniques and 3-dimensional cell patterning. Miniaturization of perfusion system by microfabrication produces biomimetic interconnected network of channels (Becker, Carstens, Elbracht, & Gartner, 2010). Current techniques include photolithography, etching, and molding. Controlled cell assembly is required to produce specific cellular microenvironments and heterogeneous cell-to-cell contact (S. Khalil & Sun, 2009a). Design models use bottom-up tissue engineering to assemble modular cell environments to achieve biomimetic spatial and temporal interactions of soluble and biological cues. Current techniques include surface patterning by standard photolithography liftoff, photoreactive chemistry, micro-contact printing with lamination, molding, and photo-polymerization (Borenstein et al., 2007). Cell migration and separation after printing can be achieved by labeling cells with magnetic nanoparticles or gradient surface treatments to substrate. Cell deposition techniques such as syringe-based cell deposition, rapid prototyping of hydrogel structures, and inkjet-based cell printing include cells as part of the working material to directly assemble biologics in 3-dimensional space (S. Khalil, Nam, & Sun, 2005). A pumping mechanism is required to precisely transport volumes of liquid to induce specific transient delivery of soluble cues and hydrodynamic strain.

Mature, functional tissue's components, assembly and the physiological process between cells in niche microenvironments are characterized in literature. The biomimetic characterization is reverse engineered into bioreactor platforms to prescriptively stimulate cells with dynamic perfusion, cyclic strain and temporal gradients of soluble cues. In vitro cell-laden model use microfabrication techniques to engineer hetero-cellular architecture and mechanical stress cues in a bioreactor environment. Biomimetic fabrication leveraging advanced micro- and nano-

manufacturing improves in vitro cell model fidelity for (1) regenerative medicine to treat injury and disease with lab-grown implants, (2) therapeutic micro-devices, (3) mechanistic model of physiological process between cells in niche microenvironments and between tissue and (4) pharmaceutical trials on human cell models (Linda G. Griffith, Wells, & Stolz, 2014). Therapeutic tissue engineering successfully combined donor cells and scaffold material to culture bladder (Atala, Bauer, Soker, Yoo, & Retik, 2006) and trachea (Omori et al., 2005) tissue to be used as a surgical implant in human patients.

Therapeutic micro-devices are reverse engineered to provide the function of tissue and organ system without building the device from the same components as native tissue. Therapeutic micro-devices supplement existing bodily function without replacing existing tissue. Wyss Institute's spleen-on-a-chip is an extracorpeal micro-device for sepsis therapy (Yung, Fiering, Mueller, & Ingber, 2009). Sepsis blood is mixed with magnetic nano-beads by injection in the microfluidic device. An electromagnet removes the nano-beads with pathogens attached before the cleansed blood is collected. Magnetic nano-bead coated with MLB-fp1 binds to C. albicans fungus with an isolation efficiency above 99%.

Human-on-a-chip network discrete cell-laden chamber to model the effect of drug on a specific cell model of a target tissue and model the sequence of pharmacokinetic and pharmacodynamic interaction downstream of the initial cell model (Marx et al., 2012). Phylogenic distinctions between laboratory animals and human diminish the reliability of animal testing for acute systemic drug toxicity. An alternative testing system are micro-devices engineered to model the causality and sensitivity of mature functional human tissue. Microfluidic platforms are an enabling technology to network cell-laden compartments and control forced convection through the cell-laden models. Further, Further, bioreactor platforms include mechanical stimulation and 3-dimensional heater-cellular arrangement for biomimetic cell-to-cell contact in niche microenvironments to capture physiology and pathophysiology (Ebrahimkhani, Neiman, Raredon,

Hughes, & Griffith). Liver-on-a-chip is of particular interest for applications to toxicity of small molecule drugs and observations of off-target reaction to proteins and regenerative therapies. A liver-on-a-chip model as a multi-chamber modular bioreactor uses low shear to model liver sinusoid hemodynamics (Mazzei, Guzzardi, Giusti, & Ahluwalia, 2010).

Wyss Institute's lung-on-a-chip mimics biochemical cell-to-cell contact using co-culture and cell mechanosensation during lung expansion/contraction using cyclic strain (Huh, Mammoto, Montoya-Zavala, & Ingber, 2010). The United Kingdom's National Center for the Replacement, Refinement and Reduction of Animals in Research (NC3Rs) 2013 prize recognized Donald Ingber and the Wyss Institute's lung on a chip as the most promising scientific advancement to reduce the use of animals in research ("UK: 3Rs Prize awarded to Donald Ingber for lung-on-a-chip device," 2013). Alternate sides of a permeable membrane are seeded with lung cells and capillary blood vessel cells. The membrane slides longitudinally into a channel, dividing the channel in half. The lung side of the channel is perfused with air and capillary side is perfused with human white blood cell-laden liquid to mimic the two phase's arrangement in lung tissue. Cyclic strain of the cell-laden membrane due to suction of vacuum chambers on either side mimic in vivo expansion/contraction during breathing. Lung-on-a-chip studies include: (1) Infection and white blood cell response is studied by introducing bacteria to the air phase. Bacteria migrate from the air, through the cell-laden membrane and become engulfed by white blood cells. (2) Pulmonary edema (accumulation of fluid in the lung's air sac) is observed in lung-on-a-chip model when the cancer drug known to cause pulmonary edema interleukin 2 (IL-2) is added to the liquid phase (Huh et al., 2012). Fluid leakage is the same as physiological observations when cyclic strain is observed. Minimal fluid leakage is observed in the model without cyclic strain to mimic breathing. (3) Toxic effects of air-born nanoparticles, confirmed in animal studies (Huh, Matthews, Mammoto, Montoya-Zavala, & Ingber, 2011).

In vitro phenotype stability and stem cell differentiation is also attributed to abiotic and biotic factors. Physical stress is a recurring stimulus to direct stem cell differentiation. Nikukar et. al. of the University of Glasgow promoted osteoblastogenisis of human mesenchymal stem cells using mechanotransduction (Nikukar et al., 2013). Cyclic nano-scale displacement on the order of 10-14 nm across the culture induced by a reverse piezoelectric caused a significant shift in total genomic expression towards osteogenic after 1 week of stimulation. Benishti and Cohen of Ben-Gurion University of the Negev used physical conditioning to direct a culture of cardiomyocytes to reorganize into a stratified biomimetic structures (Shachar, Benishti, & Cohen, 2012). Daily treatments of 1 Hz 15% compression and fluid shear stress preserved cell-specific gap junctions and growth factors and cells self-assembled into a biomimetic stratified structure.

Figure 1-1 presents images of the Griffith Lab's liver-on-a-chip for high-throughput drug toxicity and metabolism studies (left), Wyss Institute lung-on-a-chip co-culture model with breathing stimulation and air/liquid interface (center) and spleen-on-a-chip micro-device to clean pathogens from blood (right).

Griffith Lab Liver-on-a-Chip
Scalable Liver Bioreactor Technologies for High-Throughput Drug Toxicity & Metabolism Studies

http://web.mit.edu/lgglab/research/index.html

Wyss Institute Lung-on-a-Chip
Mimics mechanical and chemical function of a living breathing lung

http://wyss.harvard.edu/viewpage/240/

Ingber Lab Spleen-on-a-Chip
Extracorporeal micro-device that functions lie an artificial spleen for sepsis therapy.

Figure 1-1: State of the art bioinspiried micro-devices for tissue engineering. Bioinspiried micro-devices mimic whole human organ function have the potential to replace animal testing and bring new therapies to patients faster and at a lower cost (Baker, 2011; Huh et al., 2011).

1.1.1   In vitro cell model for drug development

Pre-clinical determinations of drug toxicity to liver would greatly improve screening technology (L. G. Griffith et al., 2005). The purpose of in vitro cell models is to represent in vivo performance. The challenge of in vitro models is to reverse engineer the spatial-temporal arrangements of the biology, chemistry and physics of the in vivo microenvironment within an acceptable tolerance. The acceptable tolerance compares the collective behavior of an in vitro culture to the behavior of tissue in the human body. In vitro models balance realism and simplicity to prevent false findings or misinterpretations (van der Meer & van den Berg, 2012). Engineering in vitro models using prescriptive environmental stimulation and advanced manufacturing to assemble biological material in 3-dimensional space can enable self-organizing behavior in cells (Fischbach et al., 2007).

In vitro models are relevant experimental, diagnostic and therapeutic tools (Sato & Clevers, 2013). Experimental tool to study the cell behavior as a response to prescriptive biological, chemical or physical conditions. Diagnostic tool to investigate patient specific function and phenomenon. Therapeutic tool have applications to regenerative medicine. Cell-laden microfluidic devices recreate *in vivo* cell-to-cell interactions, a current challenge in drug screening, through reproducible quantifiable patterning of spatial and temporal gradients (Dickson & Gagnon, 2004; Jensen, El-Ali, & Sorger, 2006; Shuler, Viravaidya, & Sin, 2004). Conventional cell culture of a monolayer on petri dish is a well-established methodology which has been optimized for various drug's ADMES-Tox profiles in humans (van Midwoud, Verpoorte, & Groothuis, 2011). However, the fidelity of conventional models is limited due to local depletion of drug-metabolizing enzymes and transporters, lack of controlled cell seeding and static medium reservoir. Failure to predict drug toxicity by conventional culture methodology is considered the principle reason 90% of new drugs fail during Phase 1 preclinical tests (Brandon, Raap, Meijerman, Beijnen, & Schellens, 2003). Biomimetic extra-cellular cues, cell-to-cell contact and definable gradient of drug conditions are

engineered into microenvironments for high throughput measurement of toxicity and pharmacokinetics (S. Kim & Marimuthu, 2011; Wu, Huang, & Lee, 2010). Cell-laden microfluidic devices improve fidelity of *in vitro* platforms by physiologically relevant surface area to volume ratio, mass transfer by diffusion, biomimetic microenvironment engineering, dynamic perfusion, and dual organ model (Buyukhatipoglu, Chang, Sun, & Clyne, 2010a; Walker, Zeringue, & Beebe, 2004).

The advantage of drug discovery by cell-laden microfluidic devices is reproducible quantifiable control over the stimulation and patterning of biological material (Yeo, Chang, Chan, & Friend, 2011). Micron-scale quantities of cell-laden matrix and microfluidic channel produce a cell to interstitial fluid volume ratio of approximately one, as is physiologically relevant (Whitesides et al., 2010). The microfluidic length scale improves uniformity of temperature field and gas supply through cell laden matrix, induce laminar flow pattern and therefore mass transfer by diffusion. These factors reduce variability caused by proportions of experimental design. Hydrodynamic forces on the cells by extracellular fluid produce physical cues stimulate and direct cell function. Dynamic perfusion causes naturally occurring gradients of diffusing chemicals and produces controllable gradient of drug conditions. Cells are assembled in 3-dimensional biomimetic microenvironments to produce biomimetic morphology, cytoskeleton alignment, cell-to-cell contact, focal adhesion of cell to matrix and signaling (Bornens et al., 2005). Lab-on-a-chip bioanalytic micro-systems introduce multi-component co-cultures to simulate an array of cells by external factors and signals secreted by the cells themselves to engineer a functional tissue. A controllable gradient of drug captures downstream effects of metabolized drug on target organ and conditions in parallel for physiologically-based pharmacokinetic (PBPK) models (Cheng et al., 2009).

Leading microfluidic devices use microfluidic systems and controlled cell seeding to produce cellular microenvironments to facilitate homotypic interaction by co-culture. Vasculature

and metatastic prostate cancer microfluidic models use co-culture to understand specific cytokines and growth behavior mechanisms (J. W. Song et al., 2009; Takayama et al., 2009). The effect of stem cells on cancer apopotosis is evaluated in vitro by unidirectional perfusion of a microfluidic device (Kong, Song, & Li, 2008). Microfluidic co-cultures of hepatocytes with non-parenchymal and stem cells are used to study 3-dimensional capillary morphogenesis and drug toxicity (Cheng, Novik, Maguire, Chao, & Yarmush, 2010; Kamm et al., 2009). In these leading microfluidic devices, microfluidic channels are fabricated in an elastoployer by soft lithography with wet chemical etching or integrated on a polystyrene biochip and cell seeding is controlled by diffusion across matrix, semi-permeable membranes or time course introduction of cell types.

1.1.2   NASA space life science interest

NASA and its partners are committed to introducing appropriate new technology to enable learning and living safely beyond the Earth for extended periods of time in a sustainable and possibly indefinite manner. In the responsible acquisition of that goal, life sciences is tasked to tune and advance current medical technology to prepare for human health and wellness in preparation for long term manned missions. The space environment changes the condition and function of biological systems from organ system level function to the shape of individual organelles.

The space environment causes psychological, physiological and pathological changes in biological behavior (Harris et al., 2010; Tamma et al., 2009; Vernikos & Schneider, 2010; Williams, Kuipers, Mukai, & Thirsk, 2009). Organ system level function to the shape and volume of individual cell organelles are effected by microgravity, stress, and radiation in space environment (Baqai et al., 2009b; Talbot, Caperna, Blomberg, Graninger, & Stodieck, 2010b). Biological systems in the space environment are subjected to a suite of environmental stimulation not present on Earth (F. A. Cucinotta, M. H. Kim, V. Willingham, & K. A. George, 2008a; Hellweg & Baumstark-Khan, 2007). NASA and its partners must characterize biological deviations between Earth conditions and space environment and possible vulnerabilities of current space flight

medicine. The effect of space stress and effectiveness of existing medical technology must be characterized to prepare appropriate health systems requirements. NASA and its partners are leveraging biomimetic design and microfluidics to fabricate in vitro ground models of biological systems. These closed systems with tunable dynamic perfusion allow provide researcher control over the environmental stimulation and transient interaction between various cell types.

1.1.2.1   Radiation

Space radiation is comprised of protons, helium nuclei, high-Z high energy ions and other high energy sub-atomic particles generated in secondary collisions with tissue and spacecraft (F. A. D. Cucinotta, M., 2009). Astronauts on the International Space Station are exposed to 50-2000 mSv (milli-Sievert) of radiation over 6 months, compared 1.8 mSv for the average human on Earth over the same period (F. A. Cucinotta & Durante, 2006; F. A. Cucinotta, M. H. Y. Kim, V. Willingham, & K. A. George, 2008b). Radiation effects biological tissue in the following two ways (1) impairment of tissue function due to significant cell death and (2) increased risk of carcinogenesis caused by genetic dysfunction due to DNA molecule damage. Additional health effects include increased incidence of early appearance of cataracts after low doses of space radiation, less than 8 mSv (F. A. Cucinotta et al., 2001).

NASA's Chief Health and Medical Office define permissible exposure limits for short term and career astronauts to limit the risk of exposure induced death from fatal cancer. A lack of proven radioprotective measures shortens an astronaut's time in space and increases the risk of serious health complications. The risk of cancer morbidity due to radiation exposure in space significantly affects the longevity of astronaut's careers and long term health. NASA's Human Research Program recognizes effective radioprotective measures as essential for interplanetary travel and long-term manned space exploration (F. A. Cucinotta et al., 2008b).

1.1.2.2   Microgravity

Gravitational forces or the lack thereof effect dispersion of interstitial fluids in the body, cell secretion and therefore biochemistry of tissues, gene expression, and volume of individual organelles (Baqai et al., 2009b; Khaoustov, Risin, Pellis, & Yoffe, 2001; Talbot, Caperna, Blomberg, Graninger, & Stodieck, 2010a). NASA's space life science enterprise studies cell function in microgravity to prepare clinical dosing requirements and pharmacological thresholds for long term manned space exploration.

1.2   Biomimetic design considerations

1.2.1   Forced convection and mechanosensation thresholds

Forced convection of blood through the body's tissues creates shear stress on cells anchored to lumen wall. Also, shifting interstial fluid in the cell's microenvironment physically deforms the cell's lipid membrane and actin cytoskeleton, which activates pathways linked to the cell's nucleus and gene expression (Hayward & Morgan, 2009; J. H. Kim et al., 2009). Mechanosensitive ion channels, such as the transient receptor potential (TRP) proteins, on the cell membrane respond to deformation in the lipid bilayer to sense the force of a vibration and osmotic membrane stretch (Kung, 2005). Cells are dynamic materials, which fluidize and reorganize under mechanical stretch.(Hayward & Morgan, 2009; Trepat & Fredberg, 2007) A cell actively responds to mechanosensation by realigning its cytoskeleton to counterbalance applied load.(Katsumi et al., 2002; Matthews, Overby, Mannix, & Ingber, 2006) Elastic and inelastic distortion of the cell effects cell function.(Yang, Beqaj, Kemp, Ariel, & Schuger, 2000) The biological response to exogenous force is governed by both the initial input force and subsequent alteration in cell generated forces.(Guilak et al., 2009)   The mechanical stretch stimulates myosin motor activity which increases tension between the cell membrane and extracellular matrix.(Balaban et al., 2001; Pelham & Wang, 1999; Tan, Stronach, & Perrimon, 2003) The cell adapts to transient changes in the cell's intracellular tension and any externally applied force by adjusting its membrane tensile force using

biochemical signaling as molecular feedback to the myosin motors.(Ridley et al., 2003; Sarasa-Renedo, Tunc-Civelek, & Chiquet, 2006; Shiu et al., 2004; Torsoni, Marin, Velloso, & Franchini, 2005; Zhao et al., 2007) Either of these stimuli may be sufficient to create a microenvironment for widespread reprogramming of function and possibly cell differentiation.

In the liver, diffusion through a 3-dimensional network of microvasculature and bile canaliculi network carries nutrients, waste, and oxygen to parenchymal cells, hepatocytes, and non-parenchymal cells, such as the Kupffer and stellate cells (Neville et al., 2008). The relative volume of interstitial fluid to cell matrix is approximately one to one in liver sinusoid. The hemodynamic system flow rate and architecture cause capillary and hydrodynamic forces acting on the cells. These forces physically strain cell membrane and actin cytoskeleton to induce biomimetic environmental stimulation and cell-to-cell contact necessary to maintain phenotype stability (L. G. Griffith et al., 2002).

1.2.2 3D Heterotypic cell-to-cell contact for biomimetic in vitro function

In vitro liver fidelity of acute drug toxicity, species specificity, and phenotype stability are improved by heterotypic interactions and 3-dimensional culture (Y. Kim, Larkin, Davis, & Rajagopalan, 2010; Y. Kim & Rajagopalan, 2010; Kostadinova et al., 2013). Kim et. al. of Virginia Polytechnic Institute and State University mimics the hepatic sinusoid using stratified structure of hepatocytes, endothelial cells, and a polyelectrolyte surface to model the space of disse and biomimetic extra-cellular matrix modulus and hydration (Y. Kim et al., 2010; Y. Kim & Rajagopalan, 2010). In Kostadinova et. al. of Hoffmann-La Roche Ltd's 3-dimensional liver co-culture system, non-parenchymal cells synthesize an extra-cellular matrix through a screen between two interconnected nylon meshes (Kostadinova et al., 2013). Kostadinova's 3-dimensional co-culture demonstrated increased sensitivity to acute drug toxicity, human vs. rat toxicology specificity, and up-regulated 3 out of 4 hepatic proteins to in vivo levels over 2-dimensional cultures.

The Hayflick phenomenon quantifies the number of times a normal cell is able to divide before cellular senescence (Hayflick, 1965). Wistar Institute researcher Leonard Hayflick empirically demonstrated normal human fetal cells divide 40-60 times before genetic transformation. Hayflick's cultures were mono-layer cell sheets, fed with medium and stored in an incubator. More recent work stabilized epithelial cells for more than 1.5 years using a 3D in vitro culture environment and the extracellular matrix material Matrigel (Sato et al., 2009). In vivo the structure of intestinal crypts collapse as a result of local depletion of Lgr-4 and Lgr-5 Wnt signal enhancer.

1.2.3   Tortuosity through the internal cell-laden features

Macro ($>10^{-3}$ m) external surface geometry and micro-scale (10^{-3}–10^{-6} m) internal pore architecture and interconnectivity is controllable using bio-additive manufacturing techniques (Yoo, 2012). Yoo of Daejin University developed a library of internal pore architecture designs into a unit cell library to design and assemble entire scaffolds (Yoo, 2012). Yoo designed and fabricated a fully interconnected porous scaffold of pre-determined exterior and interior geometry using automated process using the intersection Boolean operation recursively (Yoo, 2012).

Engineering scaffold permeability to decrease resistance of mass transport by shortening diffusion pathways improves scaffold performance (Pennella et al., 2013; Sachlos & Czernuszka, 2003). Permeability of interconnected pore structures fabricated from mathematically defined scaffolds is greater than salt leached structures (F. P. Melchels et al., 2010b; F. P. W. Melchels et al., 2010). Controllable scaffold parameters are pore size and an interconnected pore structure which optimizes phenotype specific surface area preferences, cell migration, and mass transport profiles of nutrients and waste (F. P. W. Melchels et al., 2010; Oh, Park, Kim, & Lee, 2007; Owen & Shoichet, 2010; Sobral, Caridade, Sousa, Mano, & Reis, 2011). Sobral et. al. of the University of Minho manipulated the mechanical properties and cell seeding efficiency of a 3-dimensional scaffold by optimizing the internal pore structure and gradients using rapid prototyping techniques

(Sobral et al., 2011). Pore size gradients of 750-100-750 and 100-750-100 μm increased cell seeding efficiencies from 30-40% for homogenous pore structures to 70% and 65% respectively. Oh et. al. of Hannam University published phenotype-specific scaffold pore size preferences based on in vitro cell proliferation over 8 weeks (Oh et al., 2007). Fibroblasts proliferation was fastest in 186-200μm pores of the surveyed 88-405μm pore range, possibly due to increased surface area for greater cell attachment. Melchels et. al. of University of Twente mathematically defined the pore space in a scaffold to fabricate volume fraction and size gradients as well as variable pore structures (F. P. Melchels et al., 2010b; F. P. W. Melchels et al., 2010). The Young's modulus was greatest for cube structure and the scaffold's deformation during loading was more homogenously distributed through gyroid structure than the cube (F. P. W. Melchels et al., 2010). Interconnected gyroid pore structure delays the formation of a cell colony covering the scaffold periphery and increases cell migration into the scaffold and mass transport, compared to salt-leeched scaffolds (F. P. Melchels et al., 2010b).

1.3   Methodological progress toward a high fidelity in vitro model

The key technological challenge for methodological progress of in vitro cell models is fabrication of the proportion and sequence of mass transfer through an in vitro micro-organ network (Derby, 2012). The engineering solution is technology to control and stimulate cells, including abiotic environmental factors and biotic cell-to-cell signaling. Abiotic factors include forced convection through cell-laden architecture. Nutrient renewal/waste removal is controllable by the rate of forced convection using pumping mechanisms. The mechanical sensitivity of the cells in the flowing fluid is investigated or negated by the selection of the channel geometry and fluid speed. In vivo vascular networks modeled as microfluidic channels cell volume: fluid volume closer to the biomimetic 1:1 than conventional petri-dish culture of a mono-layer of cells in a pool of medium. Additionally, microfluidic platforms require less cells and soluble agents than petri-dish experimentation. Macro-scale patterning of cell-laden architecture by scaffold-guided tissue

engineering or 3D printing techniques produces explicit architecture. The macro-scale patterning is designed to fit patient specific implant sites for regenerative medicine applications and more generally ensure diffusion to the cell-laden core for in vitro models. Micro-scale patterning mimics in vivo cell-to-cell contact and hetero-cellular packaging. Table 1-1 presents the key technology for methodological progress in microfluidic technology for drug discovery. Figure 1-2 presents resolution considerations (macro-, micro- and nano-) to assemble biomimetic cell-laden architecture.

Table 1-1. Key technology for methodological progress in microfluidic technology for drug discovery.

	In Vivo Characteristic	Advantage	Enabling Technology
Abiotic	Forced convection through tissue	Nutrient renewal/Waste removal Mechanosensation	Pumping mechanism
Abiotic	Microfluidic vascular network	Similar cell to fluid volume ratio Small sample size	Microfluidic technology
Biotic	Macro-scale patterning	Shaped to fit patient's implant site	Scaffold fabrication/3D printing
Biotic		Ensure diffusion of nutrients/waste removal	Controlled cell seeding
Biotic	Hetero-cellular packaging	Cell-to-cell contact Embed structural components and nano-scale artifacts	
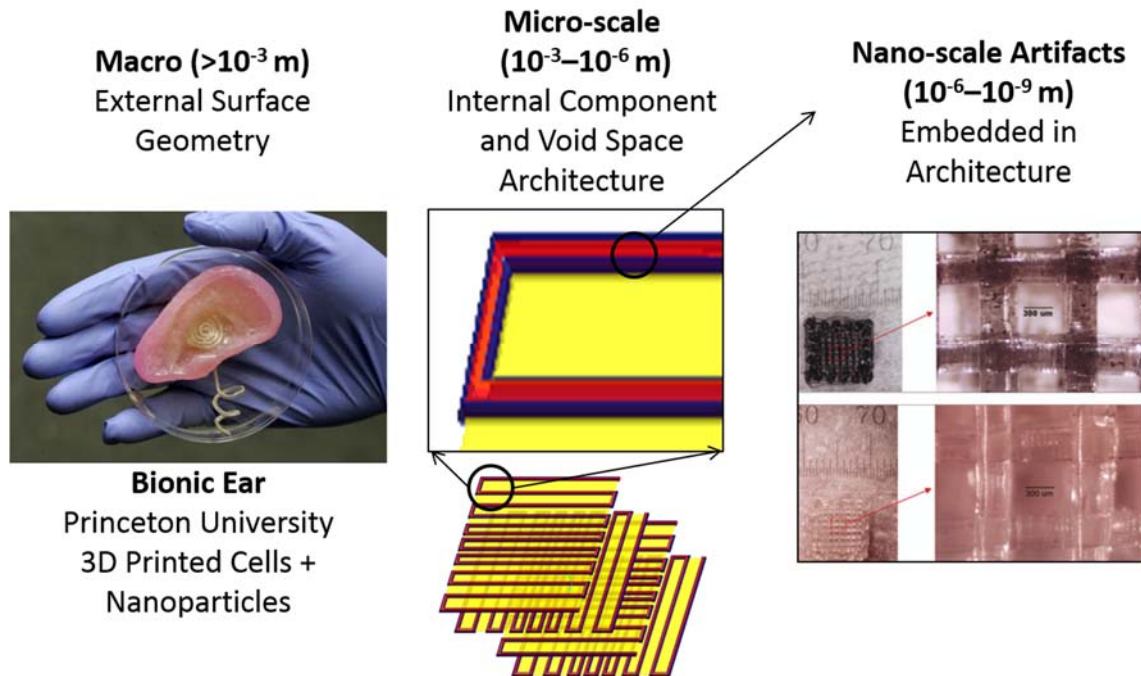
Figure 1-2: Bio-additive techniques to control architecture and interconnectivity.

1.3.1   Microfluidic technology

Decisions regarding the biologically relevant sequence of events and criticality of separating up-stream and down-stream biological responses between cells along the device's channel or between cell-laden compartments are considered. The pathway of the channels defines the sequence of events throughout the microfluidic system. The medium perfused through the channels is a source of nutrients and sink for waste, biologically synthesized proteins and other non-membrane bound paracrine/autocrine signals. Medium containing drug or other soluble cues is a source of the soluble cue and a sink for the metabolized drug or non-membrane bound biologically synthesized response to the drug. Dissolved cues lock-and-key bind to receptors on the cell's plasma membrane or are engulfed by the cell. The cell responds to the binding or absorption action with changes in viability, self-organization, and signaling or gene expression over time. Through a linear system with a single inlet and a single outlet the soluble cue first effects the biology closest to the inlet. Cells downstream of the inlet are effected by soluble cue itself and the response of the biology

upstream. The reaction time is controlled by the flow rate. The sequence of interactions between the drug and specific biological entities is controlled by distribution of such entities between the inlet and outlet. Channel patterns with a single flow path between the inlet and outlet strictly separate the reaction of the cells or distinct cell-laden compartments as a consequence of the up-stream biology. Channel patterns with a network design where channels cross cannot as easily separate up-stream and down-stream facets of the biological response. However, the bifurcating flow patterns of a network design may better model the micro-circulation and hydrodynamics forces present in mature, functional human tissue.

1.3.2   3-dimensional controlled cell seeding

Interfacing biology and architecture in built biological systems with reproducibility and engineering process control requires advanced manufacturing (Hamid, Wang, Zhao, Snyder, & Sun, 2014; W. Sun, Starly, Darling, & Gomez, 2004). Bioprinting is a computer aided manufacturing method with process control over (1) macro-scale (10^{-3}-10^{-1} m) architecture and (2) micro-scale (10^{-4}-10^{-5} m) heterogeneous packaging of components and internal features. Cell printing assembles biologics during scaffold fabrication to avoid characteristically low cell seeding efficiencies and asymmetric distribution caused by seeding post-fabrication (Li, Ma, Kniss, Lasky, & Yang, 2001; F. P. Melchels et al., 2010b). Colonization on periphery of the scaffold due to cell seeding process or limited mass transport through the scaffold prevent viable 3-dimensional colonization to the interior of the scaffold. Incorporating cells into the scaffold fabrication process provides controlled cell seeding for uniform cell density or pre-determined cell assembly.

Macro-scale architecture is critical if the built biological system is designed to physically fit into a larger system. Micro-scale heterogeneous packaging of organisms and support artifacts is critical to the function of the built biological system. Additional artifacts heterogeneously packed with the biology during printing spatial-temporally effect the built system's mechanics, physics, and chemistry. Artifact candidates include - load bearing structural elements (Hamid et al., 2011;

Shor, Guceri, Wen, Gandhi, & Sun, 2007), open porous network for diffusion(S. Khalil & Sun, 2009b), and magnetic nanoparticles(Buyukhatipoglu, Chang, Sun, & Clyne, 2010b).

The advantage of multi-nozzle deposition are summarized as (1) controlled chemical cross-linking, (2) 3-dimensional porous network for controlled gas and soluble cue exchange, and (3) heterogeneous 3-dimensional scaffold assembly.

1.3.2.1 *Controlled Chemical Cross-linking*

One fast effective method to form rigid polymer formations is chemical cross-linking. A cross-linking solution polymerizes a pre-polymer via contact during a reaction time. Controlled extrusion of both the pre-polymer and cross-linking solution is desirable to pattern the polymer structure and control volume fraction of both solutions in the reaction environment. Two techniques for the controlled extrusion include (1) single and (2) dual nozzle printing. Single nozzle printing requires mixing the matrix material and cross-linker before loading them into the dispensing chamber. Cross-linking begins when the two components are combined; prior to printing. Dual nozzle printing requires each component to be loaded into separate nozzles, and then extruded simultaneously. Mixing would take place during extrusion. Figure 1-3 presents a schematic and photograph of both techniques.

Single nozzle printing has a greater risk of nozzle occlusion and introduces geometric variation into scaffold architecture. The process parameters and applied pressure to extrude the material are constant during the printing episode. As the scaffold is printed and time passes since the components were combined, the degree of cross-link and viscosity of the printed solution increases. The applied pressure to extrude the solution remains the same, while the viscosity is increasing. Therefore, the diameter of the extruded strut will be decrease as the printing episode continues. Additionally, layers must be cross-linked prior to addition of subsequent layers. If the first layer is cross-linked, then the remaining material in the nozzle must also be cross-linked, as

components were combined at the same time. This means the nozzle is occluded and printing is not possible. Dual nozzle printing solves the occlusion risk and geometric variance by combining the components on the scaffold.

Dual nozzle printing allows the investigator to more fully leverage the multi-nozzle deposition system's capability to reproducibly print polymer scaffolds. Dual nozzle printing requires each component to be loaded into separate nozzle, and then extruded simultaneously. Mixing would take place after extrusion. The risk of occlusion can be mitigated by the position of the nozzles. Additionally, the fluid properties of the solutions remain constant during printing. Multi-nozzle deposition process parameters are tuned to control the volume fraction of both the pre-polymer and cross-linking solution during printing. Printing will be conducted using the dual nozzle printing set-up.
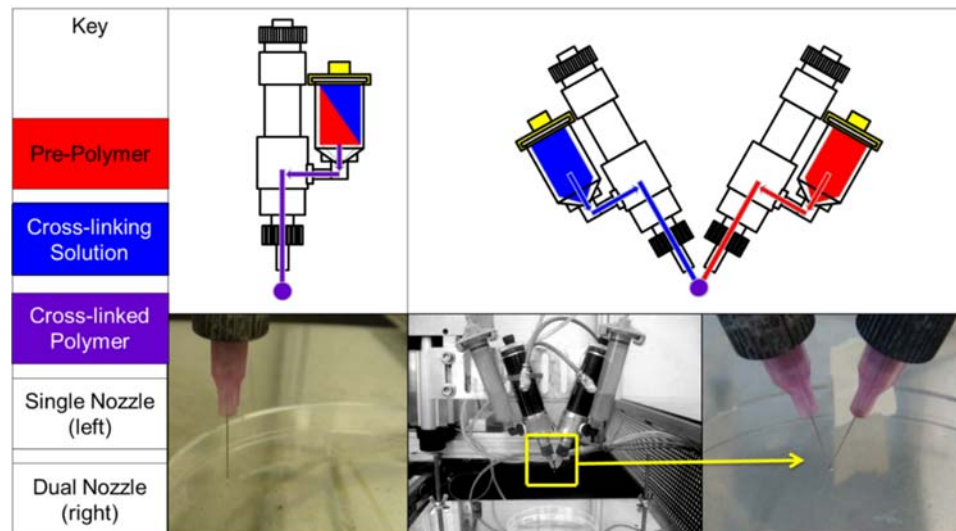
Figure 1-3: Single (left) and dual (right) nozzle techniques for controlled extrusion of pre-polymer and cross-linking solution. The flow rate of each nozzle in dual set-up is independently controlled.

1.3.2.2   3D Porous Network for Controlled Gas and Soluble Cue Exchange

Fabrication of defined pore dimensions is a significant challenge of scaffold guided tissue engineering.   Oxygen diffusion is limited to 100μm (Sant, Hancock, Donnelly, Iyer, & Khademhosseini, 2010). In vitro control over the principle spatial features of vascularized solid tissues (the lumen, endothelium, and extra-vascular space) regulates and balances mass transfer in 3-dimensional cell-laden constructs (Miller et al., 2012). Engineering control over the multi-scale architecture of pore channels and junctions, as well as lumen diameter and circularity are key advantages of bio-additive manufacturing. Miller et. al. of the University of Pennsylvania templated a porous network through a 3-dimensional cell-laden construct using a printed carbohydrate glass scaffold (Miller et al., 2012). Cell viability and function is improved over non-perfused models for near-physiologic cell densities. The porous network is templated using a carbohydrate glass scaffold fabricated using 3-dimensional printing and temperature controlled pneumatically driven extrusion.

Printed scaffolds assume two complementary environments (1) open network for diffusion of gas and soluble cues and (2) printed polymer. Figure 1-4 presents photographs of two 10+ layer scaffolds fabricated by multi-nozzle deposition. The cell-laden environment and open pore network for diffusion are engineered to maintain cell viability from the scaffold surface to the core. The additive manufacturing process uniquely offers control over internal scaffold architecture.
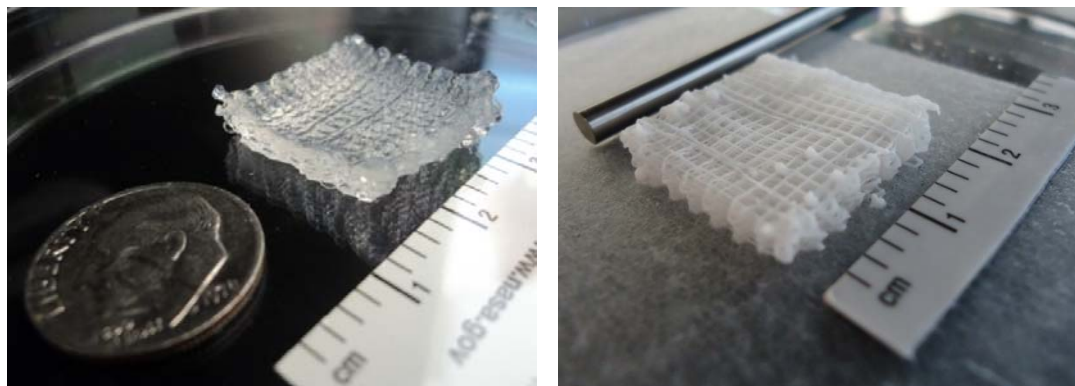
Figure 1-4: Porous printed scaffold by multi-nozzle deposition system. Scaffold is a 10-layer 3-dimensional scaffold of printed polymer square waves. Scaffold contains two complementary environments (1) open network for diffusion of gas and soluble cues and (2) printed polymer. Alg (left) and mineralized Alg -Alg-HA (right) scaffold pictured.

1.3.2.3   *Heterogeneous 3-Dimensional Scaffold Assembly*

Cell printing assembles biologics during scaffold fabrication to avoid characteristically low cell seeding efficiencies and asymmetric distribution caused by seeding post-fabrication (Li et al., 2001; F. P. Melchels et al., 2010b). Colonization on periphery of the scaffold due to cell seeding process or limited mass transport through the scaffold prevent viable 3-dimensional colonization to the interior of the scaffold. Incorporating cells into the scaffold fabrication process provides controlled cell seeding for uniform cell density or pre-determined cell assembly within a scaffold.

Macro ($>10^{-3}$ m) external surface geometry and micro-scale (10^{-3}–10^{-6} m) internal pore architecture and interconnectivity is controllable using bio-additive manufacturing techniques (Yoo, 2012). Yoo of Daejin University developed a library of internal pore architecture designs into a unit cell library to design and assemble entire scaffolds (Yoo, 2012). Yoo designed and fabricated a fully interconnected porous scaffold of pre-determined exterior and interior geometry using automated process using the intersection Boolean operation recursively (Yoo, 2012).

Multi-nozzle deposition for scaffold printing is expanded to multiple materials with additional print heads. Each print head is loaded with a unique material. Each print head is

independently controlled to fabricate specific macro- and micro- scale architecture. Architecture includes the pattern of the printed polymer, volume fraction of disperate materials, width of the printed strut, and layer-to-layer height. Figure 1-5 presents photographs of multi-material scaffold printing by multi-nozzle deposition. Scaffold is assembled by additive manufacturing layer-by-layer. The technique offers control over internal architecture of the scaffold.
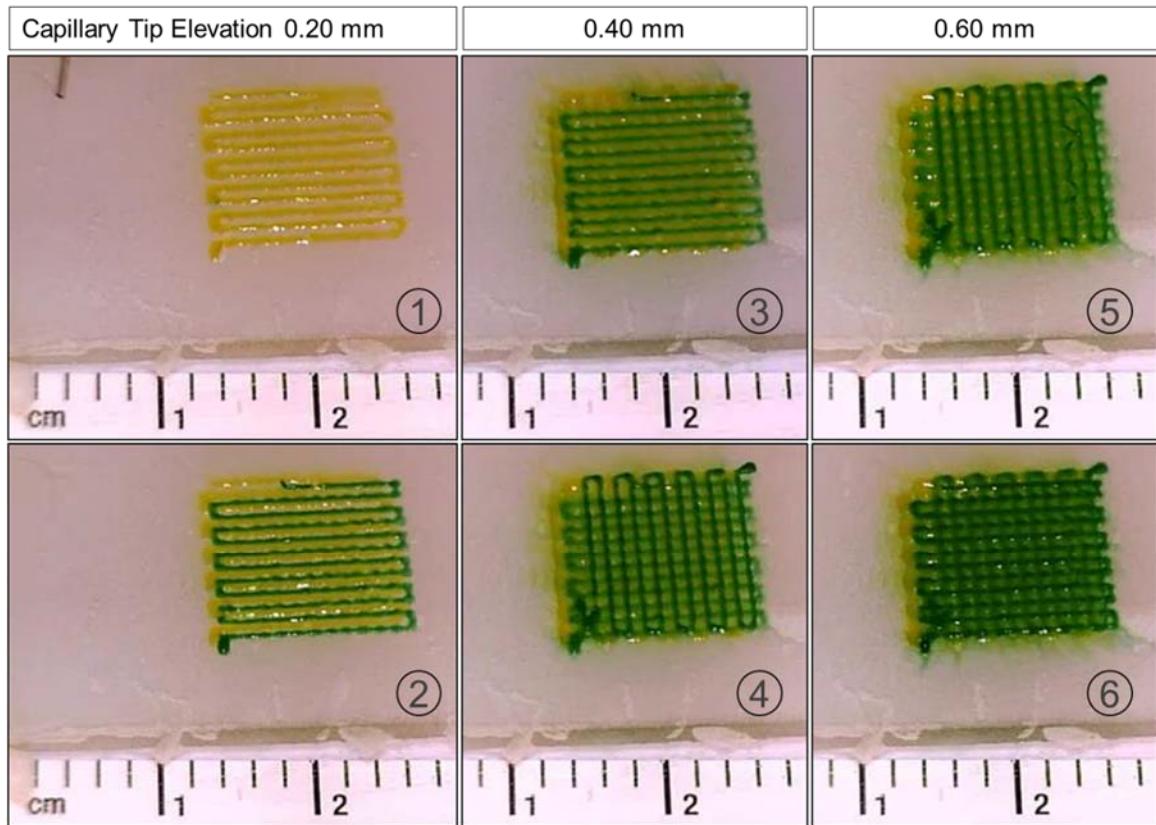
Figure 1-5: Heterogeneous 3D Scaffold Assembly by Multi-Material Deposition. Printed 3-dimensional multi-material scaffold fabricated by multi-nozzle additive manufacturing. Yellow and green polymer solutions are individually extruded into square wave pattern from independent nozzles. Dispensing capillary tip is raised up away from printing substrate to print additional layers on previous layers to fabricate 3-dimensional scaffold. Final scaffold is 3 layers. Each layer is a nested yellow and green polymer solution. Images are in time sequence from 1-6.

1.3.3   Hetero-cellular packaging

The objective of biomimetic design for tissue engineering applications is to reverse engineer the in vivo performance and responsiveness of a target tissue or set of tissues in a lab environment based on histology and physiology. The framework of concepts for biomimetic design includes define key structure-function relationships, support simplifying assumptions and design within manufacturing limitations (Hoganson et al., 2010; Nawroth & Parker, 2013). A novel synchronized multi-material bioprinter (SMMB) deposition head packages discrete solutions in a controllable 1-dimensional array to be printed as a heterogeneous filament or nano-liter droplets. The printhead is integrated with the bio-additive manufacturing technique multi-nozzle cell printing's design model, motion, and material delivery sub-systems.

Bio-additive manufacturing techniques for cell-laden 3-dimensional scaffolds and microfluidic devices are an enabling technology for high fidelity in vitro liver models. Yamada et. al. of Chiba University engineered a microfluidic device to package hepatocytes, endothelial cells, buffer, and gelation solution in a single outlet stream as a heterotypic hepatic fiber (Yamada et al., 2012). Independent regulation of each solution's flow rate controls the fiber diameter and the proportion of each phenotype to biomimic native liver. Heterotypic and homotypic interaction preserved in vitro liver-specific function during the 90 day study. A novel synchronized multi-material bioprinter (SMMB) deposition head packages discrete solutions in a controllable 1-dimensional array to be printed as a heterogeneous filament or nano-liter droplets. The printhead is integrated with the bio-additive manufacturing technique multi-nozzle cell printing's design model, motion, and material delivery sub-systems.
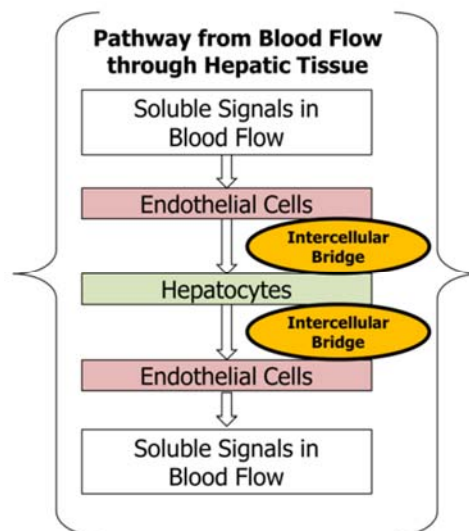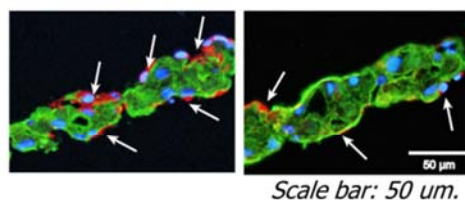
Figure 1-6: Heterotypic hepatic fiber of hepatocytes and endothelial cells fabricated using a microfluidic device (Yamada et al., 2012) and schematic of 1-dimsensional array of hepatic tissue.

Microfluidic techniques assemble multiple material inlets in a single outlet channel without mixing due to low inertial forces in micro-scale cross-sectional channels. SMMB deposition head leverage non-mixing microfluidic flow to combine multiple materials in a heterogeneous array prior to deposition. SMMB improves printing resolution over MND and offers the opportunity for mass transfer and chemical reactions, such as partial cross-linking, prior to deposition. The SMMB deposition head design process is as follows: (1) Component materials are selected based on composition of the target mature, functional tissue, support material, and requirement for cross-linking solution. (2) The arrangement of the materials is defined based on cell-to-cell contact in vivo and construction requirements. The volume fraction of each constituent component can be dynamically varied during the build cycle and is not restricted by the channel network in the deposition head. (3) The layout of the channel network is defined to assemble the materials heterogeneous layered method or axisymmetric style, as presented in figure 1-7.
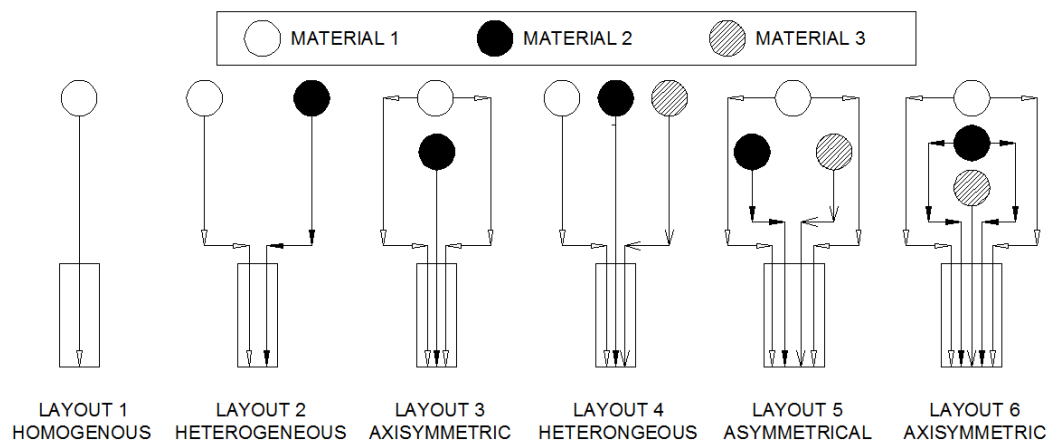
Figure 1-7: Microfluidic network layouts for homogenous, heterogeneous, axisymmetric, and asymmetrical combination of up to three materials.

Unit cell design of a fiber cross-section printed using synchronized multi-material (SMMB) system. Solutions may include cell-laden, chemically reactive, sacrificial support material to produce void space. Volume fraction of each solution can be tuned using the flow rate controlled by programmable syringe pumps. Assembly of solutions is controlled by the design of the microfluidic system. Conventional 2-dimensional microfluidic system can produce 1-dimensional array of solutions. A more sophisticated 3-dimensional microfluidic system can produce a 2-dimensional array of solutions.
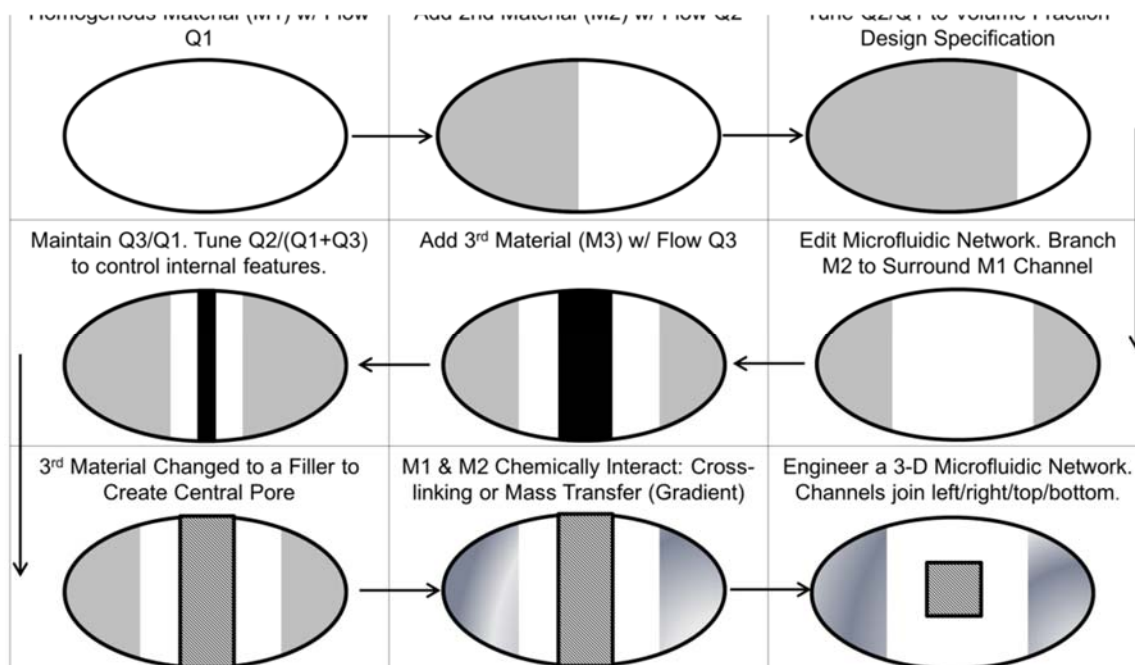
Figure 1-8: Unit cell design of a fiber cross-section printed using Simultaneous Multi-Material Print head and Bioprinter System. Solutions may include cell-laden, chemically reactive, sacrificial support material to produce void space. Volume fraction of each solution can be tuned using the flow rate controlled by programmable syringe pumps. Assembly of solutions is controlled by the design of the microfluidic system.

Conventional 2-dimensional microfluidic system can produce 1-dimensional array of solutions. A more sophisticated 3-dimensional microfluidic system can produce a 2-dimensional array of solutions.   SMMB channel networks to combine multiple materials in a 1-dimensional array are presented in figure 1-9. 3-dimensional SMMB deposition head channel networks enable more sophisticated 2-dimensional heterogeneous array of multiple materials. Figure 1-10 presents 3-dimensional SMMB channel networks to assemble multiple materials in a 2-dimensioanl array. 3-dimensional features such as arches and channels joining from the top (not just left and right) are required to achieve the presented 2-dimensional array in the SMMB combined flow outlet channel.
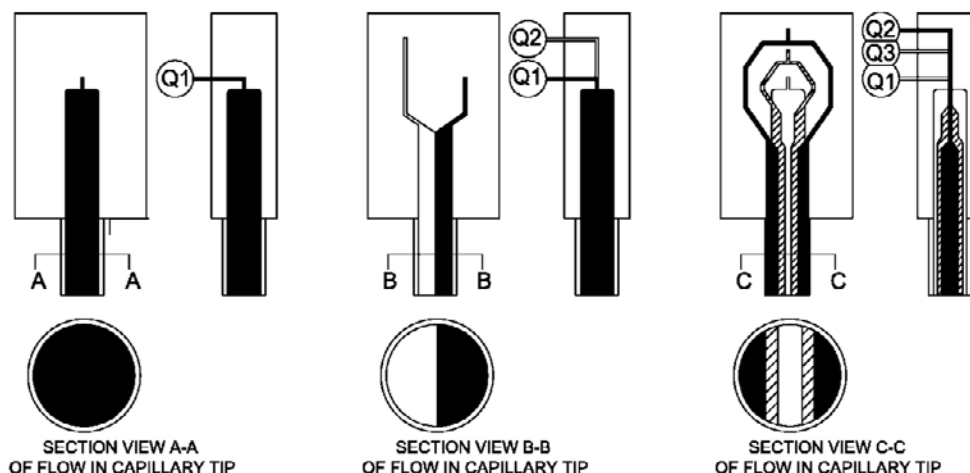
Figure 1-9: Front/right/section view of homogenous (left), layered (center) and axisymmetric (right) 2-dimensional SMMB deposition head channel concepts to assemble multiple materials in 1-dimensional array.
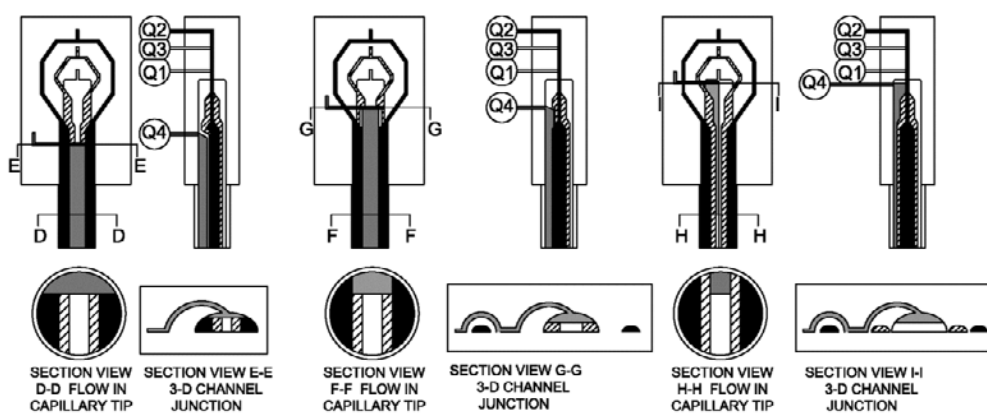
Figure 1-10: Front/right/section view of homogenous (left), layered (center) and axisymmetric (right) 3-dimensional SMMB deposition head channel concepts to assemble multiple materials in 2-dimensional array.

1.4   *Research objective and approach*

The objective of the presented research is the development of design, characterization and fabrication approaches which integrate physiologically relevant microfluidic techniques and hetero-cellular architecture for cell-laden models by leveraging combinations of the biofabrication techniques precision extrusion deposition, multi-nozzle cell printing, replica molding, and a novel

synchronized multi-material bioprinting system. This research focuses on the development of a synchronized multi-material bioprinter for the fabrication of 3D hetero-cellular constructs. The specific research objectives are:

1. To combine multi-nozzle deposition system with a microlfuidic platform for controlled cell seeding in a microfluidic device for a hetero-cellular in vitro model for drug testing.

2. To define a 3D printing and replica molding processes to fabricate microfluidic and scaffold environments with control of the macro-scale (10^{-3}-10^{-1} m) patterning of channels/structural elements and micro-scale (10^{-4}-10^{-3} m) channel cross-section of internal features.

3. To develop and characterize an integrated synchronized multi-material bioprinter system to produce nano-liter droplets and 10^{-4}-10^{-3} m diameter filaments with a heterogeneous packaging resolution of 10^{-5}-10^{-3} m.

4. To apply the synchronized multi-material bioprinter system to produce hetero-cellular models to study radioprotective drug efficacy in co-culture and metabolism rates in simulated weightlessness environments.

The presented biofabrication methods are applied to fabricate a hetero-cellular liver model to study drug efficacy of the pro-drug amifostine to shield liver from radiation genetic damage and pharmacokinetic up-take in model microgravity. An outline of the biomiemtic condition, biomanufacturing processes and apllication are presented in figure 1-11.
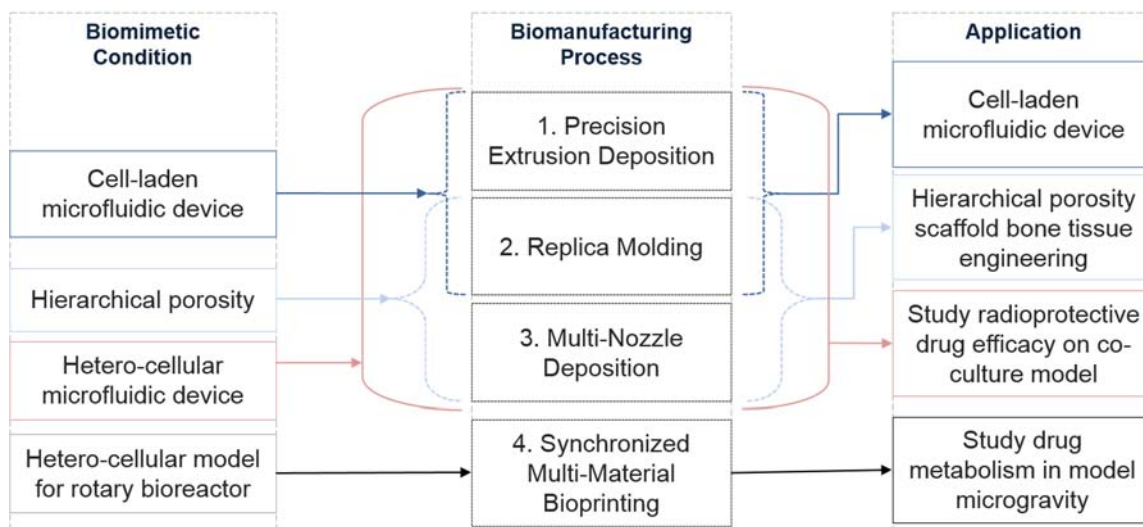
Figure 1-11: Outline of the presented research approach to combine biomanufacturing processes to achieve physiologiclaly relevant hetero-cellular architecture and perfusion with microfluidic and cell printing enabling technology.

1.5 Thesis outline

This thesis outline is as follows:

Chapter 2 develops 3D printing and replica molding processes to fabricate interconnected and hierarchical structural environments for cell culture. Two different 3D printing and replica molding processes are introduced: (1) a precision extrusion deposition and replica molding process to produces microfluidic networks and (2) a multi-nozzle deposition and freeze casting process to produce hierarchical tissue scaffolds. Both 3D printing processes integrate a 3D motion system with a continuous extrusion material delivery system to print patterns of the extruded filament. Internal features and external surfaces are explicitly assembled due to the layer-by-layer construction of the printed pattern. The 3D printing process parameters control the macro-scale structure of the printed pattern/void space (10^{-3}-10^{-1} m resolution) and extruded cross-section's shape and size (10^{-4}-10^{-3} m). Once fabricated, the printed pattern is embedded in a liquid-phase of a secondary material, which is subsequently cured. The composite printed pattern/ secondary material is either directly used or the printed pattern is removed, leaving a template of open

channels or pores. Cell-material attachment is presented. The presented processes introduces the capability to fabricate 3D hierarchical, composite or porous/open channel architecture for scaffold guided tissue engineering.

Chapter 3 integrates the advanced biomanufacturing techniques developed in chapter 2 to fully construct a hetero-cellular microfluidic devices for drug efficacy applications. 3-dimensional open channel networks fully embedded in PDMS are fabricated by precision extrusion deposition (PED) and replica molding. Forced convection through the channels is controlled by additional hardware components and a programmable syringe pump. Cell suspension is pumped into the device, left static for 12-24 hrs for adhesion and then perfused for nutrient supply/waste removal. Alternatively, multi-nozzle deposition (MND) for hetero-cellular seeding throughout the network and in channel cross-section defines the position of cell types, support material and matrix. Applications of the system include space life science in vitro models to study radioprotective pro-drug efficacy in co-culture. Hetero-cellular contact is controlled by forced convection through a multi-chamber co-culture microfluidic device. Cell-laden devices are stimulated with radioprotective drug and radiation exposure to study drug efficacy in co-culture compared to mono-culture microfluidic devices.

Chapter 4 develops the synchronized multi-material bioprinting (SMMB) system to package different cell types and structural matrix material in a heterogeneous array and extrude the heterogeneous array along a tool path to build 3D biology-laden structures. The fully integrated system includes a 3D motion system, multi-nozzle material delivery system with synchronized multi-material deposition head and temperature control system. The 3D motion system is a set of three linear slides, each independently controlled by automation software. The motion system is used in two ways (1) as a linear build cycle discretizes a design into a stack of 2D tool paths for layer-by-layer construction or (2) as a periodic build cycle to control the accumulation and dispensing of a predetermined material volume. The multi-nozzle material delivery system with a

synchronized multi-material deposition head packages tissue matrix material-laden with cells and complementary support material in a heterogeneous array. The heterogeneous array is extruded along a tool path to produce a pattern (linear build cycle) or controlled total volume with constituent volume fractions of the component materials is dispensed (periodic build cycle). The resolution of internal features of the heterogeneous array is 10^{-5}-10^{-3} m, which improves the motion system's extruded filament patterning capability of 10^{-3}-10^{-1} m. Additional nozzles containing other heterogeneous arrangements, support material or crosslinking agents are each is independently controlled by automation software. A temperature control system expands the feasible set of tissue matrix materials to include thermally cross-linked materials such as Matrigel and collagen. The effect of the process on cell viability is presented.

Chapter 5 characterizes the synchronized multi-material bioprinting system's controllability and capability to fabricate heterogeneous nano-liter droplets and 10^{4}-10^{-3} m diameter printed filaments. Applications of the system include space life science in vitro models to study metabolic rate and drug efficacy in co-culture. Printed hetero-cellular droplets are loaded into high aspect ratio vessels and conditioned to weightlessness using a rotary cell culture system to study drug metabolic rate in model microgravity.

Conclusions of the conducted research and recommendations for future work are presented in Chapter 6.

CHAPTER 2: 3D PRINTING AND REPLICA MOLDING PROCESS FOR HETEROGENEOUS CELL CULTURE ENVIRONMENTS

2.1 Rationale

3D printing of porous scaffolds produces a built volume containing a minimum of two complementary microenvironments; one of the printed material and one of the porous void space surrounding the printed material. After the material/void space is defined during 3D printing build cycle, the void space can be filled with a secondary material. The secondary injected material is not constrained by rheological limitations or damaged by physical or thermal stress during printing. The second material can be more or less viscous than the manufacturing process requires or more sensitive to phyiscal or chemical degradation than printed materials. Injection and replica molding extend the advantages of additive manufacturing to include a greater library of materials and heterogenous multi-material designs. Advantages include controlled formation of internal features during the build cycle and heterogeneous placement of multiple materials throughout the 3-dimensional volume. In this work, PDMS elastomer and ceramic slurry are injected into 3D printed structures after fabrication. The resultant structure is heterogeneous and multi-material. Replica molding to remove the original printed scaffold from the second material creates a void space templated from the printed structure. In this work, two distinct processes are introduced which leverage 3D printing to fabricate two types of open channel networks: (1) a microfluidic network of open channels in a PDMS substrate and (2) hierarchical porous networks in a ceramic scaffold.

2.2 Precision extrusion deposition and replica molding of microfluidic networks

2.2.1 Purpose and description of method

The purpose of the fabrication method is to produce an interconnected 3-dimensional network of open channels with process control of the channel's cross-sectional width and height to 10^{-3} -10^{-4} m throughout the network. Conventional subtractive manufacturing methods to produce an open network of channels leverage chemical reactions or physical bombardment to remove material. The current challenge of subtractive techniques is control of the network's internal

features across multiple layers. Replica molding addresses this challenge using template structures, which are removed after molding to produce open porous space and channel networks. Therefore, the formability advantages of additive manufacturing are applicable to the design and fabrication of void space, including microfluidic networks.

Fabrication of a microfluidic network for multi-material deposition head or device is an indirect 3-dimensional printing process. Step 1 is the design of the microfluidic network. The design includes the macro-scale pattern of the network (10^{-1}-10^{-3} meter) and micro-scale channel cross-section (10^{-3}-10^{-4} meter). Step 2 is printing the design by precision extrusion deposition. The tool path is generated from the design's macro-scale pattern. The design is discretized into a stack of 2-dimensional layers. Each layer is printed, one on top of another, to produce the complete 3-dimensional design. Manufacturing process parameters are selected to control the flow rate and consequently the dimension of the extruded filament's cross-sectional width and height. Step 3 is replica molding of the printed pattern in polydimethylsiloxane (PDMS). Printed pattern is either attached to a surface and covered with uncured liquid PDMS or suspended in a pool of PDMS. PDMS fully cures over 48 hours at room temperature. Step 4 is removal of the printed pattern from the fully cured PDMS. The technique to remove the printed pattern depends on position of the printed pattern chosen in step 3. Printed patterns attached to a substrate and covered with PDMS can be manually removed, as they are exposed once the substrate is removed. Printed patterns entirely embedded in the PDMS are removed by liquefying and draining the printed pattern. Printed pattern is thermally liquefied or chemically dissolved with no effect to the PDMS. Figure 2-1 presents the fabrication method to produce a microfluidic network in a PDMS substrate by precision extrusion deposition and replica molding.
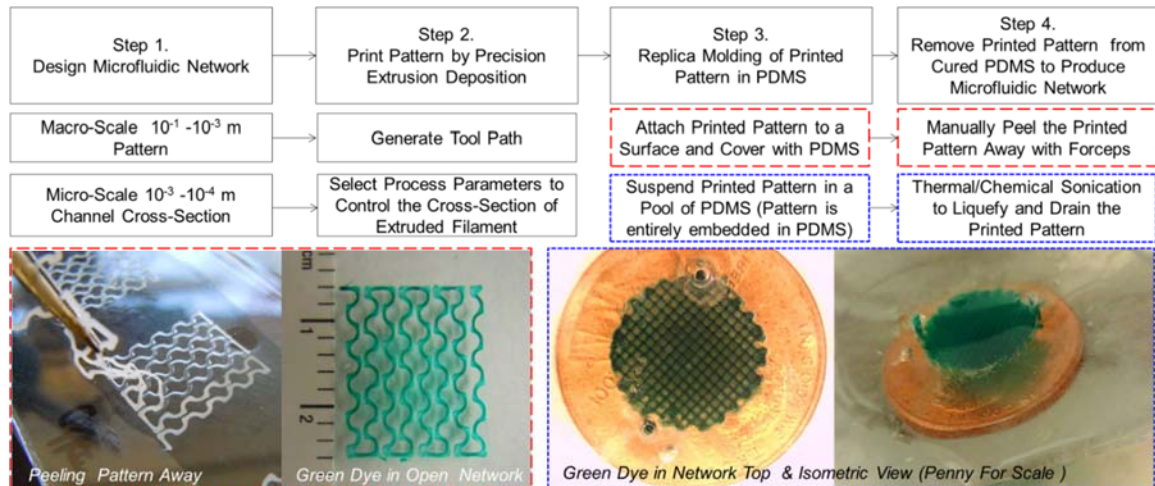
Figure 2-1: Fabrication method to produce a microfluidic network in a PDMS substrate by precision extrusion deposition and replica molding.

2.2.2   Step 1. Design microfluidic network

Step 1 is the design of the microfluidic network. The design is defined as the pathway of the channel network and geometric size of the channels. Design considerations capture the key facets of mature, functional tissue within manufacturing limitations and include the size and pathway of in vivo microfluidic networks. The microfluidic network's channels are sized to accommodate flowing fluid, viable cellular material with proliferative potential and extra-cellular matrix volume. The design includes the macro-scale pattern of the network (10^{-3}-10^{-1} meter) and micro-scale channel cross-section (10^{-4}-10^{-3} meter).

2.2.3   Step 2. Print pattern by precision extrusion deposition

Step 2 is printing a polycaprolactone (PCL) pattern by precision extrusion deposition. The tool path is programmed to draw the geometric pattern of the channel network. The design's macro-scale pattern is discretized into a stack of 2-dimensional layers. Each layer is printed, one on top of another, to produce the complete 3-dimensional network. Manufacturing process parameters are selected to produce a predetermined cross-sectional dimension and shape of the extruded filament by controlling the location and rate of material deposition. The dimension and shape of the cross-

section are defined in the set of design variables. Separate control of the printhead height and deposition rate on the substrate diminish the co-dependency of the cross-section's height and width. The PED's process information pipeline utilizes three sub-systems. Fabrication begins with (1) design model inputs to automation software, (2) motion system generates of a series of 2-dimensional tool paths, stacked layer-by-layer to produce a 3-dimensional volumetric construct, and (3) material delivery system to liquefy and extrude controlled amounts of thermoplastic material. Figure 2-2 presents the process information pipeline, as-built photograph and blow-out schematic of the material delivery system's extruder screw.
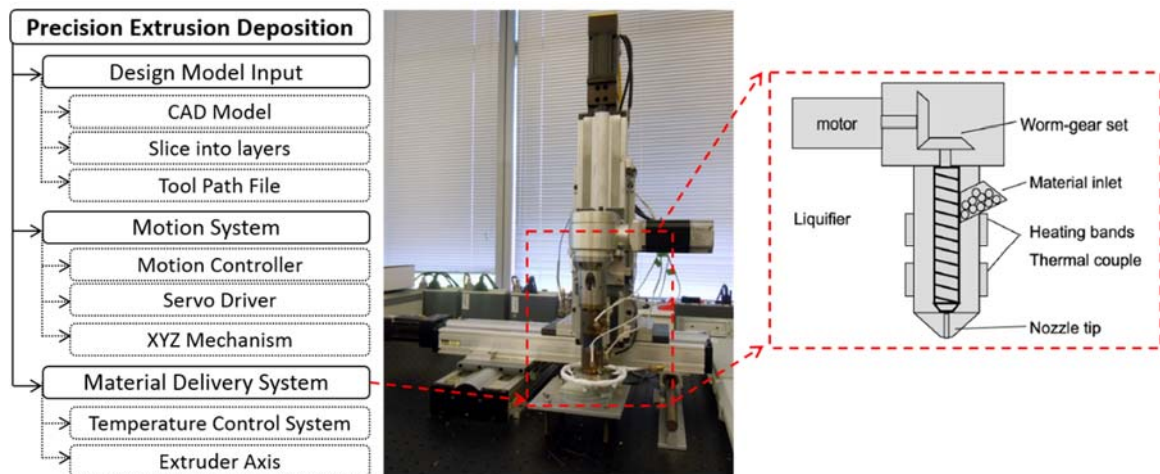
Figure 2-2: System configuration for precision extrusion deposition process. Process information pipeline and as-built system photograph presented. Inset is diagram of material delivery system extruder, reproduced from Wang et. al. 2004 (Wang et al., 2004).

A single build cycle may include variable printed geometric patterns and cross-sectional widths/heights. The set of design parameters is controlled by the process parameters, which can be automated to fluctuate during fabrication to produce gradient structures or irregular topologies. As an additive manufacturing process, this process control can be extended to internal features of a 3-dimensional printed construct. Figure 2-3 presents a time-lapse of a single layer PED build cycle. The geometric pattern and cross-sectional variations between the square wave and sinusoidal waves

are automated. Each geometric pattern and extruder screw speed are programmed to effect the printed filament shape and cross-sectional width. The extruder screw speed of the square wave is less than sinusoidal wave. Consequently, the width of the square wave is less than the width of the sinusoidal wave.

Figure 2-3: Macro-scale patterning of printed PCL square wave and sinusoid patterns by precision extrusion deposition.

2.2.3.1   *Definition of PED process parameters, material properties and design variables*

PED system performance is defined by a set of geometric design variables to arrange a thermally extruded polymer in 3-dimensional space with controlled deposition along a pathway and width/height of the extruded filament. The set of design variables, Ψ_{PED}, are a function of the set of geometric parameters of the built system X_{PED}, the set of process parameters, Ω_{PED}, and the extruded material properties, Φ_{PED}.   Process parameters are automated and can be adjusted dynamically during the build cycle period to fabricate gradient structures and multiple design variables in a single printed construct.   As such, the process parameters are a function of time. Equation 2-1 defines the set of design variables as a function of the geometric parameters, process parameters and material properties.

$$\Psi_{PED}(t) = f\{X_{PED}, \Omega_{PED}(t), \Phi_{PED}\} \qquad\qquad 2\text{-}1$$

Figure 2-4 is a schematic of the PED extruder barrel mounted to the motion system depositing a printed filament as extruder moves across a stationary printing substrate. Process parameters are identified, with the exception of extruder barrel temperature. The set of design variables are called out on cross-section of the printed filament.
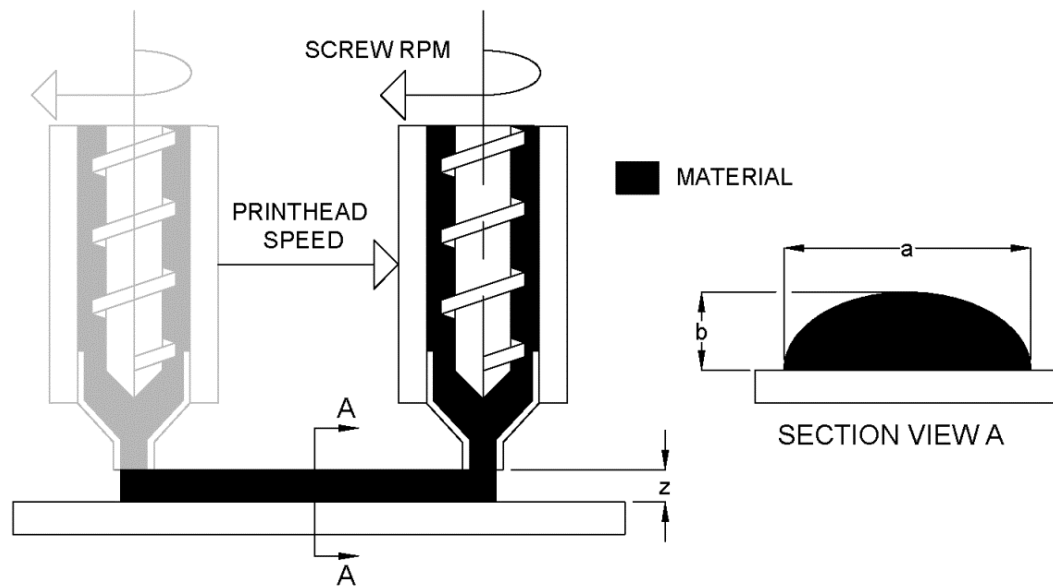
Figure 2-4: PED schematic of process parameters and printed filament design variables.

The PED system's fabrication objectives define the design variables. The fabrication objective is a 3-dimensional scaffold. The 3-dimensional scaffold's architecture features specific macro-scale ($10^{-3} – 10^{-1}$ m) placement and micro-scale ($10^{-4} – 10^{-3}$ m) cross-sectional width/height of the extruded filament. The macro-scale pathway of material deposition is controlled by the motion system to be repeatable to less than 10μm. Micro-scale design variables to characterize the printed filament's cross-section are controlled by system's process parameters. The dependence of the width and height of the printed filament is diminsihed, as each parameter is independently controllable and automated to be varied over the build cycle to transform throughout the construct.

Equation 2-2 defines the set of design variables as the printed filament's cross-sectional width, a, and height, b.

$$\Psi_{PED}(t) = [a\,(t)\quad b\,(t)\ ] \qquad\qquad\qquad 2\text{-}2$$

The raw printing material is thermoplastic pellets and are loaded into the extruder barrel, heated above the melt temperature, and extruded as a filament from a die secured to the outlet. Process parameters are defined by the system's hardware and software configuration. PED controllable process parameters are extruder die diameter, d, dispensing pressure, N, temperature of material delivery system, T_i, printhead speed, v, and height of the dispensing tip above the printing substrate, z. The temperature of the extruder barrel is regulated by two independent heating elements; (1) the first near the material inlet to melt the polymer and (2) the second near the outlet to maintain a molten polymer phase through extrusion. The pressure printhead speed, and height are automated and their value can be programmed to dynamically change during a build cycle. Such variables are presented as a function of time in equation 2-3. The diameter of the dispensing tip is selected from a prefabricated set of tips and cannot be changed dynamically during a build cycle. Equation 2-3 defines the set of independently tunable system process parameters.

$$\Omega_{PED}(t) = [d\quad N(t)\quad T_i\quad v(t)\quad z(t)] \qquad\qquad 2\text{-}3$$

The material property relevant to characterzing the flow through the extruder is visocsity. Polymer rheology is empirically defined from a parametric study of the temperature- and strain rate- dependence of viscosity. Equation 2-4 defines the set of material properties relevant to precision extrusion deposition of a thermoplastic as viscosity, μ. Viscosity is generalized as a function of strain rate γ, and temperature T.

$$\Phi_{PED} = [\,\mu = f(\gamma, T)\,] \qquad\qquad\qquad 2\text{-}4$$

Geometric parameters are measured using photographs of the as-built system and the image processing software ImageJ (NIH). Internal features of the extruder die could not be photographed and were defined using the manufacturer provided engineering drawing of the extruder die. Geometric parameters require changes to system's parts or configuration and remain constant from build cycle to build cycle. The set of PED geometric parameters are all specific to the barrel, screw and die of the extruder and include barrel diameter D, screw channel depth H, pumping zone length L, die length l, screw channel width W, die characteristic ε, screw helix angle θ, equation 2-5.

$$X_{PED} = [\ D \quad H \quad L \quad l \quad W \quad \varepsilon \quad \theta] \qquad\qquad 2\text{-}5$$

Table 2-1 presents the geometric, process, material, design, and derived parameters. Derived parameters assist in analytical characterization of the system. Derived parameters are not directly controlled by the operator and are not the specific performance objective of the process.

Table 2-1. Precision extrusion deposition system design variables, derived, geometric, material, and process parameters.

Symbol	Description	Process Window	Parameter Type
A	Cross-sectional area of printed filament	-	Derived
a	Printed filament width	-	Design
b	Printed filament height	-	Design
D	PED extruder barrel diameter	$20.0\ mm$	Geometric
d	PED extruder die diameter	$100,\ 150,\ 200,\ 250,$ $300,\ 350, 500\ \mu m$	Process
H	PED extruder screw channel depth	$3.0\ mm$	Geometric
K	PCL viscosity coefficient	$2.0 \cdot 10^7\,\mathrm{Pa}$	Material
L	PED extruder pumping zone length	$150.0\ \mathrm{mm}$	Geometric
l	PED extruder die length	$4.57\ \mathrm{mm}$	Geometric
N	PED screw RPM	$0.1 \leq N \leq 100.0\ \mathrm{RPM}$	Process
n	PCL viscosity index	-2.46	Material
Q	Net volumetric flow rate from PED extruder	-	Derived
Q_D	Drag volumetric flow rate	-	Derived

cont'd Symbol	Description	Process Window	Parameter Type
Q_N	Die restriction volumetric flow rate	-	Derived
Q_P	Pressure volumetric flow rate	-	Derived
p	Pressure in PED extruder	-	Derived
T_1	PED extruder barrel temperature, inlet	$65 \leq T_1 \leq 120°C$	Process
T_2	PED extruder barrel temperature, outlet	$65 \leq T_2 \leq 120°C$	Process
t	Time	-	
v	PED deposition head speed	$0.1 \leq v \leq 10.0 \; mm/s$	Process
v_z	Maximum down channel fluid velocity through PED extruder		Derived
$\overline{v_z}$	Average down channel fluid velocity through PED extruder		Derived
W	PED extruder screw channel width	17.0 mm	Geometric
z	Height between nozzle and substrate	$0.1 \leq z \leq 2.0$ mm	Process
α	Drag flow coefficient	$\pi DHW \cos\theta$	Derived
β	Pressure flow coefficient	$WH^3/12L$	Derived
ε	PED extruder die characteristic	-	Geometric
θ	Screw helix angle	18.5°	Geometric
μ	Material viscosity	KT^n	Material
ρ	Material density	1.145 g/cm^3	Material
ω	Die restriction coefficient	$\pi/128l$	Derived
Φ_{PED}	PED material parameters	-	Material
X_{PED}	PED geometric parameters		Geometric
Ψ_{PED}	PED design variables	-	Design
Ω_{PED}	PED process parameters	-	Process

2.2.3.2   Empirical characterization of PCL material parameters

In continuum mechanics the material property viscosity corelates the force in a fluid element with the velocity of the element, alternatively viscosity corelates the shear stress and shear rate. The form of the analytical expression requires the fluid to be classified as either (1) Newtonian or (2) non-Newtonian fluid. Linearly correlated viscous stress and fluid velocity are characteristically Newtonian fluids. Non-linear correlations are characteristically non-Newtonian fluids. The appropriate continuum mechanics classification of liquid phase PCL within PED operating

conditions is measured experimentally and then analyzed for classification. Equation 2-6 presents

the viscosity, μ, as a function of shear stress, τ, and shear rate, γ, for both fluid categories.

$$
\begin{aligned}
&(1) \quad Newtonian\ Fluid \quad\quad \mu = \tau/\gamma \\
&(2) \quad non-Newtonian\ Fluid \quad \mu = d\tau/d\gamma
\end{aligned}
\qquad 2\text{-}6
$$

The viscosity of liquid phase PCL is experimentally evaluated for thermal and mechanical

sensitivity. Equation 2-7 generalizes liquid phase PCL viscosity as a function of shear stress, γ, and

temperature, T.

$$
\mu = f\{\gamma, T\} \qquad\qquad 2\text{-}7
$$

PCL viscosity is measured using shear rate and temperature sweep to identify the

dependence of each variable. The effect of shear rate is used to classify the material as Newtonian

or Non-Newtonian. A viscometric test method to applied temperature and shear rate sweeps and

then measured shear stress in the molten thermoplastic sample. Polycaprolactone (PCL),

$(C_6H_{10}O_2)_n$ pellets (Sigma-Aldrich) are loaded between the parallel plates of TA Instrument's

AR2000ex Advanced Rheometer System. The AR2000ex Rheometer's non-contact drag cup

motor controls the angular rotation and rate of rotation of a Peltier plate. The rotating plate is a

parallel to a static plate. The testing platform temperature was controlled by the instrument's

temperature control system to within $+/- 0.1°C$ and logged with the recorded experimental data.

PCL is loaded between the rotating and static plate and heated to liquefy the pellet to liquid phase.

The controlled shear rate testing mode continuously deforms the fluid using a shear rate sweep to

exponentially increase the rotation of the plate from 0.1-100 1/s over a 45 minute test period. The

rheometer measures the Peltier plate's rate of rotation (shear rate) and motor's torque (shear stress)

and temperature. The 65°C test condition is evaluated first. Temperature is increased by 5°C for

each trial up to the maximum 90°C condition. Figure 2-5 presents photographs of the AR2000ex

advanced rheometer system with Peltier set-up and PCL pellet positioned on lower plate (center).
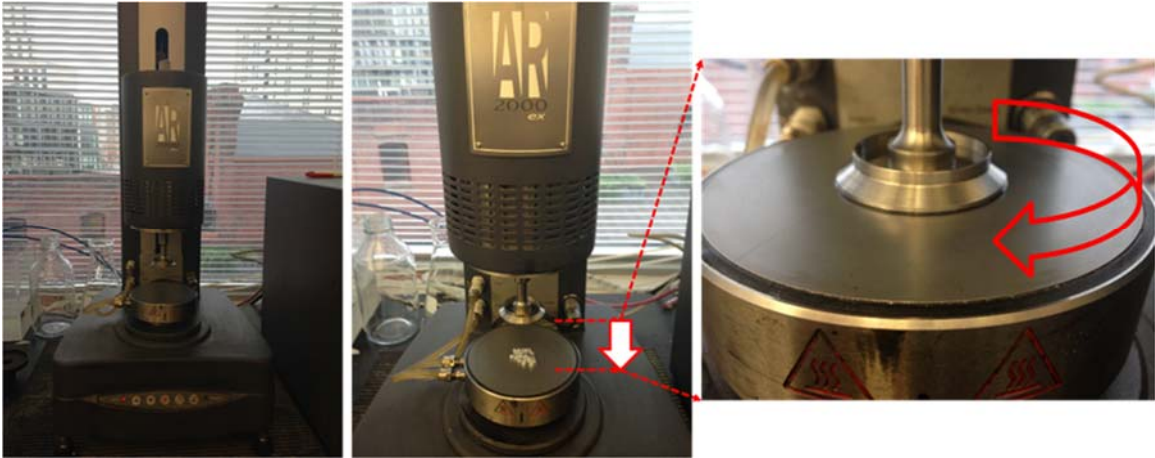
Figure 2-5: AR2000ex advanced rheometer system with Peltier plate set-up to test temperature and strain rate sensitivity of thermoplastic viscosity.

Figure 2-6 presents the rheometer study results for the strain rate- and temperature-dependence of PCL viscosity for PED system operating conditions. Strain rates between 0.1 1/s to the maximum fluid shear rate effect the fluid viscosity significantly less than 5°C change in test temperature, as each isothermal line is distinct. PCL in the PED operating conditions is classified as a Newtonian fluid. The temperature dependence of PCL viscosity is measured using a temperature sweep from 65-90°C for a constant 1.0 1/s strain rate. Liquid phase PCL viscosity is modeled as a Newtonian fluid with power law sensitivity to temperature.
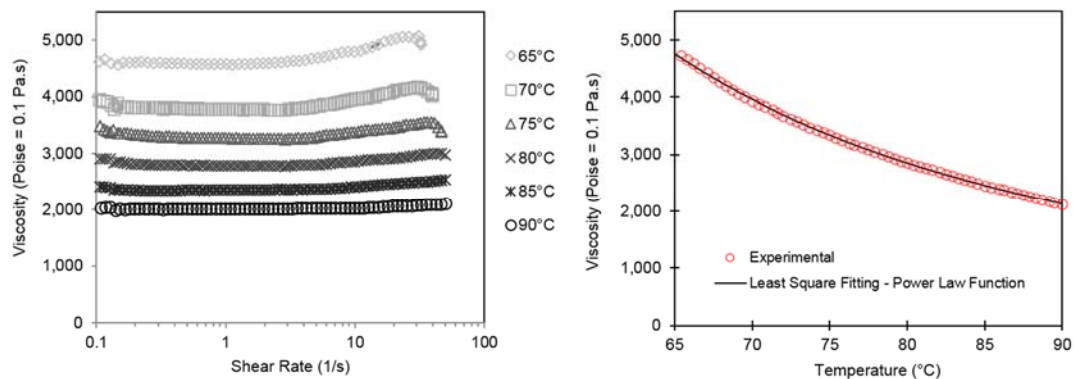
Figure 2-6: PCL viscosity as a function of shear rate (left) and experimental data with least square fitting (right).

Equation 2-8 uses the power law with a coefficient K, and index n, to define the viscosity as a function of temperature T.

$$\mu = \frac{\tau}{\gamma} = KT^n \qquad \qquad 2\text{-}8$$

Least square fitting regression using a power law model of the experimental data is a function of the form presented in equation 2-9.

$$y = Ax^B \qquad \qquad 2\text{-}9$$

The least square fitting coefficients represent the material properties for the viscosity coefficient and index are presented in equation 2-10 and 2-11, respectively.

$$K = A = e^a \qquad \qquad 2\text{-}10$$

$$n = B = b \qquad \qquad 2\text{-}11$$

Coefficients are evaluated using the experimental data of temperature (independent variable, x) and viscosity (dependent variable, y) using equation 2-12 and 2-13.

$$b = \frac{n \sum_{i=1}^{n}(ln\, x_i\, ln\, y_i) - \sum_{i=1}^{n}(ln\, x_i) \sum_{i=1}^{n}(ln\, y_i)}{n \sum_{i=1}^{n}(ln\, x_i)^2 - \sum_{i=1}^{n}(ln\, y_i)^2} \qquad \qquad 2\text{-}12$$

$$a = \frac{\sum_{i=1}^{n}(ln\, y_i) - b \sum_{i=1}^{n}(ln\, x_i)}{n} \qquad \qquad 2\text{-}13$$

The power law model of PCL viscosity as a function of temperature ($65°C \leq T \leq 90°C$) with empirical coefficients takes the form presented in equation 2-14.

$$\mu = 1.4 \times 10^8\, T^{-2.46} \qquad \qquad 2\text{-}14$$

Empirical coefficients are compared to values from similar studies of thermoplastics in peer reviewed literature. Molecular weight and density varies greatly between PCL from this and peer

studies. Standard deviation between this study and peer reviewed viscosity index is +/- 0.06. The viscosity coefficient is 2 orders of magnitude greater for our study than peer reviewed work. Variation in source, molecular weight and density contribute to the disparity.

Table 2-2. Power law model coefficients for thermoplastics polycaprolactone (PCL) and poly-L-lactice (PLLA) from literature

Polymer	Molecular Weight	Density g/cm^3	K $Pa.s^n$	n	Ref
PCL	45,000	1.15	1.4×10^8	-2.46	Experimental
PCL	62,450	1.09	1.4×10^6	-2.54	(Liang, Zhou, Tang, & Tsui, 2013)
PCL	80,000	-	8.4×10^6	-2.41	(Kalambur & Rizvi, 2006)
PLLA	100,000	2.55	1.1×10^6	-2.44	(Liang et al., 2013)

2.2.3.3   Design variables as a function of the process and material parameters

PCL flow from the PED extruder accumulates on the substrate. Conservation of mass requires the mass flow rate from the extruder is equal to the mass of PCL accumulating as a filament on the substrate.   Equation 2-15 presents the mass flow from the extruder equals the mass assumulating on the substrate in the printed structure.

$$\left(\frac{dm}{dt}\right)_{from\ extruder} = \left(\frac{dm}{dt}\right)_{substrate\ accumulation} \qquad 2\text{-}15$$

PCL is modeled as a constant density fluid. Mass and volume flow rate are proportional. The net volumetric flow rate from the extruder is equal to depsotion head speed v, multiplied by the cross-sectional area of the deposited PCL filament A, equation 2-16.

$$Q = Av \qquad 2\text{-}16$$

Cross-sectional area of the printed filament is modeled as half an ellipse. The area of the printed cross-section is a function of the major axis (width) and minor axis (height), equation 2-17.

$$A = \frac{\pi a b}{4} \qquad\qquad \textit{2-17}$$

The height of the printed filament is controlled by the height of the PED extruder die outlet above the printing substrate, equation 2-18.

$$b = z \qquad\qquad \textit{2-18}$$

PCL pellets loaded into the inlet of the PED extruder barrel are liquefied and blended by heating and the mechanical action of the screw. The rotating screw in the stationary barrels builds pressure and forces the liquefied PCL from the inlet towards the outlet at the bottom of the barrel. PCL flow through the extruder is modeled as an unrolled screw helix presented as a rectangular channel, figure 2-7, and as-built extruder with geometric parameters annotated, figure 2-8.
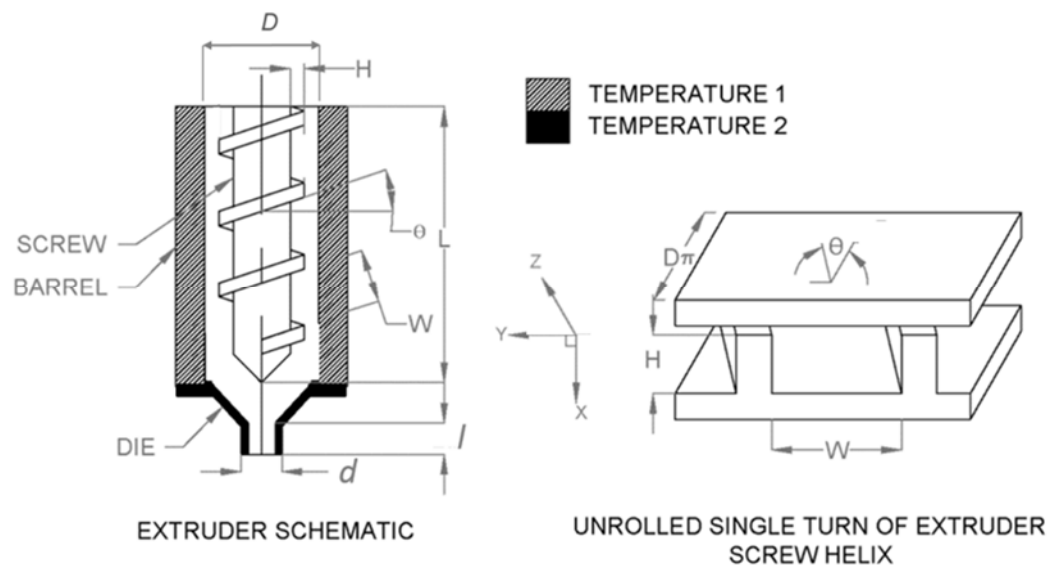
Figure 2-7: PED extruder schematic and unrolled single turn of the extruder screw helix with geometric parameters.
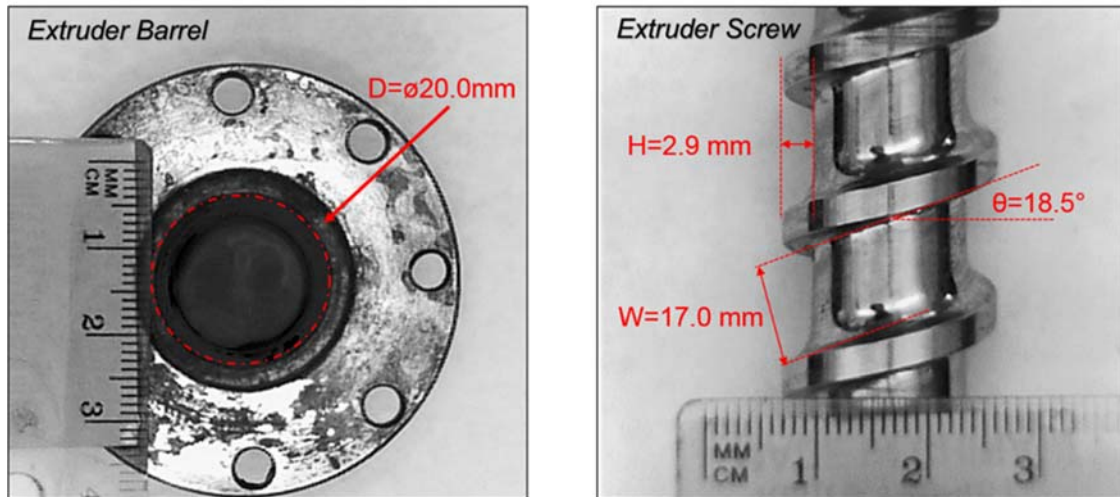
Figure 2-8: Photographs of fabricated extruder barrel and screw with geometric parameters annotated.

Die restriction at the extruder outlet shapes the extruded filament. PED system only includes a pre-fabricated set of circular cross-section die of variable diameter. Die diameter is directly measured. The die length is an internal feature and is taken from engineering drawing drafted to manufacture the die, presented in figure 2-9.
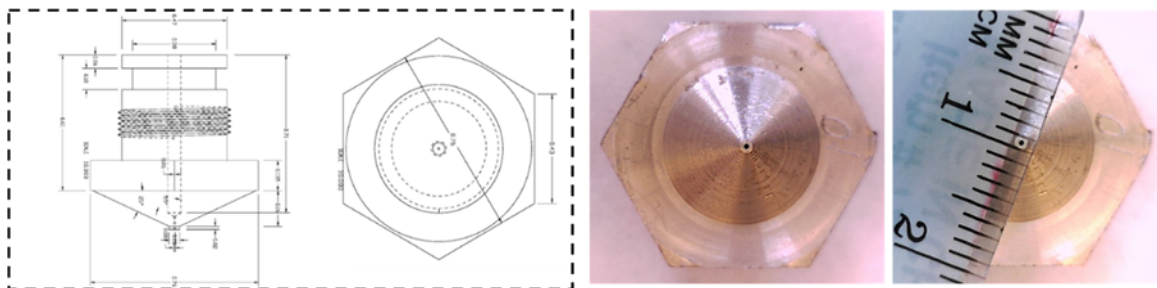
Figure 2-9: PED extruder die schematic of front and top (left) and fabricated result (right) with ruler. Geometric parameters length and diameter are read from schematic and measured from photograph respectively.

The volumetric flow rate from the extruder head is a combined Drag-Poiseuille flow. The Drag flow induced by the turning screw in the extruder barrel is opposed by pressure build up due

to the restrictor dye at the outlet. Equation 2-19 presents the net volumetric flow Q, as a combination of the Drag flow Q_D, and Poiseuille flow Q_P.

$$Q = Q_D - Q_P \qquad\qquad 2\text{-}19$$

Drag, or Couette, flow is a function of geometric parameters and the screw speed. Velocity profile through the PED extruder pumping zone is modeled as a laminar flow with a no-slip boundary condition on the rotating screw surface and stationary barrel wall. The down channel component of the velocity proportional to the screw speed, as presented in equation 2-20.

$$v_z = \frac{dz}{dt} = \pi DN \cos\theta \qquad\qquad 2\text{-}20$$

Laminar flow of a Newtonian fluid with a no-slip boundary condition produces a linear velocity profile. The average PCL velocity through the pumping zone is half the maximum fluid velocity, equation 2-21.

$$\bar{v}_z = \frac{1}{2}v_z \qquad\qquad 2\text{-}21$$

Volumetric flow rate caused by the turning screw is the down channel of the flow rate integrated over the cross-sectional area of the flow channel. Volumetric flow rate is the average fluid velocity integrated over the cross-sectional area of the channel, equation 2-22.

$$Q_D = \int_0^A \bar{v}_z \ dA = \int_0^{y=W} \int_0^{x=H} \bar{v}_z \ dx \ dy \qquad\qquad 2\text{-}22$$

Combining equation 2-20, 2-21 and 2-22 defines the drag flow rate as a function of geoemtric and process parameters, equation 2-23. Geometric parameters represented as a single drag flow coefficient α.

$$Q_D = \frac{\pi}{2} DHNW \cos \theta = \alpha N \qquad \qquad 2\text{-}23$$

Linear momentum through the pumping zone of the PED extruder's pumping zone is conserved. Poiseuille flow is produced by a pressure gradient caused by flow restriction due to an extruder die secured to the PED extruder barrel outlet, equation 2-24. Geometric parameters represented as a single Poiseuille flow coefficient β.

$$Q_P = \frac{dV}{dt} = \frac{WH^3}{12\mu_1} \frac{p}{L} = \frac{\beta}{\mu_1} p \qquad \qquad 2\text{-}24$$

Equation 2-24 and the temperature-dependent power law model of PCL, equation 2-14, are combined to form equation 2-25.

$$Q_P = \frac{\beta}{KT_1^n} p \qquad \qquad 2\text{-}25$$

Net volumetric flow rate through the extruder die is a function of the geometry of the die itself, a presented in equation 2-26.

$$Q = Q_d \qquad \qquad 2\text{-}26$$

Flow due to restriction die is a function of viscosity μ, pressure p, and die geometry coefficient ε, as presented in equation 2-27.

$$Q_d = \frac{\varepsilon}{\mu_2} p \qquad \qquad 2\text{-}27$$

Extruder die characteristic for a circular die is modeled from Hagen-Poiseuille Law as a function of geometric variables diameter d, and extrusion length l, as presented in equation 2-28.

$$\varepsilon = \frac{\pi d^4}{128 \, l} \qquad \qquad 2\text{-}28$$

Equation 2-27 and 2-28 are combined to define the flow rate through the extruder die, equation 2-29. Geometric parameters are combined by the die flow coefficient ω.

$$Q_d = \frac{\pi d^4}{128 \, l} \frac{1}{\mu_2} p = \frac{\omega d^4}{\mu_2} p \qquad \text{2-29}$$

Equation 2-29 and the temperature-dependent power law model of PCL, equation 2-14, are combined to form equation 2-30.

$$Q_d = \frac{\pi d^4}{128 \, l} \frac{1}{\mu_2} p = \frac{\omega d^4}{K T_2^n} p \qquad \text{2-30}$$

The net volumetric flow rate (equation 2-19), drag flow (equation 2-23), Poiseuille flow (eqaution 2-24), and die restriction flow (equation 2-30) are combined to solve for the pressure in the extruder barrel due to the restirctor die as a function of the process, geometric, and material parameters, equation 2-31.

$$p = \frac{\alpha K N T_1^n}{d^4 \omega \left(\frac{T_1}{T_2}\right)^n + \beta} \qquad \text{2-31}$$

The net volumetric flow rate (equation 2-19), drag flow (equation 2-23), Poiseuille flow (eqaution 2-24), and pressure in the extruder barrel (equation 2-31) are combined to solve for the net volumetric flow rate through the restirctor die as a function of the process, geometric, and material parameters, equation 2-32.

$$Q = \alpha N \left(1 - \frac{1}{d^4 \frac{\omega}{\beta} \left(\frac{T_1}{T_2}\right)^n + 1} \right) \qquad \text{2-32}$$

PCL density, ρ, is assummed constant, therefore the mass, m, and volume, Q, flow rates are propotional, equation 2-33.

$$m = Q\rho \qquad\qquad\qquad 2\text{-}33$$

Equation 2-33 combines equation 2-31 and 2-32 to present mass flow rate from the extruder as a function of the process parameters, geometric coefficients and material properties.

$$m = \alpha\rho N \left(1 - \frac{1}{d^4 \frac{\omega}{\beta}\left(\frac{T_1}{T_2}\right)^n + 1} \right) \qquad\qquad 2\text{-}34$$

Accumulation on the substrate is a function of the printhead speed and extruder flow rate (equation 2-15), model of printed filament's cross-sectional area (equation 2-16), equivalence of printed filament height to extruder tip height (equation 2-18), and net volumetric flow rate from the extruder (equation 2-32) combine to define the design variable for printed filament height, presented in equation 2-35.

$$a = \frac{4\alpha N}{\pi v z} \left(1 - \frac{1}{D_d^4 \frac{\omega}{\beta}\left(\frac{T_1}{T_2}\right)^n + 1} \right) \qquad\qquad 2\text{-}35$$

Equation 2-35 is plotted to present the theoretical effect of each process parameter on the printed filament width, presented in figure 2-10. Increasing the extruder outlet temperature increases the width of the printed filament, as does increasing the inlet temperature. Increasing screw speed also increases printed filament width, as does increasing extruder die diameter. Increasing printhead exponentially decreases speed width, as does increasing the distance between the substrate and extruder die outlet.
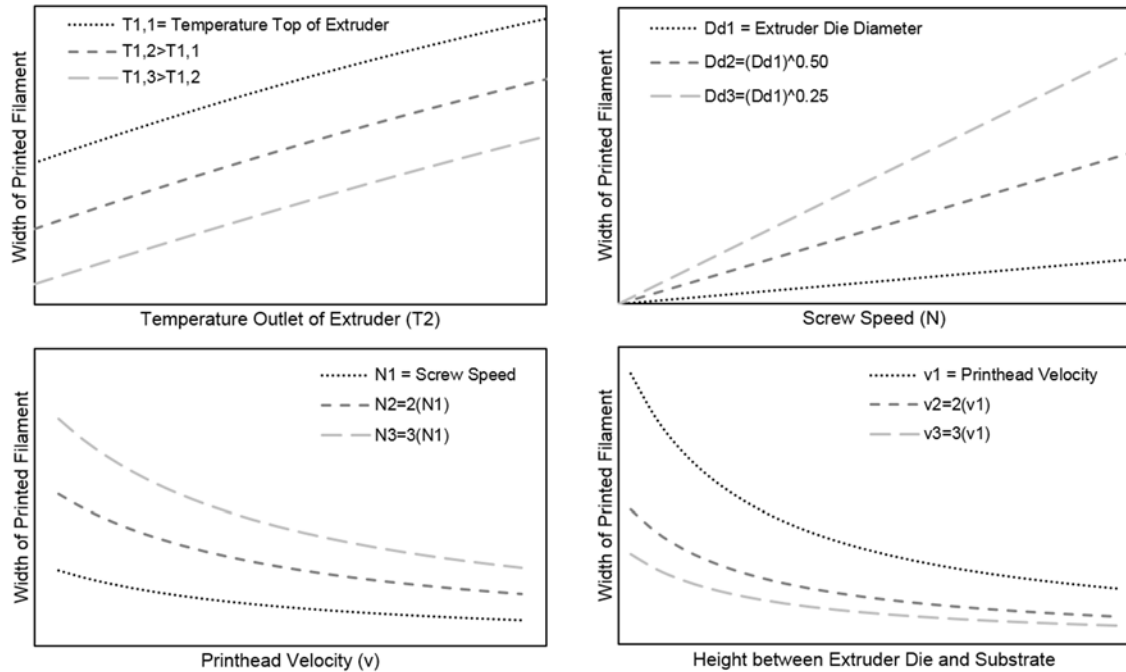
Figure 2-10: Theoretical effect of extruder temperature, screw speed, printhead velocity and height of extruder die and substrate on the print filament width

2.2.3.4   Comparison of theoretical and experimental PED extruder flow rates

PCL is loaded into 80°C PED extruder barrel with $\emptyset350\mu m$ extruder die secured to the outlet. The extruder screw is programmed for a specific displacement and RPM to force the PCL from the outlet. PCL is collected on a high precision mass balance. The time of extruded is reported by the software. Mass flow rate is experimentally quantified from the measured PCL weight and extrusion time.   Equation 2-34 is plotted to present the derived mass flow rate from the PED extruder for comparison.

$$Experimental\ Mass\ Flow\ Rate = \frac{Weight, measured}{Extrusion\ time, measured}$$

$$m_e = \frac{W_m}{t_m}$$

2-36

The theoretical and experimental mass flow rates demonstrate strong agreement between 10-120 RPM. Both the theoertical model (equation 2-34) and experimental results calculated from measurements (equation 2-36) present a propotional increase in mass flow rate per increase in screw speed rotation.
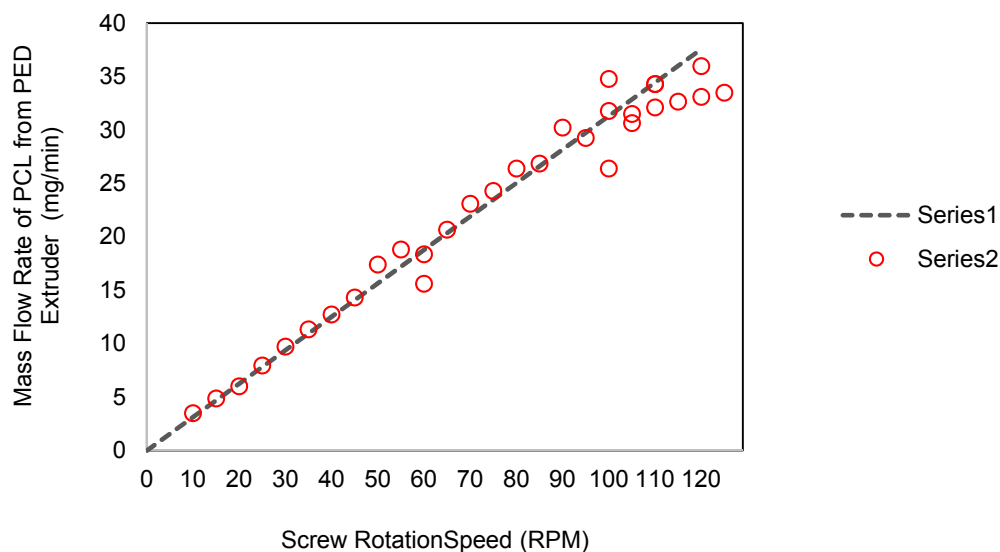
Figure 2-11: Comparison of derived and experimental mass flow rate through PED extruder with Ø350μm nozzle and uniform 80°C heating of extruder barrel.

2.2.3.5 *Independent control of printed width and height*

Height and width of printed cross-section independently controlled by printhead speed and height of the outlet tip above substrate. Elevation of the tip sets the height of the printed filament. Width of the printed filament is adjust by increasing or decreasing the total cross-sectional area. Printhead speed or screw speed can be adjusted without changing the elevation. PCL is printed with PED system to form filaments using three printhead speeds. Figure 2-12 presents three profiles of PCL extrusions fabricated using PED system examined using the Zygo NewView 6000 optical profiler. Samples are sputter coated 5 nm thick layer of platinum-palladium to provide a conductive path during imaging.   Blue profile printed with faster printhead speed than green profile. Green

profile printed with faster printhead speed than red profile. Increasing printhead speed decreases the PCL accumulation rate on the substrate, which decreases the total cross-sectional area of the printed filament. Height is determined by the elevation of the extruder outlet. The width is independently varied by increasing or decreasing the other process parameters.
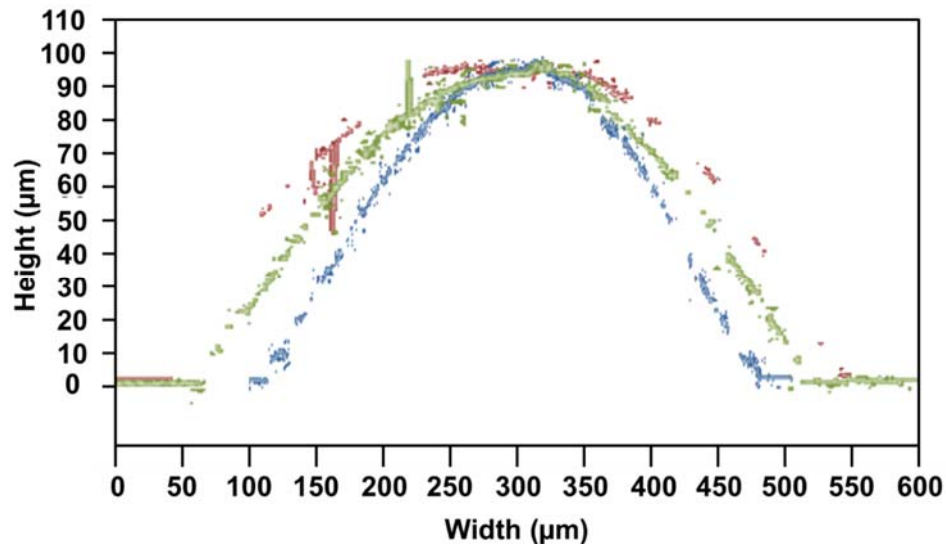
Figure 2-12: Three PED printed PCL filament cross-section. Blue profile printed with faster printhead speed than green profile. Green profile printed with faster printhead speed than red profile.

2.2.4   Step 3. Replica molding of printed pattern in PDMS

Step 3 is replica molding of the printed pattern in polydimethylsiloxane (PDMS). PDMS is selected for the microfluidic device as a biocompatible, non-toxic, optically transparent, & highly gas permeable material (Mata, Fleischman, & Roy, 2005). PDMS is Slygard 184 Silicone Elastomer (Dow Corning) base and curing agent mixed 10-15:1 respectively by weight for optimal bond strength between PDMS layers (Eddings, Johnson, & Gale, 2008). The PCL pattern is either (1) placed in a glass or polystyrene dish and covered with freshly mixed PDMS or (2) placed on partially cured PDMS and covered with freshly mixed PDMS. In the first case, the PCL pattern

produces channels on the surface of the fully cured PDMS substrate. In this case an additional cover with inlet/outlet ports is required to seal the channels in a device. In the second case, the PCL pattern produces channels embedded in the PDMS substrate. In this case no additional cover component is required to seal the channel network as a device. However, inlet and outlet ports are added as capillary tips punctured through the fully cured PDMS. Layers of PDMS are bonded by an adaptation of the stamp-and-stick room temperature bonding technique for micro-devices (Satyanarayana, Karnik, & Majumdar, 2005). A 1 mm thick layer of PDMS is poured into a polystyrene dish and stored in ambient conditions, 22°C and 1 atm, to partially cure over 12 hours. The PCL pattern is printed on top of the partially cured PDMS substrate. Additional PDMS is poured over the PCL pattern; up to an additional 1 mm. PDMS is stored for an additional 24 hours at room temperature to fully cure.
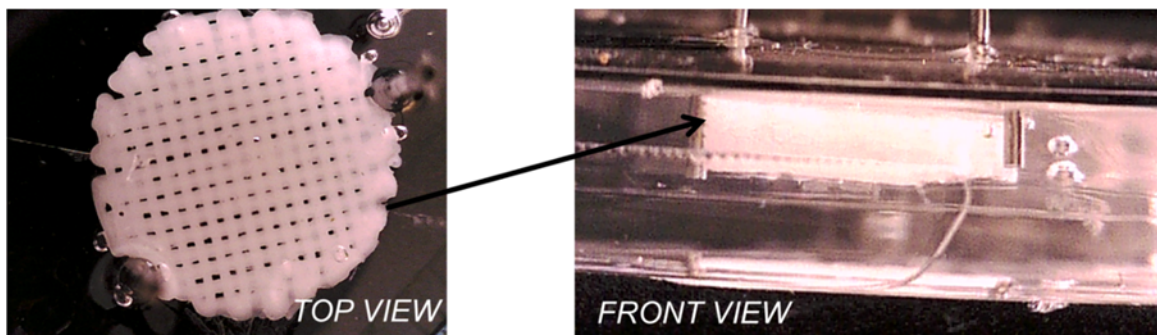
Figure 2-13: Top and front view of PCL pattern printed by precision extrusion deposition fully embedded in PDMS substrate.

2.2.5 Step 4. Remove printed pattern to produce the microfluidic network

Step 4 is removal of the printed pattern from the fully cured PDMS. The technique to remove the printed pattern depends on position of the printed pattern chosen in step 3. Printed patterns attached to a substrate and covered with PDMS can be manually removed, as they are exposed once the substrate is removed. PCL cleared from PDMS channel after curing by one of two methods (1)

gently peeling PCL from channels using forceps or (2) dissolving PCL from channels by sonication in dichloromethane (Sigman et al.) for 50 min at room temperature (Vazquez, Luduena, & Alvarez, 2007). After the printed pattern is removed, the templated network is an open set of channels.
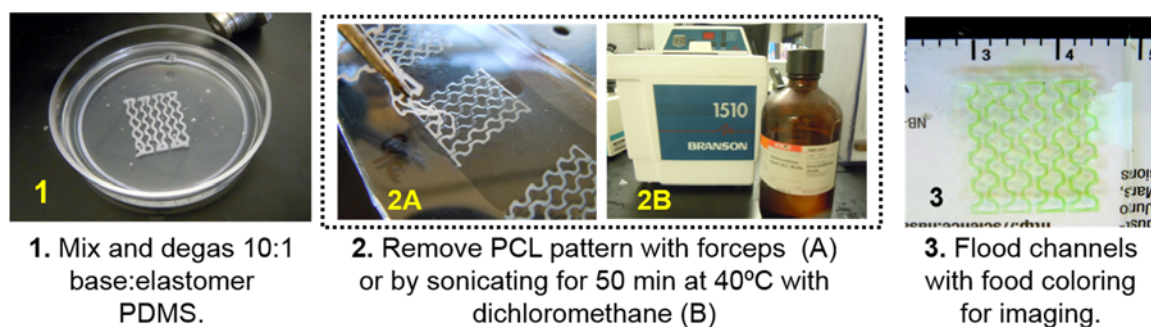
Figure 2-14: Process to remove PCL pattern from surface of fully cured PDMS substrate.

A fully embedded printed pattern is removed from fully cured PDMS by alternating melt/drain cycles and dissolve the PCL pattern without damaging the PDMS substrate. After the PDMS is fully cured, a syringe or capillary tip is used to puncture the surface of the PDMS to the embedded PCL pattern. The risk of tearing is minimized by allowing the PDMS to equilibrate to room temperature and using a droplet of water on the puncture site. Slow even pressure is applied to the capillary or syringe tip during penetration. The tip is the inlet and is plumbed to a programmable syringe pump using silicone tubes for continuous perfusion. A hole created using a capillary tip drains molten PCL out of the PDMS, leaving an open network of channels. First the PDMS substrate is placed on a hot plate, submerged in water and heated to >60°C. PCL becomes molten and perfusion from the syringe pump begins 0.2mL/hr. The flow is increased to 1.0mL/min as PCL is removed from the channels. An alternating cycle to dissolve the PCL by solvent is used to fully clear channels of PCL. The PDMS substrate is cooled to room temperature, submerged in dichloromethane and sonicated for 30-60 minutes. Dichloromethane will evaporate at high temperature, therefore the thermal and chemical processes cannot be successfully combined.

Further, dichloromethane dissolves silicone tubes and syringes used in perfusion. Contact with dichloromethane longer than 60 minutes causes PDMS substrate to deform and delaminate. The heat/perfusion and solvent/sonication cycles are alternated until channels are clear of PCL. Once channels are cleared, either from the surface or embedded in the PDMS, channels are flooded with dye for visualization.
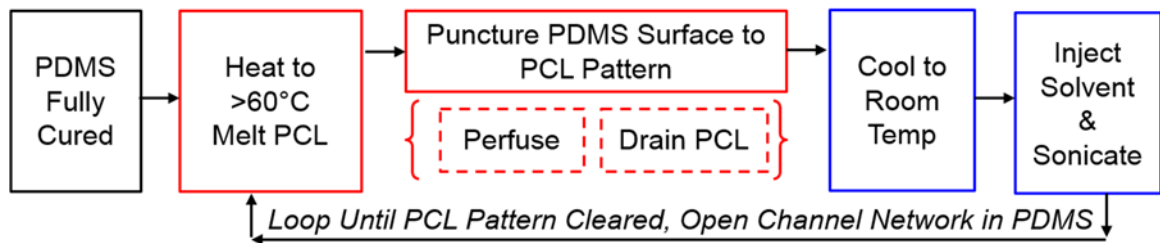
Figure 2-15: Process to remove PCL pattern embedded in fully cured PDMS substrate. Process using a heat/perfusion cycle to melt and drain PCL and a solvent/sonication cycle to dissolve PCL without damaging PDMS.
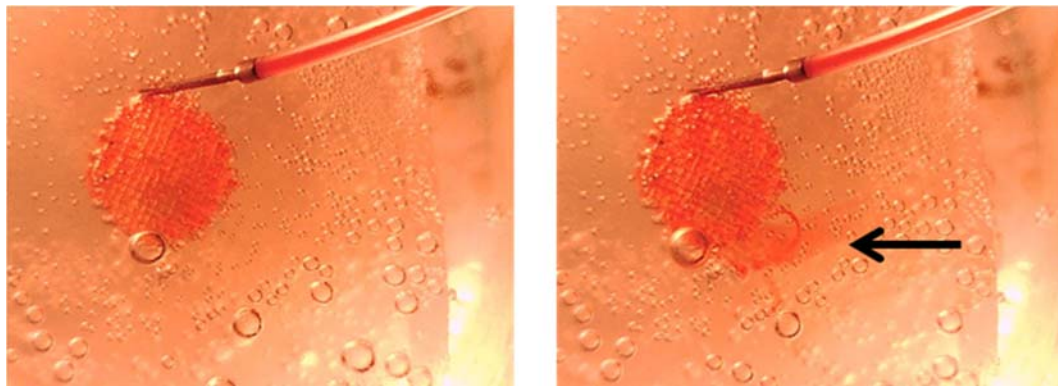
Figure 2-16: Forced convection from a programmable syringe pump plumbed to the embedded printed pattern through a syringe tip ejects melted pattern from the cured PDMS. Arrow points to ejection of water and PCL from embedded channels.
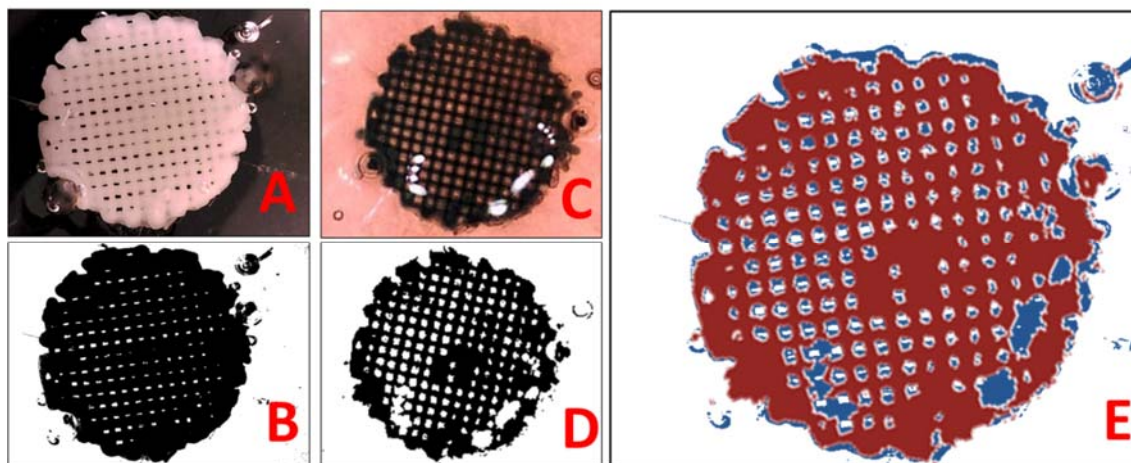
Figure 2-17: Microfluidic network templated by PCL scaffold fabricated by additive manufacturing technique precision extrusion deposition. Printed PCL scaffold cured in PDMS – photograph and binary image of PCL/PDMS (black/white) presented in Fig. A and B respectively. Thermal and chemical treatment removes PCL without damaging PDMS. After PCL is removed, the void space is perfused with water with food coloring for visualization. PDMS after PCL is removed presented in photograph and binary image of water with food coloring/PDMS (black/white) presented in Fig C and D respectively. Fig. B (blue) and D (red) superimposed in Fig. E.
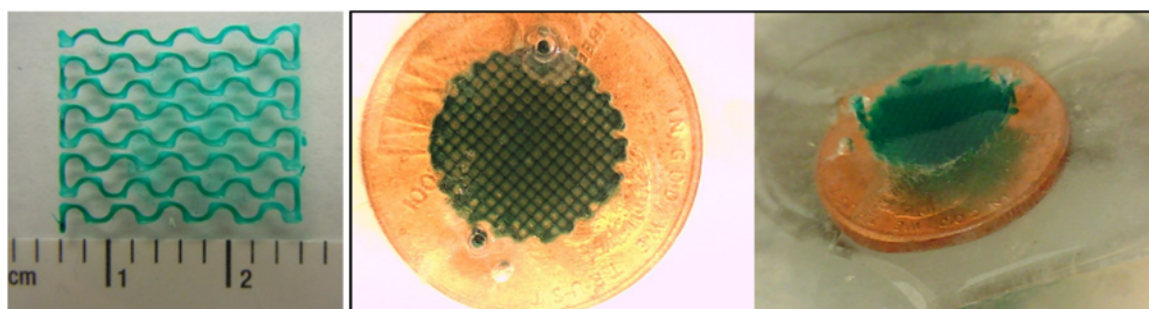
Figure 2-18: Open channel on the surface (left) and fully embedded 3-dimensional (right) microfluidic networks in PDMS substrate fabricated by precision extrusion deposition and replica molding.

2.2.6   Fabricated microfluidic networks

2.2.6.1   *Channels embedded in surface of PDMS substrate*

Inspection of two geometric designs for fabricated PCL pattern and PDMS channels was performed to demonstrate the pattern could be created, molded, and cleared from PDMS channel. In a third example the goemetric design were comined in a single interconnected microfluidic chip.

Figure 2-19 presents design model input, printed PCL pattern produced by PED system, and PDMS cured against PCL pattern for single layer square wave pattern of dimensions 20mm x 20mm with struts spaced 1mm on center. Figure 2-20 presents design model input, printed PCL pattern produced by PED system, and PDMS cured against PCL pattern for single layer square and sinusoid wave pattern of dimensions 20mm x 22mm with struts spaced 3mm on center and radius of 1mm. Figure 2-21 presents design model input, printed PCL pattern produced by PED system, and PDMS cured against PCL pattern for single layer multi-compartment array of two square and one sinusoid wave arranged in series.
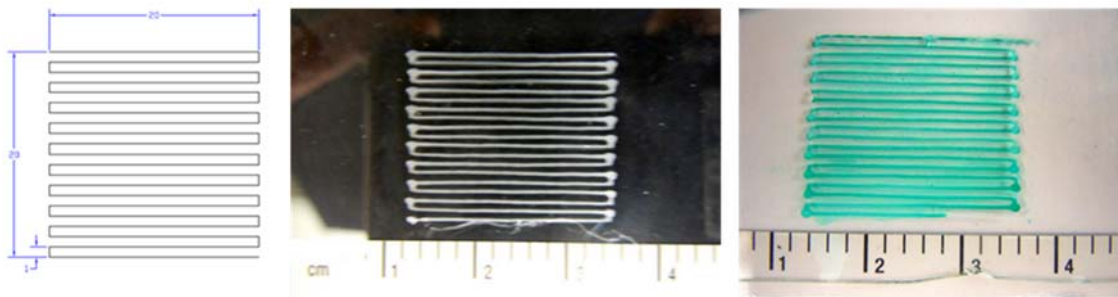
Figure 2-19: Single layer square wave pattern of dimensions 20mm x 20mm with struts spaced 1mm on center design model input (left) and printed PCL pattern produced by PED system (center) and PDMS cured against PCL pattern with channels flooded with green dye (right).
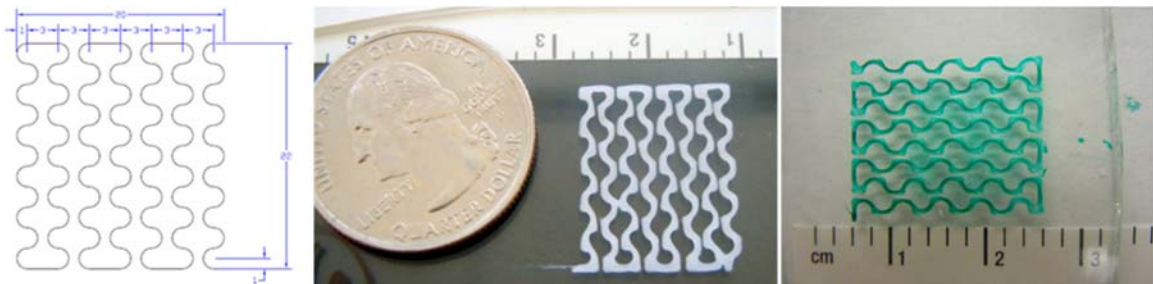
Figure 2-20: Single layer sinusoid wave pattern of dimensions 20mm x 22mm with struts spaced 3mm on center and radius of 1mm design model input (left) and printed PCL pattern produced by PED system (center) and PDMS cured against PCL pattern with channels flooded with green dye (right).
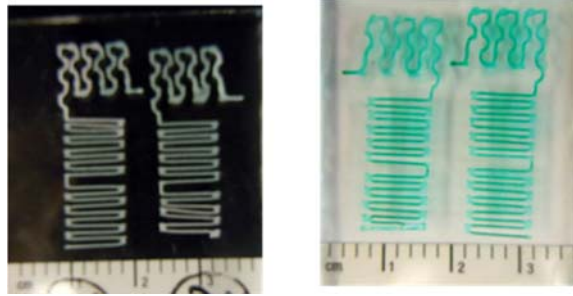
Figure 2-21: Single layer multi-compartment array of square and sinusoid wave design models printed PCL pattern produced by PED system (left) and PDMS cured against PCL pattern with channels flooded with green dye (right).

Inspection using phase contrast microscope and image analysis software was performed on fabricated samples to characterize PCL pattern and PDMS channel depth and width. Single layer square wave PCL pattern and PDMS chip were viewed from the top and then sliced through the center to inspect cross-section. Figure 2-22 presents top view and section view of printed PCL pattern and PDMS channels for square wave channel. PDMS curing against the PCL pattern yields a network of channels.
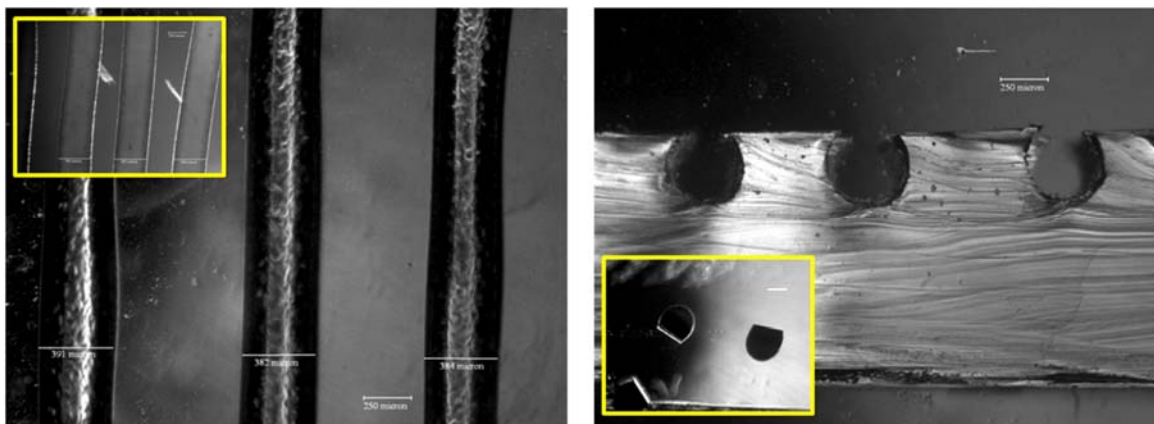
Figure 2-22: Top and section view of PDMS Channels printed using 350µm nozzle tip. Top view of PCL pattern inset.

Having established PDMS channels can be produced by PCL patterns and the micro-system structures can be controlled by PED manufacturing process parameter, we next investigated the effect of SFF to increase channel aspect ratio. Inspection using phase contrast microscope and image analysis software was performed on PDMS channel fabricated using 1, 2, 3, and 4 layers to characterize channel width, depth and aspect ratio. A scalpel is used to cut PDMS chip along its centerline to view cross-section of channels. The aspect ratio (AR) is defined as the channel depth divided by the channel width. The depth of the channel is increased by printing additional layers on top of the first layer. The width of the channel is increased by printing additional layers on top of the first layer. One layer produced a 1.0 aspect ratio channel. Two layers increased the aspect ratio 30%, three layers increased the aspect ratio 60%, and 4 layers increased the aspect ratio 120%.
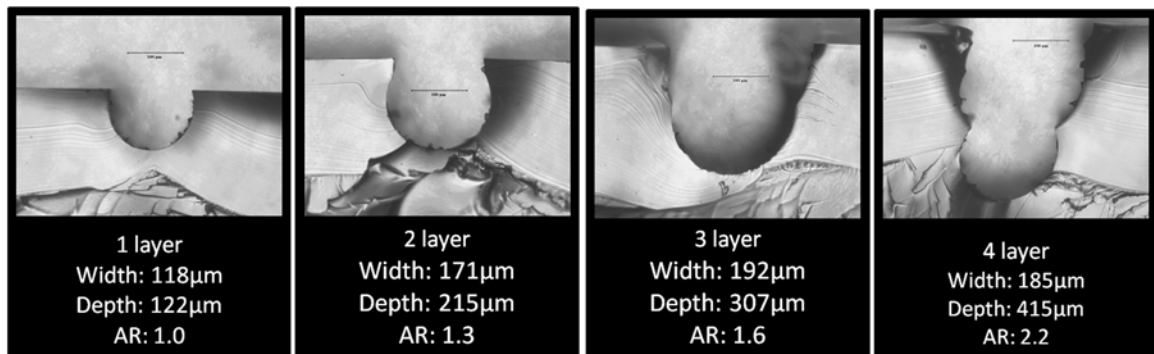
Figure 2-23: Cross section view of PDMS channels molded from multi-layer PCL patterns.

2.2.6.2   3D network of channels embedded in PDMS substrate

Having established PDMS channels can be produced by multi-layer PCL patterns and the micro-system structures can be controlled by SFF manufacturing in 3-dimensions, we next investigated the effect of mutually orthographic layers to create interconnected network of channels. Inspection using phase contrast microscope and image analysis software was performed on PCL scaffold and PDMS channel fabricated using scaffold to characterize channel width, depth and orientation.
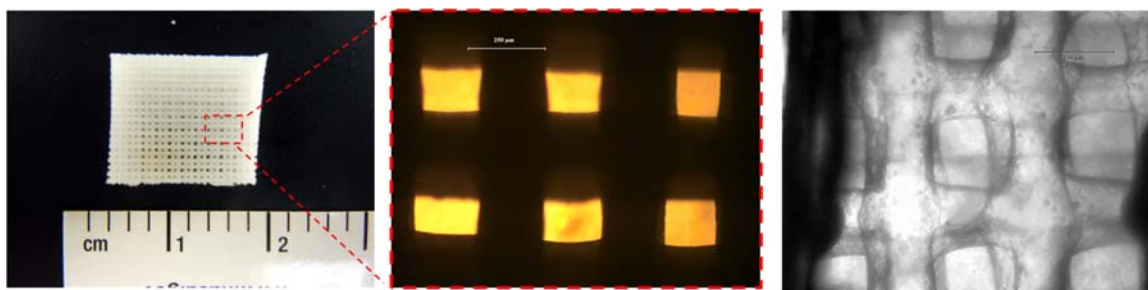
Figure 2-24: Printed 0-90 scaffold pattern using two layers as viewed from the top macroscopically and under 4 x magnifications using phase contrast microscope (B) from the top (A) and front (B). PDMS Channels after PCL is removed by sonication and the construct is viewed from the top under 4x magnification using phase contrast microscope (C).

A porous 3-dimensional PCL scaffold is produced by PED manufacturing. Two mutually orthographic layers are printed by continuous extrusion in the same z-plane. A second set of mutually orthographic layers are printed on top of the first set to produce a scaffold. PCL is continuously extruded during entire printing episode to produce a continuous pattern. PDMS cures against PCL scaffold to pattern produce a polymer replica with channel network. PCL scaffold is cleared from PDMS chip without disturbing PDMS due to the difference in material melting temperature and solubility. After replica molding PCL is cleared by 50 minutes of sonication in an 80°C dichloromethane bath. A scalpel is used to cut PDMS chip along its centerline to view cross-section of channel network. The top view of PDMS chip and two orthographic cross-section views. Two layers of channels are produced in PDMS chip. Two rows of pores are visible in both Figure 2-25 section view A and B. PED manufacturing is used to layer 2-dimensional PCL patterns to create 3-dimensional architecture. This architecture is replica molded and cleared from PDMS chip to produce a 3-dimensional microfluidic system. The depth of the channels from the top of the chip to the bottom of the lower row is 325-385μm.
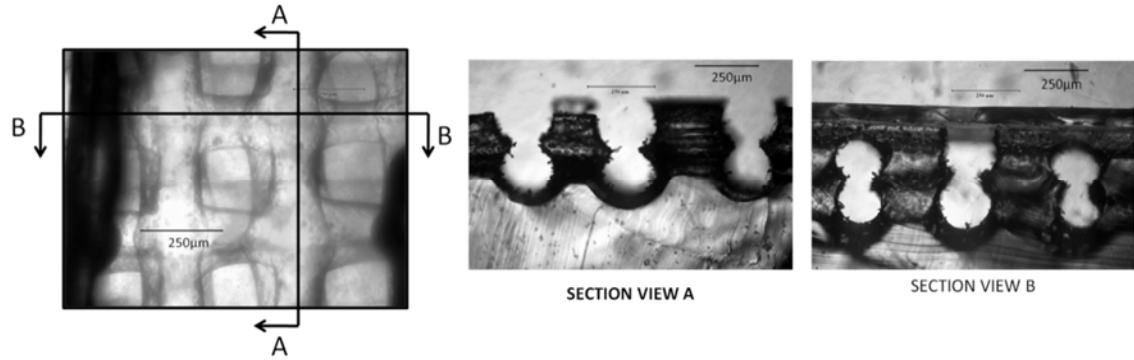
Figure 2-25: Continuous extrusion during PCL patterning creates an interconnected 3-D network for replica molding.

2.2.6.3 *Minimum feature size achieved*

The minimum set of design variables fabricated by PED printing and replica molding process is determined by experimentation. The minimim diameter extruder die is selected from a pre-fabricated set and secured to the outlet. Next the process parameters are iteratively decreased to identify the minimum temperature and screw speed for extrusion. The extruder tip height above the printing substrate is then set. Then the depsotion head speed is increased until continuous line formation is not reproducible. The set of process parameters to fabricate the set of minimum feature size is presented in equation 2-37.

$$\Omega_{PED} = \left[d = \emptyset 150 \mu m \quad N = 30\ RPM \quad \begin{matrix} T_1 = 80°C \\ T_2 = 70°C \end{matrix} \quad v = 5.0\frac{mm}{s} \quad z(t) = 150 \mu m \right] \quad \textit{2-37}$$

The minimum set of design variable for the width and height of a PED printed PCL filament are presented in equation 2-38.

$$\Psi_{PED} = [a = 255\ \mu m \quad b = 163\ \mu m\ ] \qquad\qquad \textit{2-38}$$

Figure-2-26 presents photographs of the printed PCL pattern (left), replica molded channels in PDMS substrate with red dye in network for visualization. Microscope images of a channel cross-section and top view of two parallel channels presented on the right.
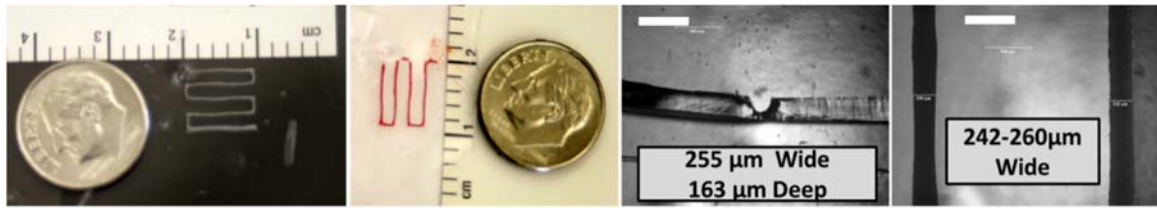
Figure 2-26: Minimum channel depth and height fabricated by precision extrusion deposition/replica molding process is 255µm and 163µm respectively.

2.2.6.4   Fabrication of microfluidic network with variable channel cross-section width and heights

Process parameters are either (1) maintained constant throughout a build cycle to produce the same set of design variables from the beginning to the end of the printed pattern or (2) adjusted dynamically over the build cycle to produce variable cross-sectional width/heights throughout the printed geometric pattern. Maintaining constant process parameters from the beginning to the end of the build cycle produces geometric pattern variation without controlled variation of the cross-sectional width/height. Figure 2-27 presents photographs of the printed PCL pattern and replica molded channel network on the surface of a PDMS substrate. Channel network is flooded with green dye for visualization.
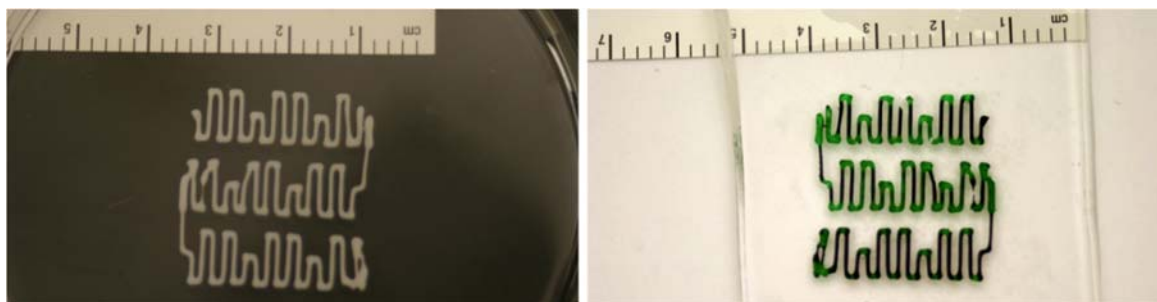
Figure 2-27: PCL pattern printed by precision extrusion deposition (left) and network on surface of PDMS substrate flooded with green dye for visualization (right).

Programmed variation in the set of process parameters fabricates a range of printed filament widths along the tool path. Consequently, the channel network produced from replica molding the printed pattern includes variable cross-sectional width and depth. This ability allows for fabrication of multiple channel cross-sectional geometries in a single fabrication/replica molding step. Process parameters can be programmed in a single build cycle to fabricate channel cross-sections from 387-1052µm wide and 267-400µm deep, as presented in figure 2-28.

10 RPM	20 RPM	30 RPM
387-485µm (W)	727-807µm (W)	958-1052µm (W)
246-265µm (D)	298-337µm (D)	387-400µm (D)
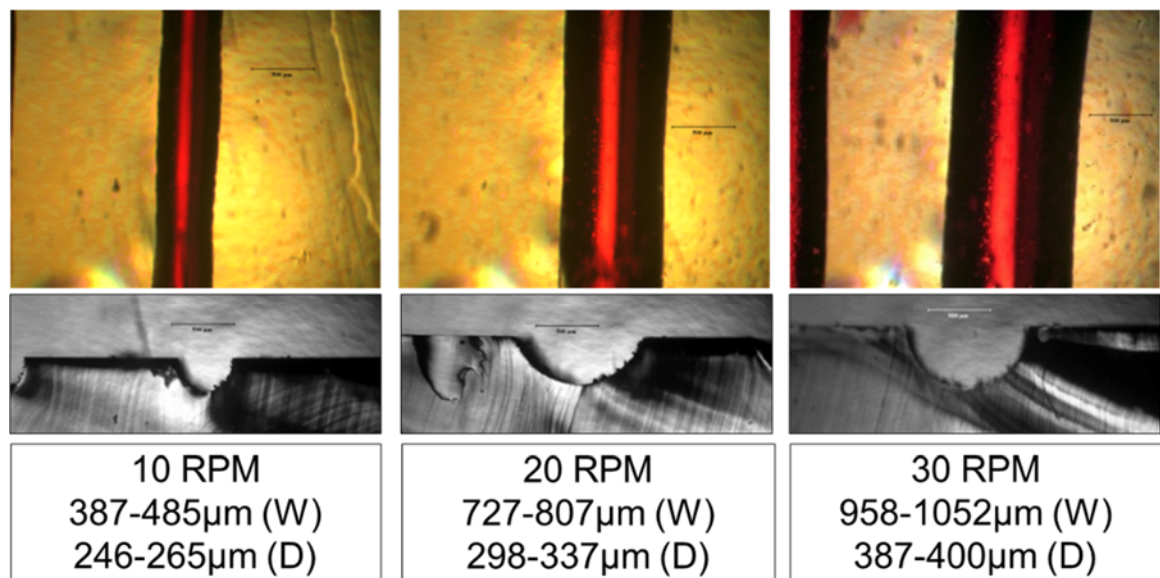
Figure 2-28: Channel cross-section with (W) and depth (D) for variable extruder RPM.

Further capability to vary the geometric pattern and channel cross-section width/depth is illustrated in figure 2-29.
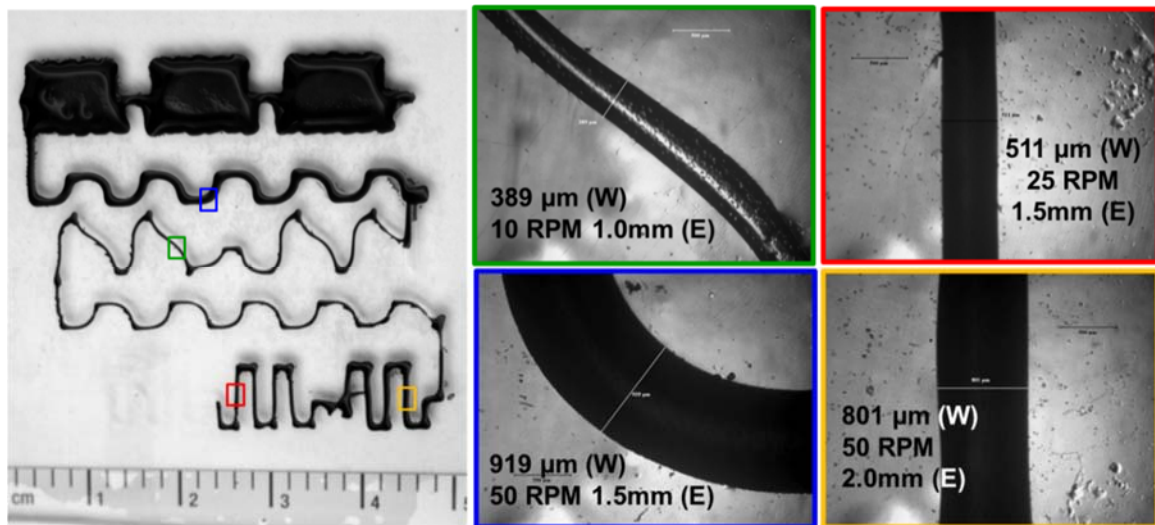
Figure 2-29: Microfluidic network on the surface of a PDMS substrate flooded with green dye for visualization. Network pattern and variable cross-sectional geometries produced during precision extrusion deposition of PCL pattern. Fabricated in a single step of replica molding.

2.3   *Multi-nozzle deposition and freeze casting of hierarchical scaffolds*

2.3.1   Purpose of method

An engineered 3-dimensional scaffold with hierarchical porosity and multiple niche microenvironments is produced using a combined multi-nozzle deposition - freeze casting technique. We present a process to fabricate a scaffold with improved interconnectivity and hierarchical porosity. The scaffold is produced using a two-stage manufacturing process which superimposes a printed porous alginate network and a directionally frozen ceramic-polymer matrix. The combination of two processes, multi-nozzle deposition and freeze casting, provides engineering control of the microenvironment of the scaffolds over several length scales; including the addition of lateral porosity and the ratio of polymer to ceramic microstructures. The printed polymer scaffold is submerged in a ceramic-polymer slurry and subsequently, both structures are directionally frozen (freeze cast), superimposing and patterning both microenvironments into a single hierarchical architecture. An optional additional sintering step removes the organic material and densifies the ceramic phase to produce a well-defined network of open pores and a homogenous

cell wall material composition. The techniques presented in this contribution address processing challenges, such as structure definition, reproducibility and fine adjustments of unique length scales, which one typically encounters when fabricating topological channels between longitudinal and transverse porous networks.

Well defined scaffold architectures and niche microenvironments are recognized mechanisms to direct cell behavior towards a functionalized tissue engineered product (Cao et al., 2006; Chu, Orton, Hollister, Feinberg, & Halloran, 2002; Tsuruga, Takita, Itoh, Wakisaka, & Kuboki, 1997; Zmora, Glicklis, & Cohen, 2002). Features of the *in vitro* culture environment are derived from native tissue and parametric studies of cell response to engineered scaffolds (Mills, Frith, Hudson, & Cooper-White, 2011; Muschler, Nakamoto, & Griffith, 2004). Microarchitecture such as pore size, geometry, and interconnectivity are tuned for maximum cell infiltration (F. P. Melchels et al., 2010a; Silva et al., 2006) and to produce substrate and diffusion conditions to promote stable phenotype proliferation (Griffon, Sedighi, Schaeffer, Eurell, & Johnson, 2006; Karageorgiou & Kaplan, 2005a; Spiteri, Pilliar, & Kandel, 2006) as well as multi-lineal differentiation (Chatrchyan et al., 2011; G. M. Sun & Gerecht, 2009). Manufacturability and reproducibility of the microarchitecture depend on automated control of independent scaffold properties (Nakamura, Iwanaga, Henmi, Arai, & Nishiyama, 2010; W. Sun & Chang, 2008). Gradient and hierarchical structures within 3-dimensional scaffolds selectively stimulate cell behavior by structural, mechanical, and chemical cues(Doran, Mills, Parker, Landman, & Cooper-White, 2009; Irimia & Toner, 2009; Ranucci, Kumar, Batra, & Moghe, 2000; Ridley et al., 2003). Unique niche microenvironments are combined in a single scaffold to model coupled physiological structure and support multiple stable phenotypes. As in osseous tissue, compact and cancellous bone are complementary microenvironments which work together to counterbalance applied stresses to maintain integrity of the tissue and house a network of blood vessels and nerves(Lutolf & Hubbell, 2005; Turner & Burr, 1993). A combination of artifacts and porosity covering sub-

micron and micro length scales are necessary to mimic 3-dimensional extracellular matrices(Holzwarth & Ma, 2011; Karageorgiou & Kaplan, 2005b) Therefore a combination of processing techniques and manufacturing expertise is necessary to fabricate multiple niche environments in a single scaffold.

Structure definition, reproducibility and fine adjustments of the microstructure on several length scales within the scaffold are challenges typically encountered with current processing techniques when engineering and fabricating a 3-dimensional set of niche microenvironments (Panoskaltsis, Mantalaris, & Wu, 2005). The objective of this work is to present a two stage processing technique to produce hierarchical porosity in a 3-dimensional scaffold. The two processing steps are (1) scaffold printing by solid freeform fabrication (SFF) and subsequent (2) directional freezing (freeze casting).

First, sodium alginate (Alg) and a cross-linking solution are simultaneously extruded using a multi-nozzle deposition (MND) printing system to produce a 3-dimensional porous scaffold of rigid hydrogel filaments (W. Sun, Chang, Emami, & Wu, 2010; W. Sun, Chang, & Nam, 2008). Second, the printed MND network is placed in a cylindrical mold, submerged in chitosan-hydroxyapatite (CS-HA) slurry and placed on a cooling plate for directional freezing (Meghri et al., 2010; Wegst, Schecter, Donius, & Hunger, 2010). Lyophilization after freeze casting removes ice from the Alg filaments as well as from the CS-HA composite, leaving transverse pore channels and open longitudinal lamellae through the scaffold, parallel and perpendicular to the cooling surface, respectively. After lyophilization, the scaffold's architecture is hierarchical and the material composition is a heterogeneous combination of the printed porous scaffold and the freeze-cast polymer-ceramic composite. An optional additional sintering process incinerates the organic material and densifies the ceramic phase to produce a homogenous material composition with a well-defined network of open pores. In an unsintered scaffold, the alginate scaffold provides a secondary physical environment for cell adhesion, migration, and mass transport into the scaffolds.

The heterogeneous material combination of rigid (CS-HA) and soft (Alg) substrates are expected to support multiple phenotypes simultaneously. Controlled cell seeding by substrate preference and microenvironment stiffness may produce a stable 3-dimensional engineered co-culture (Pelham & Wang, 1998; Yeung et al., 2005). The sintering incinerates the embedded Alg scaffold and the polymer phase of the CS-HA scaffold to produce a denser, stiffer and stronger HA-scaffold. An open network of lateral pores is produced from the embedded Alg scaffold. Sintering and not sintering each result in unique scaffold material compositions and properties, both of which can be used for scaffold guided tissue engineering.

The combination of the fabrication processes presented in this work offers unique engineering control of two hierarchical structures in the Alg scaffold and CS-HA lamellae, which together extend in three mutually orthogonal directions within the scaffold. Pores of the freeze-cast CS-HA scaffold are predominantly aligned parallel to each other, have closed cell walls and therefore exhibit limited interconnectivity, thus offering limited scope for lateral diffusion and biological mobility within the matrix. The orientation of the freeze-cast porosity is restricted to the direction normal to the cooling plate because it is templated by the ice crystals which grow parallel to the temperature gradient. Transverse porosity connecting neighboring lamellae and the surface of the scaffold is scares and irregular. The combination of scaffold printing and freeze casting allows for the creation of additional, lateral porosity in the CS-HA matrix to enhance diffusion and serve as a niche microenvironment coupled with the lamellae. The created scaffold thus has a hierarchical structure with interconnected porosity in all three mutually orthogonal directions.

The combined process enables engineering control of two distinct niche microenvironments and structures coupled in a hierarchical scaffold over several length scales; including lamellar spacing and embedded alginate filament diameter. This novel material is proposed for applications in scaffold guided tissue engineering, 3-dimensional co-culture, especially for macroscopic scaffolds where natural convection is not a sustainable mechanism for diffusion.

2.3.2 Description of method

Two independent fabrication techniques are combined to embed an engineered 3-dimensional support structure in a highly organized uni-directional freeze-cast scaffold. After sintering and polymer burnout, the resultant ceramic scaffold has porosity that is (1) template by the ice crystals during freeze casting and (2) embedded Alg filaments produced by printing. For scaffold preparation, porous Alg scaffolds are immersed in the CS-HA slurry under vacuum in a cylindrical mold for directional solidification. The wet Alg structure is rinsed with CS-HA slurry to allow the slurry to penetrate the printed scaffold before the CS-HA soaked structure is transferred to a mold filled with CS-HA slurry and exposed to a vacuum to remove any entrapped bubbles from the structure before freeze casting. After freeze casting, the sample is lyophilized to sublimate the ice-phase which templates porosity within both the printed Alg filaments and the freeze-cast polymer-ceramic scaffolds. At this point, the scaffold is heterogeneous, hierarchical and able to support cell viability. An additional processing step, sintering, removes the Alg scaffold and the CS-binder phase, opening pores that connect the longitudinal porosity of the freeze-cast scaffold, while creating a homogenous, purely ceramic HA cell wall material with increased strength. For sintering, the scaffolds are held at a temperature of 1250°C for 1 hour. The result is a ceramic scaffold with ice-templated longitudinal and Alg-templated transverse pores. Process flow to fabricate three pore structures (1) lamellae, (2) porous printed scaffold and (3) a combination of the former porosities is presented in figure 2-30.
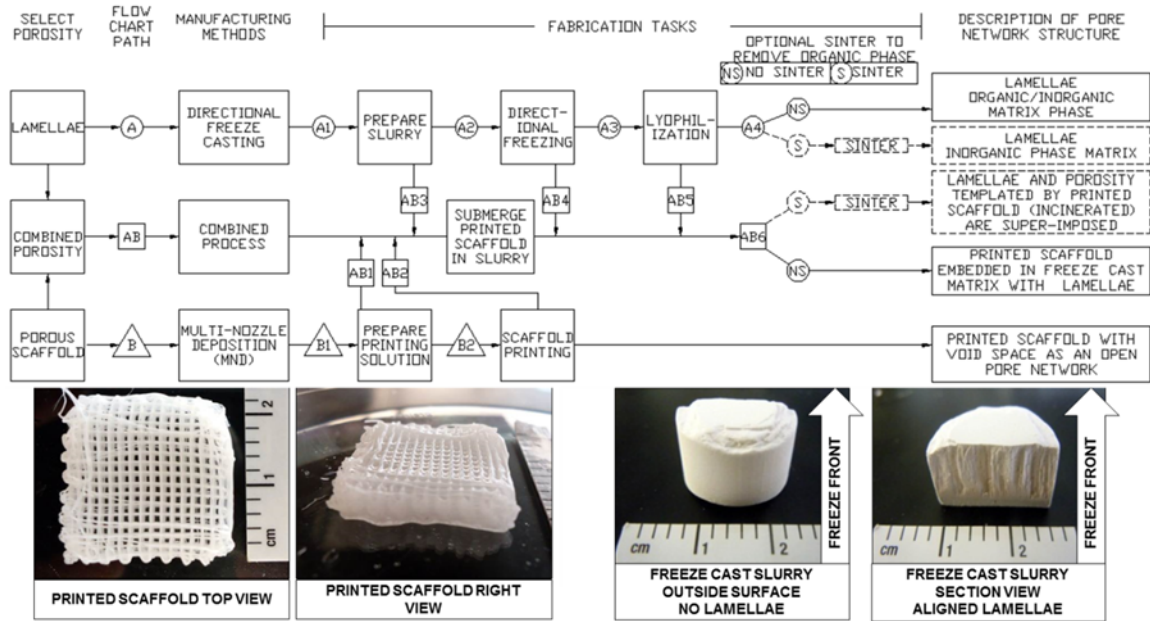
Figure 2-30: Process flow to fabricate lamellae, porous scaffold, or a combined heterogeneous porosity using directional freeze casting with lyophilization, multi-nozzle deposition, or a combined process respectively. Each manufacturing method produces a unique scaffold and pore network structure. Photograph of printed scaffold and freeze cast slurry. Lamellae in freeze cast slurry align with direction of freeze front velocity through ceramic slurry during directional freezing.

2.3.3   Step 1. Scaffold printing by multi-nozzle deposition (MND)

Solid freeform fabrication by Multi-Nozzle Deposition (MND) of biological material and matrix by engineered fluid dispensing produces well-defined 3-dimensional patterns through layer-by-layer deposition; including hydrogel scaffold laden with viable cells(Chang, Emami, Wu, & Sun, 2010; S. Khalil & Sun, 2009b; Nair et al., 2009; Snyder et al., 2011), single wall carbon nanotubes(Yildirim, Yin, Nair, & Sun, 2008), and magnetic nanoparticles(Buyukhatipoglu et al., 2010a). MND material delivery system is a network of multiple independently operated micro-nozzles integrated with the motion system and controlled by the MND system's computer aided manufacturing software. Alg and cross-linker are loaded into separate material reservoirs; each connected to its own pneumatic printing micro-nozzles. Micro-nozzles are mounted on a high precision positioning system to transport the dispensing tip during the extrusion process to produce

pre-defined patterns. Both printing micro-nozzles are oriented to extrude to the same point so that the two solutions come into contact at the capillary tip to produce a cross-linked hydrogel scaffold and maintain the printed pattern. Figure 2-31 presents a system schematic and the set-up of the MND system.
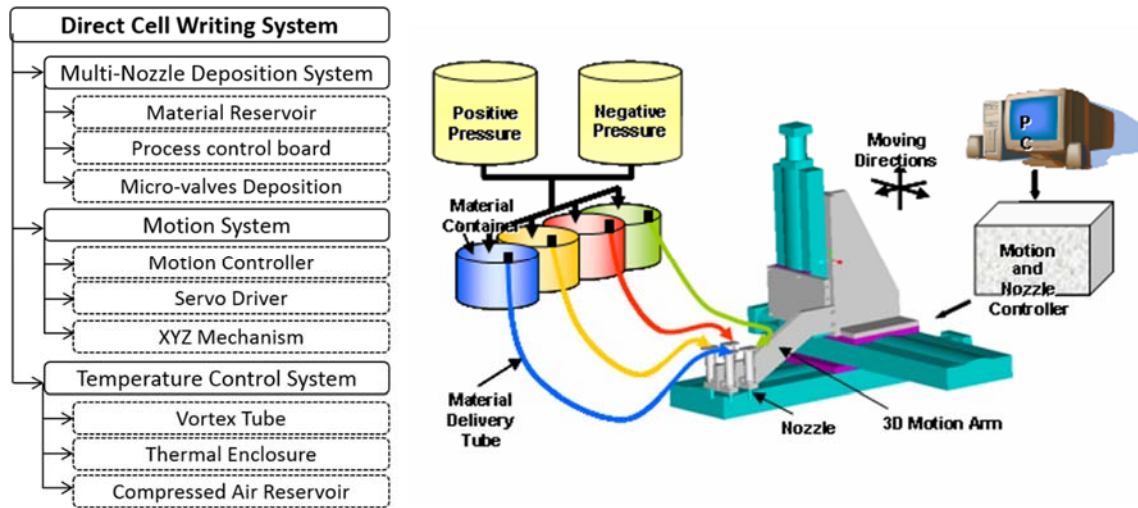
Figure 2-31: Multi-nozzle deposition system pipeline and schematic.

Deposition head is mounted to the motion system above a level stationary substrate. The flow rate of material from the nozzle is controlled by the dispensing pressure and outlet tip diameter. The geometric pattern of the printed material is fabricated by the programmed tool path. The rate material is deposited along the tool path determines the cross-sectional area of the printed structure. The cross-sectional area is a function of the flow rate process parameters and the printhead speed. Figure 2-32 presents an illustration of the MND printhead with a single nozzle printing a filament.
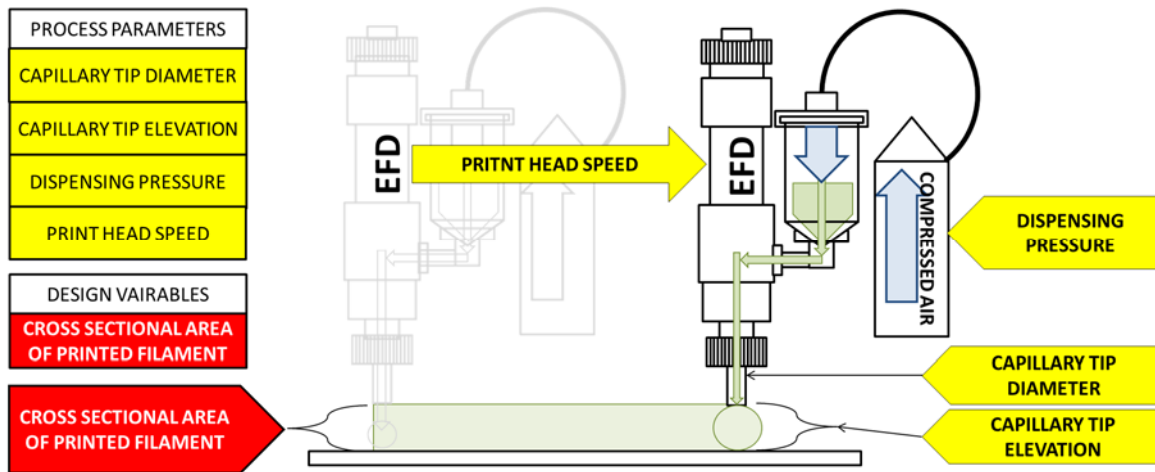
Figure 2-32: Schematic of extruding nozzle with process parameters and design variables called out. Nozzle moved from left to right in depiction. Nozzle is continuously extruding polymer solution (shown as green) through capillary tip. Flow is driven by pneumatic pressure from compressed air reservoir regulated to a pre-determined dispensing pressure. Nozzle travels parallel to printing substrate to pattern polymer.

The cross-section is modeled as an ellipse. The height of the ellipse can be no greater than the height of the outlet tip above the substrate. The relationship of printed cross-section takes two cases: (1) In the case the width of the printed filament is greater than the height, than the height is equal to the process parameter for the height of the tip above the substrate. (2) In the event the height is greater than the width, gravity will cause the not yet cross-linked solution to flow and the final height will be less than the elevation of the tip above the substrate. The second case is not as controllable as the first case. Therefore, printed width will be greater than printed height. Figure 2-32 presents the effect of decreasing the elevation of the printhead outlet (from left to right) on the printed filament height and width.
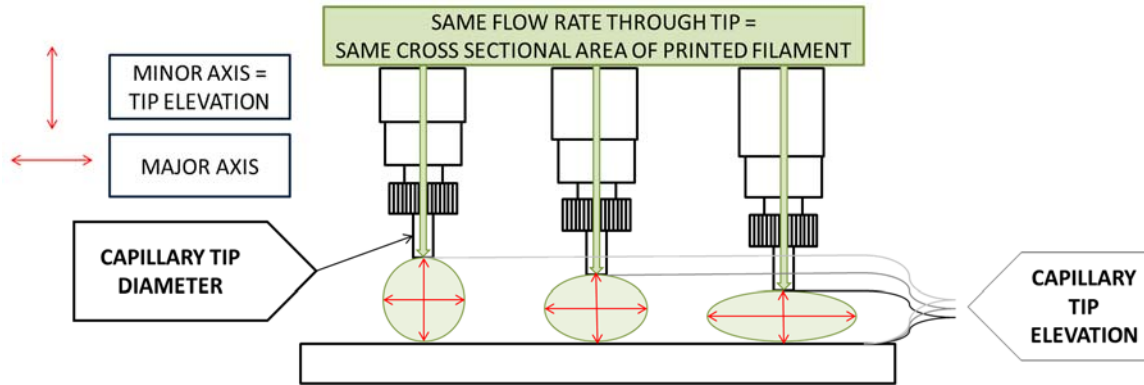
Figure 2-33: Schematic of printed filament cross-section generalized as an ellipse and defined by a major and minor axis. The minor axis will be equal to the capillary tip elevation, unless the elevation is greater than the capillary tip diameter.

2.3.3.1   Definition of MND process parameters and design variables

MND system performance is defined by a set of geometric design variables to assemble multiple materials in 3-dimensional space with controlled deposition along a pathway and width/height of the extruded filament. Design variables, Ψ_{MND}, are a function of the process parameters, $\Omega_{MND,i}$. The system is reproducible within the operating thresholds of the process parameters. Process parameters for each material are independently controlled by unique nozzles and are automated to vary over the time course of the build cycle to fabricate gradient structures or multiple sets of design variables. Equation 2-39 presents the design of the variables Ψ , as a function of the process parameters Ω, where each nozzle is described as its own indicy i, and as a variable over the course of the build cycle and therefore a function of time t.

$$\Psi_{MND,i}(t) = f\{\Omega_{MND,i}(t)\} \qquad\qquad 2\text{-}39$$

The MND system's fabrication objectives define the design variables. The fabrication objective is a 3-dimensional built biological system using multiple materials with specific macro-scale ($10^{-3} – 10^{-1}$ m) pathways of material deposition and micro-scale ($10^{-5} – 10^{-3}$ m) cross-sectional width/height of the deposited material. The macro-scale pathway of material deposition is

controlled by the motion system to be repeatable to less than 10μm. Micro-scale width, c, and height, d, of the printed cross-section define the set of design variables. Each cross-section is fabricated by a unique nozzle, as indicated by the indicy i in equation 2-40.

$$\Psi_{MND,i}(t) = [c_i\,(t) \quad d_i\,(t)\ ] \qquad\qquad\qquad 2\text{-}40$$

Process parameters are defined by the system's hardware and software configuration. MND controllable process parameters are dispensing tip diameter, D, dispensing pressure, P, printhead speed, v, temperature of material delivery system, T, and height of the dispensing tip above the printing substrate, z. Each of the material delivery system's nozzles are independently controlled with their own set of process parameters, except for temperature. A single thermal enclosure surrounds all nozzles. The pressure printhead speed, and height are automated and tunable during a build cycle. The diameter of the dispensing tip, is selected from a prefabricated set of tips and cannot be changed dynamically during a build cycle. Material parameters characterize the rheology during MND system operation. The concentration of solute or additives, N, to the printing solution is included in the set of process parameters.

$$\Omega_{MND,i}(t) = [D_i \quad P_i(t) \quad N \quad v_i(t) \quad T \quad z_i(t)\ ] \qquad\qquad 2\text{-}41$$

Derived parameters assist in analytical characterization of the system. Derived parameters are not directly controlled by the operator and are not the specific performance objective of the process. Table 2-3 presents the MND system's design, derived, material, and process parameters.

Table 2-3: Multi-Nozzle Deposition (MND) system design, derived, material, and process parameters

Symbol	Description	Operating Threshold				Parameter Type
A	Cross Sectional Area of Printed Filament					Derived
c	Major Axis of Printed Ellipse					Design
D	Dispensing Tip Diameter	100	150	200	μm	Process
		250	330	410		
d	Minor Axis of Printed Ellipse					Design
i	Index to identify a specific nozzle					-
m	Mass Flow Rate					Derived
N	Solute or Additive Concentration					Process
P	Dispensing Pressure		> 40.0 psi			Process
Q	Volumetric Flow Rate					Derived
v	Printhead Speed		> 15.0 mm/s			Process
T	Temperature of Material Reservoir		0-4°C			Process
t	Time					-
z	Height of Tip Above Printing Substrate		$100\mu m \leq z \leq D$			Process
ρ	Material Density					Material
Ψ_{MND}	The set of MND design variables					
Ω_{MND}	The set of MND process parameters for each nozzle.					-

2.3.3.2 Motion System

Motion is discretized into three mutually orthographic directions by Parker Daedal's 400XR three axis high precision linear motor system. Gemini digital servo drives apply torque, velocity and encoder tracking to each of the three linear slides. Each drive is controlled by a 6K4 Computroller controller. All controllers communicate with Parker's Motion Planner automation software through the serial port SR-232. The displacement, speed, acceleration, and deceleration along each of the three linear slides is programmable as individual commands or a complete program. Displacement and bidirectional repeatability resolution are +/-10μm and +/-1.3μm, respectively.

2.3.3.3   Multi-nozzle deposition system

The material delivery system is mounted to a high precision positioning system to deposit material on a stationary substrate placed underneath the tool path. Each of the four EFD pneumatic microvalve nozzles are independently controlled using automation software for dispense and hold during a build cycle. Nozzle actuation and the 3-dimensional tool path are both defined in the same Parker Motion Planner software program. Each nozzle is plumbed a dedicated material reservoir. Microvalve controller is pressurized to 70-80psi using a compressed air cylinder (AirGas) to actuate the valve. Material reservoir is pressurized to 0.1-40.0 psi to induce a desired flow rate through the extruder when the valve is open during printing. The dispensing tip fastened to the nozzle outlet determined the approximate width of the printed filament. The tip is selected from a set of prefabricated EFD steel capillary tips.

Configuration options for the nozzle are flexible between build cycles using a bracket mounting system for each nozzle, but cannot be adjusted during the build cycle. Options include: (1) nozzles are mounted adjacent to one another or at an angle or (2) pointed to extrude to the same point. Layer-by-layer printing achieves 3-dimensional scaffold architecture by stacking structures printed. After the structure is printed, the nozzle tip is raised and a second layer is printed on the first. To begin, a second layer is printed on top of the first. The programmed trajectory of the second layer is at 0-90 configuration to the first. This forms a grid structure or pores and extruded material.
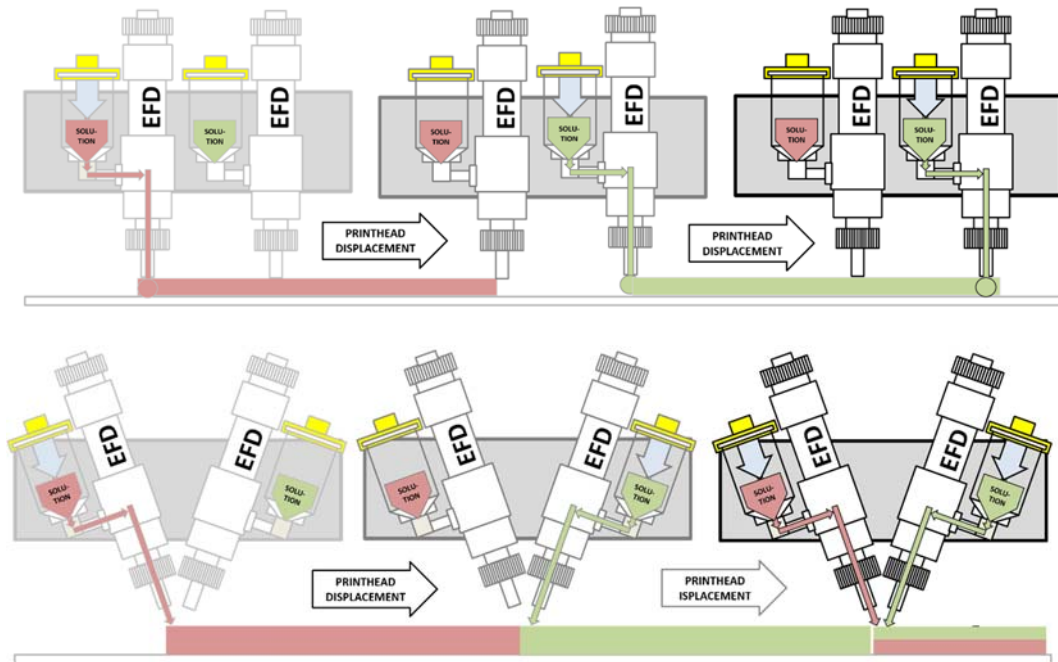
Figure 2-34: Multi-nozzle configuration of nozzles mounted side-by-side for controlled sequential deposition (top row) and two nozzle oriented to the same point for individual or simultaneous extrusion (bottom row).

2.3.3.3.1   Printhead speed selection for a set of design variables

MND printing   is a controllable engineering process. A given set of MND process parameters produce a specific filament diameter; which can theoretically be varied from 250μm - 800μm. A derived model for the printed filament width as a function of the MND process parameters and measured mass flow rate is presented. The derived model is a tool to define the MND process parameter for deposition head speed to fabricate specific filament widths. The mass flow rate from the material delivery system is equal to the mass flow rate of substrate accumulation. Further, the mass flow rate is gnerally equal to the material density and volumetric flow rate at any given point in the process, presented in equation 2-42.

$$\left(\frac{dm}{dt}\right)_{from\ material\ delivery\ system} = \left(\frac{dm}{dt}\right)_{substrate\ accumulation} = \rho_i Q_i \qquad 2\text{-}42$$

The working solution is modeled as an incompressible fluid. The change in density of the working solution is neglected between the pressurized material delivery system and ambient substrate accumulation, presented in equation 2-43.

$$\rho_{from\ material\ delivery\ system} = \rho_{substrate\ accumulation} \qquad 2\text{-}43$$

The flow rate from the material delivery system is equal to the MND deposition head speed v and cross-sectional area of the printed filament A, presented in equation 2-44.

$$Q_{from\ material\ delivery\ system} = vA \qquad 2\text{-}44$$

Conservation of mass between the MND material resevoir and ambient substrate (equation 2-42), constant density (equation 2-43) and volume flow rate from the material delivery system (equation 2-44) are combined for equation 2-45.

$$vA = m/\rho \qquad 2\text{-}45$$

The density of the working solution is a function of the concentration of solute, N, added to distilled water, presented in equation 2-46.

$$\rho = 1 + N \qquad 2\text{-}46$$

Where ρ is the density of the working solution and N is the percentage of solute added to distilled water in mass per volume. The cross-section of the printed filament is modeled as an ellipse. The major and minor axis of the printed filament are parallel and perpendicular to the printing substrate respectively, presented in equation 2-47.

$$A = \frac{\pi c d}{4} \qquad 2\text{-}47$$

The design variable for the printed filament height, or minor axis, is equal to the MND process parameters for the height of the dispensing tip over the substrate, equation 2-48.

$$d = z \qquad\qquad 2\text{-}48$$

The design variable for the width of a MND printed filament is defined by combining equation 2-45, 2-4, 2-47, and 2-48, as presented in equation 2-49.

$$c = \frac{4m}{\pi d v (1 + N)} \qquad\qquad 2\text{-}49$$

The mass flow rate of two working solutions, alginate (Alg) and alginate blended with hydroxylapatite particles (Alg-HA) is experimentally measured. The MND micro-nozzle valve is opened and the extruded material is collected and weighed. The mass flow rate is determined from the measured weight and time using equation 2-50. The MND dispensing tip diameter and length, solute concentration of the working material, dispensing pressure, and temperature are constant during mass flow measurements.

$$Mass\ Flow\ Rate = m = f\,(D, N, P, T) = \frac{m_{material\ collected\ during\ extrusion}}{t_{nozzle\ is\ open}} \qquad 2\text{-}50$$

The minimum applied dispensing pressure to extrude 6% alginate through a 250µm diameter capillary tip is 15 psi. This dispensing pressure yields the smallest feasible mass flow rate of both materials; 6% Alg and 6% Alg-HA. Mass flow rate increases from 0.25/0.26 mg/s at 15 psi to 0.61/0.62 mg/s at 30 psi for Alg and Alg-HA respectively. Mass flow rate results in figure 2-35.
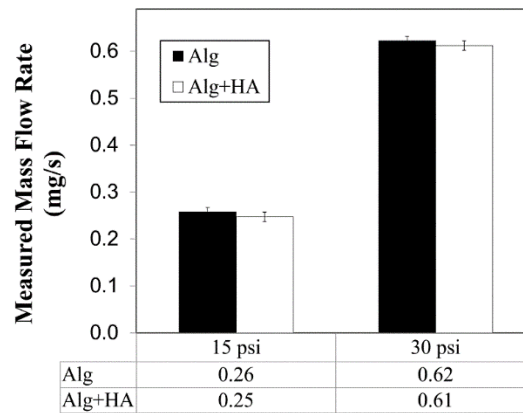
Figure 2-35: Experimental measurements of Alg and Alg-HA MND system mass flow rate through a 250μm capillary tip.

The effect of dispensing pressure and printhead velocity on the printed filament width is studied using the experimentally determined mass flow rates (equation 2-50) and derived model (equation 2-49). A graphical presentation of equation 2-49 and experimental results are presented in figure 2-36. Results are applicable to Alg and Alg-HA working solution using the partial set of MND process parameters including a $\emptyset 250\mu m$ tip positioned 200μm above substrate with a dispensing pressure of either 15 or 30psi.
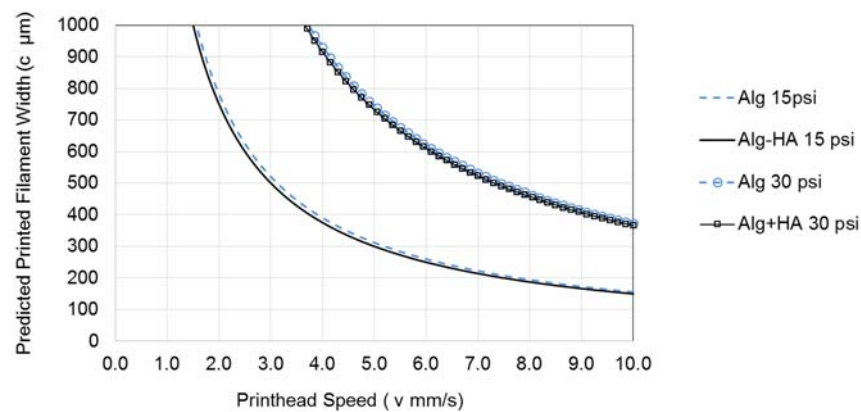
Figure 2-36: The effect of dispensing pressure and printhead velocity on the theoretical printed filament diameter of 6.0% alginate and blended alginate-hydroxylapatite extruded through a $\emptyset 250$μm capillary tip positioned $200\mu m$ above the printing substrate.

The design variable set for Alg and Alg-HA printing is defined to be a width and height of 250μm and 200μm are presented in equation 2-50.

$$\Psi_{MND,i} = [c_i\,(t)\,\mu m \quad d_i\,(t)\,\mu m\ ]$$

$$\Psi_{MND,i} = [250 \quad 200\ ] = f\{\Omega_{MND,i}\} \qquad\qquad 2\text{-}51$$

Table 2-4 presented the printhead velocity to fabricate the set of design variables presented in equation 2-51.

Table 2-4. MND printhead velocity to fabricate 250μm filament width of either 6.0% alginate (Alg) and blended alginate-hydroxylapatite (Alg-HA) extruded through a ⌀250μm capillary tip positioned 200μm above the printing substrate.

Material	Printed Filament Width	Dispensing Pressure	Printhead Velocity
Alg	$c = 250$ μm	$P = 15$ psi	$v = 5.0$ mm/s
Alg	250	30	11.9
Alg-HA	250	15	4.8
Alg-HA	250	30	11.7

Either dispensing pressure is theoretically capable of producing the set of design variables. The lower dispensing pressure is used in the experimental work to limit shear stress on the working material. This consideration for mechanical perturbations during printing is critical for future cell-laden Alg or Alg-HA printing.

$$\Omega_{MND,i} = [D_i\ \mu m \quad P_i(t)\ psi \quad N \quad v_i(t)\ mm/s \quad\quad T\ °C \quad\quad z_i(t)\ \mu m\ ]$$

$$\Psi_{MND,i} = [c_i\,(t)\,\mu m \quad d_i\,(t)\,\mu m\ ]$$

$$\Psi_{MND,i} = [250 \quad 250\ ] = f\{\Omega_{MND,i}\}$$

$$= f\left\{\begin{matrix} Alg \\ Alg + HA \\ CaCl_2 \end{matrix}\right\} = f\left\{\begin{bmatrix} 250 & 15.0 & 6\% & 5.0 & - & 200 \\ 250 & 15.0 & 6\% + 50\,mg/mL & 5.0 & - & 200 \\ 400 & 1.0 & 10\% & 5.0 & - & 200 \end{bmatrix}\right\} \qquad 2\text{-}52$$

2.3.3.3.2 Alginate cross-linked with CaCl$_2$

Alginate (Alg) for MND printing is prepared from alginic acid sodium salt from brown Algae (Sigma Aldrich Corp., St. Louis, MO) in distilled water to a final concentration of 6.0% (w/v). The cross-linking solution for MND printing is prepared from calcium chloride ACS grade (BDH) in distilled water to a final concentration of 10% (w/v). MND process parameters are set to Ø250 and Ø400μm dispensing tip and 15.0/1.0 psi for Alg and CaCl$_2$ solutions respectively. Nozzles are oriented to the same point and extruded simultaneously to cross-link Alg or Alg-HA during 3-dimensional scaffold printing. Printhead speed is set to 5.0 mm/s and the height of the tip above substrate (and height increment between layers) is 200μm. The scaffold is a 20-layer stack of square waves. The scaffold is a single unbroken extruded filament printed to form a network of struts and interstitial pore space. A design model is programmed to a square wave with 20.0 mm center-to-center filament spacing. A complete scaffold consists of 20 layers, where consecutive layers are mutually orthogonal, with 200μm between layers. Figure 2-37 presents a 20-layer Alg scaffold respectively printed using MND. The set of process parameters to fabricate the results presented in equation 2-53. Printed filament width is measured to be 275μm. The target printed filament width being 250μm.

$$\Omega_{MND,i} = [D_i\ \mu m \quad P_i(t)\ psi \quad N \quad v_i(t)mm/s \quad T\ °C \quad z_i(t)\ \mu m\ ]$$

$$\begin{bmatrix} Alg \\ CaCl_2 \end{bmatrix} = \begin{bmatrix} 250 & 15.0 & 6\% & 5.0 & - & 250 \\ 400 & 1.0 & 10\% & 5.0 & - & 250 \end{bmatrix} \qquad \textit{2-53}$$
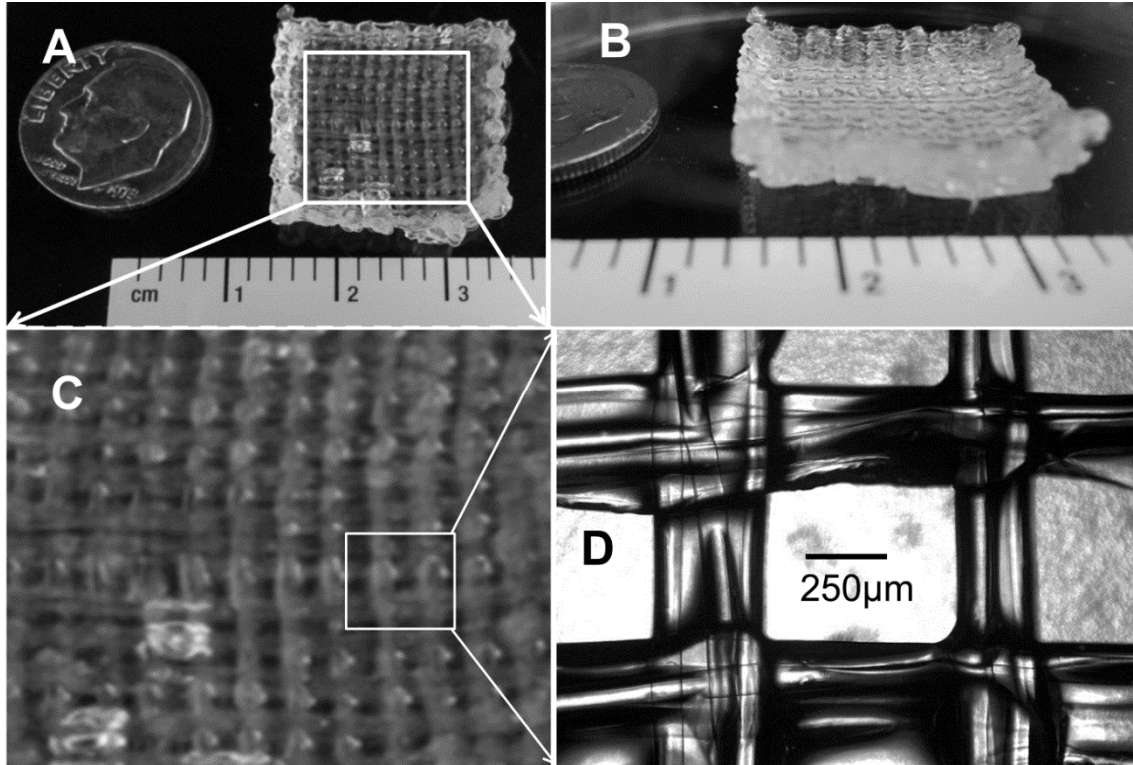
Figure 2-37: Porous 20-layer scaffold fabricated by Multi-Nozzle Deposition (MND). Scaffold photographed from (A) top, (B) front (C) 4x magnification of top view, and (D) 20x magnification top view of a pore.

2.3.3.3.3   Alg-HA blend cross-linked with CaCl$_2$

Native alginate's surface chemistry prohibits substantial cell attachment (K. Y. Lee & Mooney, 2012). Additives, such as HA particles, enable cell anchorage and cell-material (Wei & Ma, 2004). Alg and calcium chloride cross-linking solution is prepared as previously described. Alg-HA blend is prepared from HA (Trans-Tech Inc., Adamstown, MD) in Alg solution to a final concentration of 50 mg/mL. Alg-HA and calcium chloride cross-linking solution are loaded into separate nozzles. Figure 2-38 presents a 20-layer Alg scaffold respectively printed using MND. The set of process parameters to fabricate the results presented in equation 2-54. Printed filament width is measured to be 244µm. The target printed filament width being 250µm.

$$\Omega_{MND,i} = [D_i \, \mu m \quad P_i(t) \, psi \quad N \quad v_i(t) mm/s \quad T \, °C \quad z_i(t) \, \mu m \quad]$$

$$\begin{bmatrix} Alg + HA \\ CaCl_2 \end{bmatrix} = \begin{bmatrix} 250 & 15.0 & 6\% + 50\frac{mg}{mL} & 5.0 & - & 200 \\ 400 & 1.0 & 10\% & 5.0 & - & 200 \end{bmatrix} \qquad 2\text{-}54$$
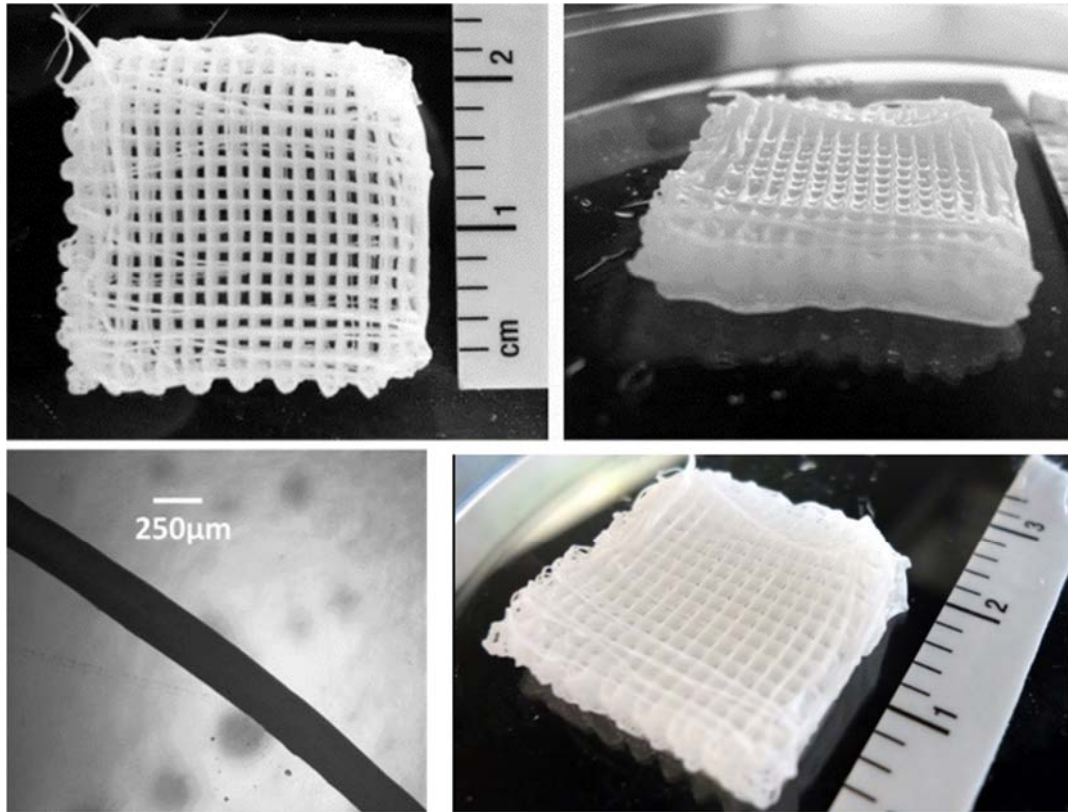
Figure 2-38: Porous 3-dimensional scaffold fabricated by Multi-Nozzle Deposition (MND). The 20-layer 6% Alg (Alg) with 50 mg/mL Hydroxyapatite (HA) scaffold fabricated by the following set of MND process parameters: 15 psi dispensing pressure, 250μm/12.7mm diameter/length capillary, and 5.0mm/s printhead speed.

2.3.3.3.4   Fibrin scaffold from MND printing of fibrinogen and thrombin

Fibrin glue is composed of two agents; fibrinogen and thrombin. Fibrinogen is the base and thrombin is the cross-linker. When mixed together, thrombin converts the fibrinogen into fibrin much like the body's natural clotting cascade. The proportion of thrombin to fibrinogen affects the material properties of the resultant fibrin construct and cross-linking time. Thrombin and fibrinogen

supplied by Advanced Technologies and Regenerative Medicine (ATRM) from EVICEL Fibrin Sealant (Human) (Omrix Therapeutics).

Cross-linking time is of critical importance to layer-by-layer manufacturing of fibrin scaffold. Without sufficient cross-linking time during the addition of layers, the scaffold's formability is not sufficiently stable for layer-by-layer fabrication. During this work, minimum thrombin dilution to stably gel the construct to minimize detoeriation of macro- and micro- scale patterning are investigated. The lower limit of the process window for thrombin dilutions is set by minimum cross-linking time. The thrombin dilution may be increased from this limit to tune the material properties of the printed fibrin for structural and biomimetic design cues.

Cross-linking time is a function of fibrinogen and thrombin concentration. ATRM and Drexel timed the cross-linking of fibrin (EVICEL™ Fibrin Sealant (Human), Omrix Therapeutics) using a serial dilution of thrombin. The time to print a single layer is 0.5-1.0 minutes, therefore the fibrin must be cross-linked in under 0.5 minutes for layer-by-layer manufacturing techniques. The results of the experiment are presented in Table 2.

Table 2-5: Estimated cross-linking time for a series of thrombin

Dilution	Thrombin (mL)	PBS (mL)	Cross-linking time (minutes)
1:16.67	0.30	4.70	0.5
1:125	0.04	4.96	4.0
1:625	0.01	4.99	15.0

The 1:16.37 dilution of thrombin cross-linked the fibrinogen in 0.5 minutes. Less dilute thrombin solutions took longer than 0.5 minutes to cross-link. The 1:16.67 thrombin dilution is the minimum dilution for use in fibrin printing, more dilute solutions gel too slowly for fibrin printing. Nozzles are oriented to the same point and extruded simultaneously to cross-link fibrinogen and thrombin during scaffold printing. The design model used for previous Alg 20-layer scaffold

printing is used again for Alg-HA scaffold. The set of MND process parameters are presented in equation 2-55.

$$\Omega_{MND,i} = \begin{bmatrix} D_i \ \mu m & P_i(t) \ psi & N & v_i(t) \ \frac{mm}{s} & T \ °C & z_i(t) \ \mu m \end{bmatrix}$$

$$\begin{bmatrix} Fibrinogen \\ Thrombin \end{bmatrix} = \begin{bmatrix} 150 & 2.0 & No\ Dilution & 5.0 & - & 200 \\ 150 & 2.0 & 1:16.67 & 5.0 & - & 200 \end{bmatrix} \qquad 2\text{-}55$$
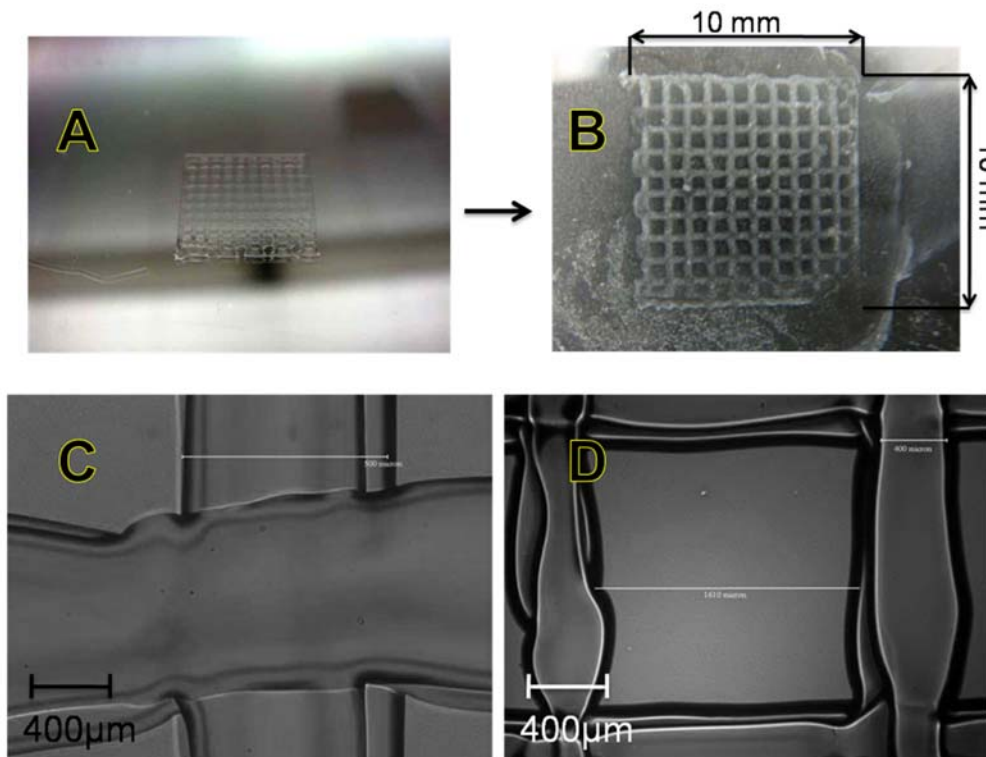
Figure 2-39: Multi-layer fibrin scaffold printed by multi-nozzle deposition of thrombin and fibrinogen. Macroscopic photograph of dual nozzle printing fibrin (A,B) and light microscope of 4-layer scaffold (C,D).

Cells-laden fibrinogen is prepared and printed a one layer series of intersecting circles and lines. The set of MND process parameters are presented in equation 2-56. Printing formable single layer structures of cell-laden fibrin is feasible. Further analysis of cell survival and function post-printing is left to future work.

$$\Omega_{MND,i} = \begin{bmatrix} D_i & \mu m & P_i(t) & psi & N & v_i(t) \dfrac{mm}{s} & T \, °C & z_i(t) \, \mu m \end{bmatrix}$$

$$\begin{bmatrix} Fibrinogen + Cells \\ Thrombin \end{bmatrix} = \begin{bmatrix} 150 & 2.0 & No\ Dilution + 1.0 \times 10^6 & 5.0 & - & 200 \\ 150 & 2.0 & 1:16.67 & 5.0 & - & 200 \end{bmatrix} \qquad \text{2-56}$$
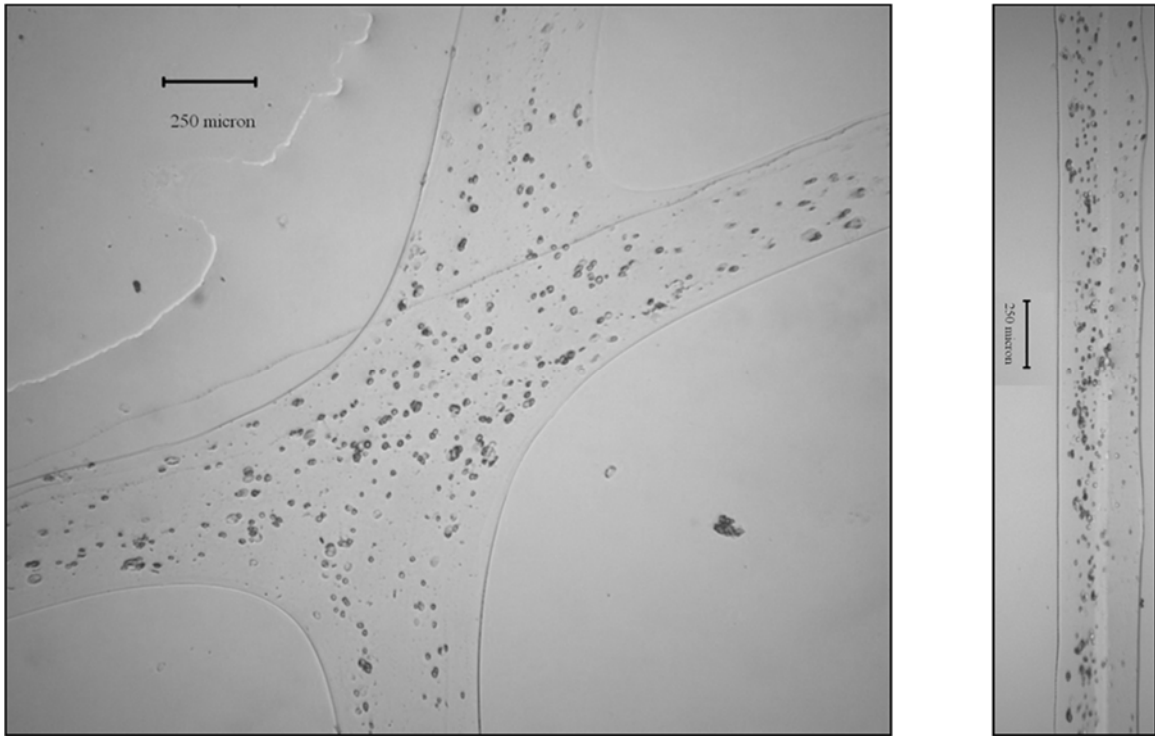
Figure 2-40: Cell-laden polymer printed to form an intersecting line (top) and line (bottom) by multi-nozzle deposition of cell-laden fibrinogen and cross-linking agent thrombin. Process parameters defined as 250μm diameter capillary tip, 8 psi dispensing pressure, printhead speed 10 mm/s. Materials include $1.0\mathrm{E}10^6$ mesenchymal stem cells / mL fibrinogen.

2.3.3.4   Temperature control system

2.3.3.4.1   Rationale and description

Temperature control system is designed to prevent the viscosity of a thermally cross-linking printing solution from increasing during a build cycle. Partial curing due to uncontrolled ambient temperature conditions increases material viscosity. Consequently, material formability becomes a function of the amount of time the material has been exposed to gel-inducing temperature

environment. Partial gelation diminishes reproducibility of the printed results. Complete curing causes the material delivery system to occlude and prevents further deposition. Therefore, the working material visacosity is stabilized using temperature control. All components of the multi-nozzle material delivery sub-system are housed in a thermal enclosure with temperature control.

The temperature control system includes a thermal enclosure, vortex tube, compressed air reservoir, and thermometer. The nozzles and material reservoir are placed in the thermal enclosure and mounted to the stage on the motion system. Air passes from the compressed air cylinder, through the vortex tube, and the cold air stream enters the thermal enclosure to cool the working material. Hot air stream from the vortex tubes is vented to the ambient environment. The MND printing operator visually monitors the thermometer and manually increases or decreases the flow rate from the air cylinder to cool or warm the thermal enclosure during printing. Figure 2-41 presented the components of the temperature control system.
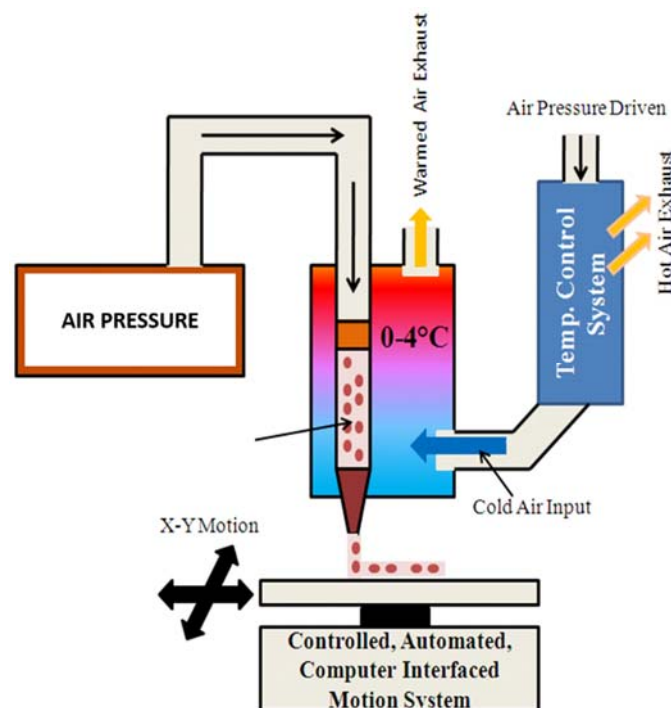
Figure 2-41: Temperature control system schematic mounted around material delivery system.

2.3.3.4.2   Matrigel thermally cross-linked

A promising extracellular matrix is a gelatinous protein mixture Matrigel, which imporves in vitro biomimetic cell function through bioactive factors and essential macromolecules (Dutta & Dutta, 2010; Kleinman & Martin, 2005; Moghe et al., 1996). However, existing printing techniques are unable to dispense cell-laden Matrigel because the devices operate above the material's gelation temperature. Matrigel thermally cross-links above 4ºC, and this occludes an ambient temperature dispensing capillary and prevents further extrusion. A novel temperature controlled printing system is presented in this work to pattern Matrigel and leverage both biological cues from Matrigel matrix and physical cues from physiologically derived cell patterning to improve biomimetic function of in vitro tissue analog (Allen, Khetani, & Bhatia, 2005; Nahmias, Schwartz, Hu, Verfaillie, & Odde, 2006). Printing technology allows researchers to leverage geometric positioning and proximity of specific biologics to bring functional abilities to cell aggregates (Barron, Wu, Ladouceur, & Ringeisen, 2004; Ciocca, De Crescenzio, Fantini, & Scotti, 2009; Murray, Garcia-Godoy, & Hargreaves, 2007). In this work, cells are printed in square wave form to ensure nutrient and drug diffusion to the core of the extruded filament, apply structural cues to cells, and quality control over equal dispensing for each sample.

The feasibility of temperature controlled cell printing depends on cell viability after the mechanical and thermal stress of printing. Prior to patterning cell-laden Matrigel and further study of printed structures, cell survival and viability 48 hours after printing is studied. Human mammary epithelial of the cell line M10 (ATCC) are cultured in the Alpha Modification of Eagle's Medium supplemented with 10% (v/v) fetal bovine serum and 1% (v/v) penicillin streptomycin. Cells are rinsed with PBS, trypsinized, and counted using exclusion dye Trypan Blue and hemocytometer. Once counted, cells are with the gelatinous protein mixture Basement Phenol Red-free Matrigel (BD Bioscience) over ice to prevent gelation. Cells are homogenously distributed throughout the Matrigel using a gentle tapping technique with minimal pipetting to a concentration of 1.0×10^6 cells

per mL. Final printing solution is 50% cells and 50% Matrigel (v/v) solution. The cell-laden solution is stored on ice for 5-10 minutes prior to printing to prevent gelation. After printing, the viability of cells is qualitatively assessed using the fluorescence based Live/Dead Viability/Cytotoxicity Kit for mammalian cells. Printed constructs were screened using fluorometric indicators of the commercially available Live/Dead kit for live (green) and dead (red) cells. Figure 2-42 presents the fluorescent images of cells less than 30 minutes and 48 hours after printing. Process parameters are presented in equation 2-57.

$$\Omega_{MND,i} = [D_i\ \mu m \quad P_i(t)\ psi \quad N \quad v_i(t)\ mm/s \quad T\ °C \quad z_i(t)\ \mu m\ ]$$

$$Matrigel + Cells = \begin{bmatrix} 150 & 12.3 & 50\% + 1.0 \times 10^6\ \dfrac{cells}{mL} & - & 2 & - \end{bmatrix} \qquad 2\text{-}57$$
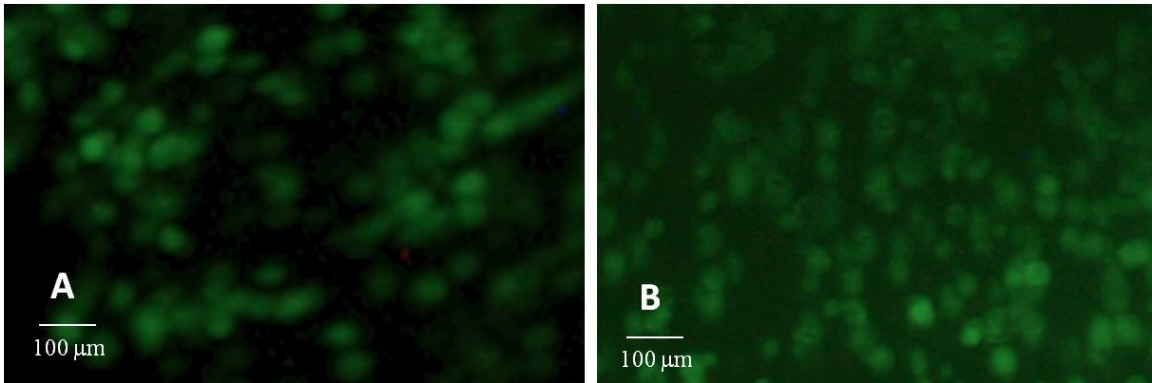
Figure 2-42: Human mammary epithelial cells embedded in Matrigel labeled (A) less than 30 minutes and (B) 48 hours after printing.

Necrotic effects of the process are not quantitatively observed in the printed cells. Temperature controlled printing yielded high cell survivability and viable cells remained 48 hours later. Minimal cell proliferation is observed, which is to be expected due to cell encapsulation.

After observing cell survive the printing process, the authors printed a square wave of cell-laden Matrigel. The pattern has a high surface area to volume ratio for cell/drug contact during

pharmacokinetic studies. Human mammary epithelial of M10 cell line were prepared in a Matrigel matrix as described previously and printed using the process parameters presented in equation 2-58. Cell arrangement post-printing is qualitatively evaluated using fluorescence based Live/Dead Viability/Cytotoxicity Kit for mammalian cells (Molecular Probes).

$$\Omega_{MND,i} = [D_i\ \mu m \quad P_i(t)\ psi \quad N \quad v_i(t)\ mm/s \quad T\ °C \quad z_i(t)\ \mu m \quad]$$

$$Matrigel + Cells = \left[250 \quad 12.3 \quad 50\% + 1.0 \times 10^6 \frac{cells}{mL} \quad 10.0 \quad 2 \quad 200\right] \qquad 2\text{-}58$$
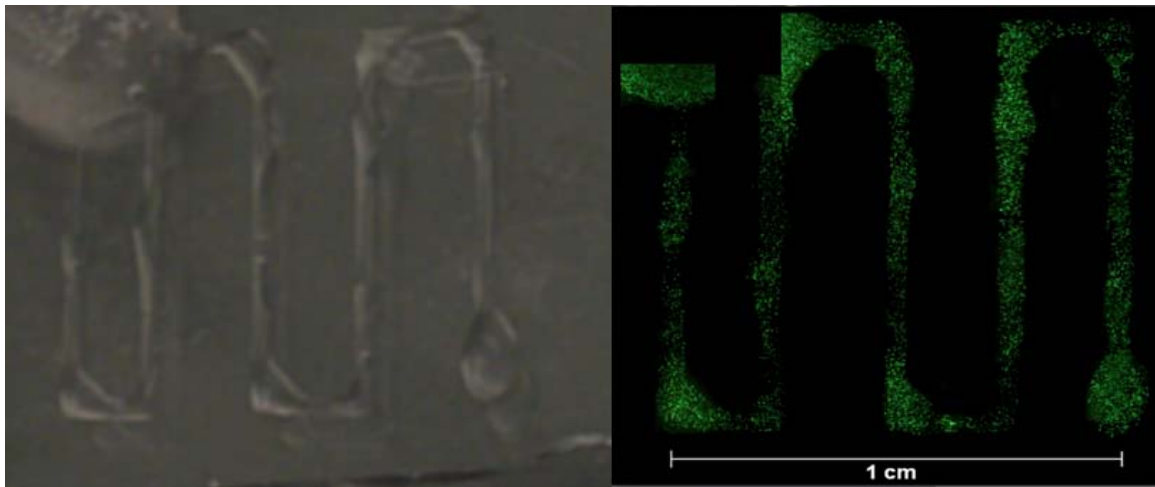
Figure 2-43: (Left) photograph of printed construct and (right) fluorescent image of cells in printed construct.

2.3.4   Step 2. Embed scaffold in ceramic slurry

MND printed 20-layer scaffolds of both alginate (Alg) and alginate-hydroxylapatite (Alg-HA) are fabricated as previously described in sections 2.3.3.3.2 and 2.3.3.3.3 respectively. The printed scaffold is moved to an absorbent towel to drain cross-linking solution from pore space. Then, printed scaffold is submerged in ceramic slurry under vacuum to remove air trapped in solution. The ceramic slurry is prepared from chitosan (CS) solution for freeze casting is prepared by diluting 2.4% (w/v) chitosan (low molecular weight, Sigma Aldrich Corp, St. Louis, MO) in

100 mL of 1% (v/v) acetic acid in doubly distilled water. To completely dissolve the CS, the solution is rolled on a bottle roller for at least 24 hours. Subsequently, 10g of HA (Trans-Tech Inc., Adamstown, MD) is added to 10 mL of CS solution to obtain the CS-HA slurry. The printed scaffolds are rinsed with CS-HA slurry before being transferred to a cylindrical PTFE mold, which is filled with the CS-HA slurry and sealed by a copper bottom plate. Any remaining bubbles from the submerged structure of the mold are removed by exposing the filled mold to a vacuum.

2.3.5   Step 3. Freeze casting and lyophilization

Scaffold microarchitecture and material properties of freeze-cast scaffolds are correlated to material composition and processing parameters (Hunger, Donius, & Wegst, 2012, 2013). To begin freeze-casting, the mold with printed scaffold immersed in CS-HA slurry is placed with its copper bottom atop a cold finger. The mold is immersed in a liquid nitrogen bath (Wegst et al., 2010). The cooling rate applied by the cold finger is regulated with a PID-controller that is attached to a thermocouple at the top of the cold finger and a band heater just below it to counteract the liquid nitrogen cooling. The directional freezing of a polymer-ceramic slurry in a cylindrical mold results in a highly aligned assembly of lamellar pure ice crystals, between which the polymer-ceramic phase is concentrated. The applied freezing rate, which can be carefully controlled, determines the sample cooling rate as well as the velocity of the freezing front within the mold, and through it the ice crystal thickness and lamellar spacing within the freeze-cast composite scaffold. The samples of this study are frozen at a cooling rate of 10°C per minute until completely solidified, removed from the PTFE mold and transferred to a lyophilizer (FreeZone 4.5, Labconco, Kansas City, MO), where they are held for at least 48 hours to remove the ice phase.
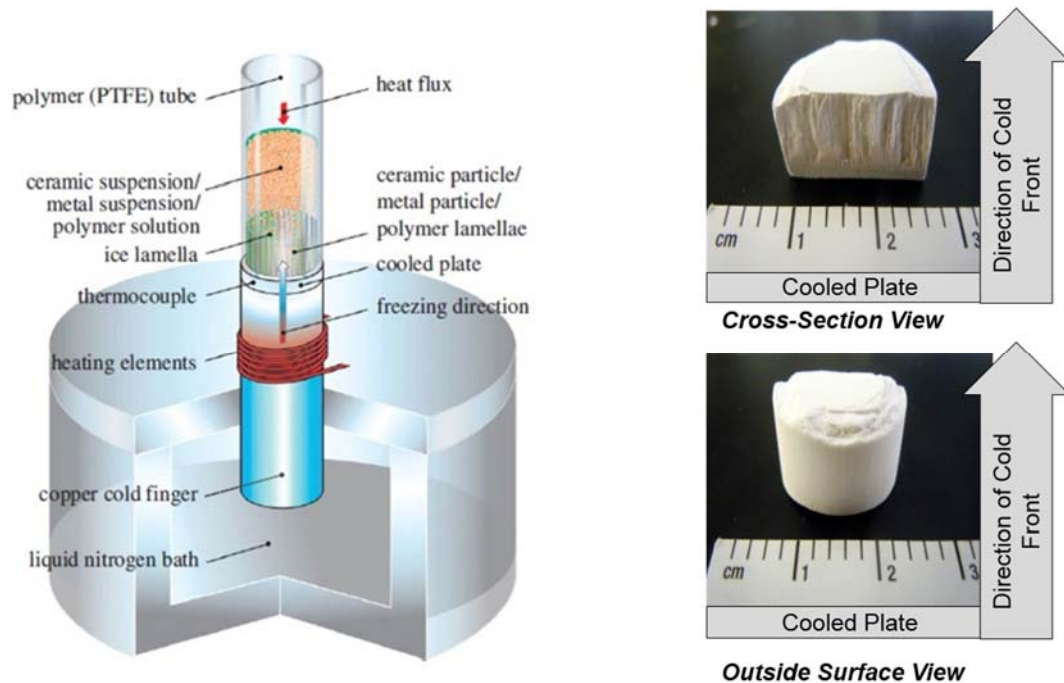
Figure 2-44: Schematic of freeze-casting system, reproduced from Wegst et. al. (Wegst et al., 2010) and freeze cast CS-HA scaffold after lyophilization to sublimate ice phase. Front view (top right) presents the outside surface of the scaffold. No significant porosity to exchange gas or liquid between the core of the scaffold and ambient environment is evident. Section view (bottom right) of the same scaffold present lamella network; orthographic to the cooling plate. Lamellae are open pores in scaffold formed when ice phase is sublimated during lyophilization.

2.3.5.1   *Scanning electron microscope characterization*

Scanning electron microscopy is performed at high vacuum with a Zeiss Supra 50VP SEM (Carl Zeiss Microscopy, LLC, Thornwood, NY) at an accelerating voltage of 6 kV and a working distance of 4 to 6 mm. All investigated specimens were sputter coated with a 5 nm thick layer of platinum-palladium to provide a conductive path during imaging.

2.3.5.2   *MND printed scaffold embedded in freeze cast scaffold*

Combining the printing with the freeze-casting process superimposes the embedded transverse Alg network with a scaffold in which the lamellae are longitudinally aligned to produce a hierarchical microarchitecture with a heterogeneous cell wall material composition. The size and spacing of the uni-directional lamellae network is controlled by the rate of freezing. The embedded

Alg network remains in the polymer-ceramic composite after freeze drying. These filaments produce a regular lateral porosity, which is orthogonal to the longitudinal lamellae. The longitudinal lamellae are in plane with the imaged cross-section. The lateral pores, created by the Alg filaments, are normal to the imaged cross-section. Figure 2-45 presents images of a cross-section of such CS-HA-Alg scaffold without sintering. Regular pores, two along the top row and two along the bottom row, are visible in the SEM. An Alg filament is emerging from a pore in the upper right corner and extends across the scaffold cross-section.
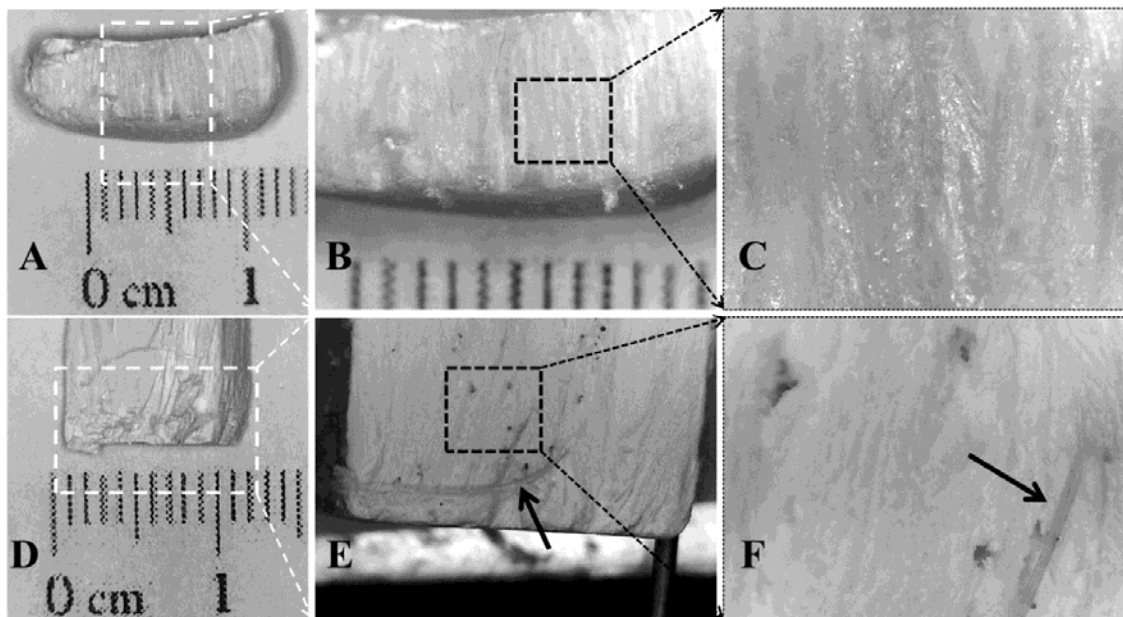
Figure 2-45: (A-C) CS-HA and CS-HA-Alg (D-F) scaffolds after freeze casting (no sintering) and then sectioned longitudinally. (A, D) Photographs of cross-section of scaffold to expose a longitudinal view of lamellae network and side view of embedded Alg scaffold. (B, E) 4 x magnifications of A and D, respectively. (C,F) 10 x magnifications of A and D, respectively. Arrows in E and F point to Alg filaments protruding from section.

2.3.5.3 *Sintering CS-HA matrix*

Sintering removes the embedded Alg as well as the CS binder from the CS-HA matrix to produce open pores, while a monolithic HA-ceramic scaffold with increased stiffness and strength

is created (Ruys et al., 1995). Figure 2-46 presents SEM micrographs of un-sintered and sintered freeze-cast CS-HA scaffold.
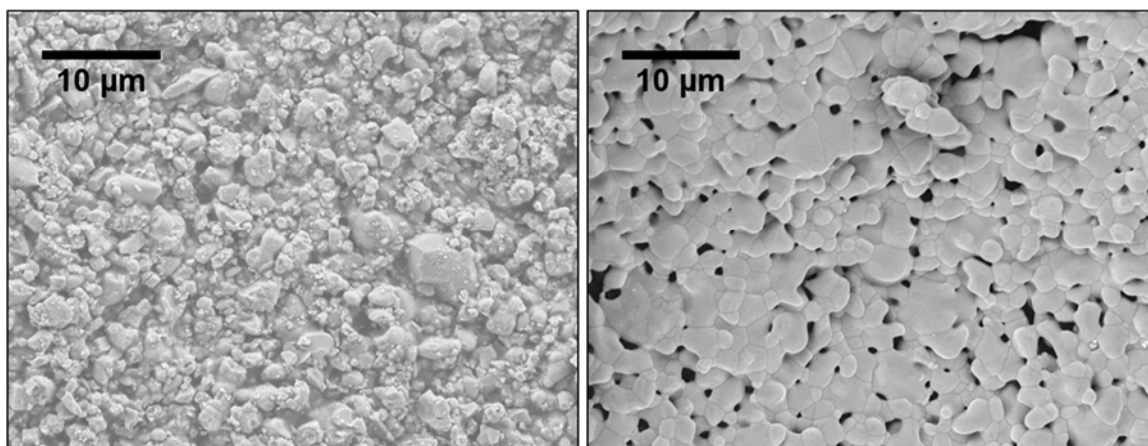
Figure 2-46: SEM micrographs of un-sintered (left) and sintered (right) freeze cast CS-HA. Sintering incinerated CS and sinters HA particles.

The embedded MND network templates the transverse pore network within the lamellar CS scaffold, resulting in hierarchical, porosity. The lamellar structure is maintained after sintering and thus provides high stiffness and strength while providing longitudinal porosity for cell migration, innervation and vascularization as well as the transport of nutrients or metabolic waste. Further, through the initial incorporation of the printed Alg scaffold, there exist transverse pores in the structure, which result in a network of pores between and through the ceramic lamellae. Two sets of mutually orthogonal pores are superimposed because of the combined process. Unidirectional lamellae extend longitudinally through the cylindrical scaffold. Sintering incinerates CS and Alg components of the scaffold leaving HA. After sintering, scaffolds sectioned longitudinally and presented in figure 2-47.

The structure of each scaffold component can be independently varied to produce a hierarchy of microenvironments within a single scaffold and enhanced diffusion. An SEM

micrograph of a longitudinal section of the composite scaffold after sintering with a binary inset of an Alg templated pore is presented in figure 2-46. Images are converted to 8-bit and analyzed using the Image J (NIH) Analyzed Particles routine. The average pore cross-sectional area is 13,731 μm^2 +/- 1984 μm^2 with an average major axis of 163μm +/- 28 μm and average minor axis of 115 μm +/- 17 μm.
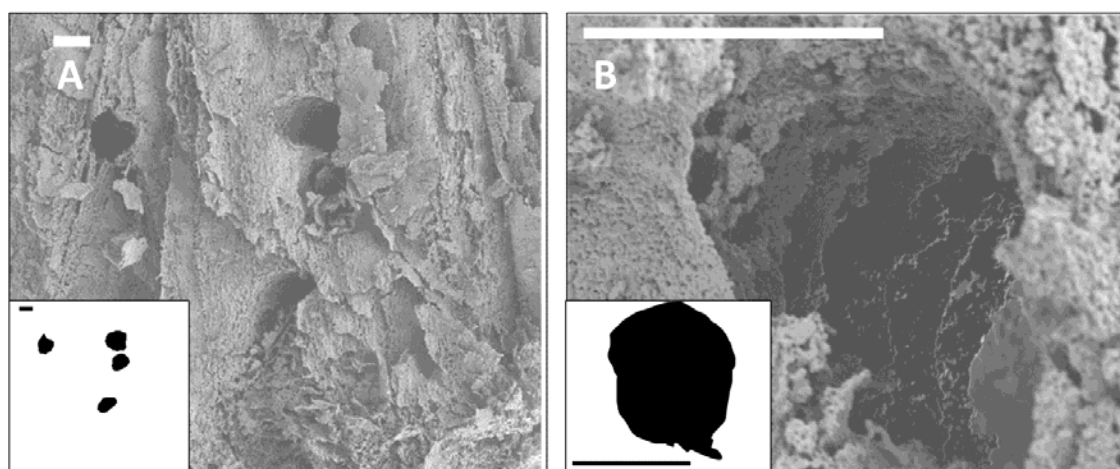
Figure 2-47: SEM of longitudinal section view of CS-HA-Alg, scaffold produced by the combined process after sintering, to expose lateral porosity produced by embedded porous scaffold. (A) Far field view of several Alg pores and (B) close view of single pore (bottom). Inset are binary images of A and B to show of pore produced by embedded Alg scaffold. Scale bar is 100μm.

2.3.6 Cell attachment to printed substrates after 24 hrs

Because Alg, CS-HA and CS-HA-Alg could be substrates within the scaffold, when the scaffold is not sintered, each substrate is evaluated for cell viability after 24 hours. Mouse osteoblasts from bone marrow of the 7F2 cell line (ATCC) are cultured in alpha minimum essential medium (Sigman et al.) supplemented with 2mM l-glutamine (Sigma Aldrich Corp., St. Louis, MO), 1mM sodium pyruvate without ribonucleosides and deoxyribonucleosides (Sigma Aldrich Corp., St. Louis, MO) and 10% (v/v) fetal bovine serum (Gibco). A suspension of 10^6 7F2 cells / mL of complete cell culture medium is placed in a non-adherent culture dish with 0.5 g Alg, CS-

HA or CS-HA-Alg substrate (n=3). After 24 hours, the substrate is rinsed 3 times with fresh medium and then stained with Live/Dead Viability/Cytotoxicity Kit (Molecular Probes) according to manufacturer specified protocol to examine the substrate for viable and adherent cells. Figure 2-47 presents live cells and dead cells attached to variable substrate materials after 24 hours. Alg shows significantly less viable cells than the other substrates.
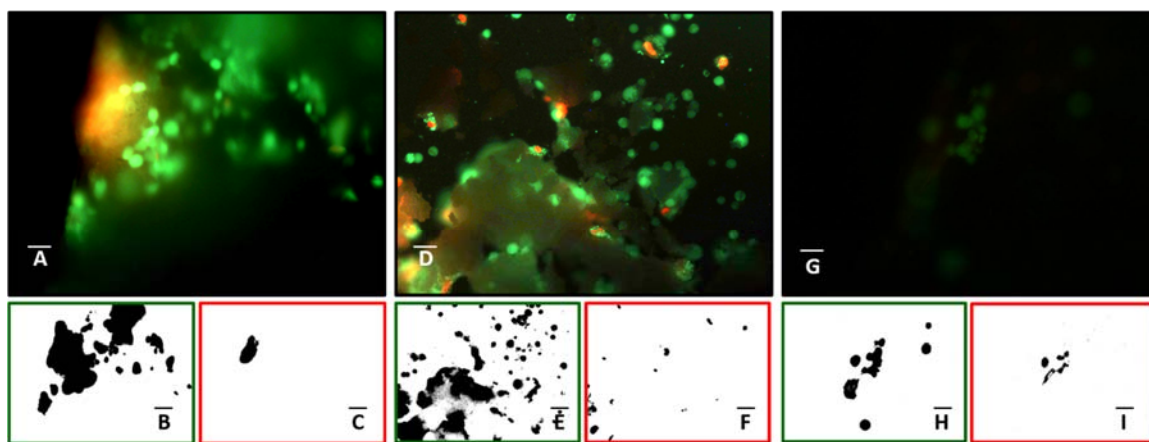
Figure 2-48: 7F2 cells seeded on variable material substrates; CS-HA-Alg scaffold produced by the combined process without sintering (A-C), freeze cast CS-HA (D-F), and printed Alg (G-I). Fluorescent image of live and dead stain (A,D,G), binary image of live cell signal (BE,H), and binary image of dead cell signal (C,F,I).   Scale bar is 100µm.

Fluorescent images for CS-HA, and CS-HA-Alg are analyzed by ImageJ (NIH) to quantify the area live and dead cells occupy in culture, as presented in figure 2-48. The number of live cells are significantly greater than dead cells for CS-HA containing substrates. The Alg substrate has less live cells and more dead cells than both the CS-HA and CS-HA-Alg substrates.

	Live	Dead
CS-HA-Alg	13,569	58
CS-HA	5,485	1,529
Alg	644	4,596
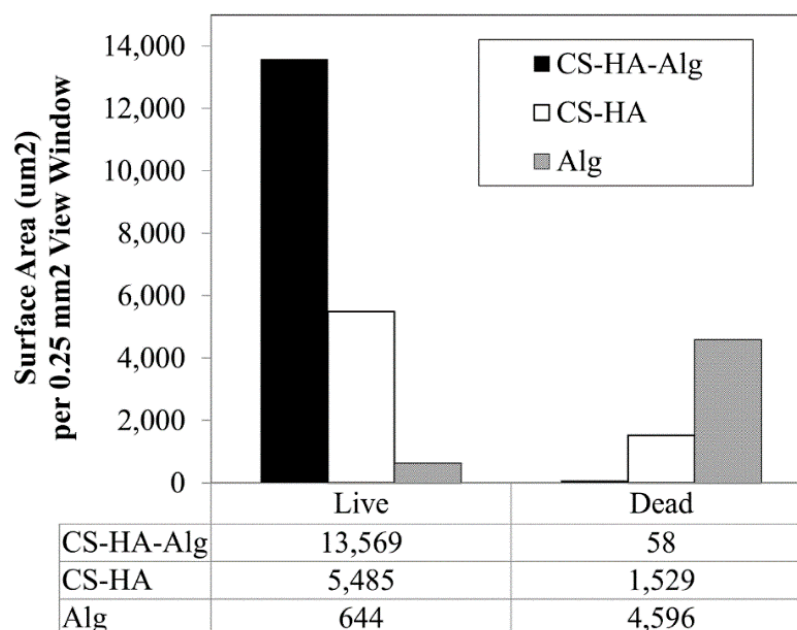
Figure 2-49: Area live and dead cells occupy on variable material substrates; scaffold produced by the combined process without sintering CS-HA-Alg, freeze cast CS-HA, and printed Alg.

2.3.7 Discussion

The objective of this work is to present a processing technique to produce an engineered hierarchical architecture with lateral and longitudinal porosity. Without sintering, the freeze-cast scaffold conjugates two niche material microenvironments in a single engineered CS-HA-Alg scaffold. With sintering, the scaffold couples two open pore networks of the lamellae, longitudinal, and transverse network templated by the printed 3-dimensional alginate scaffold. Sintering increases scaffold stiffness and strength. Mass transfer and cell mobilization in sintered and un-sintered scaffolds offer advantages for a variety of tissue engineering applications and *in vitro* cell culture.

The two-step processing technique offers several advantages. It overcomes the limitation of many freeze-cast scaffolds which offer only a limited or no lateral diffusivity between adjacent pores and the scaffold surface. Two porous networks are super-imposed by combining the two bio-

additive manufacturing techniques (1) SFF using a MND system to print a 3-dimensional porous scaffold and (2) directional freeze casting and lyophilization to fabricate lamellae and directional porosity in a CS-HA matrix.

Engineering process control over both the lamellae network and 3-dimensional porous scaffold is due to the independence of each of the two fabrication techniques - MND and freeze casting. Engineering analysis of the MND process parameters, including the flow rate and printhead velocity, defines the manufacturing expertise required to fabricate a pre-determined filament diameter. Freeze casting process parameters include the rate of cooling, possible additives and the position of the cooling probe; in this work a cylindrical mold of CS-HA-Alg is placed on a flat cooling plate. The set of processing parameters used during fabrication determines the lamellar thickness and spacing as well as the shape of the longitudinal pores. The set of parameters used during fabrication engineer a controlled set of traverse and longitudinal microenvironments; the Alg filament diameter and lamellae. Consequently, sintering incinerates Alg leaving an open network of pores templated by the embedded printed scaffold. The combined freeze casting and MND fabrication technique retains independent process control of porosity in 3 directions by combing the lamella and MND network.

The combined MND and freeze casting process produces a hierarchical microarchitecture. In addition to the sub-micron scale of the lamellae, the embedded MND network produces an average pore cross-sectional area of 13,731 μm^2 +/- 1984 μm^2 with an average major axis of 163μm +/- 28 μm and average minor axis of 115 μm +/- 17 μm. Lamellae and MND network are mutually orthogonal and cover 3-4 orders of magnitude, sub-micron lamellae to 100 μm MND pore diameter. Before sintering, the CS-HA-Alg is a heterogeneous material. Material stiffness and surface chemistry are significant factors in phenotype-specific function through cell-material interaction(Bhumiratana et al., 2011; Genes, Rowley, Mooney, & Bonassar, 2004; Pek, Wan, & Ying, 2010) After sintering, the Alg and CS are removed, leaving a network of open pores and

homogenous HA material composition. The diameter of the printed filament is significantly larger than the quantified lateral pore size after directional freeze casting and sintering. This is attributed to shrinkage of the ceramic scaffold during sintering.

Both the CS-HA and CS-HA-Alg, maintain viable cells for 24 hours after cell seeding. After rinsing, the cells remain attached to CS-HA containing substrates. Mouse osteoblasts attach to CS-HA containing substrates after 24 hours. Alg is not cytotoxic but cannot support cell viability. Mouse osteoblasts did not adhere to the Alg substrate due to the material's surface chemistry (K. Y. Lee & Mooney, 2012). It is the CS-HA component of the CS-HA-Alg scaffold which supports cell growth, specifically the HA particles(Wei & Ma, 2004).

CHAPTER 3: FABRICATION OF HETERO-CELLULAR MICROFLUIDIC DEVICE AND APPLICATION

In this chapter, hetero-cellular microfluidic devices are constructed from a channel network fabricated by the precision extrusion deposition/replica molding process previously described. Cell-laden microfluidic devices are adventageous for the following environmental and structural factors (1) forced convection through a cell-laden matrix, (2) cell to interstitial fluid volume, (3) cell seeding, and (4) residence time of drug or other soluble cues. We investigate two types of cell-laden devices; the first with a 3-dimensional channel networks fully embedded in a PDMS substrate and the second a channel network on the surface of the PDMS substrate for cell printing directly into device channels. Fully embedded networks are leak-resistant with simplified construction methods. However, surface channel networks are partially exposed; which allows for controlled cell seeding by multi-nozzle deposition throughout the network. Hetero-cellular arrangement throughout the microfluidic device improves the in vitro model's biomimetic attributes and hold promise to increases in vitro model fidelity. A hetero-cellular microfluidic device to model human liver is designed, fabricated and applied to study the effect of hetero-cellular arrangement on radioprotective drug efficacy.

3.1   Final construction of a cell-laden microfluidic device

3.1.1   Rationale

The precision extrusion deposition of a PCL pattern followed by replica molding produces a 3-dimensional interconnected channel network embedded in a PDMS substrate. The process has the following advantages: (1) channel network is sealed in PDMS, meaning no additional cover component is required to construct the device and (2) the geometric pattern of the channel network and their cross-sectional width/height are achieved by tuning automated process parameters. In this work, we construct a complete microfluidic device using an embedded channel network, inject cells and test the maximum flow rate using a programmable syringe pump. The objective is to present the precision extrusion deposition/replica molding process as a viable and potentially advantageous

fabrication method for leak-resistant 3-dimensional microfluidic devices. The leak-resistant claim comes from no requirement for a cover, as the network is embedded. Perfusion occurs through capillary tips inserted from the surface to the open channels.
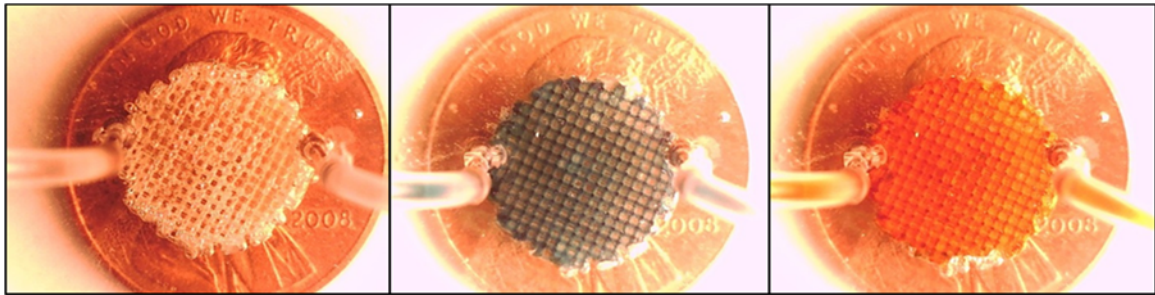
Figure 3-1: Microfluidic device without fluid (left), with blue fluid perfusion (center) and with red fluid perfusion (right).

3.1.2　Description of method

Cell-laden microfluidic device is fabricated by (1) precision extrusion deposition and replica molding of microfluidic network, (2) fix capillary tips to inlet and outlet, (3) plumb with silicone tubes to pump, and (4) sterilize and inject cell-laden solution.
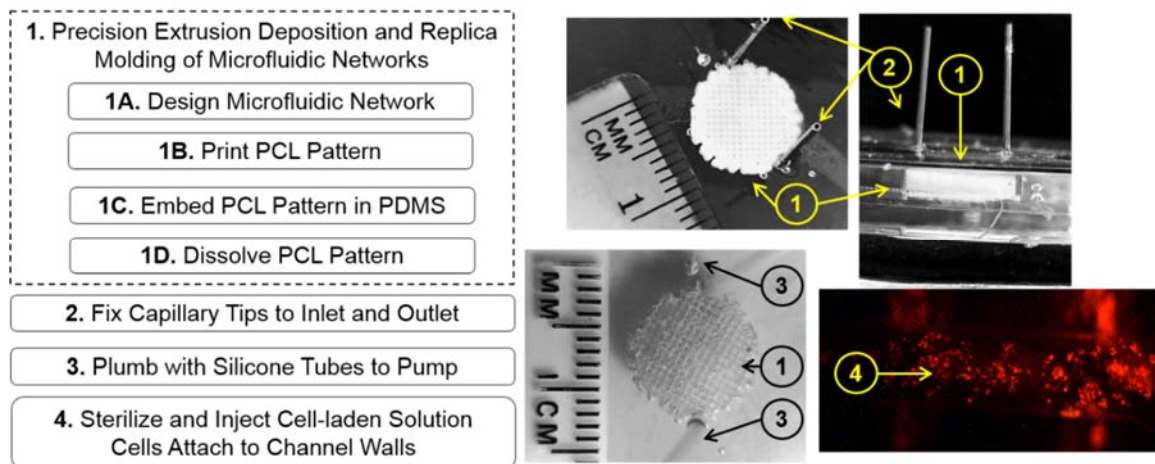
Figure 3-2: Step-by-step fabrication process to produce a cell-laden microfluidic device with channel network embedded in a PDMS substrate.

3.1.2.1   Step 1. Precision extrusion deposition and replica molding of microfluidic network

This step requires the same considerations as those presented in section 2.2 description of the precision extrusion and replica molding process.

3.1.2.2   Step 2. Fix capillary tips to inlet and outlet

Capillary or syringe tips are used to clear PCL pattern embedded in the PDMS substrate during the fabrication process. Add a droplet of lubricant, water is sufficient, to the PDMS surface prior to puncturing in the surface to minimize PDMS tearing. A prefabricated steel 250-350µm inner diameter capillary tip is used for inlet and outlet. The tip size is selected to fit in silicone tube without leakage or additional means of fastening.
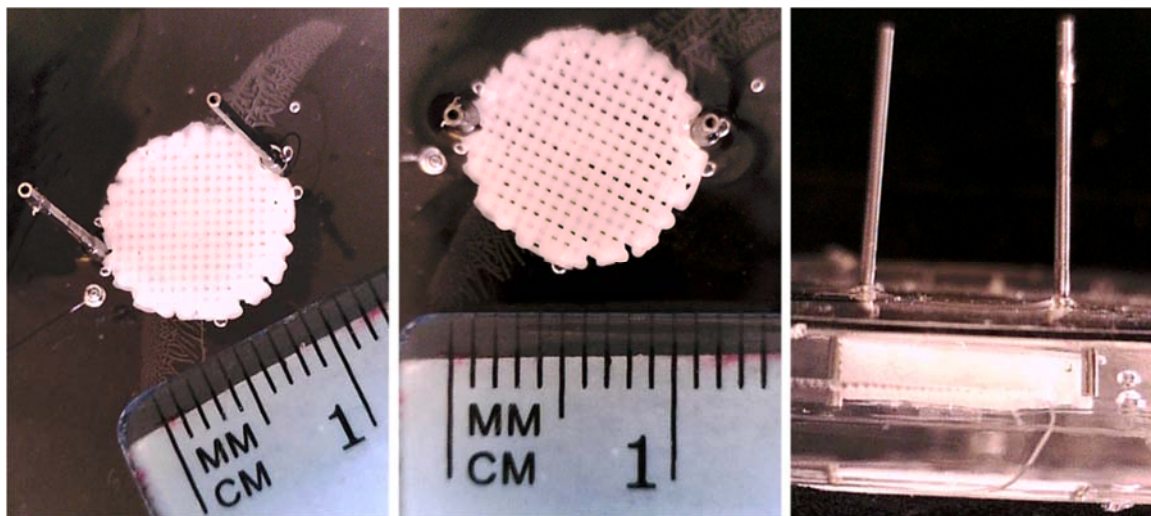
Figure 3-3: Printed PCL pattern embedded in PDMS with 350µms inner diameter steel capillary tips inserted through PDMS to PCL pattern. Capillary tips serve as inlet/outlet of device. No additional ports or cover needed.

3.1.2.3   Step 3. Plumb with silicone tubes to pump

Silicone tubes inserted over the capillary tips are plumbed back to syringe pump. A prefabricated 250-350µm inner diameter capillary tip is also inserted into the other end of the

silicone tube. Luer lock housing molded around the tip mates to a luer lock syringe. Fluid is loaded into the syringe and diffused through microfluidic device using a programmable syringe pump.

3.1.2.4   *Step 4. Sterilize and inject cell-laden solution*

Sterilization by autoclave or 70% ethanol rinse prepare the microfluidic device for cell culture. The cell population is expanded in tissue culture dishes with cell culture medium as specified by cell provider. To prepare a cell solution for injection, first collect the cell pellet by trypsin and centrifugation. Next, re-suspend cell pellet in less than the estimated volume of the channel network. Aseptically load solution in sterile syringe. Fix a 25-350μm capillary tip to the end of the syringe and directly inject solution into microfluidic network. Inject slowly to minimize additional perturbation to cells. Store device in incubator overnight to allow for cell attachment.

Cell attachment to the channel walls of the microlfuidic device is observed using a human hepatocyte cell line and fluorescence based kit. Human hepatocytes of the HepG2 cell line (ATCC) are cultured in Eagle's Minimum Essential Medium base medium (ATCC) supplemented with 10% (v/v) fetal bovine serum (FBS) (Invitrogen) and 1% (v/v) antibiotic/antimycotic (Invitrogen). Cells are maintained at 32ºC and 5% CO_2 for less than 3 passages after thawing prior to experiment. Microfluidic device is sterilized and cells are injected as described. After 12 hours, the cell-laden device is connected to a programmable syringe pump and perfused 1.0 mL/hr for 3.0 hours. The estimated volume of the microfluidic network is less than 0.5 mL; this estimate is based on the volume injected from a syringe to fill the network after the device's final construction. After perfusion, cells are fixed with 70% ethanol and stained using fluorescence based Live/Dead Viability/Cytotoxicity Kit for mammalian cells (Molecular Probes).

Figure 3-4 presents a light microscope image of the channels (left) and fluorescent image of one region of the light microscope image to show the cells in the channel (right). Cells labeled green and red are visible in the fluorescent image. The kit labels live cells (cells with an intact

membrane) green and dead cells (cells with a ruptured membrane) red. Cells were fixed to preserve their location and enhance visualization prior to staining. Necrosis caused by the environment or cell seeding process would be rinsed away before fixation or staining. The appearance of both green and red fluorescent probes in the image means not all cells were fixed or fixation was incomplete. However, the location of the cells in the channel is apparent. The green probe is further proof the cells were able to attach and survive in the PDMS microfluidic channel for the overnight static incubation and 3 hour perfusion periods.
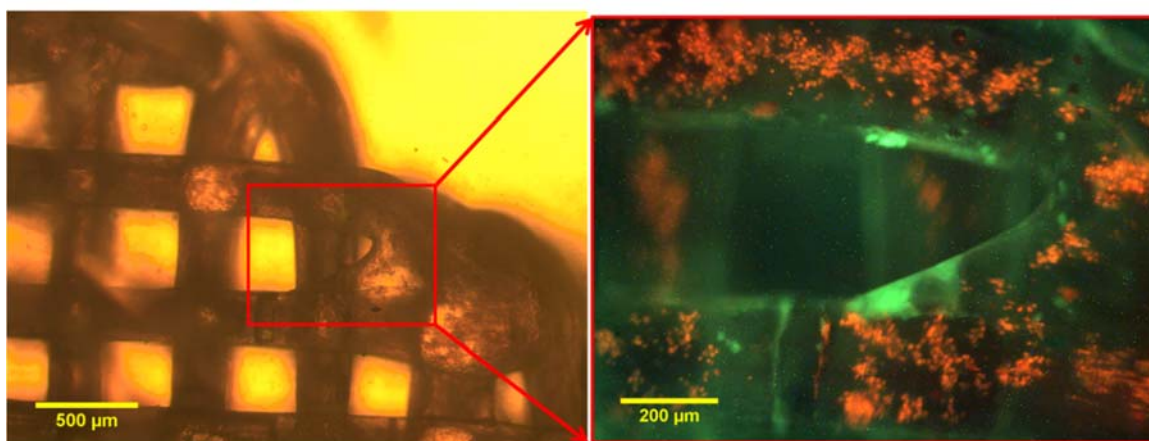
Figure 3-4: Image of microfluidic device under 4x magnification (left) and fluorescent image of cells labeled with green and red Fluorochrome (right).

Figure 3-5 presents a section of the microfluidic network with cells. The figure shows the same view field four times to compare channels/cells and two focal planes. Light microscope images of the channel network (A,C) present the channel network and fluorescent images of labeled cells (B,D). Cells are present in the channels after dynamic perfusion for 3 hours. Two focal planes, one near field (A,B) and far field (C,D) demonstrate the microfluidic network is 3-dimensional with perfusion and cells throughout the network of channels.
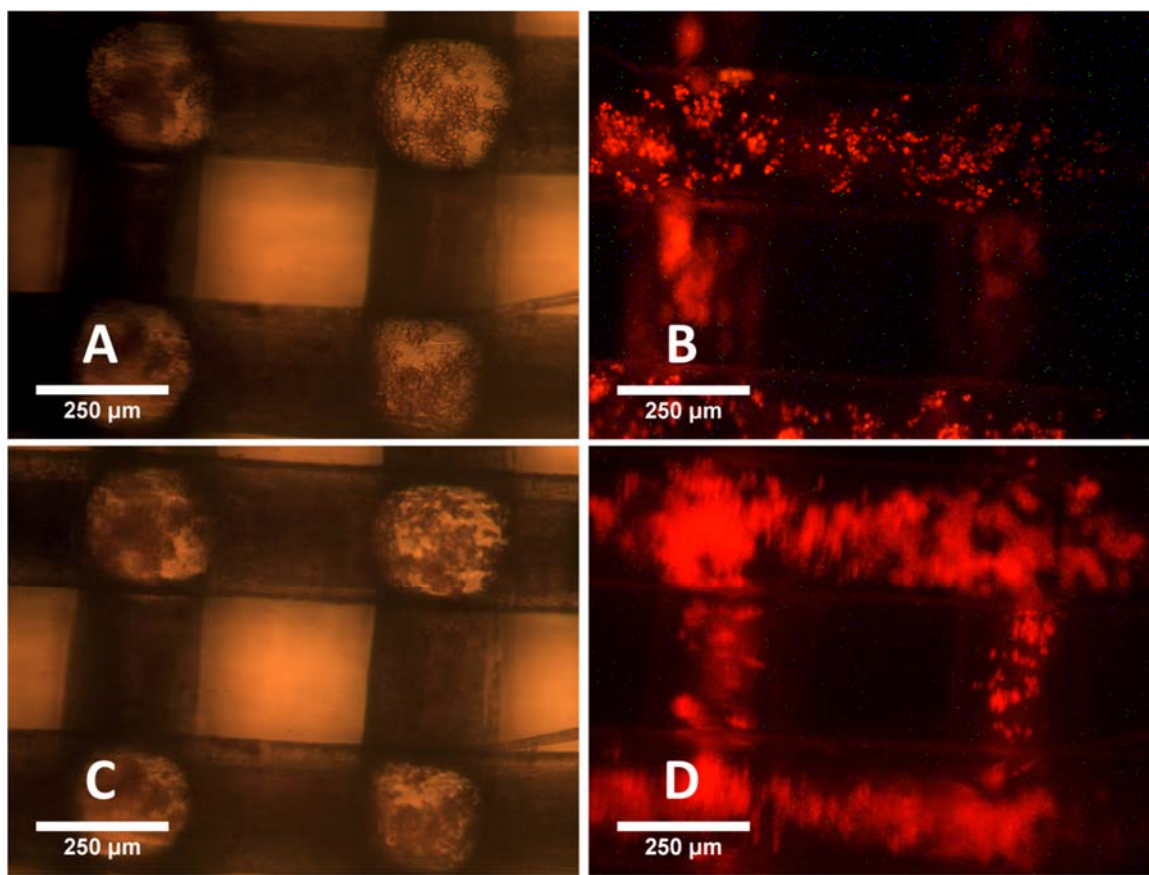
Figure 3-5: Cell seeded in the channels of the microfluidic device adhere to the walls of channels. Cells adhere to channels on multiple levels.

3.1.3   Leak resistance during forced convection

Connectivity of the open network channels from the inlet and outlet are deomstrated by the perfusion of fluid through the microfluidic device. Figure 3-6 presents a time lapse photo sequence of PDMS microfluidic device being perfused. Each frame contains a top (left) and front (right) view of the device. The leak resistance of a fully constructed microfluidic device is evaluated using a programmable syringe pump. Syringes are filled with water colored with food die. Perfusion rate was maintained at 2.0 mL/min for 10 minutes. No leaks were observed from the insertion points of the capillary tips. Figure 3-7 presents a 30 second time-lapse set of images to show perfusion of 1.0mL of fluid across the microfluidic device without leakage. Yellow arrows in the intial and final photograph call attention to the beginning and ending position of the second hand.
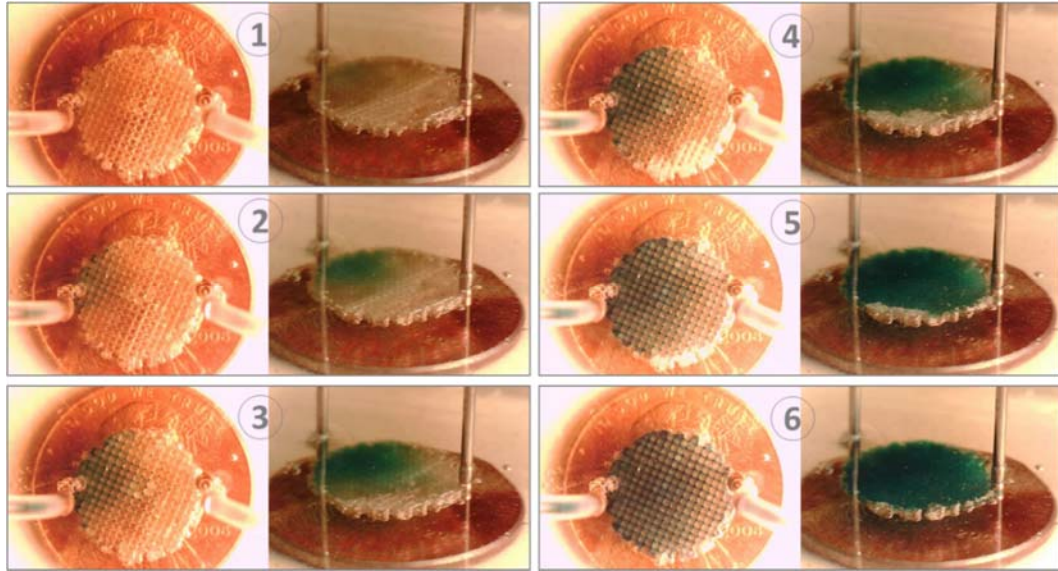
Figure 3-6: Time lapse photo sequence of PDMS microfluidic device being perfused. Each frame contains a top (left) and front (right) view of the device.
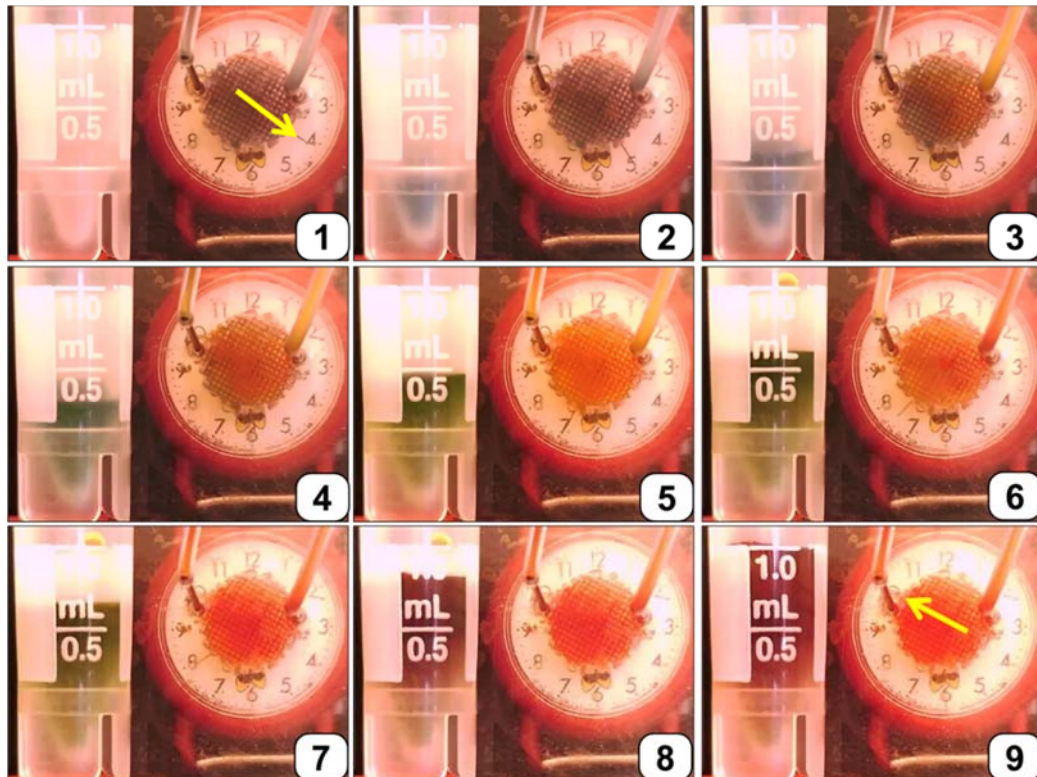
Figure 3-7: Controlled perfusion of microfluidic device by programmable syringe pump. Figure presents time lapse photographs of 30 seconds of 2 mL/min perfusion. The clock face behind the microfluidic device counts through 30 seconds. Yellow arrows in frames 1 and 9 point out the initial and final location of the second hand. The final volume perfused after 30 seconds is 1 mL.

3.2   Cell printing in channels of a microfluidic device

3.2.1   Rationale

In this work, multiple cell-laden solutions are selectively assembled through an open channel network using multi-nozzle printing. The objective is to fabricate a cell-laden microfluidic device with controlled arrangement of multiple cell types between the inlet and outlet of the device.

3.2.2   Definition of method

The combined SFF patterning and replica molding process produces a cell-laden microfluidic device with channel designed to biomimic liver physiology and flow design. First, microfluidic channel pattern is designed from in vivo liver structure. Second, microfluidic pattern is printed using precision extrusion deposition. PDMS is cured against the PCL pattern in a single step of replica molding to produce PDMS substrate. PCL pattern is cleared from PDMS, which leaves a network of open channels. The PDMS microfluidic chip is plasma treated to decrease surface energy for homogenous surface wetting during printing. Cell-laden matrix is directly printed into the channels using direct cell writing system. Cell-laden microfluidic chip is sealed and cell culture medium is perfused to deliver nutrients and remove waste using a programmable syringe pump.   Figure 3-8 pesents the process to fabricate the cell-laden microfluidic device with controlled cell arrangement in microfluidic channels by cell printing.
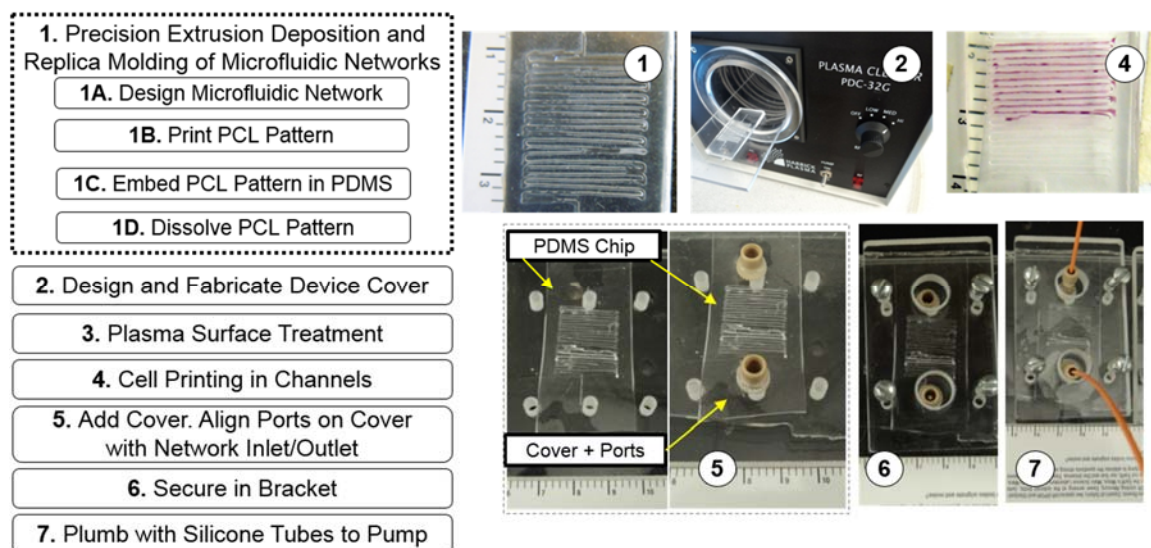
Figure 3-8: Step-by-step fabrication process to produce a cell-laden microfluidic device leveraging cell printing for controlled assembly of cells and matrix material in the device channel network. Channels are on the surface of PDMS substrate. Cover with ports aligned to channel network inlet/outlet also required to seal system.

3.2.2.1   Step 1. Precision extrusion deposition and replica molding of microfluidic network

This step requires the same considerations as those presented in section 2.1.2, the description of the precision extrusion and replica molding process.

3.2.2.2   Step 2. Design and fabricate device cover

The microfluidic device's cover serves the following role: (1) closes channels open on the surface of the PDMS substrate, (2) includes ports to fasten hosing from the syringe pump to the channel network and (3) is of sufficient surface area to create a seal against leakage. The surface area of the cover is sufficient to close all open channels on the surface of PDMS substrate plus at least a 1.0 cm border for sealing. The location of ports on the cover is mapped to the inlet and outlet of microfluidic network. The cover is made of either glass or PDMS. Holes through the cover and the attachment of ports depends on the cover material. All cover ports are flat bottom nano-ports (UpChurch Scientific). For the glass cover, through holes are made using a diamond tip bit and a hand drill. Ports are attached over the holes using adhesive with a gasket, following the

manufacturer's direction. For the PDMS cover, ports are glued to a petri dish with water soluble adhesive. PDMS is prepared 10:1 base to elastomer and poured in the dish around the ports as a 5-10mm deep pool. After PDMS has cured, the cover is peeled away from the petri dish, cut to size using a scalpel and washed with warm soap and water. The cover, either glass or PDMS, is sterilized by autoclave.

3.2.2.3   Step 3. Plasma surface treatment

Plasma surface treatment oxidizes the PDMS substrate methyl groups to form silanol groups (Whitesides, Ng, Gitlin, & Stroock, 2002). The wettability of cross-linking solution and printed alginate matrix is controllable and homogenous on post-plasma treated surface. PDMS substrate is placed in RF plasma chamber (Harrick Plasma) for 90 seconds less than 2 minutes prior to printing.
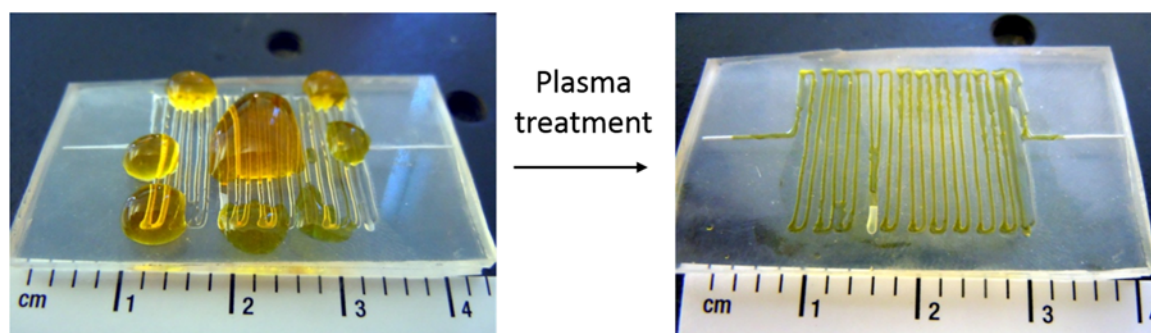
Figure 3-9: Effect of 90 second air plasma treatment on homogeneity PDMS substrate wettability

3.2.2.4   Step 4. Cell printing in channels

Cell printing by multi-nozzle deposition produces explicitly designed 3-dimensional patterns of cell-laden matrix in microfluidic device (W. Sun et al., 2010; W. Sun et al., 2008). The material delivery system is mounted to a high precision positioning system to print the cells into microfluidic channels. The design input model for cell printing tool path is reproduced from PED model programmed to fabricate the PCL pattern used to template the open network of channels.

Figure 3-10 presents system configuration for direct cell writing system aligned to PDMS substrate to print cells into microfluidic channels.
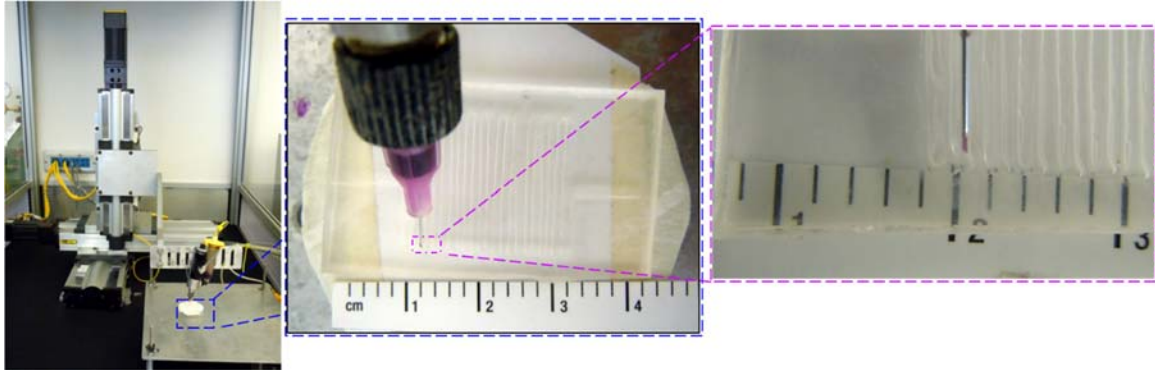
Figure 3-10: PDMS substrate positioned under bioprinter printhead to directly deposit cells and matrix into microfluidic channels.
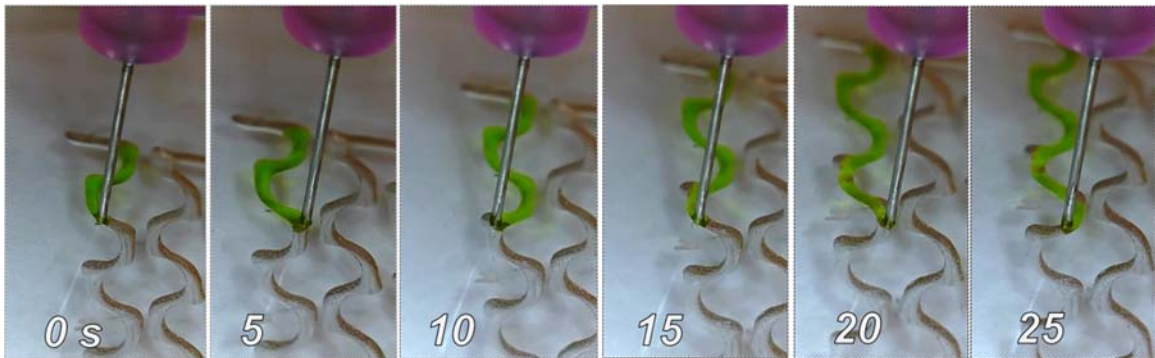
Figure 3-11: Time lapse photographs of MND system extrusion of alginate into sinusoid channel network on the surface of a PDMS substrate.

The volume of dispensed material is controllable by manufacturing process parameters. A set of fully defined direct cell writing process parameters produces a unique volume dispensed per unit surface area of channel. Process parameters can be varied independent of printed pattern to produce patterns of extruded filaments of variable diameter. The volume dispensed per unit area of substrate is a function of the flow rate and speed of material delivery system. The flow rate through the nozzle is a function of the capillary tip diameter and length, material viscosity, and dispensing

pressure. The matrix viscosity is a function of the material and cells concentration, which are selected for to support cell growth after printing. Dispensing tip is selected from a set of prefabricated tips and fixed to material delivery system before printing. Dispensing pressure and speed of material delivery system can be adjusted during printing and tuned to create variable filament diameters. Figure 3-12 presents matrix extruded through 150µm nozzle tip at 5psi with variable speeds of material delivery system. Equation 3-1 presents the MND process parameters.

$$\Omega_{MND,i} = [D_i \ \mu m \quad P_i(t) \ psi \quad N \quad v_i(t) \ mm/s \quad T \ °C \quad z_i(t) \ \mu m \ ]$$

$$\begin{bmatrix} Alg \\ CaCl_2 \end{bmatrix} = \begin{bmatrix} 150 & 5.0 & 5\% & variable & - & 200 \\ 400 & 1.0 & 10\% & variable & - & 200 \end{bmatrix} \qquad 3\text{-}1$$
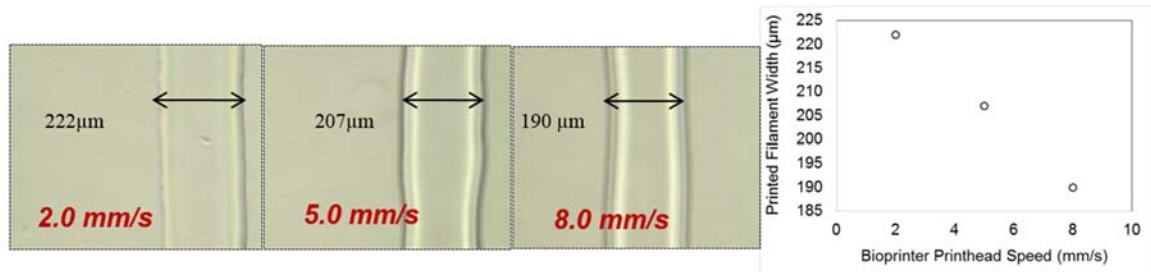
Figure 3-12: Bioprinting variable filament width using the manufacturing process parameters. Dispensing pressure 5psi, dispensing tip diameter 150µm and variable traveling speed. Photographs with measured filament width presented on left. Plot of measured filament width as a function of programmed printhead speed on right.

Cell-laden matrix is prepared and loaded into multi-nozzle deposition (MND) direct cell writing system and printed. Human hepatocytes of the HepG2 cell line (ATCC) are cultured in Eagle's Minimum Essential Medium base medium (ATCC) supplemented with 10% (v/v) fetal bovine serum (FBS) (Invitrogen) and 1% (v/v) antibiotic/antimycotic (Invitrogen). Cells are maintained at 32ºC and 5% CO_2 for less than 3 passages after thawing prior to experiment. Alginate matrix prepared from 6.0% (w/v) alginic acid sodium salt from brown algae (Sigman et al.) in deionized water is sterilized by serial filtration through 0.2µm mesh (VWR). Cells are mixed with

alginate for final concentration of 2.0×10^6 HepG2 cells per mL aqeuous alginate solution. Prior to printing, channels are flooded with 5.0% (w/v) calcium chloride (Sigman et al.) in deionized water cross-linking solution. Cell viability post-printing is qualitatively evaluated using fluorescence based Live/Dead Viability/Cytotoxicity Kit for mammalian cells (Molecular Probes). Two-color discrimination by the fluorescent probes enthedium calcein AM and ethidium homodimer-1 labels live cells as green and dead cells as red. Samples were analyzed using a DM RIB inverted microscope (Leica) with UV source. Images of all cells were captured electronically by Insight 4.0Mp Monochrome digital camera (Spot Insight) and manufacturer provided imaging software. Cells are fluorescently labeled after printing to demonstrate their position. Figure 3-13 presents hepatocytes-laden alginate printed into microlfuidic channels fabricated by the combined preciison extrusion depostion and replica molding process. The set of MND process parameters for direct cell writing are presented in equation 3-2.

$$\Omega_{MND,i} = \begin{bmatrix} D_i \ \mu m & P_i(t) \ psi & N & v_i(t) \ mm/s & T \ ^\circ C & z_i(t) \ \mu m \end{bmatrix}$$

$$\begin{bmatrix} Alg + Cells \\ CaCl_2 \end{bmatrix} = \begin{bmatrix} 150 & 5.0 & 5\% + 2.0x10^6 \frac{cells}{mL} & 5 & - & 200 \\ 400 & 1.0 & 10\% & 5 & - & 200 \end{bmatrix} \qquad 3\text{-}2$$
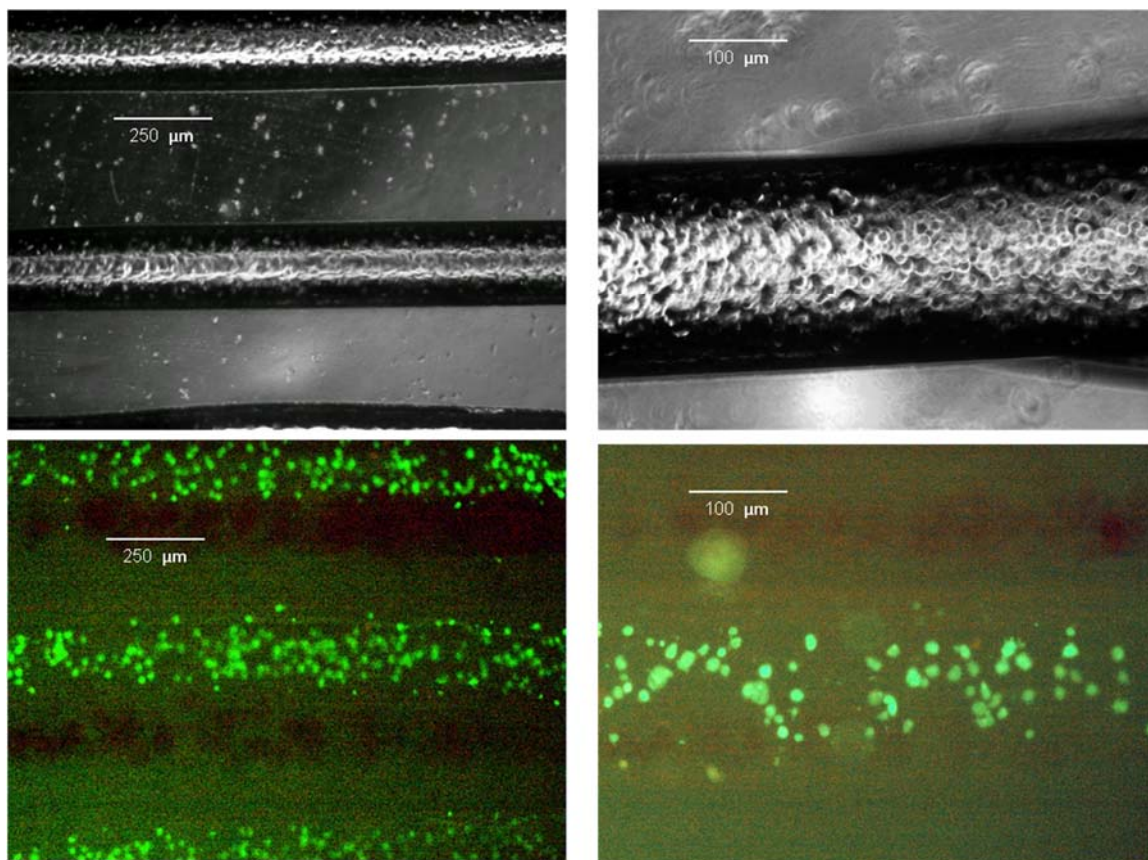
Figure 3-13: Hepatocytes in alginate printed into channels labeled with the Live/Dead stain and photographed under phase contrast (top row) and fluorescent (bottom row) microscope.

Fluorescent imaging confirmed viable hepatocytes were printed into microfluidic channels on PDMS chip. No necrotic effects of the process on the healthy cells is qualitatively observed in the healthy cells. Cell printing enables control over geometric pattern and specific area of cell-laden matrix in channels. Further, cell printing by multi-nozzle deposition automates 3-dimensional deposition relative to (1) global coordinate space and (2) the other working solution being printed. The methods to arrange the discrete working solutions in microfluidic channels include any or a combination of the following:

- **Direct all nozzles at a single point and extrude concurrently.** Control the volume fraction of each solution by the selection of process parameters for each nozzle.

- **Direct all nozzles to a single point and selectively open and close each valve while tracing the microfluidic channel trajectory.** Produce an alternating pattern of homogenous phenotypes, support material, or scaffolding throughout the network.

- **Open one valve while tracing the microfluidic channel trajectory, then re-trace the microfluidic channel trajectory with another valve open.** Produce a layered structure in the channel, with the second layer in contact with fluid and therefore any soluble cues or drugs, before the shielded layer.
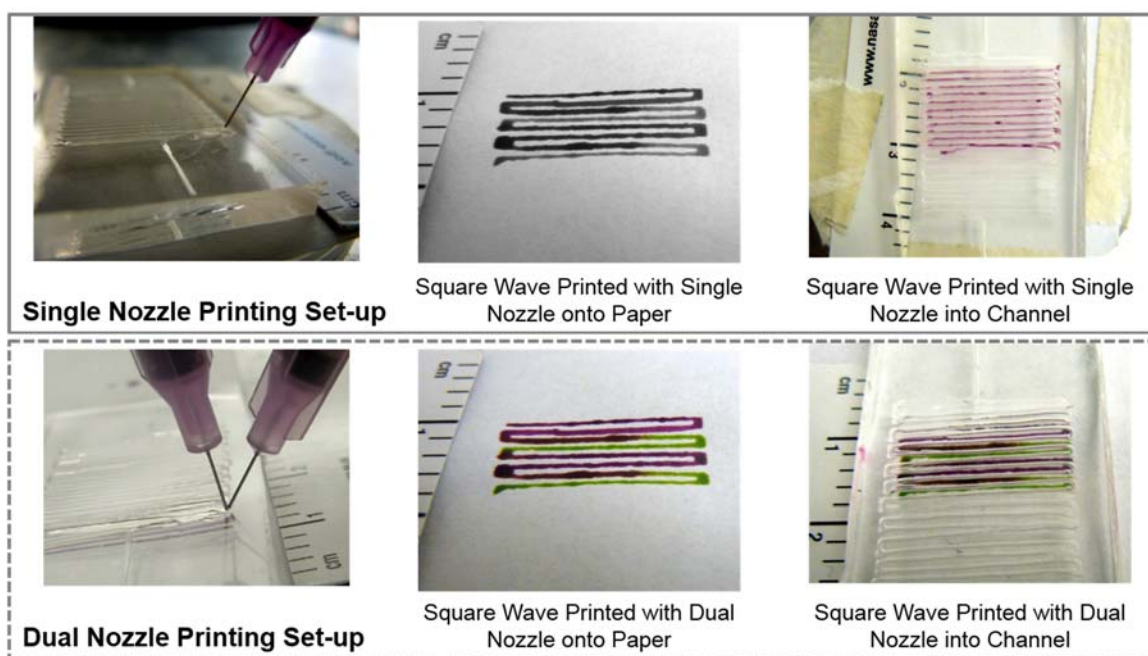
Figure 3-14: Single and dual nozzle printing into channel to control the arrangement of multiple materials throughout the microfluidic network.

Hepatocytes are seeded into channels using multi-nozzle deposition for direct cell writing of two different cel types. The purpose is to demonstrate control over the arrangement of discrete cell types throughout the channel network. Hepatocytes are prepared as previously described. However, before printing cell-laden solution is split into two equal volumes. One volume is stored

in 37°C water bath. The other volume is repeatedly frozen/thawed between -210°C liquid nitrogen and 37°C water bath to lyse cells. Each solution (healthy and lysed) is loaded into separate nozzles and printed into alternating channels of a square wave network. Live/Dead staining after printing fluorescently labels the lysed and healthy cells red and green respectively. Imaging of the cells after printing demonstrates the position of each cell solution after multi-nozzle deposition. Figure 3-15 presents the two types of cells printed into alternating channels of the microfluidic device. Equation 3-3 presents the set of process parameters for MND direct cell writing of both cell types. Multi-nozzle deposition successfully assembled healthy cells (green) and lysed cells (red) in alternating channels of the network. The damage to the lysed cells is not a consequence of the printing process of channel environment. Cells were purposely lysed prior to printing for imaging purposes.

$$\Omega_{MND,i} = [D_i \ \mu m \quad P_i(t) \ psi \quad N \quad v_i(t) \ mm/s \quad T \ °C \quad z_i(t) \ \mu m \ ]$$

$$\begin{bmatrix} Alg + Cells \ (Green) \\ Alg + Cells \ (Red) \\ CaCl_2 \end{bmatrix} = \begin{bmatrix} 150 & 5.0 & 5\% + 1.0x10^6 \frac{cells}{mL} & 5 & - & 200 \\ 150 & 5.0 & 5\% + 1.0x10^6 \frac{cells}{mL} & 5 & - & 200 \\ 400 & 1.0 & 10\% & & & \end{bmatrix} \qquad 3\text{-}3$$
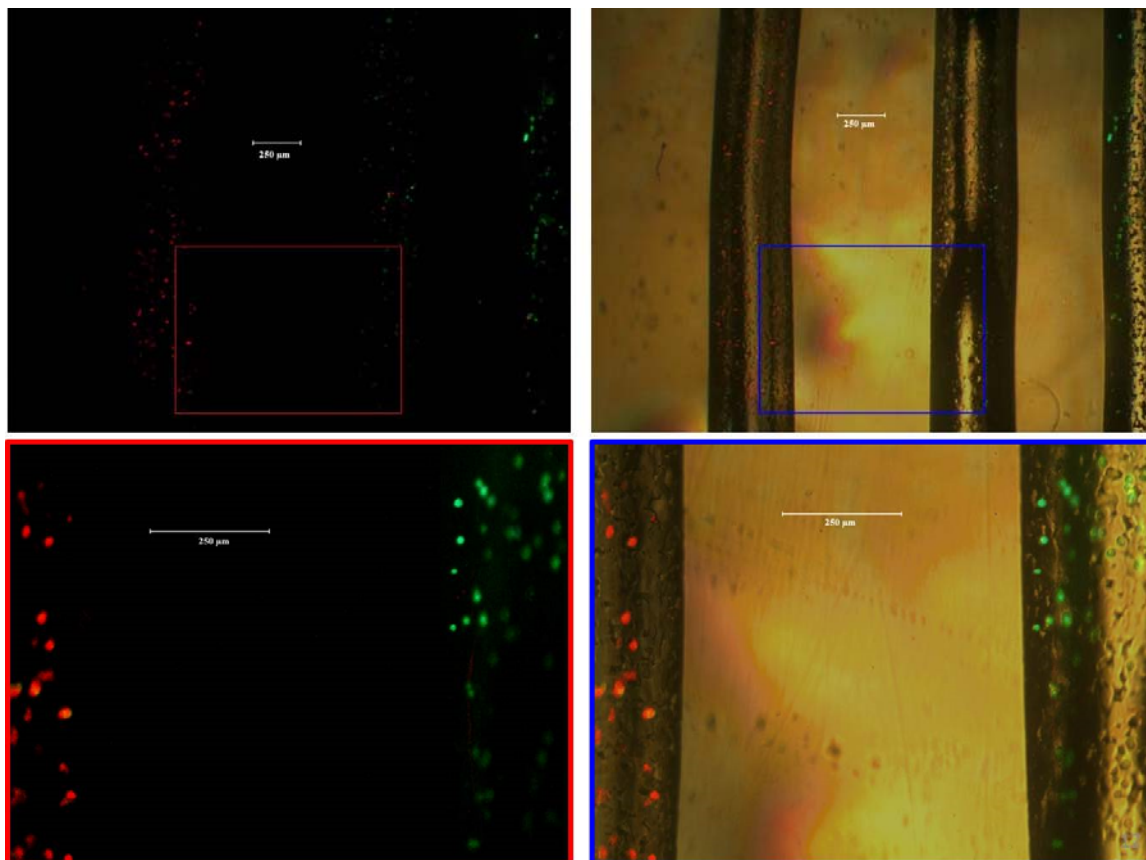
Figure 3-15: Controlled cell seeding of two cell types by multi-nozzle bioprinting. Two fluorescently labeled cells (red and green) are printed in alternating channels.

3.2.2.5   Step 5. Add cover and align ports to channel inlet/outlet

Manually align inlet/outlet of channel network on PDMS substrate with ports on cover and place cover. Plasma surface treatment on PDMS substrate improves substrate/cover seal.

3.2.2.6   Step 6. Secure in bracket

Align holes in bracket's cover with inlet/outlet ports on the microfluidic device's cover and place the device in bracket. Secure the bracket with screws. Manually tighten screws to achieve a seal with the minimal amount of compression to PDMS components.

3.2.2.7   Step 7. Plumb with silicone tubes to pump

Cell-laden PDMS microfluidic chip and PDMS cover fitted with nano-port assemblies (Upchurch Scientific) secured together by polycarbonate brace to form a microfluidic circuit. System perfused by programmable syringe pump (Next Era) and flow tested to 10µL/hr with media.
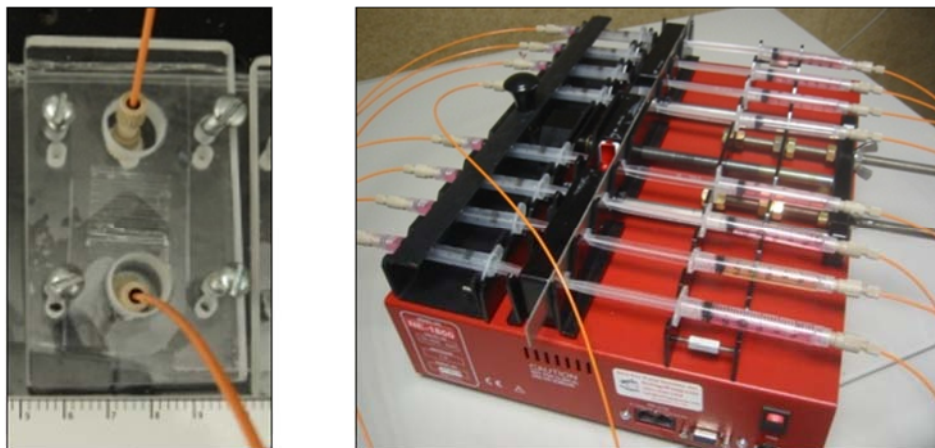
Figure 3-16: Photograph of cell-laden microfluidic device in bracket with silicone tubes to inlet and outlet (left) plumbed to programmable syringe pump (right).

3.2.3   Discussion

The objective of this work is to fabricate a cell-laden microfluidic device by combined solid freeform patterning and replica molding with direct cell writing into channels. MND for direct cell writing defines a set of process parameters to control over cell to fluid volume ratio and arrangement of cell types. Precise volumes of fluid in a microfluidic device are transported through microfluidic device through continuous network of channels up to a flow rate of 10µL/hr.

Cell seeding is controlled by direct cell writing of cell-laden matrix into microfluidic channels. SFF manufacturing by MND for direct cell writing traces channel pattern to dispense cell-laden matrix into channels. The direct cell writing process has multi-nozzle capability to pattern different types of biologics within a single microfluidic device during a single printing

episode. The direct cell writing motion system has the capability to move in 3-dimensional space to layer and pattern biologics. MND for direct cell writing is a feasible biofabrication method to introduce hierarchical patterning of cell/biologics densities or cell types throughout the depth of the chip, in addition to the planar patterning, to cell arrangement throughout a microfluidic device.

Direct cell writing process produces manufacturing control of volume of printed material per unit area of substrate and therefore control of cell to interstitial fluid volume ratio. The diameter of the extruded cell-laden filament is a function of the nozzle diameter, feed rate (dispensing pressure), matrix viscosity, and travel speed of the material delivery system. In this work, we used 150μm capillary tip. Remaining process parameters were derived from previous work printing alginate using direct cell writing process to produce threshold minimum filament diameter, as it is the limiting case. The filament diameter can be increased by increasing the volume of material dispensed per unit area of substrate. This can be accomplished by increasing dispensing rate, decreasing matrix viscosity, or decreasing travel speed of the material delivery system. Since the cross-section of the microfluidic channel has been characterized, operator produce a cell to interstitial fluid ratio close to one by tuning direct cell writing process parameters. The process allows for independent control over the filament cross-section and pattern. Printed pattern and set of process parameters manufactures a unique 3-dimensional cell-laden construct.

3.3   Effect of hetero-cellular microfluidic device on radioprotective drug efficacy

3.3.1   Rationale for study

Advancements in multi-nozzle deposition and microfluidic technology enables controlled spatial deposition of several cell types in a single microfluidic network with reproducible engineering process control. Such techniques are leveraged to study the impact of co vs. mono-culture on drug efficacy. The objective of this study is to determine the effect of an engineered co-culture on the radioprotective efficacy of the pro-drug amifostine on human liver cells in a microfluidic device. Tissue engineering applications of this work include the biomimetic co-culture

design and in vitro drug discovery platforms. Research tasks include (1) design and fabrication of a built biological model of native human hepatic niche, (2) identify a radiation source and exposure to model of extraplanetary radiation and (3) experimentally compare the radioprotective effect of drug on liver's parenchymal cells type in mono- and co-culture with epithelial cells.

The built biological model of liver tissue leverages multi-nozzle deposition bioprinting and microfluidic technology. Multi-nozzle deposition bioprinting enables controlled arrangement of the cells in the microfluidic device. The arrangement of cells in the device determines the sequence of drug-cell interactions and consequently, if the drug is in active or in-active form. Each cell type is contained in a separate chamber within the microfluidic device. Chambers are connected by a microfluidic network perfused with cell culture medium. The arrangement of the chambers and uni-directional flow through the device separates drug-cell type interactions chronologically and by phenotype. The effect of drug's interaction with epithelial cells is effected through soluble cues when the drug flows from the epithelial chamber into the hepatocyte chamber. The residence time of the drug in each chamber is controlled using a programmable syringe pump.

3.3.2   Model design and fabrication

High fidelity in vitro models are achieved through advanced manufacturing and environmental controls. The cell model design objective is a predetermined geometric pattern to achieve sufficient diffusion for cell viability and biomimetic hetero-cellular arrangements. A biomimetic environment and transient control after fabrication is achieved using engineered devices to deliver prescriptive amounts of physiologically relevant physical, soluble, and biological stress (P. J. Lee, Hung, & Lee, 2007; Tourovskaia, Figueroa-Masot, & Folch, 2005). These deliberate environmental components are meant to enhance culture's function beyond the activity of a single cell type aggregate to synergistic and cooperative activity of multiple cell types (Dash et al., 2009; Gebhardt et al., 2003). The microfluidic model in this study physically segregated each cell type into separate chambers of a microfluidic system. The transient interaction between

compartments of the device, and therefore cell types, is controlled by the flow rate of the pump. In this study, we model the radio protective drug efficacy on human liver using a co-culture of hepatocyte and epithelial cells. Each cell type is relegagated in discrete compartment of a microfluidic device and serially connected. Soluble cues, such as drug, are carried throughout the body in the cariovasular system's lumen. Nutrients and drugs diffuse from the lumen, through an epithelial cell lining and into the trabeular space of the lumen network where the parenchymal cells are positioned. From the blood stream drug first contacts the epithelial cell lining of ther lumen, then the hepatocytes in the functional unti of the tissue. Therefore, in the in vitro microfluidic model the drug passes through the epithelial cell comparment and then the heptocyte compartment. Figure 3-17 presents the biofabrication process to print two cell types in a microlfuidic device using MND for direct cell deposiiton.
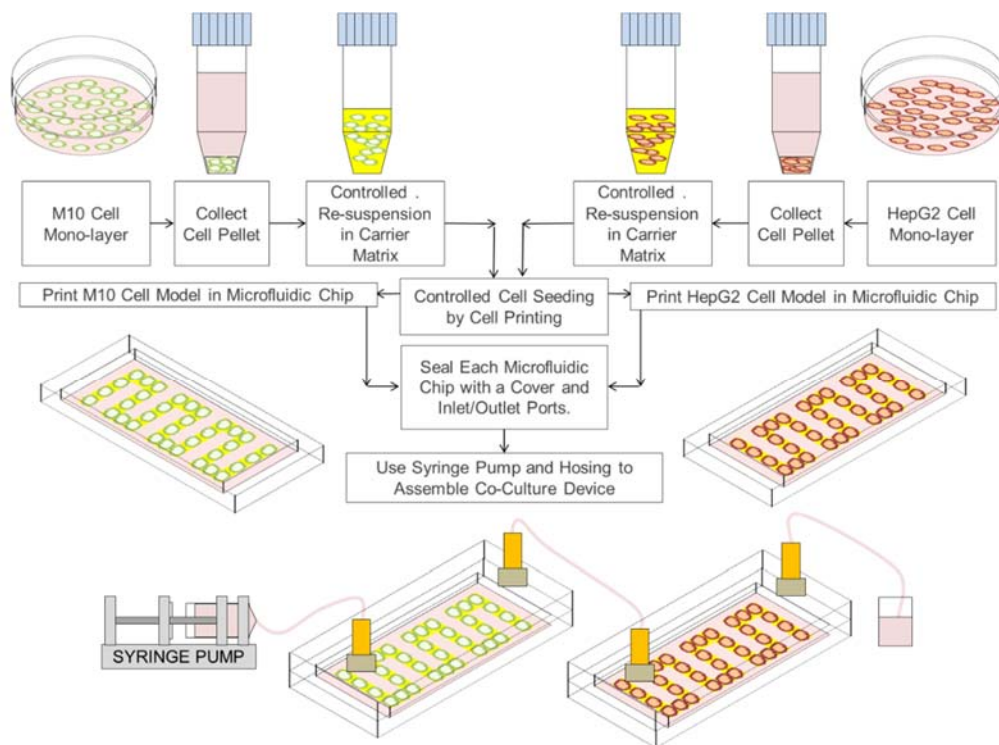
Figure 3-17: Method to assemble a co-culture microfluidic system with controlled cell seeding and dynamic perfusion through an array of cell model compartments. Macro- and micro- cell patterning in the chip controlled by cell printing.

Two immortalized cell lines are co-cultured in the co-culture environment. Human hepatic carcinoma cells of the cell line HepG2 (ATCC) and human mammary epithelial of the cell line M10 (ATCC) are cultured in the Alpha Modification of Eagle's Medium supplemented with 10% (v/v) fetal bovine serum and 1% (v/v) penicillin streptomycin. Half volume of culture medium is changed every other day. Cultures are maintained $37^{\circ}C$ and at 5% carbon dioxide. Cell culture medium and supplements purchased from Invitrogen unless otherwise noted. Separate cell-laden solutions of epithelial and hepatocytes are created in an identical manner. Cells are rinsed with PBS, trypsinized, and counted using exclusion dye Trypan Blue and hemocytometer. Once counted, cells are mixed with the gelatinous protein mixture Basement Phenol Red-free Matrigel (BD Bioscience) over ice to prevent gelation. Cells are homogenously distributed throughout the Matrigel using a gentle tapping technique with minimal pipetting to a concentration of 1.0×10^6 cells per mL. Final printing solution is 50% cells and 50% Matrigel (v/v) solution. The cell-laden solution is stored on ice for 5-10 minutes prior to printing to prevent gelation.

All components of printing system to come in contact with cell-laden material is flushed with 70% ethanol three times and dried overnight under UV light for sterilization in laminar flow laboratory hood (NuAir). A 150μm diameter flexible precision dispensing tip (EFD) is fixed to the end of a 3mL luer lock tip syringe (BD Syringe). Vortex cooling from compressed the air cylinder cools temperature controlled enclosure to $2.0^{\circ}C$ +/-$2.0^{\circ}C$. Once temperature is stably within target range, the cell solutions are loaded into their respective nozzles. Extrusion pressure is set to 12.3 Pa. The height of the dispensing tip above the PDMS substrate is set to 200μm. Hepatocyte constructs are printed first, one at a time for each PDMS substrate, followed by epithelial cell constructs. Each cell construct is printed in their own compartment of their own dedicated PDMS substrate. After printing, a cover is added to seal the open channels. Cover and substrate secured in a bracket. Tubes connect ports on the cover to network cell-laden compartment to each other, to a source of fresh cell culture medium and to a drain. The flow rate through the system is set to

30µL/hr. All devices are stored 37°C and 5% CO_2. The set of MND process parameters are presented in equation 3-4. Figure 3-17 presents the biofabrication process to print two cell types in a microlfuidic device using MND for direct cell deposiiton. Figure 3-18 presents photographs of the fully assembly cell-laden microfluidic device prepared for the study.

$$\Omega_{MND,i} = [D_i \ \mu m \quad P_i(t) \ psi \quad N \quad v_i(t) \ mm/s \quad T \ ℃ \quad z_i(t) \ \mu m \ ]$$

$$\begin{bmatrix} Matrigel + HepG2 \\ Matrigel + M10 \end{bmatrix} = \begin{bmatrix} 150 & 2.0 & No \ Dilution & 5.0 & 2 & 200 \\ 150 & 2.0 & 1:16.67 & 5.0 & 2 & 200 \end{bmatrix} \qquad 3\text{-}4$$
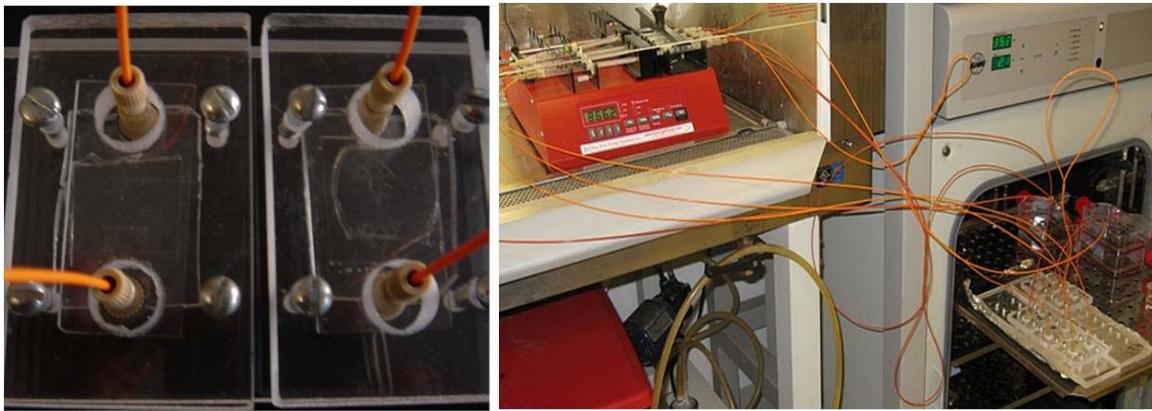
Figure 3-18: Microfluidic chip containing cell-laden constructs serially connected to biomimic in vivo pathogenesis.

3.3.3 Experimental design

The pro-drug drug amifostine must be metabolized to active form to effect radiation shielding on cells and genetic material. The metabolizing tissue is epithelial, which is chosen because its bio-signature is more suited to metabolizing amifostine, as compared to the target tissue. The target tissue is hepatocytes, which is chosen for its sensitivity to radiation and because as a monoculture it less capable of converting amifostine to active form. In this study, we serially connect epithelial constructs and hepatocytes and introduce amifostine to observe cell function after

printing and environmental control provided by the microfluidic platform. Figure 3-19 is a schematic of the dual micro-fluidic set-up.
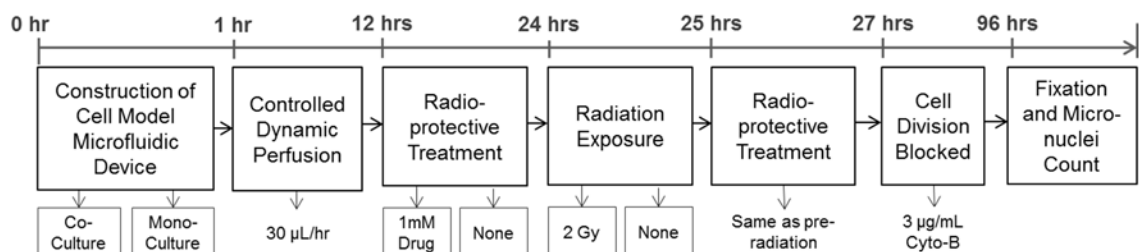
Figure 3-19: Method to study the effect mono- vs. co-culture microfluidic devices, radioprotective treatment and radiation on population fraction of genetically healthy vs. mutated HepG2 cells.

Amifostine enters the microfluidic system through a nano-port above the metabolizing tissue, which is the epithelial construct. Amifostine is in its inactive WR-2721 form (Aydemir, Sevim, Celikler, Vatan, & Bilaloglu, 2009). Epithelial cells secrete alkaline phosphatase, which is capable of activating the drug by stripping the amifostine of its phosphate group. Alkaline phosphatase in the epithelial cells de-phosphorylated the amifostine and convert the drug to active WR-1065 form. Dynamic perfusion forces the converted drug to the target tissue, which is the hepatocyte construct. The alkaline phosphatase activity in the hepatocyte is much less than the metabolizing construct. The drug metabolized to active form by the metabolizing construct protects the target tissue from radiation damage. The single tissue model is only the target tissue and does not include the metabolizing tissue.
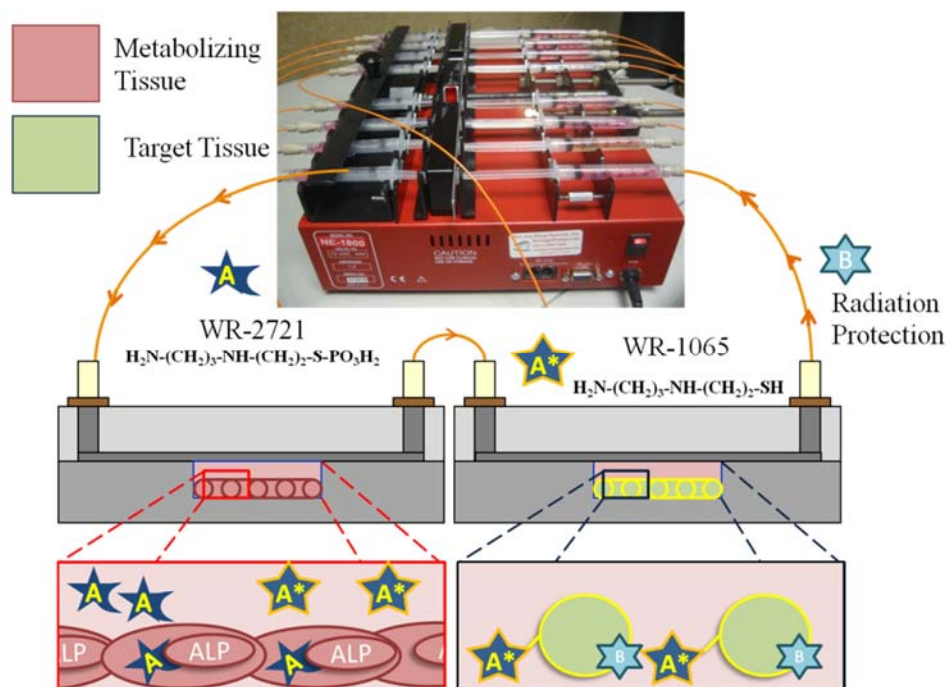
Figure 3-20: Schematic representation of the biomimetic pathogenesis of amifostine metabolism using dual tissue microfluidic device

3.3.3.1 *Ground model of extraplanetary radiation exposure.*

Radiation treatment was administered by the University of Pennsylvania School of Medicine Department of Radiation Oncology using a ^{137}Cs gamma -ray source with a dose rate of 86 cGy per minute. Irradiated samples were exposed to a 2 Gy dose over 1.72 minutes. Hepatocyte constructs remained sealed in microfluidic chip during exposure. Only select hepatocyte constructs are exposed to radiation, however all biological samples in this experiment are transported to treatment facility and remain outside incubated environment for an equal amount of time.

3.3.3.2 *Radioprotective drug treatment by pro-drug amifostine*

Anti-radiation treatment is perfusion of the radioprotective agent amifostine (Sigman et al.) through the cellular construct both before and after radiation exposure. Powder amifostine is mixed with culture medium to final concentration of 1mM amifostine. Amifostine is perfused through the constructs at a rate using a multi-channel programmable syringe pump (New Era Pump Systems)

for three hours prior to radiation exposure and for two hours after exposure. Equation 3-5 presents a selection method for the volumetric flow rate through the microfluidic device, Q, as a function of the the geometric parameter for chamber volume, V, and design variable for residentce time, t_R.

$$Q = \frac{V}{t_R} \qquad\qquad 3\text{-}5$$

The residence time of the drug in each chamber is 3 hours. The chamber volume is measured from the empty as-built microlfuidic chip. The volumetric flow rate is determined to be 30 μL/hr.

3.3.3.3   *Radiation damage by micronuclei count*

Micronuclei count quantified radiation damage of samples. After anti-radiation treatment is complete, cells are recovered from Matrigel matrix using BD MatriSperse Cell Recovery Solution (BD Bioscience) and plated on tissue treated polystyrene culture plates (Corning) for in culture medium with 3μg/mL permeable mycotoxin Cytochalasin B (Sigman et al.) to block cytoplasm division. After 72 hours cells are fixed in 50% (v/v) Methanol solution, genetic material is labeled with the fluorescent probe DAPI Nuclear Counter stain (Molecular Probes), and examined. Samples were analyzed on a Zeiss Axioplan fluorescence microscope. Images of all cells were captured electronically using a Sensys charge-coupled device (CCD) camera (Photometrics Ltd.) and the MacProbe computer software developed by Applied Imaging. All samples were coded and scored blind. Cells are qualitatively sorted into three categories (1) mono-nucleated (2) bi-nucleated without micronuclei and (3) bi-nucleated with micronuclei. Figure 3-21 presents categories of cells prepared for micronuclei count. Only bi-nucleated cells with micronuclei are considered damaged. The results of the count are presented as a percentage of radiation damage cells determined by the number of bi-nucleated cells with micronuclei relative to total number of bi-nucleated cells.

Figure 3-21: Classification of cells post-radiation (A) mono-nucleated (B) bi-nucleated without micronuclei (C) bi-nucleated with micronuclei.

3.3.4   Effect of radiation, drug and hetero-cellular culture on drug efficacy

HepG2 cells contained in a mono-culture microfluidic device are irradiated without radioprotective drug treatment. The effect of radiation on the population fraction of HepG2 cells with genetic mutation is compared to non-irradiated HepG2 also contained in a mono-culture microfluidic device. Each cell is categorized as healthy or genetically mutated based on a micronuclei count. The population fraction of genetically mutated vs healthy HepG2 cells for irradiated (2 Gy Radiation) and non-irradiated (0 Gy Radiation) devices is presented in figure 3-22. The 2 Gy radiation treatment is not the exclusive cause of genetic mutation for HepG2 cultured in the presented microfluidic device. Non-irradiated HepG2 present micronuclei and are therefore categorized as genetically mutated. Radiation exposure increases the population fraction of genetically mutated cells by 22.1% from 3.6% to 25.7%. Consequently, the population of healthy cells decreases from 96.4% to 74.3% after 2 Gy radiation exposure.
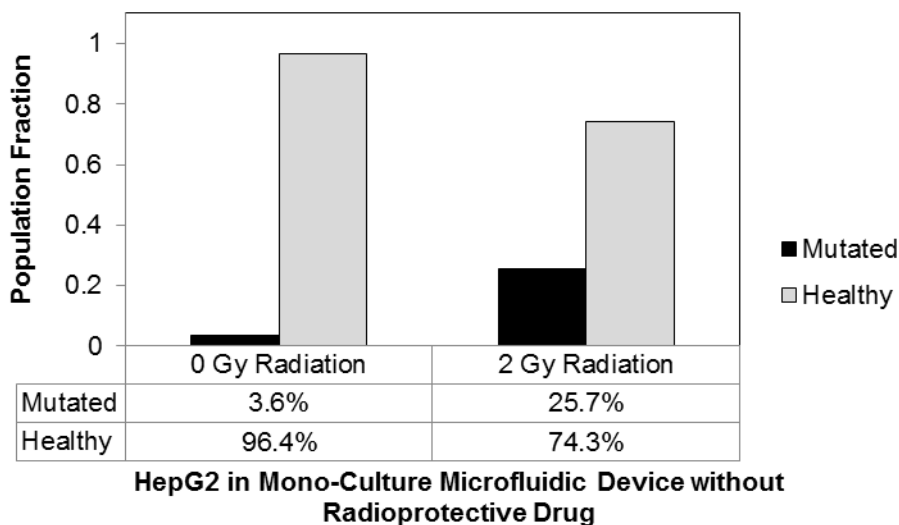
Figure 3-22: Effect of 2 Gy gamma radiation on population fraction of genetically mutated vs. healthy HepG2 cells in mono-culture microfluidic device without radioprotective drug treatment.

HepG2 cells contained in a mono-culture microfluidic device are irradiated with and without radioprotective drug treatment. Each cell is categorized as healthy or genetically mutated based on a micronuclei count. The population fraction of genetically mutated vs healthy HepG2 cells after radiation with (1mM Drug) and without (0mM Drug) radioprotective drug treatment is presented in figure 3-23. Radioprotective drug decreases the population fraction of genetically mutated cells by 19.1% from 25.7% to 6.6%. Consequently, the population of healthy cells increases from 74.3% to 93.4% with radioprotective drug treatment.
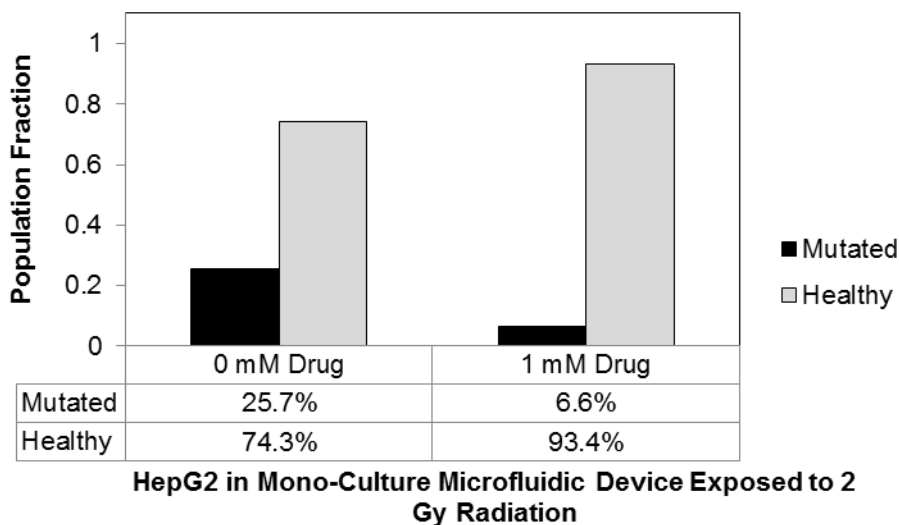
Figure 3-23: Effect of 1 mM radioprotective drug on population fraction of genetically mutated vs. healthy HepG2 cells in mono-culture microfluidic device after 2 Gy gamma radiation exposure.

HepG2 and M10 cells contained in a co-culture microfluidic device are irradiated with radioprotective drug treatment. The effect of co-culture with M10 cells on the population fraction of HepG2 cells with genetic mutation after radiation and radioprotective drug treatment is compared to HepG2 cells in a mono-culture microfluidic device. The population fraction of genetically mutated vs healthy HepG2 cells for mono- vs. co-culture microfluidic devices is presented in figure 3-24. HepG2 present genetic mutations in mono- and co-culture environments. Co-culture of HepG2 with M10 cells decreases the population fraction of genetically damaged cells from 6.6% in mono-culture to 3.3% in co-culture devices.
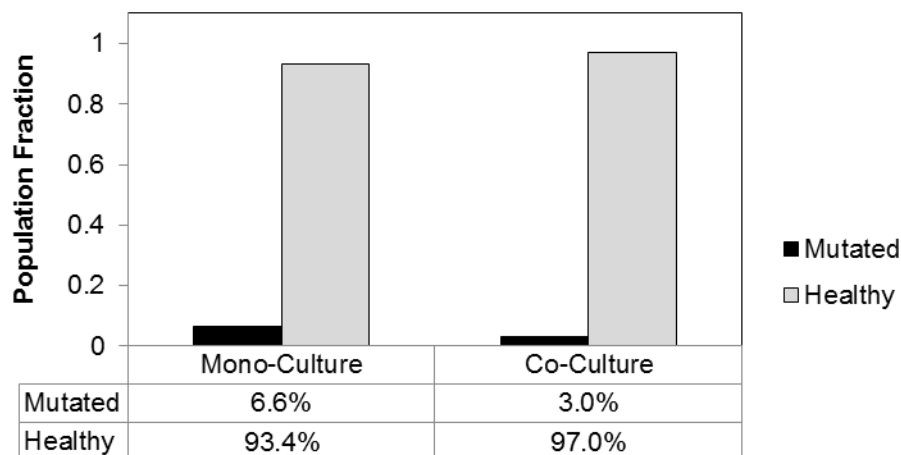
Figure 3-24: Effect of mono- and co-culture microfluidic device on population fraction of genetically mutated vs. healthy HepG2 cells exposed to 2 Gy gamma radiation and treated with 1mM radioprotective drug.

3.3.5 Discussion

The space environment causes a physiological and pathological change in biological behavior, which must be characterized for NASA to prepare appropriate health systems requirements. A new method of bio-printing and bioreactor design is offered in this research work. The solution is tailored to accommodate pharmaceutical testing using human derived cellular material in exotic environments, like space. Specifically, to create high fidelity tissue analogs to study multi-cellular metabolism of anti-radiation medication for long term space flight. Microfluidics were designed and manufactured to study the drug metabolism and radiation shielding in a hetero-cellular environment. The radioprotective benefits of the pro-drug amifostine were fully realized by incorporating hetero-cellular arrangement througut a micrlofluidic system. The single organ model was not a complete or accurate representation of the conversion of drug to active form, and consequently modeled diminished drug efficacy as diminished radiation shielding.

The co-culture condition is a more authentic representation of *in vivo* pathogenesis and tissue function. The single tissue model gives the false conclusion amifostine is not an effective radioprotective agent. Microfluidics were used in this work to control and organize the transient interactions between two cell types. A metabolizing organ and target organ were serially connected in microfluidic chip and dynamically perfused with the anti-radiation drug amifostine. The metabolizing organ converts the drug to active form by producing the enzyme alkaline phosphatase, which strips the drug of phosphates. The active form of the drug then perfuses the target organ and shields the organ from radiation damage. The micronuclei count demonstrates the active form of the drug is an effective form of radioprotection. The percentage of radiation damaged cells for the dual organ is 3% compared to 4% for non-irradiated controls. Without the metabolizing tissue, less of the drug is converted to active form and less radiation protection is observed. The percentage of radiation damaged cells for the single organ is more than twice the dual organ. Table 3-1 summarizes the experimental variables and results of the presented study.

Table 3-1. Effect of culture condition, radiation exposure and radioprotective drug treatment on percentage of genetically mutated hepatocytes.

Culture Condition	Radiation Exposure	Radioprotective Treatment	Mutated Cells	Assessment
Co-Culture	2 Gy	1 mM Drug	3.0 %	Healthiest
Mono-Culture	0	0	3.6 %	
Mono-Culture	2 Gy	1mM	6.6 %	
Mono-Culture	2 Gy	0	25.7 %	Most Damaged

The instances of radiation damage for the single organ model are twice that of the non-irradiated control. However, this is because the drug is not converted to active form. The metabolizing organ represents cooperate and synergistic relationship between cell types in the human body. The dual organ model demonstrates the radioprotective benefits of amifostine by metabolizing the drug as would happen *in vivo* conditions.

Radioprotective benefits of amifostine would not have been observable without the dual organ culture environment. The simpler single organ model would have falsely underestimated benefits of amifostine. The microfluidic platform provides researchers a portable tool to study synergistic coupled behavior between various cell types. The dynamic perfusion provides control over the transient interaction and dynamic effluent collection to understand effect of environmental stress on tissue and organ level function. The microfluidic platform is an improved vetting technique for drug discovery and fundamental characterization of cell behavior.

The organization and patterning of the cells is controlled by cell printer. Printing technology allows researchers to leverage geometric positioning and proximity of specific biologics to bring functional abilities to cell aggregates (Barron et al., 2004; Ciocca et al., 2009; Murray et al., 2007). Physicians and researchers study *in vivo* tissue composition and cellular orientation to characterize critical mechanisms of tissue and organ systems (Alini et al., 2008; Gabbay et al., 2006). This body of knowledge defines healthy tissue; which can then be used as a template to conceptually design functional tissue from basic biological building blocks. Bio-modeling is the engineered combination of physical components into a specific spatial construction in a flexible digital workspace. Additionally, biologics are spatially organized to allow nutrient diffusion to the core of a matrix and subvert cell death due to hypoxia. Automation of dispensing control also ensures consistent material allocation for each sample.

CHAPTER 4: DEVELOPMENT OF A SYNCHRONIZED MULTI-MATERIAL BIOPRINTING SYSTEM

4.1   Rationale and fabrication

4.1.1   Rationale

The previously presented multi-nozzle deposition system (MND) leverages discrete nozzles to dispense separate phenotypes, cross-linking solution, and support material during SFF of hydrogel scaffolds. Each nozzle extruded a homogenous cell-laden filament. Multiple nozzle produce hierarchical environments. In this work, we design, fabricate and characterize a novel synchronozed multi-material bioprinting (SMMB) system to improve the resolution of the MND system. The novel deposition system combines aquesous solutions into a single outlet stream without mixing. The deposition head is mounted to motion system with independently controlled movement in the x-, y-, and z-direction. The deposition head extrudes the heterogenous assembly of materials along a pre-programmed 3-dimensional tool-path. The objective of the multi-input microfluidic printhead is to improve the resolution of the bioprinter by packaging multiple phenotypes in a single filament.

The snynchronized multi-material bioprinter's novel deposition head fabricates both (1) hetereogenous filaments printed into geoemtric patterns defined using automation software and (2) heteregenous nano-liter droplets with variable volume from 200-600nL and shape (torus droplets or solid sphereical droplets). Figure 4-1 presents the block diamgram of the synchronized multi-material bioprinter integrated with the multi-nozzle deposition cell printer for temperature controlled geometric patterning of heterogeneous cell-laden filaments to build 3-dimensional scaffolds or controlled cell seeding in the channels of a microfluidic device.
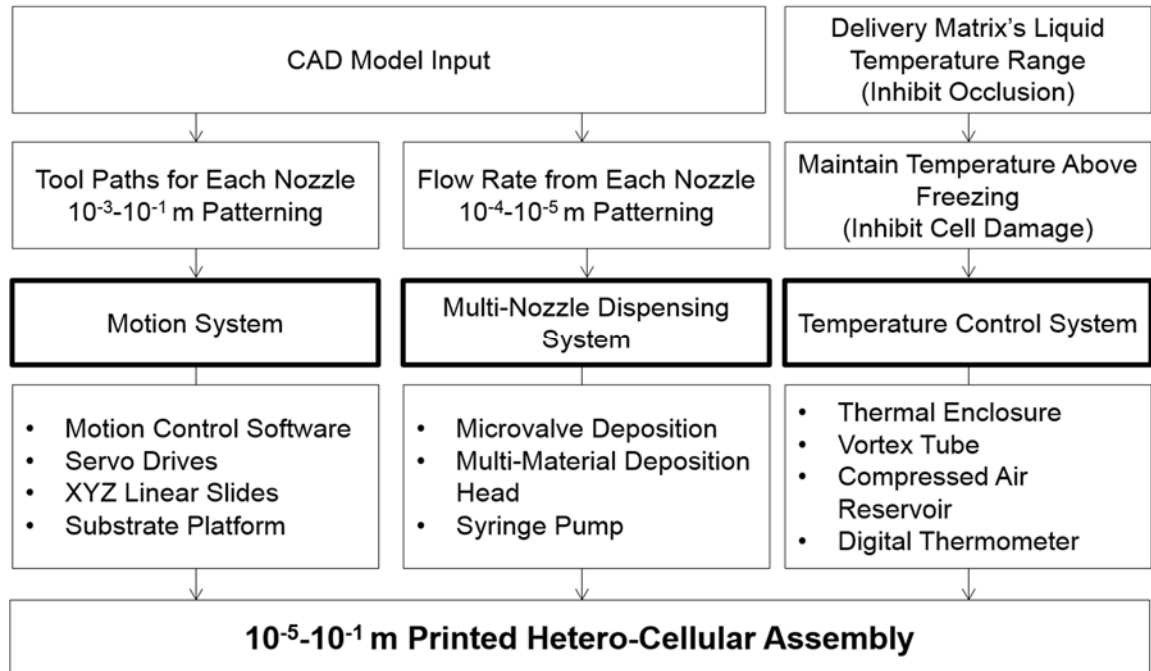
Figure 4-1: Block diagram of the synchronized multi-material bioprinter (SMMB) which integrates a deposition head for controlled heterogeneous extrusion with multi-nozzle deposition (MND) system.

The design of the heterogeneous filament extruded by the SMMB is controlled by the channel network in the deposition head. Figure 4-2 presents several networks design to package multiple materials in a 1-dimensional array prior to printing. Figure 4-3 is a photograph of the fabricated SMMB deposition head perfused with three different solutions laden with die for visualization purposes.
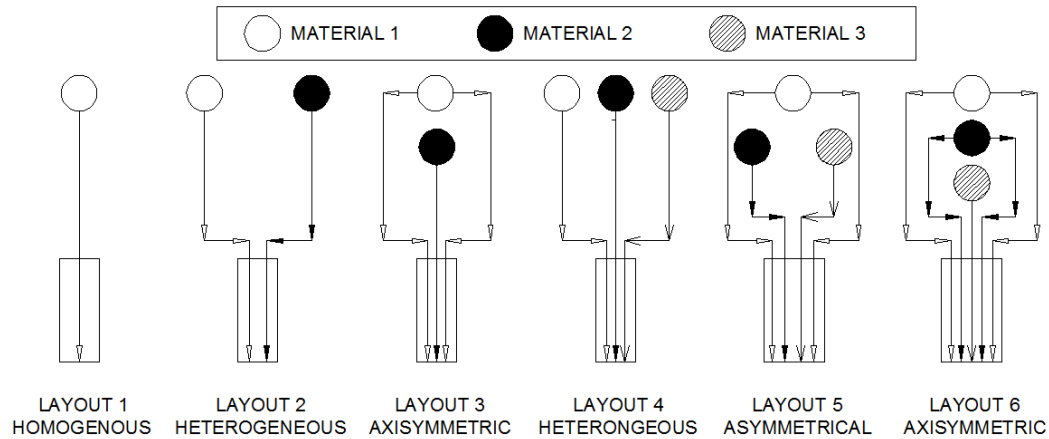
Figure 4-2: Microfluidic network layouts for homogenous, heterogeneous, axisymmetric, and asymmetrical combination of up to three materials.
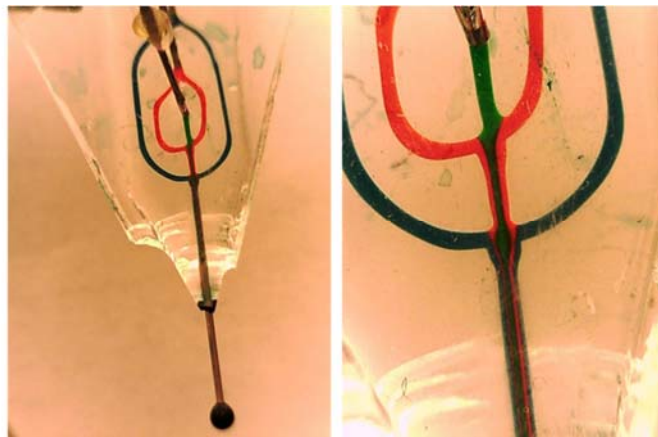
Figure 4-3: As-built Simultaneous Multi-Material Print head perfused with 3 inputs to produce 5 discrete streams in the outlet channel.

4.1.2   Fabrication of SMMB deposition head

SMMB deposition head packages multiple fluid streams into a single heterogeneous array. Each material enters the deposition head through its own inlet port. The design of the channel network defines the flow path of each material to collect in a pre-determined arrangement in a single combined flow outlet channel. Figure 4-4 presents the PCL pattern and flow design schematic as well as a photograph of the fabricated PDMS SMMB deposition head.
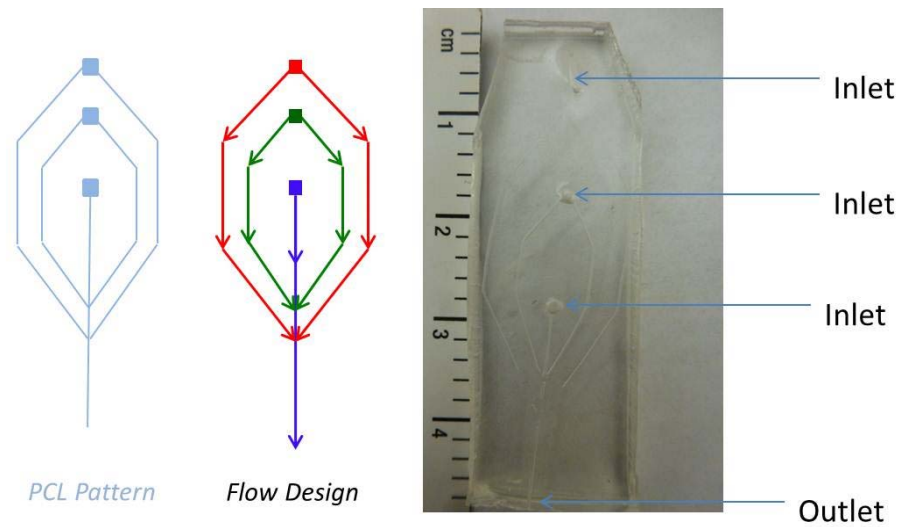
Figure 4-4: Multi-inlet microfluidic design and fabricated printhead.

The channel network is embedded in a PDMS substrate. Embedding the channel network circumvents the need for an additional cover components and prevents leakage. Step 1 is the design and fabrication of the channel network embedded in PDMS by the two stage process precision extrusion deposition and replica molding, process is described in section 2.2. Step 2 is shaping the outlet to a point using a blade. Step 3 is to insert a steel capillary tip in to the outlet channel. Step 4 is insert capillary tips into inlet ports. Silicone tubes are attached to the inlet tips and plumbed back to the material reservoir placed in a syringe pump.
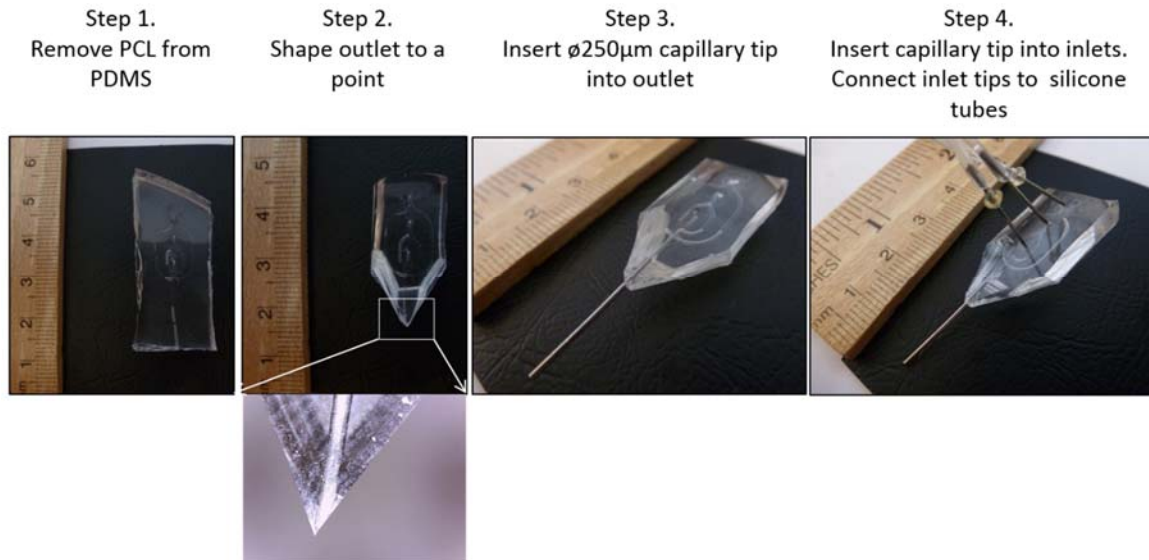
Figure 4-5: SMMB deposition head construction in four steps from left to right: Step 1: Design and fabricate channel network. Step 2: Shape outlet. Step 3: Insert capillary tip into outlet. Step 4: Inset capillary tips into each inlet and connect silicone tubes.

The channel network is a 3-dimensional interconnected set of features which include vertical channel perpendicular to the rest of the network, bifurcations and arch structures. These are necessary for the following reasons:

- **Channel bifurcations:** Produce axisymmetric material arrays using a single inlet for each channel.

- **3-dimensional arch structures:** Cross material channels without mixing.

- **Channels perpendicular to the flow network:** Material inlets ports without crossing other channels or producing arches.

Channel network is fabricated using a printed PCL template. The PED system's capability to fabricate 3-dimensional structures is the limiting technology to produce features in the channel network. Here we present the PED system's capability to fabricate vertical filaments and arches to be used for the SMMB deposition head. Figure 4-6 presents the PED printing vertical filaments,

filaments perpendicular to the printing substrate. The rest of the SMMB deposition head channel template is parallel with the printing substrate.
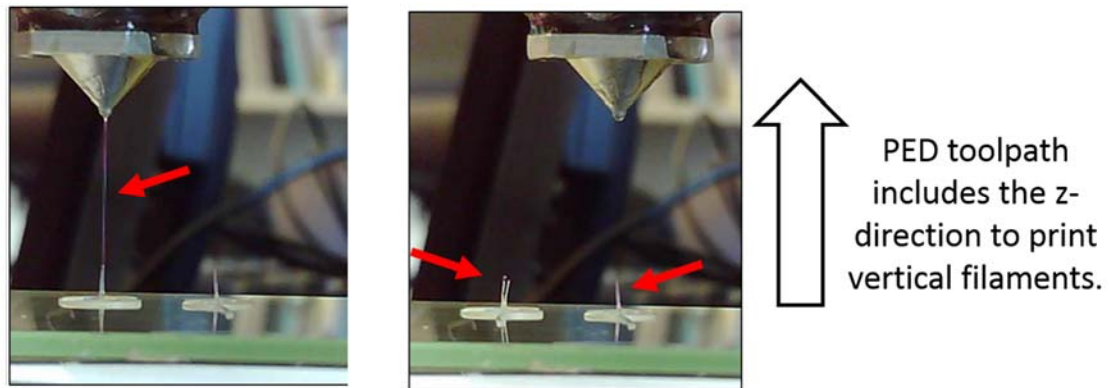
Figure 4-6: View of PED system printing SMMB deposition head design to be replica molded. PED tool path includes z-direction perpendicular to the printing substrate to fabricate vertical filaments. Red arrows point to vertical filaments.

Figure 4-7 presents a photograph of PED system printed PCL arch structures. The purpose of the arch is to provide clearance for a second channel to pass under the arch. In this way, more complex material arrays become feasible. The inconsistent cross-section and shape of the arch does not diminish the feature's ability to provide clearance for another channel underneath, and therefore successfully enable materials channel to cross without mixing within the SMMB deposition head network.
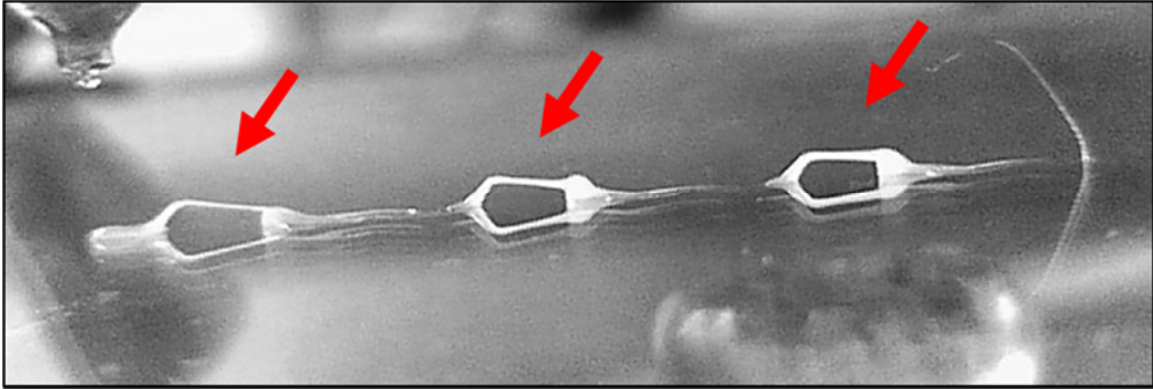
Figure 4-7: PED system printed PCL arches for possible use in SMMB deposition head. Arches identified by red arrows.

4.2 SMMB process parameters, material properties and design variables

SMMB system performance is defined by a set of geometric design variables to assemble a set of materials in a heterogeneous array as a single extruded filament and print that filament to produce a programmed geometric pattern. Design variables, Ψ_{SMMB}, are a function of the geometric parameters of the SMMB deposition head, X_{SMMB}, process parameters, Ω_{SMMB}, and material properties, Φ_{SMMB}. The system is reproducible within the operating thresholds of the process parameters. Process parameters are automated and can be adjusted dynamically during the build cycle period to fabricate gradient structures and multiple design variables in a single printed construct. Equation 4-1 defines design variables as a function of the geoemtric parameters, process parameters and material properties.

$$\Psi_{SMMB}(t) = f\{X_{SMMB}, \Omega_{SMMB}(t), \Phi_{SMMB}(t)\} \qquad \text{4-1}$$

The SMMB system's fabrication objectives define the design variables. The fabrication objective is a 3-dimensional built biological system using thermally extruded polymer with specific macro-scale ($10^{-3} - 10^{-1}$ m) pathways of material deposition and micro-scale ($10^{-5} - 10^{-3}$ m) cross-sectional width/height of the polymer. The macro-scale pathway of material deposition is controlled by the motion system to be repeatable to less than 10μm. Micro-scale design variables to

characterize the printed filament's cross-section are controlled by system's process parameters. The size of the printed filament are independently controllable and automated to be varied over the build cycle to transform throughout the construct. Each material is combined in a single outlet of the deposition head. The volume fraction of each material and the width of a single material or combination of material streams are designed to mimic in vivo conditions. Reaction time between solutions in the deposition head determines chemical reactions prior to extrusion to induce a particular amount of partial cross-linking prior to extrusion. Equation 4-2 defines the set of design variables as the printed filament's cross-sectional width, c, and height, d, reaction time between solution in the printhead, t_r, width of a combination of material stream i and j, w_{ij}, and volume fraction of material i to material j, γ_{ij} .

$$\Psi_{SMMB}(t) = [c(t) \quad d(t) \quad t_r(t) \quad w_{ij}(t) \quad \gamma_{ij}(t)] \qquad 4\text{-}2$$

Process parameters are defined by the system's hardware and software configuration. Each material is prepared and loaded into its own independently controlled programmable syringe pump. Material is pumped from its reservoir, through its own SMMB inlet port, into the combined outlet channel and extruded as part of a single heterogeneous filament onto the printing substrate. SMMB controllable process parameters are the flow rate of each material, Q, printhead speed, v, height of the dispensing tip above the printing substrate, z, and height between build cycles, d_z. All parameters are automated and tunable during a build cycle. During the course of the build cycle, process parameters can be adjusted to fabricate multiple sets of design variables in a single construct. Equation 4-3 defines the set of independently tunable system process parameters.

$$\Omega_{SMMB}(t) = [Q_i(t) \quad v(t) \quad z(t) \quad d_z(t)] \qquad 4\text{-}3$$

The set of design variables for a heterogeneous multi-material printed filament require the flow through the deposition head be laminar and incompressible. The criteria to define laminar flow is Reynolds number, which coorelates the inertial forces of the system's hardware and channel

geometry with viscous forces in the fluid. The criteria for incompressible flow is Mach number. The Mach number couples the inertial forces to the material's compressibility. Equation 4-4 defines the set of material properties to describe material rheology as density, ρ_i, absolute viscosity, μ_i, and kinematic viscosity, v_i, and material compressibility as material bulk modulus, E_i.

$$\Phi_{SMMB}(t) = [\; E_i \quad \mu_i \quad v_i \quad \rho_i] \qquad\qquad 4\text{-}4$$

Geometric parameters are designed to maintain laminar flow and restrict shear stress in the flowing fluid to maintain threshold precentages of viable cells in printed constructs. Parameters are measured using photographs of the as-built system evaluated using the image processing software ImageJ (NIH). Geometric parameters require changes to system's parts or configuration and remain constant from build cycle to build cycle. The set of SMMB geometric parameters are all specific to the combined flow outlet channel cross-section width, a, and height, b, and total length from where the individual streams combine to where they are dispensed to the ambient environment, L. The total length is divided into the length inside PDMS deposition head, L_{PC}, and capillary tip length, L_{CT}. The combined flow outlet channel cross-section shape coefficient, ω, defines the combined flow as either a half or full ellipse. Equation 4-5 presents the set of geometric parameters.

$$X_{SMMB} = [\; a \quad b \quad L \quad L_{CT} \quad L_{PC} \quad \varepsilon \quad] \qquad\qquad 4\text{-}5$$

Table 4-1 presents the geometric, process, material, design, and derived parameters. Derived parameters assist in analytical characterization of the system. Derived parameters are not directly controlled by the operator and are not the specific performance objective of the process.

Table 4-1. Synchronized multi-material bioprinter (SMMB) system design variables, derived, geometric, material, and process parameters.

Symbol	Description	Process Window	Parameter Type
A	Cross-sectional area of printed filament	-	Derived
A_c	Cross-sectional area of SMMB deposition head outlet channel		Derived
a	SMMB deposition head channel cross-section width	-	Geometric
b	SMMB deposition head channel cross-section height	-	Geometric
c	Printed filament width	-	Design
d	Printed filament height	-	Design
D	SMMB deposition head outlet channel diameter		
D_h	Hydraulic diameter		
E_i	Material bulk modulus		Material
L	SMMB deposition head combined outlet channel total length		Geometric
L_{pc}	SMMB deposition head combined outlet channel length inside PDMS		Geometric
L_{CT}	SMMB deposition head outlet capillary tip length		Geometric
M	Mach number		Derived
Q	Net volumetric flow rate SMMB deposition head outlet	-	Derived
Q_i	Individual material flow rate into SMMB deposition head	$1.67 \times 10^{-3} \leq Q_i \leq 2.00$ mL/min	Process
Re	Reynolds number		Derived
Re_l	Maximum Reynolds number for laminar flow in a closed channel	2300	Derived
t	Time	-	
t_r	Reaction time between materials in SMMB deposition head	-	Design
v	SMMB printhead speed	$0.1 \leq v \leq 15.0$ mm/s	Process
v_d	SMMB material deposition speed		Derived
v_z	Fluid speed in SMMB deposition head		Derived
w_{ij}	Width of a combination of material stream i and j		Design
z	Height of SMMB deposition system outlet above printing substrate	$100 \leq z \leq 1000$ μm	Process
μ_i	Material absolute viscosity		Material

cont'd Symbol	Description	Process Window	Parameter Type
ν_i	Material kinematic viscosity		Material
ρ_i	Material density		Material
γ_{ij}	Volume fraction of material i to material j		Design
ω	Channel cross-section shape coefficient	Full Ellipse $\omega = 4$ Half Ellipse $\omega = 2$	Geometric
Υ	Cell survival		Design
X_{SMMB}	SMMB geometric parameters		
Φ_{SMMB}	SMMB material parameters	-	Geometric
Ψ_{SMMB}	SMMB design variables	-	Design
Ω_{SMMB}	SMMB process parameters	-	Process

4.2.1 Design parameters definition

The set of design parameters is specifically defined for a three material flow pattern. The 1-dimensional array of solutions analyzed in this work is symmetric about the longitudinal axis of the printhead. A schematic of the flow is shown in figure 4-8. Each solution and its flow rate are numbered, beginning at the longitudinal axis of the outlet channel and moving out radially. In this analysis there are three solutions. Each solution is independently controlled by its own dedicated programmable syringe pump.
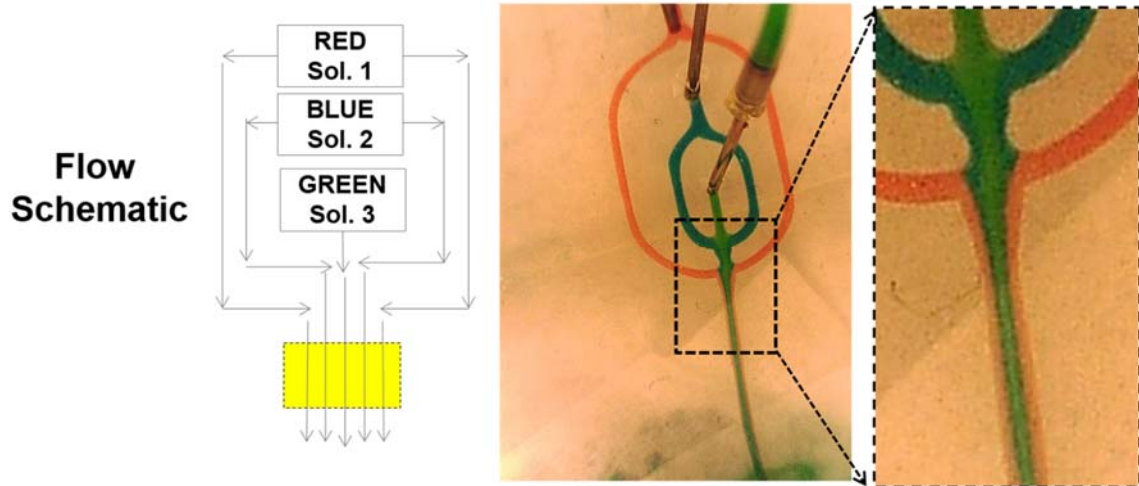
Figure 4-8: SMMB deposition head with three fluid inputs combined in a single outlet stream to be extruded as a single heterogeneous filament. Flow schematic and photograph of fully developed three material flow through fabricated deposition head.

In this case solution 1 and 2 are cell-laden. Solution 3 is a cross-linking solution. The set of design parameters for the axisymmetric 3-material array, where the outer most solution is a cross-linking solution are presented in equation 4-2 (reporduced below).

$$\Psi_{SMMB}(t) = [c(t) \quad d(t) \quad t_r(t) \quad w_{ij}(t) \quad \gamma_{ij}(t)]$$

- c Total width of the heterogeneous printed filament

- d Total height of the heterogeneous printed filament

- t_r Gelation time in the device

- γ_{ij} Biomimetic ratio of the two cell-laden solutions

- w_{ij} A target width of solution 1 and 2 (excluding solution 3, the cross-linker)

The design variables and geometric parameters for the three material input axisymmetric design is presented in figure 4-9. Extruded material is not presented in the figure 4-9 graphic, therefore the width/height of the combined material outlet channel (represented as a and b

respectively in geoemtric parameter set) are equal to the total width/height of the heterogenous

filament (represented as c and d respectively in the design variable set) .
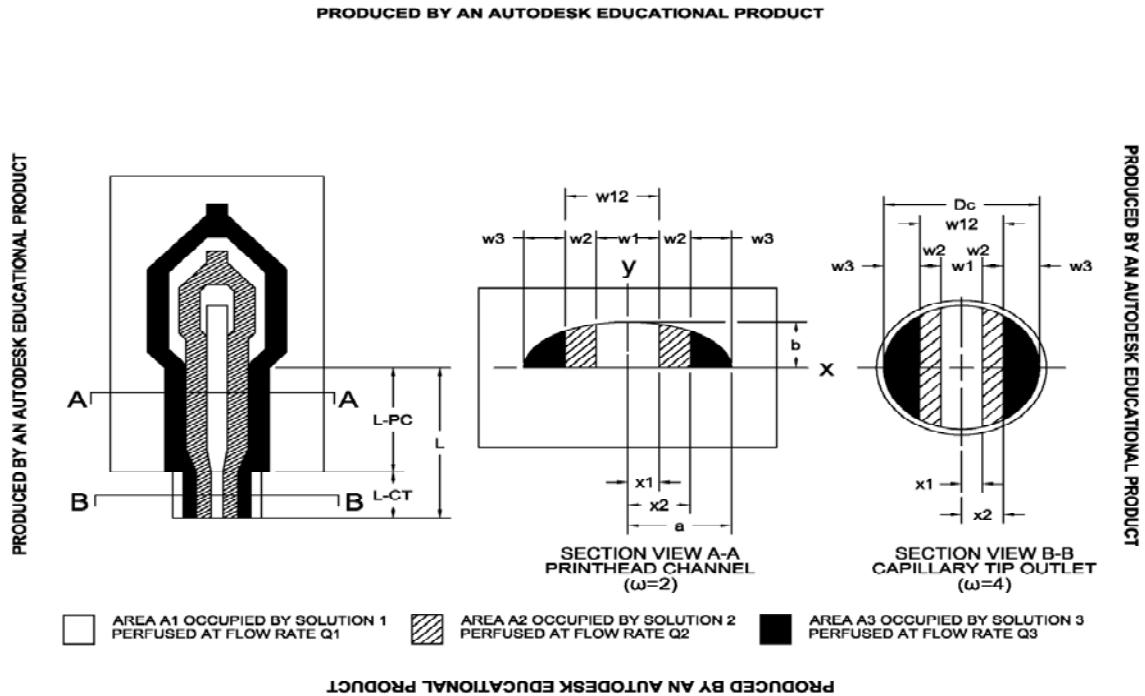
Figure 4-9: Schematic of geometric and process parameters for synchronized multi-material deposition head. Each material flows in through a port in the top of the SMMB and is combined in a single outlet channel at the bottom.

4.2.1.1 *Volume fraction of each material*

System requirements determine the fluid is incompressible. Consequently, the volume

fractions of the solutions are a function of the flow rate. Equation 4-6 through 4-8 define the volume

fraction of solutions to the flow rate.

$$\gamma_{1,2} = \gamma_{2,1}^{-1} = \frac{Q_1}{Q_2} \qquad \qquad 4\text{-}6$$

$$\gamma_{1,3} = \gamma_{3,1}^{-1} = \frac{Q_1}{Q_3} \qquad \qquad 4\text{-}7$$

$$\gamma_{2,3} = \gamma_{3,1}^{-1} = \frac{Q_1}{Q_3} \qquad\qquad\qquad 4\text{-}8$$

4.2.1.2   Width of each material in combined flow

The three material input axisymmetric design schematic presented in figure 4-9 defines the design variables for the width of the solution as a function of the geometric parameters of the SMMB deposition head channel. The width each individual material stream is presented in equation 4-9 through 4-11.

$$w_1 = 2x_1 \qquad\qquad\qquad 4\text{-}9$$

$$w_2 = (x_2 - x_1) \qquad\qquad\qquad 4\text{-}10$$

$$w_3 = a + x_1 - x_2 \qquad\qquad\qquad 4\text{-}11$$

The width of a combination of adjacent materials is presented in equation 4-12 and 4-13. The total width of all the materials is equal to the width of the fabricated channel.

$$w_{1,2} = 2x_2 \qquad\qquad\qquad 4\text{-}12$$

$$w_{2,3} = a - x_1 \qquad\qquad\qquad 4\text{-}13$$

4.2.1.3   Reaction time between materials in outlet channel

The duration of chemical reactions, including cross-linking, between adjacent materials in the combined flow outlet channel is the controllable design parameter named reaction time. The reaction time is a function of the length of the combined flow outlet channel, material's flow rate and the cross-sectional area the material occupies in the channel, equation 4-14.

$$\int_0^{t_R} dt = \int_0^L A_c \left(\sum_{i=0}^3 Q_i \right)^{-1} dL \qquad\qquad\qquad 4\text{-}14$$

The flow rate and cross-sectional area a material occupies is constant throughout the length of the channel. Equation 4-13 is integrated to define the reaction time as a function of a material's geometry and process parameters, equation 4-15.

$$t_R = \frac{A_c L}{Q_1 + Q_2 + Q_3} \qquad \textit{4-15}$$

The average velocity of the combined flow is a function of the total cross-sectional area and net volumetric flow rate and the individual material cross-sectional are and individual flow rate, presented in equation 4-15. The cross-sectional area of the capillary tip inserted in the outlet and outlet channel embedded in the PDMS deposition head are the equal.

$$\frac{L}{t_R} = \frac{Q_1 + Q_2 + Q_3}{A_c} = \frac{Q_1}{A_1} = \frac{Q_2}{A_2} = \frac{Q_3}{A_3} \qquad \textit{4-16}$$

4.2.2 Controllable process parameters operating thresholds

Process parameters for simultaneous multi-material print head integrated with the bioprinter are flow rate for each input, print head speed over substrate, height of print head above printing substrate, and displacement in z. The set of bioprinter process parameters are as follows:

$$\Omega_{SMMB}(t) = [Q_i(t) \quad v(t) \quad z(t) \quad d_z(t)]$$

The hardware limitation of the New Era Pump Systems programmable syringe pump defines the maximum and minimum flow rates for the as-fabricated system, equation 4-18.

$$1.67 \times 10^{-3} \ \frac{mL}{min} \ \leq \ Q_i \ \leq \ 2.00 \ \frac{mL}{min} \qquad \textit{4-17}$$

The hardware limitation of the Parker Motion System linear slides defines the maximum and minimum print head speed for x, y, and z direction, as presented in equation 4-18.

$$0.1 \, \frac{mm}{s} \, \leq \, v \, \leq 10.0 \, \frac{mm}{s} \qquad\qquad 4\text{-}18$$

Thresholds for process parameters are driven from hardware limitations are the set presented in equation 4-19.

$$\Omega_P = \begin{bmatrix} 1.67 \times 10^{-3} \, \leq \, Q_i \, \leq \, 2.00 \, \dfrac{mL}{min} \\ 0.1 \, \leq \, v_p \, \leq 10.0 \quad \dfrac{mm}{s} \\ 100 \, \leq \, z \, \leq 2000 \quad \mu m \\ 0.1 \, \leq \, d_z \, \leq 50 \quad mm \end{bmatrix} \qquad\qquad 4\text{-}19$$

4.3   System requirements and material selection criteria

Flow through the deposition head must be laminar, incompressible and fully developed to successfully arrange multiple fluid streams in a heterogeneous array. Process limitations are defined by characterizing operating windows which maintain laminar, incompressible and fully developed flow through the SMMB deposition head channel network.

Table 4-2. System requirements for printing heterogeneous material filament with controllability using SMMB deposition head.

Requirement	Criteria	Process Window to maintain requirements		
Laminar Flow	Reynolds Number	**Inertial Forces** Hardware Limitations Channel Geometry	↔	**Viscous Forces**
Incompressible	Mach Number	**Inertial Forces** Hardware Limitations Channel Geometry	↔	**Compressibility Forces**
Fully Developed		Channel Length	↔	Channel Hydraulic Diameter
Cell Viability	Shear Stress Thresholds	**Inertial Forces** Hardware Limitations Channel Geometry	↔	**Viscous Forces**

Streamlines maintained by the flow due to viscous forces define laminar flow and prevent mixing. The criteria to analyze laminar flow is Reynolds number. The Reynolds number relates the inertial forces of the system's hardware and channel geometry with viscous forces in the fluid. The Reynolds number criteria defines the set of viscosities which can and cannot be successfully printed without mixing. The criteria for incompressible flow is Mach number. The Mach number couples the inertial forces to the material's compressibility. The Mach number criteria defines the set of densities and bulk modulus which can and cannot be successfully printed without compression. Fully developed flow is assumed for the outlet channel length is significantly greater than the channel's hydraulic diameter.

4.3.1   Inertial and viscous thresholds coupled by Reynolds number

The synchronized multi-material deposition head combines multiple material inputs into a single combined material outlet. The volume fraction of each constituent material is controllable by the manufacturing process parameters. The volume fraction of each material is preserved even if each constituent material mixes in the outlet channel. However, distinct hierarchical structures in the extruded combined flow are present and their shape controllable if the materials do not mix. The criteria to define the mixing behavior of a flowing fluid is the Reynolds number, which relates the inertial to viscous forces in a flowing fluid.
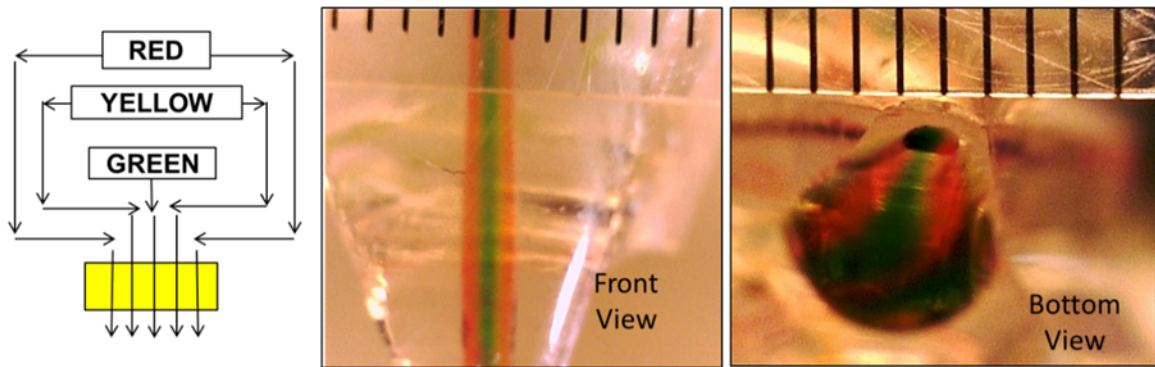
Figure 4-10: Heterogeneous filament produced at deposition tip because streamlines are maintained in laminar flow process window. Viscous forces are sufficient to prevent mixing due to inertial forces in the flowing fluid. Each calibration at the top of the photograph is 500μm apart.

The ratio of inertial to viscous forces quantifies the relative influence of both forces on the flow pattern of a fluid (Rott, 1990). Three distinct flow regimes are defined as (1) inertial force dominant, (2) viscous force dominant and (3) transitional. Viscous force dominant flow, or laminar flow, maintains streamlines without mixing. Inertial force dominant flow, or turbulent flow, has chaotic motion with mixing and flow instabilities. Transient flow does not reliably present the predictable streamlines of laminar flow or the full mixing of turbulent flow. The Reynolds number in a closed channel defines each of the three flow regimes as a function of the ratio of inertial to viscous forces. The Reynolds number is a function of the average fluid speed, hydraulic diameter of the channel and kinematic viscosity of the fluid. Each regime is presented in equation 4-20.

$$Re = \frac{inertial\ forces}{viscous\ forces} = \frac{VD_h}{v} = \begin{cases} Re_l & < 2300 & Laminar \\ Re_{l \to t} & 2300 < 4000 & Transient \\ Re_t & > 4000 & Turbulent \end{cases} \qquad 4\text{-}20$$

Process windows for the synchronized multi-material bioprinter system are designed to maintain a Reynolds number less than 2300 to preserve laminar flow and prevent mixing. The criteria to maintain laminar flow is a function of the known maximum ratio of inertial to viscous forces for laminar flow (maximum laminar Reynolds number for closed channel) and variable

which define the Reynolds number. The ratio of inertial to viscous forces required which define the upper limit of non-mixing or inertial dominant flow is presented in equation 4-21.

$$2300 > Re = \frac{VD_h}{v} \qquad\qquad 4\text{-}21$$

The inertial forces in the deposition system are a function of the maximum and minimum force generated by the syringe pump and cross-sectional area of the outlet channel. The viscous forces are a material property. The maximum and minimum force generated by the syringe pump and cross-sectional area of the outlet channel are known. The maximum allowable Reynolds numbers is 2300 to prevent mixing. Therefore, a selection criteria for material rheology is presented to preserve laminar flow by maintaining a ratio of inertial to viscous forces less than 2300, equation 4-22.

$$v > \frac{VD_h}{2300} \qquad\qquad 4\text{-}22$$

Equation 4-22 is algebraically manipulated and combined with the maximum laminar flow Reynolds number in equation 4-21 to present the kinematic viscosity as a function of Reynolds number and inertial forces, equation 4-21. Average fluid speed is a function of the flow rate and channel cross-sectional area. The cross-sectional area is the outlet channel where the material inlets combine and mixing is of concern. The number of inlet channels combining in the outlet channel effects the total flow rate as each inlet channel is plumbed to its own programmable syringe pump. Therefore the hardware limitations only apply to a single inlet stream and the maximum possible flow rate is incrementally raised with the addition of inlet streams.

$$v_z = \frac{\sum_{i=1}^{n} Q_i}{A} \qquad\qquad 4\text{-}23$$

The maximum and minimum flow rate are defined by the hardware limitations of the programmable syringe pump. The hardware limitation of the New Era Pump Systems programmable syringe pump defines the maximum and minimum flow rates for the as-fabricated system.

$$1.67 \times 10^{-3} \; \frac{mL}{min} \;\; \leq \; Q_i \; \leq \; 2.00 \; \frac{mL}{min} \qquad\qquad 4\text{-}24$$

The outlet channel is a capillary tip with a circular cross-section. The hydraulic diameter is proportional to the ratio of the cross sectional area to the perimeter. The hydraulic diameter for a capillary tip is equal to the diameter of the tip.

$$D_h = \frac{4A}{P} = D \qquad\qquad 4\text{-}25$$

Tips are purchased a prefabricated set of steel capillary tips.

$$\begin{aligned} D_{min} &= 150 \; \mu m \\ D_{max} &= 2000 \mu m \end{aligned} \qquad\qquad 4\text{-}26$$

The cross-sectional area of the capillary tip outlet is a function of the diameter.

$$A = \frac{\pi D^2}{4} \qquad\qquad 4\text{-}27$$

Combining equation 4-3, 4-4 and 4-9 to define the kinematic viscosity as an explicit function of the total flow rate in the outlet of all the combined inlet materials and the hydraulic diameter.

$$v > \frac{4}{Re_l \pi} \frac{\sum_{i=1}^{n} Q_i}{D^2} \qquad\qquad 4\text{-}28$$

The syringe pump produces a flow rate and inertial forces on the working solution. The maximum and minimum inertial force caused by the system is defines by the hardware limitation

of the pump and the hydraulic diameter of the cross-section. The hydraulic diameter of a capillary

tip is the diameter. Maximum and minimum fluid velocity defined in equation 4-29 and 4-30.

$$v_{z,min} = \left(\frac{Q}{D_h^2}\right)_{min} = \frac{\sum_{n=1}^3 Q_{min}}{D_{c,max}^2} = 2.09 \times 10^{-5} \frac{m}{s} \qquad \textit{4-29}$$

$$v_{z,max} = \left(\frac{Q}{D_h^2}\right)_{max} = \frac{\sum_{n=1}^3 Q_{max}}{D_{c,max}^2} = 4.44 \ \frac{m}{s} \qquad \textit{4-30}$$

The maximum inertial force produced by the programmable syringe pump through the outlet

channel is defined by the hardware limits and the geometry of the channel. The maximum and

minimum kinematic viscosity to maintain laminar flow is defined in equation 4-31 and 4-32.

$$v_{max} = \frac{4 \, D_{c,min} \, v_{z,max}}{\pi Re_l} = 3.69 \times 10^{-7} cSt \qquad \textit{4-31}$$

$$v_{min} = \frac{4D_{c,max} \, v_{z,min}}{\pi Re_l} = 2.31 \times 10^{-11} cSt \qquad \textit{4-32}$$

Selection criteria for the working material rheology to maintain laminar flow in the

combined flow outlet channel is presented in equation 4-33.

$$v = \begin{cases} < 2.31 \times 10^{-11} cSt & \rightarrow & \textit{Never Laminar Flow} \\ 2.31 \times 10^{-11} < v < 3.69 \times 10^{-7} cS & \rightarrow & V = \frac{Q}{D_h} > \frac{4v}{\pi Re_l} \\ > 3.69 \times 10^{-7} cSt & \rightarrow & \textit{Always Laminar Flow} \end{cases} \qquad \textit{4-33}$$

Material rheology, flow rate and capillary diameter are tuned to maintain laminar flow

through print head capillary tip. Hardware limitation for maximum and minimum flow rate and

capillary diameter bound inertial forces of flowing fluid. Working solution rheology bounds

viscous forces of the system. Kinematic viscosity increases linearly with alginate density in solution

from 0.94 and 1.69 cSt for 0.1 and 0.75 g/L respectively (Gomez-Diaz & Navaza, 2003). Kinematic

viscosity of water decreases linearly with temperature from 1.00 and 0.65 cSt for 20ºC and 40ºC

respectively. The rheology of calcium chloride cross-linking solution and buffer solutions are approximated as water.

4.3.2   Inertial and incompressible thresholds coupled by Mach number

The material properties are a function of the inertial forces in the system to maintain subsonic flow The Mach number defines a criteria to determine the significance of compressibility in a flowing fluid. The Mach number is the ratio of inertial to compressive forces in a fluid (Shajii & Freidberg, 1996).

$$M = \frac{inertial\ forces}{compressibility\ forces} \qquad\qquad 4\text{-}34$$

The Mach number characterizes the effect of compressibility as negligible (incompressible) and significant (compressible), as shown in equation 4-35. Negligible compressible effects are less than 5% change in density per volume, equation 4-36.

$$M = \left\{ \begin{array}{lll} M < 0.3 & Subsonic & Incompressible \\ 0.3 < M < 0.8 & Subsonic & Compressible \\ 0.8 < M < 1.2 & Transonic & Compressible \end{array} \right\} \qquad\qquad 4\text{-}35$$

$$M < 0.3 \rightarrow \frac{d\rho}{dV} < 5\% \qquad\qquad 4\text{-}36$$

The circumstances which define the range of inertial forces in the system are determined by the hardware limitation of the programmable syringe pump and cross-sectional area of the channel. The acoustic velocity expressed with Hook's Law is a function of the material modulus and density, equation 4-37.

$$M = \frac{v_z}{c} = \frac{fluid\ speed}{speed\ of\ sound} = \frac{\sum_{i=1}^{n} Q_i}{A} \sqrt{\frac{\rho}{E}} \qquad\qquad 4\text{-}37$$

The criteria for subsonic incompressible flow defines the inertial to compressive ratio for the system (equation 4-36) and closed form analytical definition for Mach number (equation 4-37) combine to produce equation 4-38.

$$0.3 > M = \frac{\sum_{i=1}^{n} \dot{Q}_i}{A_c} \sqrt{\frac{\rho}{E}} \qquad \text{4-38}$$

The maximum and minim fluid velocity are determined from the fundamental process and geometric parameters. The feasible set of bulk modulus is defined by the Mach number and system parameters. The minimum bulk modulus for subsonic flow under any flow rate is determined from the minimum fluid velocity, assuming one fluid stream (n=1). The minimum bulk modulus for subsonic flow under any flow rate is determined from the maximum fluid velocity, assuming three streams (n=3). Equation 4-39 and 4-40 present the minimum and maximum bulk modulus for incompressible flow through the SMMB deposition head.

$$E_{min} > \rho \left(\frac{\sum_{i=1}^{1} \dot{Q}_{i,min}}{0.3 A_{c,max}} \right)^2 = \rho \left(\frac{V}{0.3} \right)^2 \qquad \text{4-39}$$

$$E_{max} > \rho \left(\frac{\sum_{i=1}^{3} \dot{Q}_{i,max}}{0.3 A_{c,min}} \right)^2 = \rho \left(\frac{V}{0.3} \right)^2 \qquad \text{4-40}$$

The selection criteria for a material based on bulk modulus and density to maintain incompressibility is presented in figure 4-12. The figure presents three regimes, subsonic SMMB deposition head operation under some flow and under all possible flow.
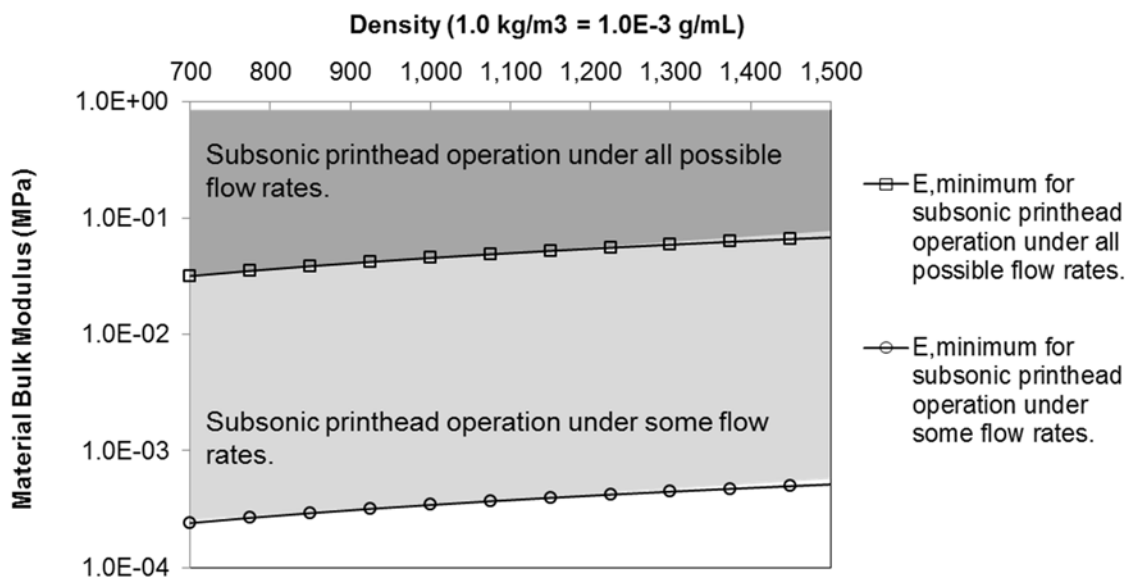
Figure 4-11: Material bulk modulus and density criteria for subsonic flow in printhead.

The bulk modulus and density of common liquids presented in table 4-3 all fall in the subsonic printhead operation under all possible flow rate regime of figure 4-12. Compressibility is not considered a significant factor for common liquids in the SMMB deposition head. Flow through the channels is modeled as incompressible.

Table 4-3: Bulk modulus and density of common liquids from published references.

Material	Temperature °C	Density (ρ) 1.0 kg/m3 = 1.0E-3 g/mL	Bulk Modulus SI Units MPa
Acetone	25	785	920
Benzene	25	874	1,050
Ethyl Alcohol	20	789	1,060
Gasoline	16	737	1,300
Glycerin	25	1259	4,350
Kerosene	16	820	1,300
Mercury	-	13,590	28,500
Petrol, natural	60	711	1,070 – 1,490
Seawater	25	1025	2,340
Water	20	1000	2,150

4.3.3 Control maximum shear stress to achieve permissible level of cell viability

Shear stress in the flowing solution during printing inelastic and elastic defomration to the cell membrane, which diminishes the cell's viability and phenotype stabilty post-printing. The effect of shear stress in the flowing fluid on cell viability is repoduced from a peer reviewed publication by Nair et. al. and is presented in equation 4-41 (Nair et al., 2009).

$$Cell\ Survival \quad \begin{matrix} Y > 90\% & \to & \le & 10\ kPa \\ Y > 80\% & \to & \le & 40\ kPa \\ Y > 70\% & \to & \le & 60\ kPa \\ Y > 60\% & \to & \le & 180\ kPa \end{matrix} \qquad \textit{4-41}$$

Shear stress in the SMMB head will be kept below a threshold levels to maintain a pre-determined standard of cell viability. The maximum shear stress occurs in the smallest orifice, for the print head that is the capillary tip at the outlet. The generalized case of a Non-Newtonian fluid is presented in equation 4-42.

$$\tau_{max} > K\left(\frac{du}{dx}\right)^n \qquad \textit{4-42}$$

The equation for the maximum shear stress of fully developed incompressible laminar flow through a capillary tip is presented in equation 4-43 (Nair et al., 2009).

$$\tau_{max} > K\left(\frac{8Q}{\pi D^3}\right)^n \qquad \textit{4-43}$$

Equation 4-43 is algebraically manipulated to explicity present the flow rate, equation 4-44. The flow rate is a combination of n individually controlled material inputs.

$$\sum_{i=1}^{n} Q_{i,max} < \frac{\pi D^3}{8}\left(\frac{\tau_{max}}{K}\right)^{1/n} \qquad \textit{4-44}$$

For a three material input design, the individual flow rate of any one material to induce a predetermined limit of cell damage is defined by equation 4-45.

$$Q_{i,max} < \frac{\pi D^3}{24}\left(\frac{\tau_{max}}{K}\right)^{1/n} \qquad\qquad 4\text{-}45$$

Sodium alginate aqueous solution is the cell-laden delivery matrix material used during SMMB cell printing. The rheology of alginate and water are derived from literature and presented in table 4-4.

Table 4-4: Sodium alginate aqueous solution and water consistency coefficient and index. Reference are 1(S. E. D. Khalil, 2005) or 2 (Rezende, Bartolo, Mendes, & Maciel, 2009).

Material	Concentration w/v	Consistency Coefficient (K Pa s^n)	Consistency Index (n)	Ref
Sodium alginate aqueous solution	1.0 %	0.610	0.66	1
	1.5 %	1.259	0.70	1
	2.0 %	2.010	0.78	1
	2.0 %	2	0.87	2
	3.0 %	8.587	0.76	1
	3.0 %	6	0.84	2
	5.0 %	28	0.84	2
Water 30°C	-	0.798	1	-

The effect of the maximum allowable individual flow rate is calculated for several concentrations of sodium alginate and water using equation 4-45 and rheological properties presented in table 4-4. The SMMB hardware limit for the flow rate is 2.0 mL/min. Results are presented in table 4-5. The maximum hardware limit is significantly less than the flow limit to produce cell viability less than 90%. Theoretically, SMMB printed cell-laden models presents greater than 90% viability.

Table 4-5: Maximum individual flow rate through SMMB to maintain design specific cell viability, represented as a percentage of surviving cells.

Cell Viability	Maximum Individual Flow Rate (mL/min)					
	Water	Alg 1.0%	Alg 1.5%	Alg 2.0%	Alg 3.0%	Alg 5.0%
> **90**%	66.4	1.29×10^4	1.98×10^3	2.91×10^2	57.4	5.80
> **80**%	2.66×10^2	1.05×10^5	1.43×10^4	1.72×10^3	3.56×10^2	30.2
> **70**%	3.99×10^2	1.95×10^5	2.56×10^4	2.89×10^3	6.06×10^2	49.0
> **60**%	1.20×10^3	1.03×10^6	1.23×10^5	1.18×10^4	2.57×10^3	1.81×10^2

The effect of the flow rate on cell viability is experimentally evaluated using HepG2 cells (ATCC) in 0.5% (w/v) sodium alginate collected after printing using variable flow rates. After printing, cell viability is detected using metabolic indicator alamar blue. The fluorescent intensity after 4 hours is not significantly different for the control or any printed sample. The printing process and the selection of flow rate had no significant effect on the relative metabolic activity (linearly related to cell number), results presented in figure 4-13. Therefore, the SMMB depostion head is a feasible method to print live cells.
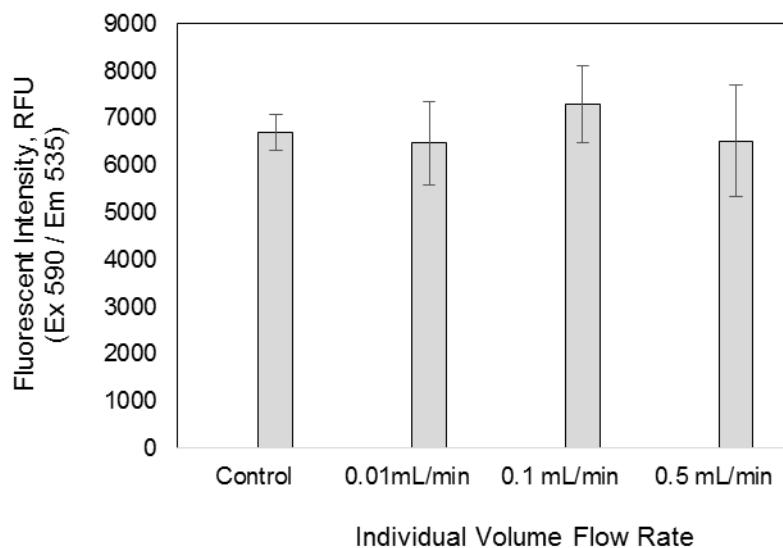
Figure 4-12: Fluorescent intensity of Alamar blue after 4hrs of incubation with printed cell-laden samples and an un-printed control group.

4.4 *Process parameters as a function of the design variables*

4.4.1 Cross-sectional area of a fully developed flow

An individual material's volume fraction of a cross-sectional area in the combined flow outlet is proportional to the fraction of the material's flow rate over the total flow rate. The cross-sectional area of an individual material, A_i, as a fraction of the total channel cross-section, A_C, is proportional to the material's flow rate, Q_i, as a fraction of the total flow rate of n individual material streams.

$$\frac{A_i}{A_c} = \frac{Q_i}{\sum_{i=1}^{n} Q_i} \qquad 4\text{-}46$$

For a three input system with three independently controllable flow rates the fraction of the total cross-section area occupied by each material is presented in equation 4-47, 4-48 and 4-49.

$$\frac{A_1}{A_c} = \frac{Q_1}{(Q_1 + Q_2 + Q_3)} \qquad 4\text{-}47$$

$$\frac{A_2}{A_c} = \frac{Q_2}{(Q_1 + Q_2 + Q_3)} \qquad 4\text{-}48$$

$$\frac{A_3}{A_c} = \frac{Q_3}{(Q_1 + Q_2 + Q_3)} \qquad 4\text{-}49$$

The average velocity of flow in the channel is the deposition velocity from the SMMB deposition head to the substrate. The deposition velocity, v_d, is a function of the total flow rate and total cross-sectional area, as presented in equation 4-50.

$$v_d = \frac{(Q_1 + Q_2 + Q_3)}{A_c} = \frac{Q_1}{A_1} = \frac{Q_2}{A_2} = \frac{Q_3}{A_3} \qquad 4\text{-}50$$

4.4.2 Area fraction as a function of internal geometry of multi-material outlet channel

The cross-sectional area is specific to the size and shape of the channel cross-section. A generalized equation for the area of a circular, full or half elliptical cross-section is derived using a shape coefficient, major and minor axis. A full ellipse is four quadrants ($\omega = 4$) when the center of ellipse is mapped to the center of a Cartesian coordinate system. A half ellipse is two quadrants ($\omega = 2$) when the center of ellipse is mapped to the center of a Cartesian coordinate system. Figure 4-13 presents the schematic of the fully developed non-mixing flow through the combined outlet channel of the SMMB deposition head. The flow design is 3 material axisymmetric flow. The figure 4-13 schematic presents the variable cross-section shapes and reference geometries utilized in the derived model
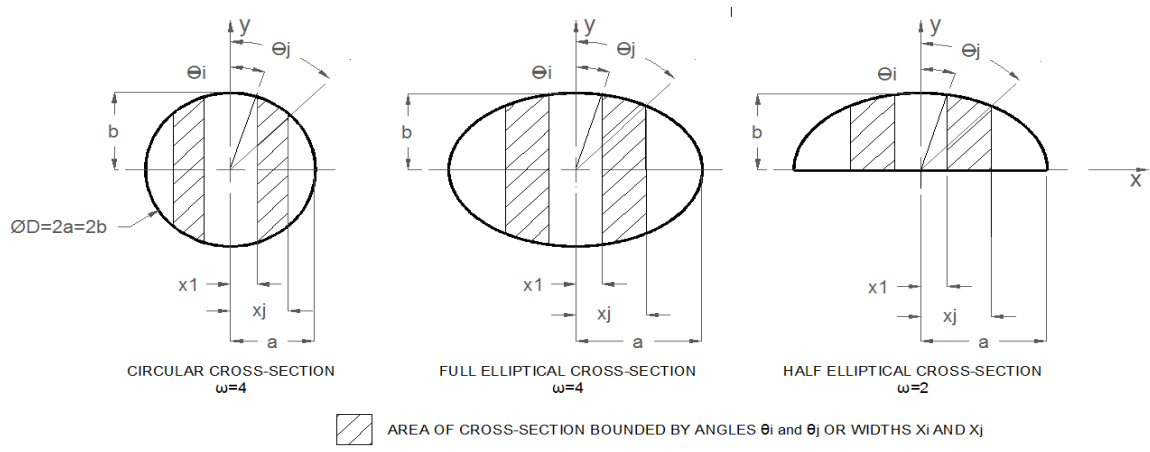
Figure 4-13: Fully developed non-mixing flow through the combined outlet channel of theSMMB deposition head. Schematic presents variable cross-section shapes and reference geometries utilized in the derived model.

For the generalized case of an elliptical cross-section the x- and y- coordinates of the perimeter are related by the major and minor axis, as presented in equation 4-51.

$$\frac{x^2}{a^2} + \frac{y^2}{b^2} = 1 \qquad\qquad 4\text{-}51$$

The standard form is algebraically manipulated to express the y coordinate on the perimeter of the ellipse as a function of the geometry and x-coordinate, as presented in equation 4-52.

$$y = \frac{b}{a}\sqrt{a^2 + x^2} \qquad\qquad 4\text{-}52$$

The area of a fraction of an ellipse bounded by i and j is the integration between two locations along the x-axis, , as presented in equation 4-53.

$$A_{ij} = \int_{x_i}^{x_j} y(x)dx \qquad\qquad 4\text{-}53$$

The definite integral is bounded by the geometric limits of the ellipse, as presented in equation 4-54.

$$0 \leq x_i < x_j \leq a \qquad\qquad 4\text{-}54$$

The area is for one quadrant of the cross-section. The area is multiplied by the number of quadrants to determine the total area. The number of quadrants is either 2 for a half ellipse or 4 for a full ellipse, as defined in equation 4-55.

$$\omega = 2, 4 \qquad\qquad 4\text{-}55$$

The area of an elliptical cross-section or fraction thereof partitioned symmetrically from the minor axis as shown in figure 4-13 is presented in equation 4-56.

$$A_{ij} = \omega \int_{x_i}^{x_j} \frac{b}{a}\sqrt{a^2 + x^2} \; dx \qquad\qquad 4\text{-}56$$

Cartesian coordinates are converted to polar coordinates for the integration. The conversions are summarized as presented in equations 4-57, 4-58 and 4-59.

$$x = a \sin \theta \qquad\qquad 4\text{-}57$$

$$dx = a \cos \theta \, d\theta \qquad\qquad 4\text{-}58$$

$$0 \leq \theta_i < \theta_j \leq \frac{\pi}{2} \qquad\qquad 4\text{-}59$$

The area in terms of polar coordinate is a combination of the area integral (eqaution 4-56) and cartesian to polar identities (equations 4-57, 4-58 and 4-59), as presented in equation 4-60.

$$A_{ij} = \omega \int_{\theta_i}^{\theta_j} \frac{b}{a} \sqrt{a^2 - (a \sin \theta)^2} \, (a \cos \theta) \, d\theta \qquad\qquad 4\text{-}60$$

Equation 4-60 is simplified to equation 4-61.

$$A_{ij} = ab\omega \int_{\theta_i}^{\theta_j} \sqrt{1 - (\sin \theta)^2} \, (\cos \theta) \, d\theta \qquad\qquad 4\text{-}61$$

Euclidean geometry's Pythagorean Theorem defines a right triangle's lengths and angles in the function presented in equation 4-62.

$$1 - \sin^2 \theta = \cos^2 \theta \qquad\qquad 4\text{-}62$$

The area function is simplified using Pythagorean Theorem is equation 4-63.

$$A_{ij} = ab\omega \int_{\theta_i}^{\theta_j} \cos^2 \theta \, d\theta \qquad\qquad 4\text{-}63$$

Considering the following trigonometric identity from the Double-angle formula presented in equation 4-64.

$$\cos^2 \theta = \frac{1}{2}(1 + \cos 2\theta) \qquad\qquad 4\text{-}64$$

The area function is simplified as presented in equation 4-65:

$$A_{ij} = \frac{ab\omega}{2} \int_{\theta_i}^{\theta_j} 1 + \cos 2\theta \ \ d\theta \qquad \qquad 4\text{-}65$$

The area function in polar coordinates is presented in equation 4-66:

$$A_{ij} = \frac{ab\omega}{2} \left[\theta + \frac{\sin 2\theta}{2} \right]_{\theta_i}^{\theta_j} \qquad \qquad 4\text{-}66$$

The Double Angle Theorem is identified in equation 4-67:

$$\sin 2\theta = 2 \sin \theta \cos \theta \qquad \qquad 4\text{-}67$$

Equation 4-66 and 4-67 are combined to form equation 4-68.

$$A_{ij} = \frac{ab\omega}{2} [\theta + \sin \theta \cos \theta]_{\theta_i}^{\theta_j} \qquad \qquad 4\text{-}68$$

Polar and Cartesian coordinates are related by trigonometry derived from schematic shown in figure 4-13 and defined by equations 4-69, 4-70 and 4-71.

$$\theta = asin\frac{x}{a} \qquad \qquad 4\text{-}69$$

$$\sin \theta = \frac{x}{a} \qquad \qquad 4\text{-}70$$

$$\cos \theta = \sqrt{1 - \sin^2\theta} = \sqrt{1 - \frac{x^2}{a^2}} = \frac{1}{a}\sqrt{a^2 - x^2} \qquad \qquad 4\text{-}71$$

The area function in Cartesian coordinates is presented in equation 4-72:

$$A_{ij} = \frac{ab\omega}{2} \left[asin\frac{x}{a} + \frac{x}{a^2}\sqrt{a^2 - x^2} \right]_{x_i}^{x_j} \qquad \qquad 4\text{-}72$$

The area of a bounded portion of the cross-section is equation 4-73.

$$A_{ij} = \frac{ab\omega}{2}\left(asin\left(\frac{x_j}{a}\right) - asin\left(\frac{x_i}{a}\right) + \frac{1}{a^2}\left(x_j\sqrt{a^2 - x_j{}^2} - x_i\sqrt{a^2 - x_i{}^2}\right)\right) \qquad \textit{4-73}$$

The cross-section of material 1, 2 and 3 are defined as equation 4-74, 4-75 and 4-76.

$$A_1 = A_c\,(0 \le x \le x_1)\ = \frac{ab\omega}{2}\left(asin\left(\frac{x_1}{a}\right) + \frac{x_1}{a^2}\sqrt{a^2 - x_1{}^2}\right) \qquad \textit{4-74}$$

$$A_2 = A_c\,(x_1 \le x \le \frac{D_{1,2}}{2})$$

$$A_2 = \frac{ab\omega}{2}\left(asin\left(\frac{D_{1,2}}{2a}\right) + \frac{D_{1,2}}{2a^2}\sqrt{a^2 - \frac{D_{1,2}^2}{4}} - asin\left(\frac{x_1}{a}\right) - \frac{x_1}{a^2}\sqrt{a^2 - x_1{}^2}\right) \qquad \textit{4-75}$$

$$A_3 = A_c\,(\frac{D_{1,2}}{2} \le x \le a)\ = \frac{ab\omega}{2}\left(\frac{\pi}{2} - asin\left(\frac{w_{1,2}}{2a}\right) - \frac{w_{1,2}}{2a^2}\sqrt{a^2 - \frac{w_{1,2}^2}{4}}\right) \qquad \textit{4-76}$$

4.4.3 Flow rate as a function of the design variable reaction time

Equation 4-15 presents the reaction time as function of the outlet channel length, cross-sectional area and flow rate, as previously presented. The deposition speed of material from the outlet is equal to the flow rate divided by the cross-sectional area, either for the total channel or a fraction of the channel a single material occupies. Equation 4-16 is algebraically manipulated to be an explicit function of reaction time, equation 4-77.

$$t_R = \frac{A_c L}{Q_1 + Q_2 + Q_3} = \frac{A_1 L}{Q_1} = \frac{A_2 L}{Q_2} = \frac{A_3 L}{Q_3} \qquad \textit{4-77}$$

Equation 4-77 and equation 4-76, the area fraction of material three as a function of the geometric parameters, are combined to present the flow rate of material 3, the cross-linking solution, as a function of process and geometric parameters, equation 4-78.

$$Q_3 = \frac{ab\omega L}{4\,t_R}\left(\pi - asin\left(\frac{w_{1,2}}{2a}\right) - \frac{w_{1,2}}{2a^2}\sqrt{a^2 - \frac{w_{1,2}^2}{4}}\right) \qquad \text{4-78}$$

4.4.4 Flow rate as a function of the design variables

The deposition speed of the combined material flow or portion of the flow are equal. Consequently the ratio of material 3 flow rate to cross-sectional area is equal to either (1) the same ratio of material 1 or 2 OR (2) the combination material 1 and 2, presented by equation 4-79.

$$\frac{Q_3}{A_3} = \frac{Q_1 + Q_2}{A_c - A_3} \qquad \text{4-79}$$

The design variable volume fraction defines the ratio of material 1 to material 2, derived from equation 4-6 to produce 4-80.

$$Q_1 = \gamma_{12}Q_2 \qquad \text{4-80}$$

The flow rate for a three inlet material axisymmetric array where each solution is independently controlled by a programmable syringe pump as a function of design variables and geometric is presented in equation 4-81, 4-82 and 4-83.

$$Q_1 = \frac{ab\omega L\gamma_{12}}{2(1+\gamma_{12})t_R}\left(asin\left(\frac{w_{1,2}}{2a}\right) + \frac{w_{1,2}}{2a^2}\sqrt{a^2 - \frac{w_{1,2}^2}{4}}\right) \qquad \text{4-81}$$

$$Q_2 = \frac{ab\omega L}{2(1+\gamma_{12})t_R}\left(asin\left(\frac{w_{1,2}}{2a}\right) + \frac{w_{1,2}}{2a^2}\sqrt{a^2 - \frac{w_{1,2}^2}{4}}\right) \qquad \text{4-82}$$

$$Q_3 = \frac{ab\omega L}{2t_R}\left(\frac{\pi}{2} - asin\left(\frac{w_{1,2}}{2a}\right) - \frac{w_{1,2}}{2a^2}\sqrt{a^2 - \frac{w_{1,2}^2}{4}}\right) \qquad \text{4-83}$$

The behavior of variable volume fraction and material 1-2 width is studies using the dimensionless flow rate. Dimensionless variables for flow rate, total channel width and combined material width are presented in equations 4-84, 4-85 and 4-86.

$$Q_i^* = \frac{2t_r Q_i}{abL\omega} \qquad\qquad 4\text{-}84$$

$$a^* = 1 \qquad\qquad 4\text{-}85$$

$$w_{1,2}^* = \frac{w_{1,2}}{a} \qquad\qquad 4\text{-}86$$

The dimensionless flow rate are presented in equation 4-87, 4-88 and 4-89. The equations are plotted to grpahically present the dependence of design variables for volume fraction and the width of center two material streams in a three material axisymmetric flow design. A study of the effect of parametric changes to the volume fraction of two materials in a three material design (as previously described) on the set of flow rates using the derived model is presented in figure 4-15. A study of the effect of parametric changes to the combined width of the central two materials i a three material design (as previously described) on the set of flow rates using the derived model is presented in figure 4-16.

$$Q_1^* = \frac{\gamma_{12}}{(1 + \gamma_{12})}\left(asin\left(\frac{w_{1,2}^*}{2}\right) + \frac{w_{1,2}^*}{2}\sqrt{1 - \frac{\left(w_{1,2}^*\right)^2}{4}} \right) \qquad 4\text{-}87$$

$$Q_2^* = \frac{\gamma_{12}}{(1 + \gamma_{12})}\left(asin\left(\frac{w_{1,2}^*}{2}\right) + \frac{w_{1,2}^*}{2}\sqrt{1 - \frac{\left(w_{1,2}^*\right)^2}{4}} \right) \qquad 4\text{-}88$$

$$Q_3^* = asin\left(\frac{w_{1,2}^*}{2}\right) + \frac{w_{1,2}^*}{2}\sqrt{1 - \frac{\left(w_{1,2}^*\right)^2}{4}} \qquad 4\text{-}89$$
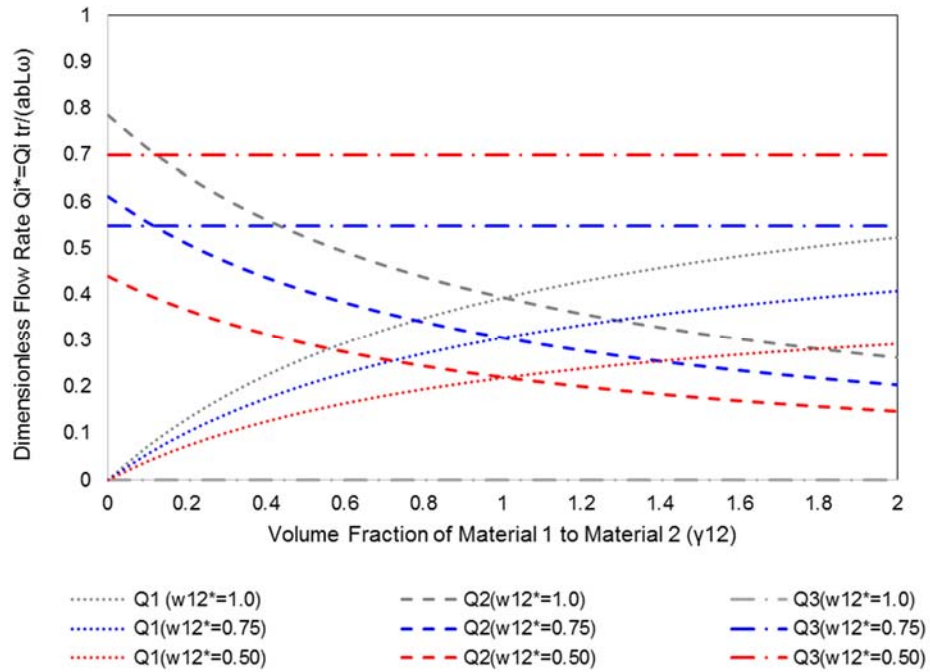
Figure 4-14: Theoretical selection of the dimensionless flow rate to achieve a design-specific volume fraction of material 1 to 2, assuming a total of three material streams.
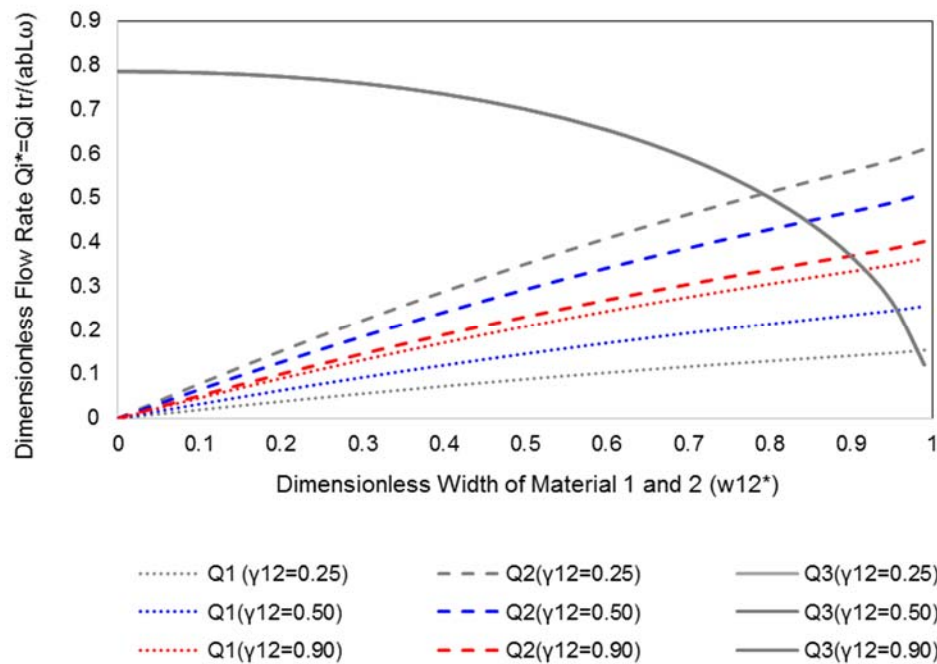
Figure 4-15: Theoretical selection of the dimensionless flow rate to achieve a design-specific dimensional width of the internal two material streams.

4.5   *Comparison of experimental and theoretical results*

Internal features of the heterogeneous array are constructed based on the design of the SMMB deposition head channel network and selection of the process parameter set. The design variables for the internal features can also be dynamically adjusted over the build cycle, as the process parameters can be tuned during fabrication. The width of individual or collections of adjacent material is one such controllable design variable. A parametric study swept through a set of flow rates to decrease the combined width of two materials in an axisymmetric combined outlet channel. Figure 4-16 presents photographs of the three material deposition head. From left to right, the flow rate of red material is increased, the flow rate of green and yellow is maintained constant. The combined width of green and yellow decreases from left to right. The volume fraction of green to yellow is maintained constant, as the flow rates are equal.
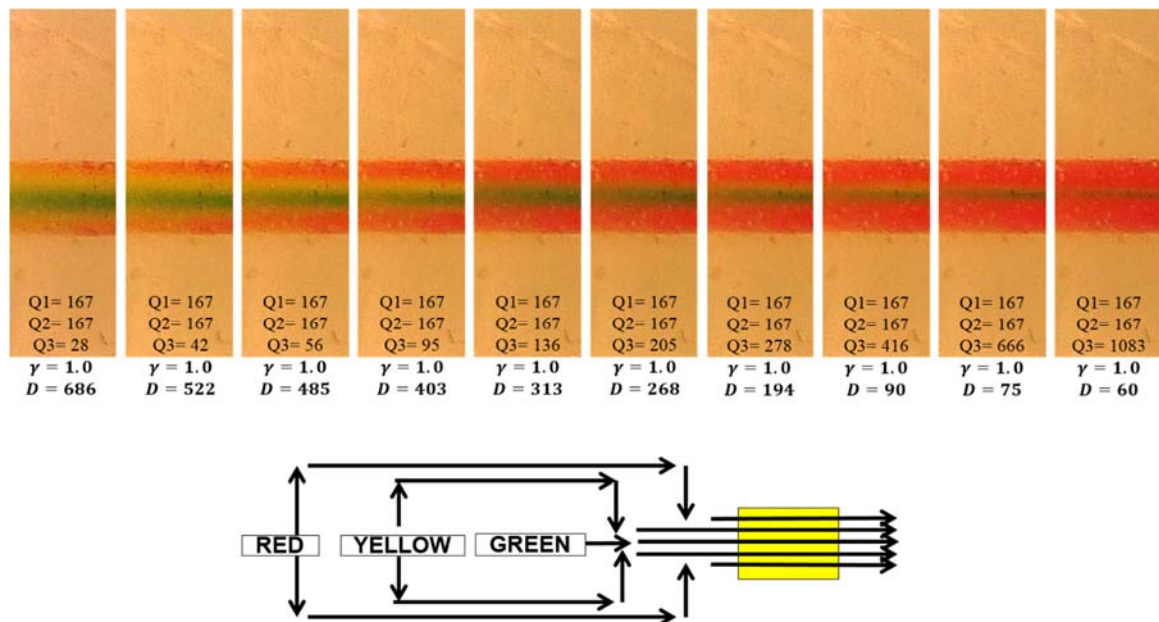
Figure 4-16: Effect of flow rates on architecture of internal feature of heterogeneous flow. Flow rates are numbered from the longitudinal axis beginning with 1 and moving out radially. Flow rates are μL/s and diameter is the width of yellow and green measured in μm.

Experimental result and the derived model are compared in figure 4-17. The trend for theoretical and experimental results agree. Experimental results are quantified using ImageJ (NIH) analysis with the threshold color plug-in for pixel count. The derived collective width of the center two materials in a three material axisymmetric is calculated using equations 4-81, 4-82 and 4-83. The experimental results are directly measured from photogrpahs using the reference system presented in figure 4-9.
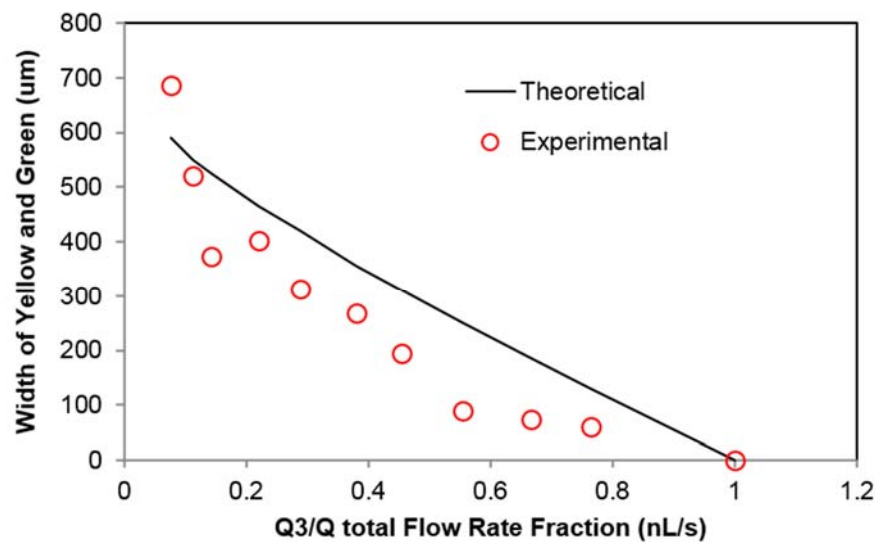
Figure 4-17: Theoretical and experimental effect of volumetric flow rate on width of a combination of two adjacent longitudinally-centered materials in a three-material axisymmetric flow.

The volume fraction of solution can be adjusted, while maintaining the combined width of the two solutions constant. Figure 4-18 presents photographs of the SMMB deposition channel during the volume fraction adjustments. In a second parametric study, the red flow rate is maintained constant and combined flow rate of yellow and green are maintained constant, but the volume fraction of yellow to green is adjusted. From left to right, the volume fraction of green is increased by increasing the proportion of green flow rate to yellow. The total flow rate of yellow

and green is constant. The volume fraction of red is constant throughout the study, as the proportion of red to the total flow rate is constant.
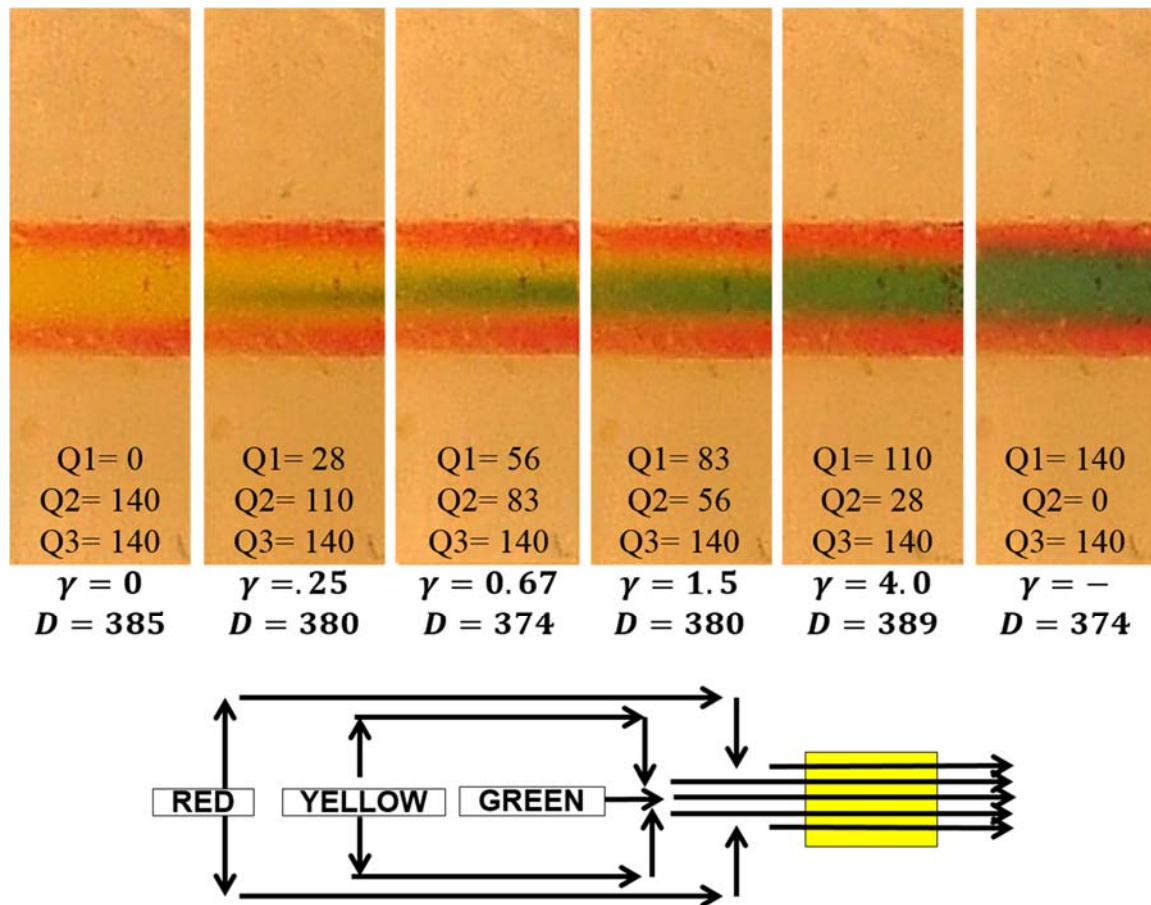
Figure 4-18: Effect of flow rates on architecture of volume fraction of heterogeneous flow. Flow rates are numbered from the longitudinal axis beginning with 1 and moving out radially. Flow rates are µL/s and diameter is the width of yellow and green measured in µm.

Experimental results are quantified using ImageJ (NIH) analysis with the threshold color plug-in for pixel count. The volume fraction defined by the derived model is presented in equation 4-6 and experimental volume fraction from images is presented in equation 4-90.

$$\gamma_{12,experimental} = \frac{\sum pixel_{green}}{\sum pixel_{yellow}} \qquad 4\text{-}90$$

Results are compared in figure 4-19. The trend for theoretical and experimental results agree. Agreement is stronger for flow rate less than 0.05 mL/min, relatively weaker for 0.1 mL/min and again weaker for 0.25 mL/min.
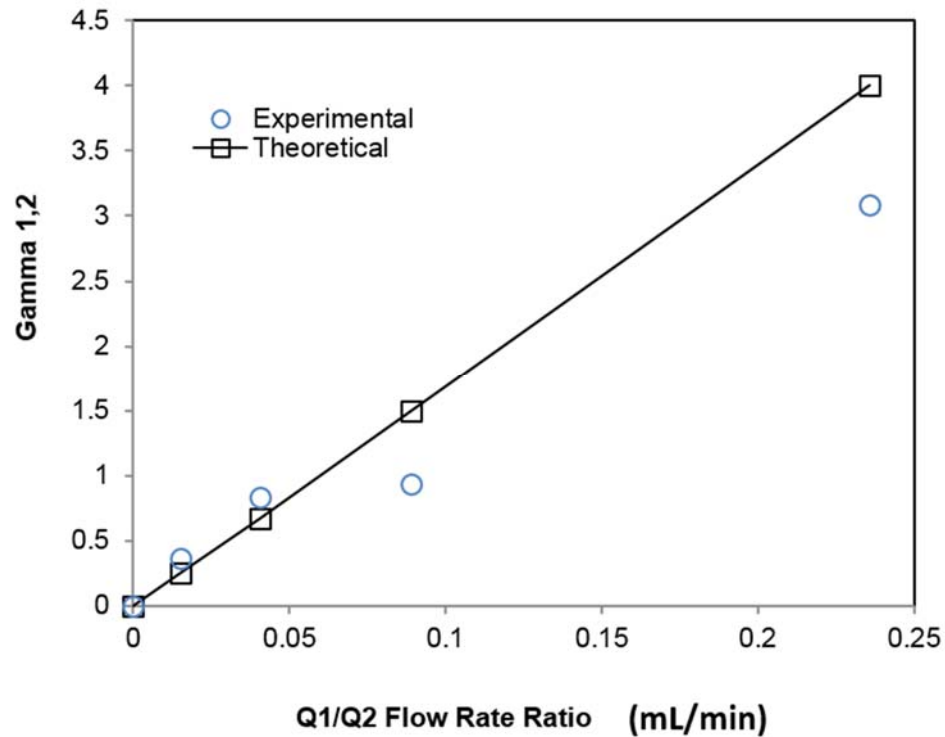
Figure 4-19: Theoretical and experimental effect of volumetric flow rate on volume fraction of two materials in a three-material flow.

4.6   *Advantages of SMMB*

Advantages include of the synchronized multi-material bioprinter (SMMB) include:

1. Improves resolution of existing extrusion based bioprinting: Multiple materials are packaged as a heteregenous array in the SMMDH in a single combined outlet flow without mixing. The pattern of the materials across the combined flow cross-section and volume fraction of the materials are controllable design parameters. Existing bioprinting techniques leverage multiple

nozzles to place each material independently during a buidl cycle. The minimum feature size is constrained by the resolution of the nozzle and motion system hardware. The SMMDH addresses this challenge by combing multiple materials in a single printed filament, thereby decreasing the minimum feature size and improving the resolution of extrusion based bioprinters.

2. Variable volume fraction and internal geomtry of the material array during the build cycle: The flow rate of each material is independently controlled using a programmable and can be varied during the build cycle. Consequently, the design variables for volume fraction is directly controllable by the user interface on the syringe pump. The internal arrangement of the materials is determineed by the design of the open network channel in the SMMDH and also the flow rate.

3. *Controlled chemical reactions for partial cross-linking prior to deposition to minimize fluid flow from the location the material is extruded:* In addition to the constituent materials required in the design, we include cross-linking solution to fully or patrailly gel the aqeuous solution while it is still in the depositoin head. This is advantageous during extrusion as without the cross-linking the aqeuous solution will distort as it flows free from beng released from the outlet channel until it is cross-linked by the subsequent application of a cross-linking solution. Further, the residence time between the cross-linking and aqueous solutions in the deposiiton head is controllable according to the length of the combined outlet channel and flow rate of each material.

4. *Flexibility to fabricate heteregenous nano-liter droplets (torus droplets or solid sphereical droplets) or patterned filaments:* The combined outlet flow is extruded along a 3-dimensional tool path to fabricate either (1) nano-liter droplets or (2) patterned filaments, which with layer-by-layer fabrication produce 3-dimensional volumetric scaffolds. Nano-liter droplets are a more adapatable platform, as the droplet is simpler to design and can be used in many existing bioreactor designs. Heterogenous filaments are desirable for controlled cell seeding in the channels of microfluidic devices and for free-standing scaffold design for regenerative medicine and tissue

engineering applications. To fabricate droplets, the combined flow accumulated on the outlet tip of the SMMDH. The tip is cyclically dipped in a pool of cross-linking solution to produce a droplet on contact. The period of the cycle and flow rate determine the volume of the droplet. The relative flow rate of the materials determine the volume fraction of each constituent material. The cross-linking time is a function of the aqueous solution being printed and cross-linking solution. Once the material accumulated on the outlet tip contacts the cross-linking pool, the accumulated material flows away from the tip as it is being cross-linked. There exists a set of printed material to cross-linking solution concentration which the time required for cross-linking is slightly longer than the time it takes for the material to flow from the tip (leaving a hole in the center of the droplet). This forms a torus shape. There also exists a set of material concetrations where the cross-linking time is slightly less than the time it takes for the material to flow away from the tip and thereby there is no hole and the droplet is a solid sphereical shape. During heteregenous filament printing, the combined flow is extruded from the SMMDH mounted to a motion system on to a stationary substrate. The tool path patterned the extruded material layer-by-layer to build 3-dimensional volumetric structures of hetergenous filaments. Both the nano-liter droplet printing and heteregenous filament printing can be combined a single build cycle to fabricate various structures and artifacts.

CHAPTER 5: CHARACTERIZATION OF THE SYNCHRONIZED MULTI-MATERIAL BIOPRINTING SYSTEM AND APPLICATION

5.1   *Printing filaments and nano-liter droplets with SMMB*

SMMB system packages multiple materials in a heterogeneous array and deposits those materials along a pre-programmed 3-dimensional tool paths. The automation of this process offers two distinct opportunities for formability:

(1) **Heterogamous filaments:** Layer-by-layer fabrication of a free-standing scaffold or controlled cell seeding in channels of a microfluidic device require deposited along a tool path. Multiple deposition heads can be simultaneously integrated in a single SMMB system. Multiple integrated deposition head offer the same benefit as multi-nozzle printing; including supplemental cross-linking solutions or secondary heterogeneous set of materials.

(2) **Heterogeneous nano-liter droplets**: The build cycle period defined by the SMMB motion system controls the frequency of an event to print droplets. Droplet volume is a controllable process parameter.
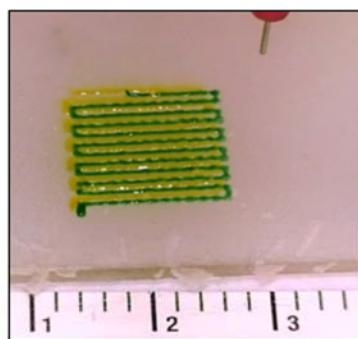
Extrusion along a tool path to
print scaffold.
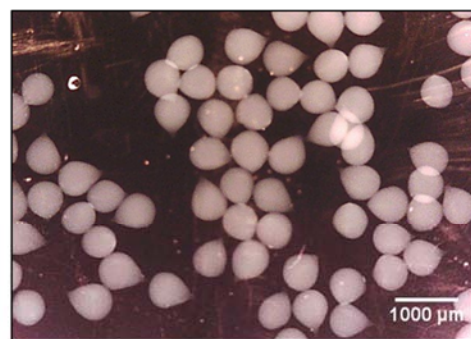
Control the frequency of an
event to print droplets.

Figure 5-1: Photographs of extrusion along a tool path to build a free-standing scaffold (left) and extrusion over a controlled build cycle to print droplets (right).

SMMB's automated material delivery system and motion system produce both filaments and droplets. SMMB scaffold printing improves the resolution of multi-nozzle deposition (MND) printing and offers the combined outlet channel as an opportunity for chemical reactions or mass species transfer during a controlled time interval. Partial or complete cross-linking is one method to leverage the combined outlet channel. SMMB droplet printing produces a simpler product than scaffold printing. However, printed droplets are a more accessible and adaptable technology. Droplets are simpler to design, fabricate and ensure sufficient nutrient diffusion to the cell-laden core. Droplets can also be used in many existing bioreactor platforms. In this work, printed co-culture nano-liter droplets are the model of human liver to study the effect of microgravity on cell morphology and drug up-take using a rotary cell culture system.

5.2   Printing heterogeneous filaments

The synchronized multi-material bioprinter (SMMB) dispensing system is integrated with the existing multi-nozzle deposition (MND) system to continuously extrude heterogeneous filaments along a tool path. SMMB system performance to pattern a heterogeneous filament along a tool path is defined by a set of geometric design variables to control printed filament cross-sectional width/height, reaction time in the outlet channel. Design variables, $\Psi_{SMMB,D}$, is defined by printed filament width, c, and height, d, reation time, t_r, and volume fraction of material i to material j, γ_{ij}. The set of design variables are presented in equation 5-1. The printed filament width and height, reaction time and volume fraction are a function of the process parameters, which are varied over the time course of the build cycle to produce hierarchial and gradient structures. The time variable, t, denotes the parameter are adjustable over the course of the build cycle and consequenly non-static over the full dimensionalty of the built structure.

$$\Psi_{SMMB,F}(t) = \begin{bmatrix} c(t) & d(t) & t_r\,(t) & \gamma_{ij}(t) \end{bmatrix} \qquad\qquad 5\text{-}1$$

SMMB derived, geometric, material, and process parameters have been previously defined

in section 4.2 definition of SMMB process parameters, material properties and design variables.

Table 5-2 presents SMMB droplet printing variables. The set of design variables, geometric and

process parameters are presented in table 5-1 and figure 5-2.

Table 5-1. Synchronized multi-material bioprinter (SMMB) system design variables, derived, geometric, material, and process parameters to print a heterogeneous filament.

Symbol	Description	Process Window	Parameter Type
A	Cross-sectional area of printed filament	-	Derived
a	SMMB deposition head outlet channel width	-	Geometric
b	SMMB deposition head outlet channel height	-	Geometric
c	Printed filament width (parallel to printing substrate)	-	Design
d	Printed filament height (perpendicular to printing substrate)	-	Design
D_c	SMMB deposition head capillary outlet channel diameter	100 150 200 250 330 410 μm	Geometric
n	Number of material streams	-	Design
Q_i	Volume flow rate	$1.67 \times 10^{-3} \leq Q_i \leq 2.00$ mL/min	Derived
t_R	Reaction time between materials in the SMMB outlet channel	-	Design
v	SMMB deposition head speed over printing substrate	$0.1 \leq v \leq 15.0\ mm/s$	Process
z	SMMB deposition head outlet height above printing substrate	$100 \leq z \leq 1000\ \mu m$	Process
ρ_i	Material density	-	Material
$\Psi_{SMMB,F}$	Set of SMMB design variables to print heterogeneous filament		Design
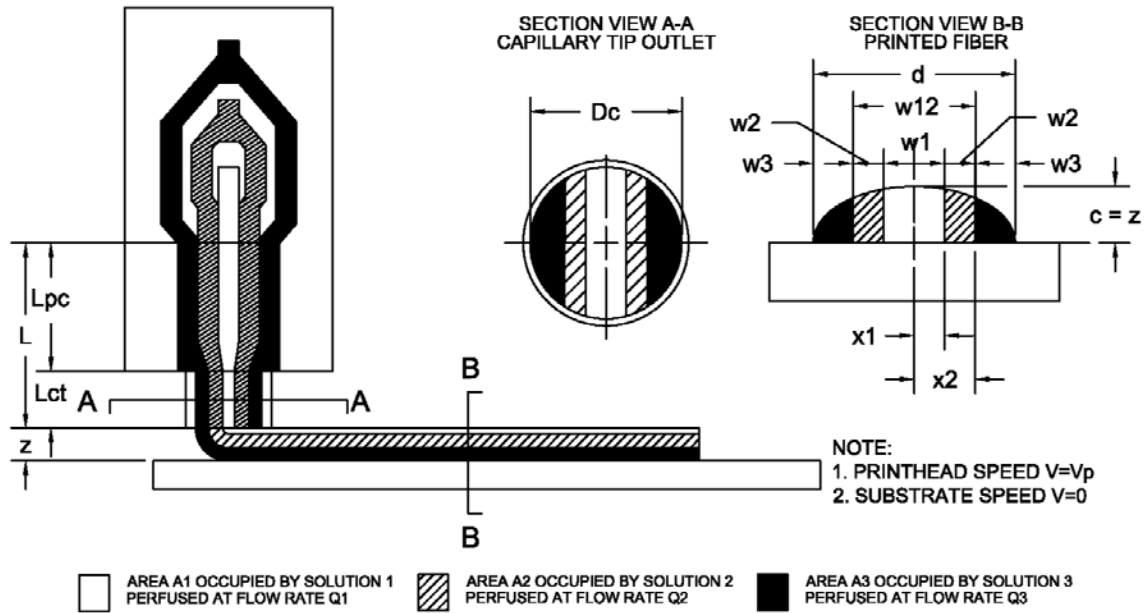
Figure 5-2: Schematic of synchronized multi-material deposition head mounted to motion system printing heterogonous line with process control of the volume fraction of each material and internal architecture of printed filament.

The flow from the printhead accumulates in an elliptical fiber on the substrate, as presented in equation 2-42 reprinted below.

$$\left(\frac{dm}{dt}\right)_{from\ material\ delivery\ system} = \left(\frac{dm}{dt}\right)_{substrate\ accumulation} = \rho_i Q_i$$

Flow from the SMMB deposition system is combination of the flow rate of each material. An independently controlled three material case is presented in equation 5-2.

$$\left(\frac{dm}{dt}\right)_{from\ SMMB\ deposition\ system} = \sum_{i=1}^{n} Q_i \rho_i = Q_1 \rho_1 + Q_2 \rho_2 + Q_3 \rho_3 \qquad 5\text{-}2$$

The accumulation of material on the substrate along the tool path is defined by the cross-sectional area of the printed filament and print head speed, equation 5-3.

$$\left(\frac{dm}{dt}\right)_{substrate\ accumulation} = v(A_1\rho_1 + A_2\rho_2 + A_3\rho_3) \qquad\qquad 5\text{-}3$$

SMMB hardware is not capable of generating the inertial force required for compressible flow. The continuity model is augmented in favor of control volume analysis, equation 5-2 and 5-3 combine to produce equation 5-4.

$$Q_1 + Q_2 + Q_3 = vA \qquad\qquad 5\text{-}4$$

The cross-section of the printed structure is modeled as an ellipse defined by a major axis (parallel to the printing substrate) and minor axis (perpendicular to the printing substrate), presented in equation 5-5.

$$A = \frac{\pi cd}{4} \qquad\qquad 5\text{-}5$$

The minor axis of the printed filament is controllable as long as it is greater than the major axis, as presented in section 2.3.3.3.1 printhead speed selection for a set of design variables. The SMMB printed filament width is a function of process parameters for flow rate, deposition head traveling speed and the height of the outlet above the printing substrate. The design variable printed filament width is an explicit function of process parameters in equation 5-6, a combination of equation 5-4 and 5-5.

$$c = \frac{4}{\pi vz}(Q_1 + Q_2 + Q_3) \qquad\qquad 5\text{-}6$$

Equation 4-15 defines the total flow rate as a function of design parameter reaction length and the geometric parameters outlet channel length and cross-sectional area. The deposition head traveling speed defined as a function of the geometric and design variables is presented in equation 5-7, a combination equation 4-15 and 5-5. The process parameter deposition head traveling speed as an explicit function of the (1) design variables printed filament cross-sectional width/height and

reaction time and (2) geometric parameters SMMB deposition head outlet channel cross-section width/height and channel length. Equation 5-7 is a predictive tool to define the deposition head traveling speed based on a set of design variables for the printed filament and the geoemtric parameters of the SMMB deposition head's combined flow outlet channel.

$$v = \frac{abL}{cdt_R} \qquad \textit{5-7}$$

Equation 5-7 is the general case of an elliptical outlet channel defined by the major and minor axis. The specific case of a capillary channel outlet is equation 5-8.

$$v = \frac{D_c^2 L}{cdt_R} \qquad \textit{5-8}$$

Heterogeneous printed filament in square wave pattern printed using bioprinter and a multi-material deposition head with two inlet channels of red and green solution. Figure 5-3 presents a photograph of the printed alginate filament in square wave pattern (A) and binary contrast enhancement of green (B) and red (C) alginate are shown.
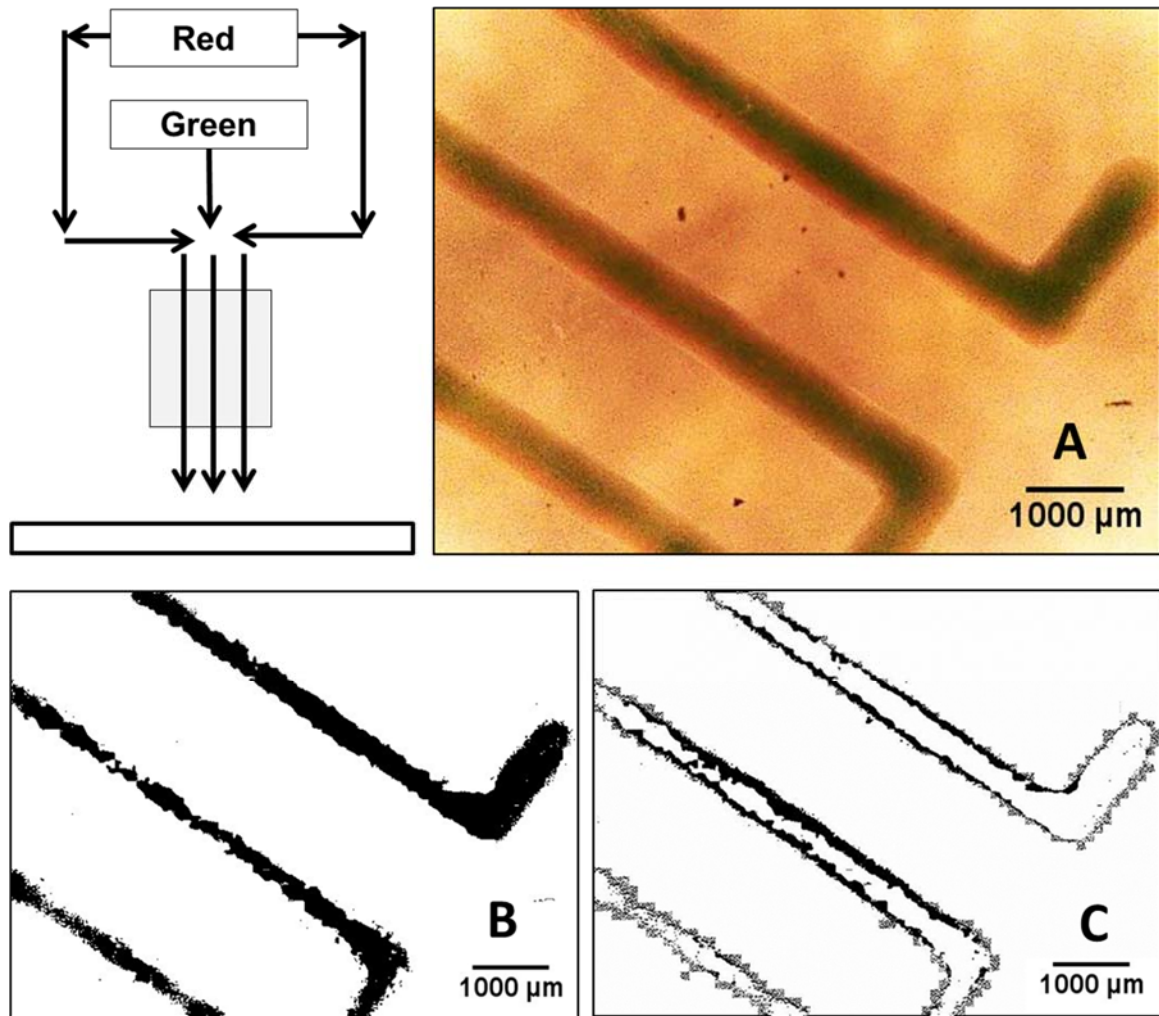
Figure 5-3: Heterogeneous printed filament in square wave pattern printed using bioprinter and a multi-material deposition head with two inlet channels of red and green solution. Schematic of the microfluidic network in multi-material deposition head depicts the red and green flows are combined in a single outlet channel. Bioprinter's motion system carries the deposition head over the stationary substrate to produce the square wave pattern. Photograph of the printed alginate filament in square wave pattern (A) and binary contrast enhancement of green (B) and red (C) alginate are shown.

5.3 *Printing heterogeneous nano-liter droplets*

5.3.1 Description of process and variables

The SMMB material delivery system's flow rate controls the nano-liter volume which accumulates on the outlet of the outlet tip. The motion system introduces cyclic motion to dip the accumulated material in a cross-linking reservoir. The process is specifically suited for a chemically

cross-linking matrix; such as sodium alginate cross-linked with calcium chloirde. Sodium alginate aqueous solutions of alginic acid sodium salt from brown algae (Sigman et al.) and cross-linking solution of ACS grade calcium chloride are prepared from distilled water, respectively. Alginate solution is loaded into SMMB material delivery system and cross-linking solution floods the reservoir pool positioned below the printing tip. SMMB deposition head outlet tip is lowered to less than 100µm above cross-linking pool. The programmable syringe pump extrudes alginate through the deposition head. The alginate accumulates on the tip, until contact with the cross-linking reservoir. On contact, the droplet is released from the tip and gels to form an alginate pool in the cross-linking reservoir. The build cycle period, or time to printing one droplet, is adjusted using the process parameters to fabricate variable size droplets. Figure 5-4 presents a schematic of the process stages and figure 5-5 presents time-lapse photographs of one print cycle.
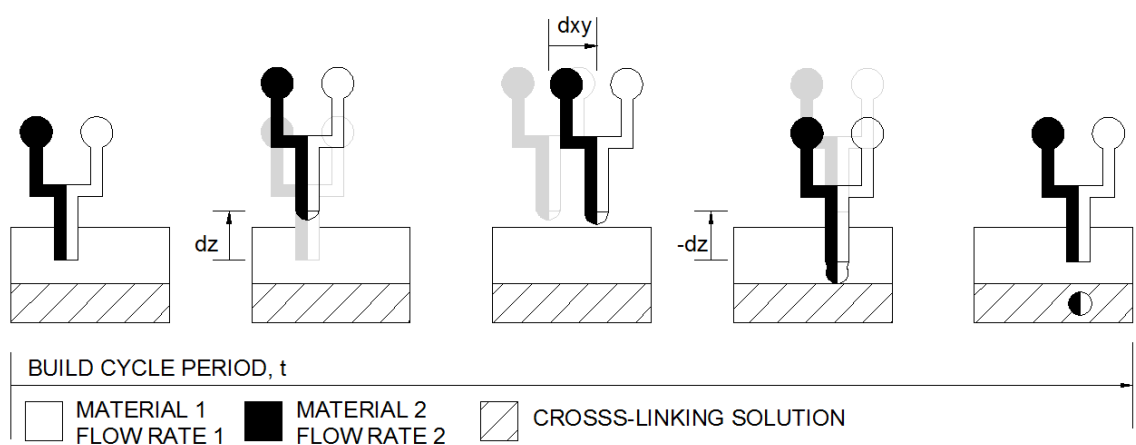
Figure 5-4: Schematic of SMMB droplet printing process using two materials.
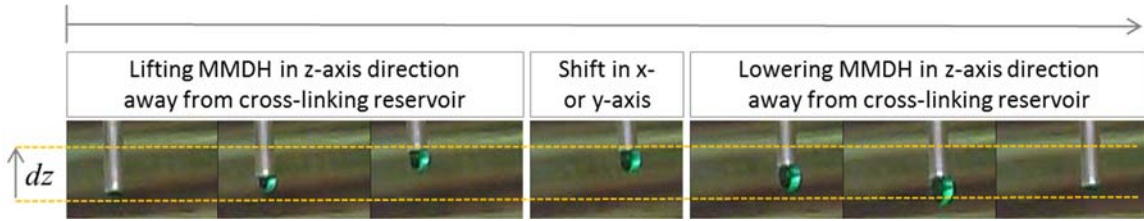
Figure 5-5: Time lapse photo of single build cycle printing droplet Process schematic for printing droplets using

SMMB system performance to print nano-liter droplets is defined by a set of geometric design variables to control droplet size and volume fraction of the constituent materials. Design variables, $\Psi_{SMMB,D}$, is defined by reaction time in the SMMB deposition head combined outlet channel, t_R, droplet volume, V_D, and volume fraction of material i to material j, γ_{ij}. The set of nano-liter droplet design variables is presented in equation 5-9.

$$\Psi_{SMMB,D} = \begin{bmatrix} t_R & V_D & \gamma_{ij} \end{bmatrix} \qquad \textit{5-9}$$

The complete set of SMMB process parameters are amended to print droplets to include the displacement and speed in the x-, y- and z-direction and the flow rate of each material input, as presented in equation 5-10.

$$\Omega_{SMMB,D}(t) = \begin{bmatrix} d_x & & v_x \\ d_y & Q_i & v_y \\ d_z & & v_z \end{bmatrix} \qquad \textit{5-10}$$

SMMB derived, geometric, material, and process parameters have been previously defined in section 4.2 definition of SMMB process parameters, material properties and design variables. Table 5-2 presents SMMB droplet printing variables.

Table 5-2. Synchronized multi-material bioprinter (SMMB) system design variables, derived, geometric, material, and process parameters to print a heterogeneous nano-liter droplet.

Symbol	Description	Process Window	Parameter Type
A	Cross-sectional area of printed droplet	-	Derived
d_x	Displacement in x-direction	$100 \leq d \leq 1000\ \mu m$	Process
d_y	Displacement in y-direction	$100 \leq d \leq 1000\ \mu m$	Process
d_z	Displacement in z-direction	$100 \leq d \leq 1000\ \mu m$	Process
D_c	SMMB deposition head capillary outlet channel diameter	100 150 200 250 330 410 μm	Geometric
D_P	Printed droplet diameter		Derived
n	Number of material streams	-	Design
Q_i	Volume flow rate	$1.67 \times 10^{-3} \leq Q_i \leq 2.00\ \mathrm{mL/min}$	Derived
t_B	Build cycle period, time to print one droplet	-	Derived
t_R	Reaction time between materials in the SMMB outlet channel	-	Design
v_x	SMMB deposition head traveling speed in x-direction	$0.1 \leq v \leq 15.0\ mm/s$	Process
v_y	SMMB deposition head traveling speed in y-direction	$0.1 \leq v \leq 15.0\ mm/s$	Process
v_z	SMMB deposition head traveling speed in z-direction	$0.1 \leq v \leq 15.0\ mm/s$	Process
V_D	SMMB printed droplet volume	-	Design
γ_{ij}	Volume fraction of i material to j material	-	Design
ρ_i	Material density	-	Material
$\Psi_{SMMB,D}$	Set of SMMB droplet printing design variables	-	Design
$\Omega_{SMMB,D}$	Set of SMMB droplet printing process parameters	-	Process

5.3.2 Theoretical printed droplet volume and volume fraction

The accumulation of material at the outlet of the SMMDH is a function of the flow rate through the printhead and the period of the build cycle. The build cycle period and flow rate are independent derived parameters, which can be independently tuned through process parameters to fabricate nano-liter droplets. The droplet volume of a two material SMMB printed droplet is a

function of the process parameter flow rate, design parameter volume fraction, and derived parameter build cycle period, as presented in equation 5-11.

$$V_D = Q_2(1 + \gamma_{12})t_B \qquad \textit{5-11}$$

The build cycle period is the amount of time material accumulates at the tip between dispensing droplets. The trajectory of the SMMB is discretized into several movements, each along a single axis, as presented in equation 5-12.

$$t_B = \sum_{i=1}^{3} \frac{d_i}{v_i} = \frac{d_x}{v_x} + \frac{d_y}{v_y} + \frac{d_z}{v_z} \qquad \textit{5-12}$$

The printhead speed and distance in x- and y-axis are equal. Additionally, motion occurs in either the x- or y-axis and only as a single movement per build cycle. The variables for x- and y-axis movement are combined into a single variable. Equation 5-13 and 5-14 present the process parameter for x- and y-axis speed and distance, respectively, as a single variable.

$$v_{xy} = v_x = v_y \qquad \textit{5-13}$$

$$d_{xy} = d_x = d_y \qquad \textit{5-14}$$

The z-axis movement occurs twice for each build cycle; once to lift the SMMB tip away from the cross-linking reservoir and once to bring the SMMB tip back in contact with the reservoir to print droplet, as presented in equation 5-15.

$$t_B = \frac{d_{xy}}{v_{xy}} + \frac{2d_z}{v_z} \qquad \textit{5-15}$$

The change in height in the z-direction (away from the cross-linking pool surface and then back to the surface) must be greater than the diameter of the droplet to prevent contact and uncontrolled dispense during the build cycle. The printed droplet is modeled as sphere to define the

minimum z-direction shift must be greater than the droplet diameter, defined as a function of the droplet volume, as presented in equation 5-16.

$$d_z > \sqrt[3]{\frac{6V_D}{\pi}} \qquad\qquad 5\text{-}16$$

Droplet aggregation during printing due to repeated deposition on the same site is diminished by moving during the build cycle. This step is not mandatory if the reservoir is agitated causing the droplet to separate on their own. The minimum and maximum x- or y- direction displacement are zero and the hardware limit, as presented in equation 5-17.

$$0 \le d_{xy} \le 1000 \ \mu m \qquad\qquad 5\text{-}17$$

Equations 5-11 and 5-15 combine to define the printed droplet volume as a function of the process parameters for flow rate, tool path length and deposition head traveling speed and design variables for the volume fraction of the two materials, as presented in equation 5-18.

$$V_D = Q_2(1 + \gamma_{12})\left(\frac{d_{xy}}{v_{xy}} + \frac{2d_z}{v_z}\right) \qquad\qquad 5\text{-}18$$

The theoretical effect of the process parameters and design parameter for volume fraction of material 1 to material 2 on the printed droplet volume are defined by equation 5-18. The effect of independent variable on the printed droplet volume are further examined in figure 5-6. The flow rate of material 2 and printed droplet volume are directly proportional. Further, the volume fraction is also directly proportional to the printed droplet volume. The distance along any of the three axis is proportional to the printed droplet volume, as it will increase build cycle period. The speed in any direction is inversely related to the printed droplet volume.
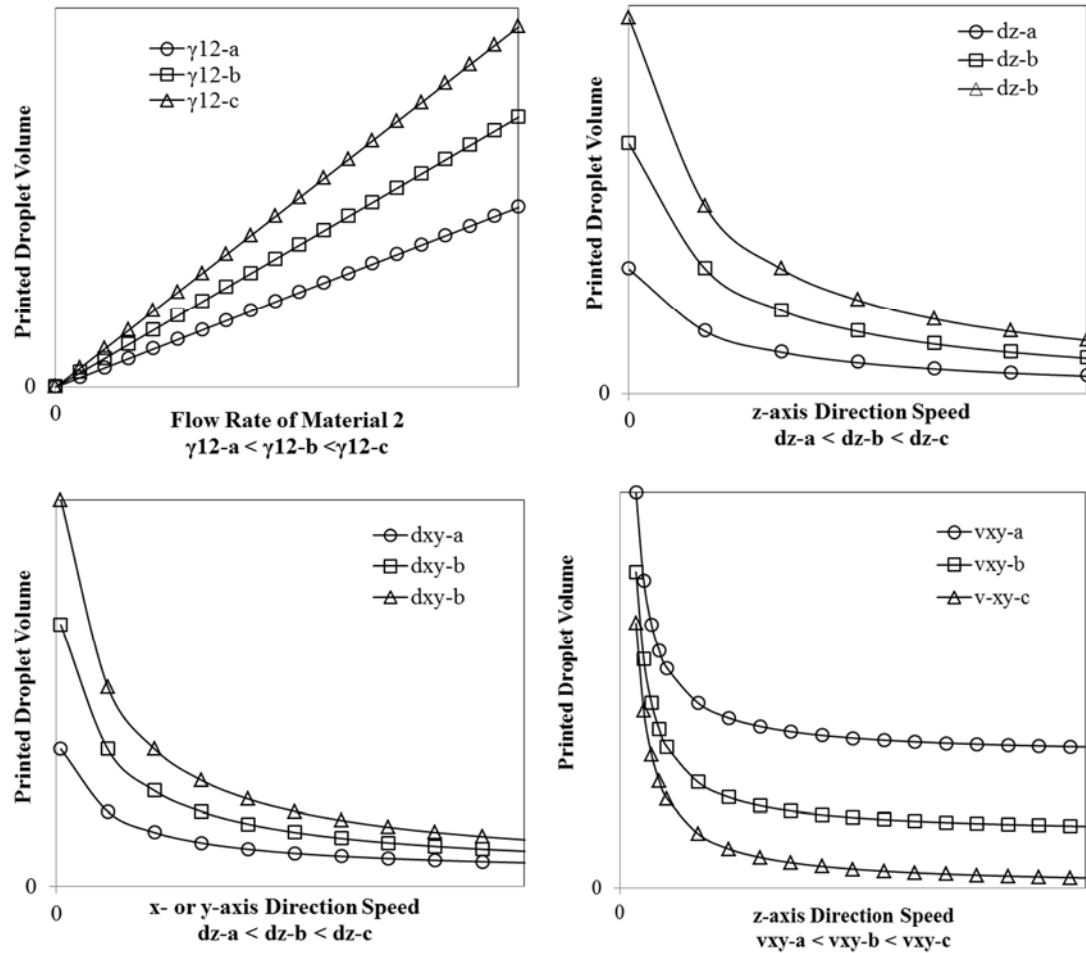
Figure 5-6: Theoretical effect of process parameters and design parameter for volume fraction of material 1 to material 2 on printed droplet volume.

5.3.3 Printing heterogeneous droplet

Material accumulates on the tip of the deposition head as a nano-liter droplet. Photographs of the accumulating droplet are analyzed for mixing. A homogenous droplets presents red coloring. The heterogeneous droplets presents both red and green coloring. The two colors are presented on discrete sides of the droplet. Figure 5-7 presents the droplet and color threshold images.
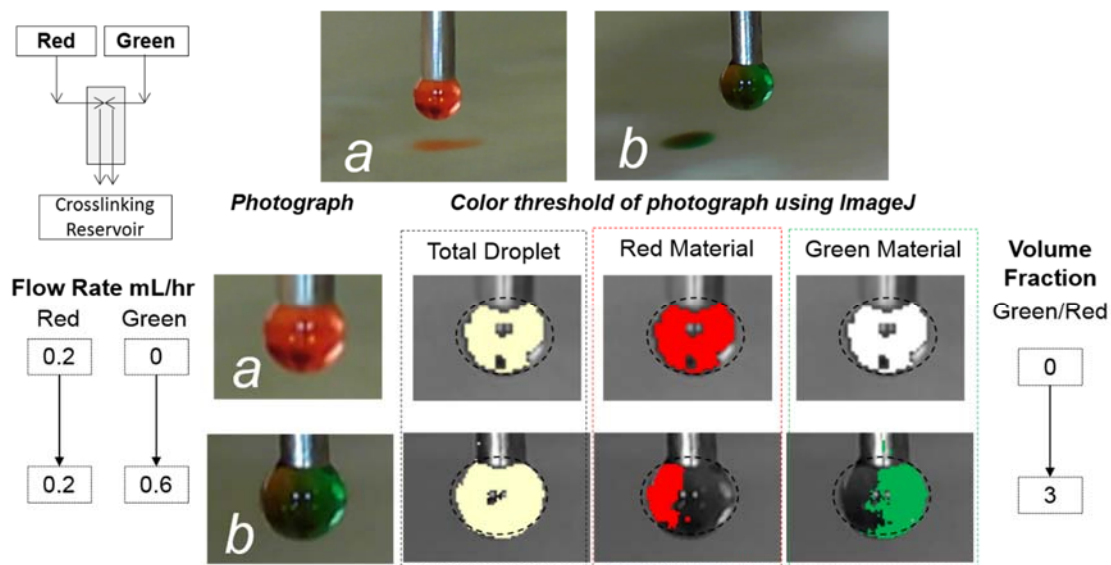
Figure 5-7: Photographs of red and green alginate accumulating on tip of deposition head as nanoliter droplet. Photographs are color threshold to present separate streams of red and green as heterogeneous

5.3.4   Effect of cross-linking solution concentration on droplet formability

The success of droplet formability requires the alginate gel in the cross-linking bath before dispersing in the bath due to the inertial force the printing process. The inertial forces of the flowing fluid degrades the droplet's spherical structure before gelation, if the cross-linking concentration is low. Aqueous alginate solution will flow until sufficient time in contact with cross-linking solution causes gelation. Further, printed droplet solidity (torus or sphere) are generated by controlled the cross-linking time. Cross-linking time is a function of the alginate and calcium chloride concentration. Cross-linking concentration is increased 0.2-1.0 g/mL calcium chloride in distilled water. Alginate concentration is constant 0.5% (w/v) throughout the study. The length of time required for cross-linking is inversely related to the concentration of the crossing solution, for a given concentration of alginate. Time lapse photography of the droplet dispensing into the cross-linking pool present the effect of cross-linking solution concentration on formability of droplets and the ability to produce torus structures. Figure 5-8 presents alginate dispersed into 0.2 g/mL calcium chloride. The printed material flow away from the deposition point and degrades any

printed structure. Further perturbation of the cross-linking reservoir will cause the droplet to twist and lose all recognizable shape.
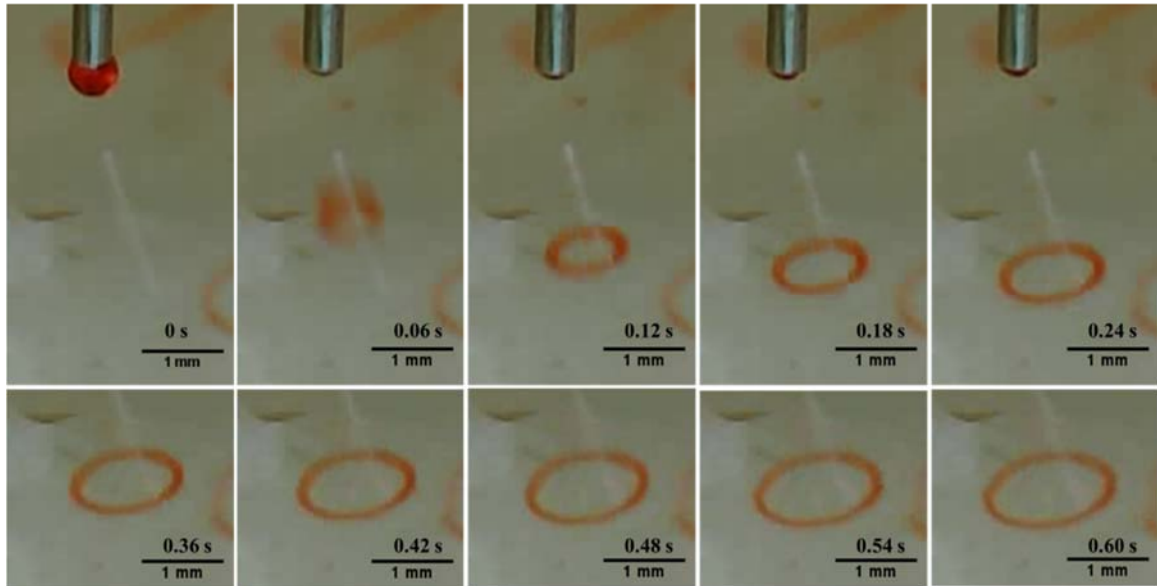
Figure 5-8: Time lapse photography of printed 0.5% (w/v) sodium alginate droplet in 0.2 g/mL calcium chloride cross-linking reservoir forming an unstable ring. Each photograph is 0.06 seconds apart. Calibration mark is 1 mm.

Figure 5-9 presents alginate dispersed into 0.3 g/mL calcium chloride. The printed material flow away from the deposition point. The droplet is cross-linked before the structure completely degrades. However, the alginate had sufficient time to flow away from the deposition point, leaving a material void in the center of the printed structure. The results is a printed torus droplet.
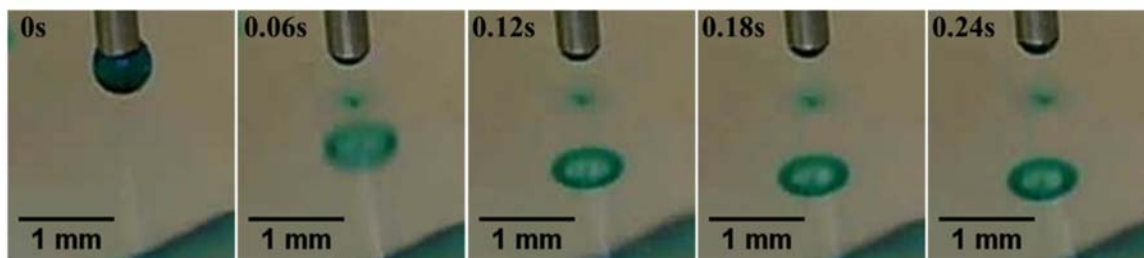
Figure 5-9: Time lapse photography of printed 0.5% (w/v) sodium alginate droplet in 0.3 g/mL calcium chloride cross-linking reservoir forming a stable torus. Each photograph is 0.06 seconds apart. Calibration mark is 1 mm.

Figure 5-10 presents alginate dispersed into 0.5 g/mL calcium chloride. The printed material gels as it is deposited in the cross-linking reservoir. Material void in the center of the printed droplet is not apparent. The results is a printed spherical droplet.
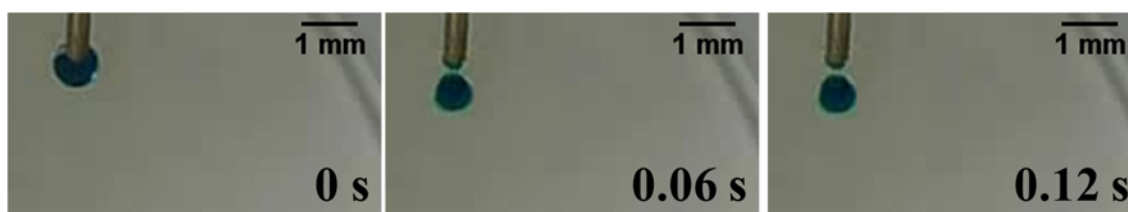
Figure 5-10: Time lapse photography of printed 0.5% (w/v) sodium alginate droplet in 0.5 g/mL calcium chloride cross-linking reservoir forming a stable solid droplet. Each photograph is 0.06 seconds apart. Calibration mark is 1 mm.

Figure 5-11 presents alginate dispersed into 1.0 g/mL calcium chloride. The printed material gels on contact with the cross-linking bath. The printed material does not have sufficient time to sink into the cross-linking bath to form a sphere shape. The shallow disc is an unstable shape. Any perturbations to the cross-linking bath cause the shallow disc to twist and lose all recognizable shape.
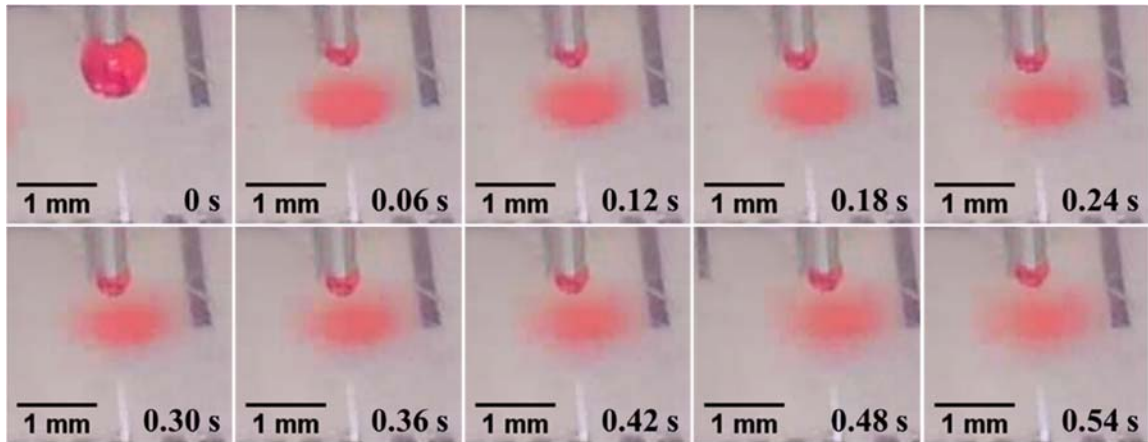
Figure 5-11: Time lapse photography of printed 0.5% (w/v) sodium alginate droplet in 1.0 g/mL calcium chloride cross-linking reservoir forming a stable solid droplet. Each photograph is 0.06 seconds apart. Calibration mark is 2 mm.

The feasible set of cross-linking concentration for printing 0.5% (w/v) sodium alginate range from 0.3-1.0% (w/v) calcium chloride. Alginate disperses into the cross-linking reservoir too quickly to gel for concentration less than 0.3%. Conversely, alginate gels too quickly in concentration greater than 1.0% to become submerged and cross-linked from all sides of the sinking droplet. Torus droplets (partial flow away from the deposition site) and spherical droplets (solid in appearance) are a consequence of the cross-linking concentration, as presented in figure 5-12. Further control of droplet solidity and symmetry may be controllable with a more in-depth study of the concentration.
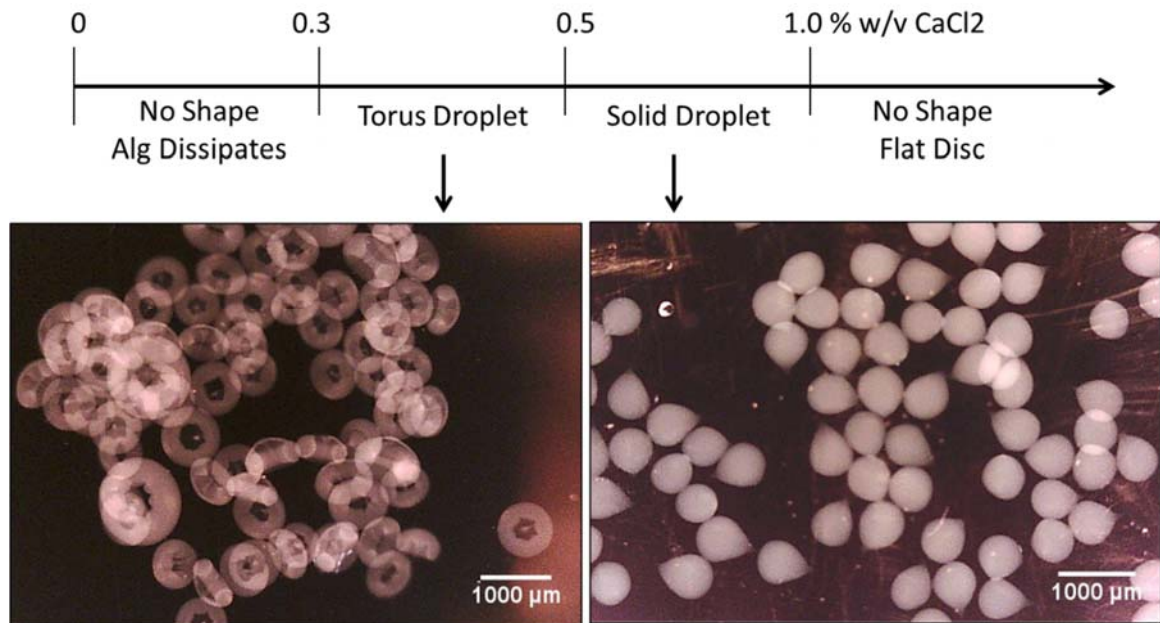
Figure 5-12: Effect of cross-linking solution concentration on solidity of printed droplets. Two of the four process windows successfully fabricate stable droplets. The two extreme process windows, 0-0.30g/L and >1.00 g/L calcium chloride result in no shape.

5.3.5   Comparison of theoretical and experimental printed droplet volume.

The derived model of droplet volume as a function of the process parameters is compared to experimental results. Solution are prepared and loaded into the SMMB material delivery system syringe pump for controlled extrusion during the build cycle. In this work, sodium alginate aqueous solutions of alginic acid sodium salt from brown algae (Sigman et al.) and cross-linking solution of ACS grade calcium chloride are prepared from distilled water, respectively. Droplets are single material inlet 0.5% (w/v) sodium alginate printed into 0.5% (w/v) calcium chloride cross-linking solution. Sets of 200 individual droplets with volumes 200-600 nL are fabricated by SMMB in a single build. Figure 5-13 presents photographs of the printed droplets from each variable volume set.
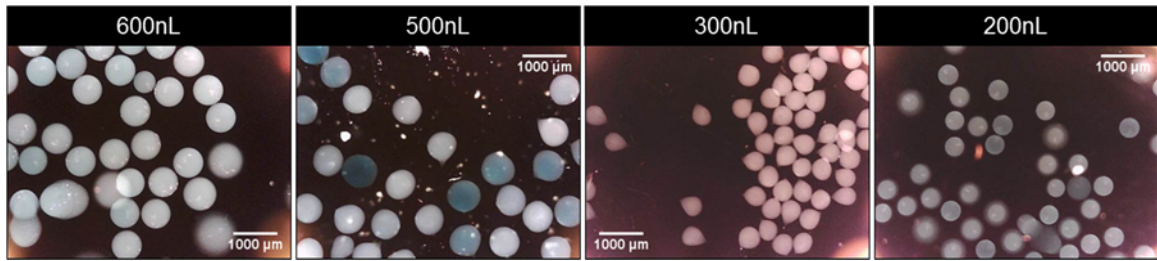
Figure 5-13: Photographs of 20-30 individual droplets of variable volume 4printed droplet ranging from 200-600nL.

Photographs of the printed droplets analyzed by ImageJ (NIH) color threshold plug-in. Each photograph is planar view of the droplets. Figure 5-14 presents photographs of the printed droplets. Area of each droplet measured using binary images.
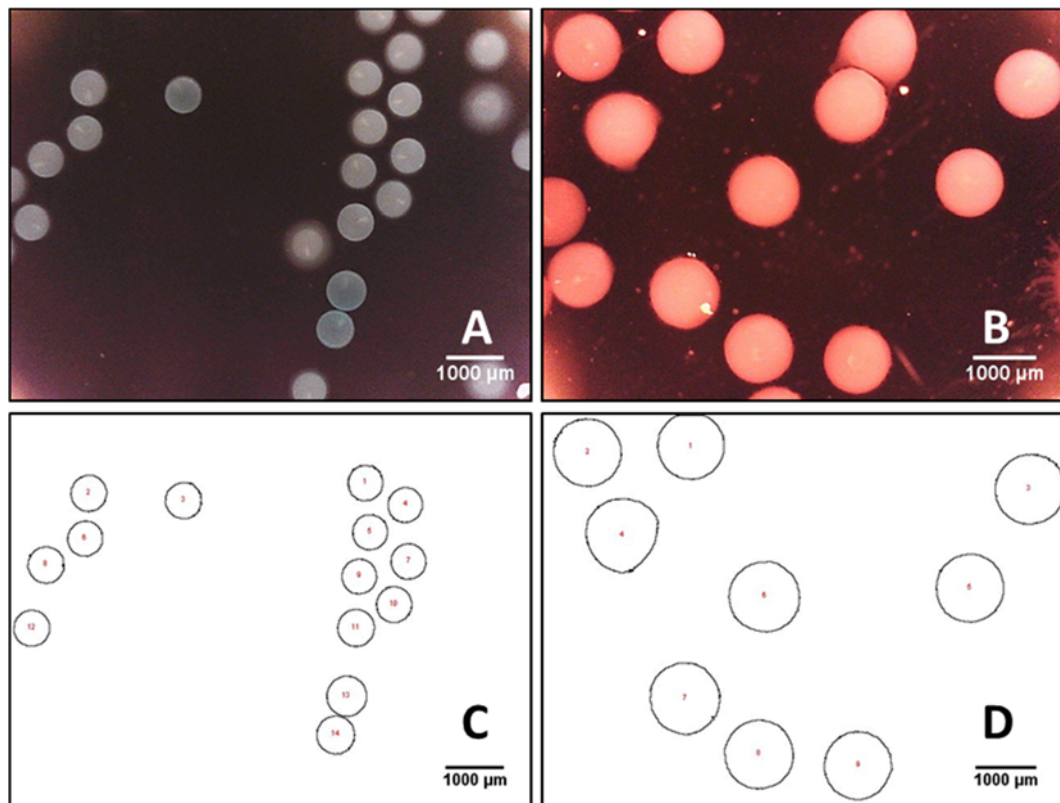
Figure 5-14: Photograph of 200 (A) and 600 (B) nL printed droplets. Outlines of binary contrast enhancement of 200 (C) and 600 (D) nL printed droplets using photographs A and B respectively.

Droplets are modeled as a sphere to estimate the printed volume from the measured area. The experimental volume is calculated from the measured area, equation 5-19. Equation 5-20 for a single material input is equation 5-18 amended for a single material defined by a single flow rate, equation 5-17. The derived model for droplet volume (equation 5-20) and calculated volume from experimental results (equation 5-19) are compared in figure 5-15.

$$V_{D,experimental} = \frac{4}{3\sqrt{\pi}} (A_{measured})^{3/2} \qquad\qquad 5\text{-}19$$

$$V_{D,theoretical} = Q \left(\frac{d_{xy}}{v_{xy}} + \frac{2d_z}{v_z} \right) \qquad\qquad 5\text{-}20$$
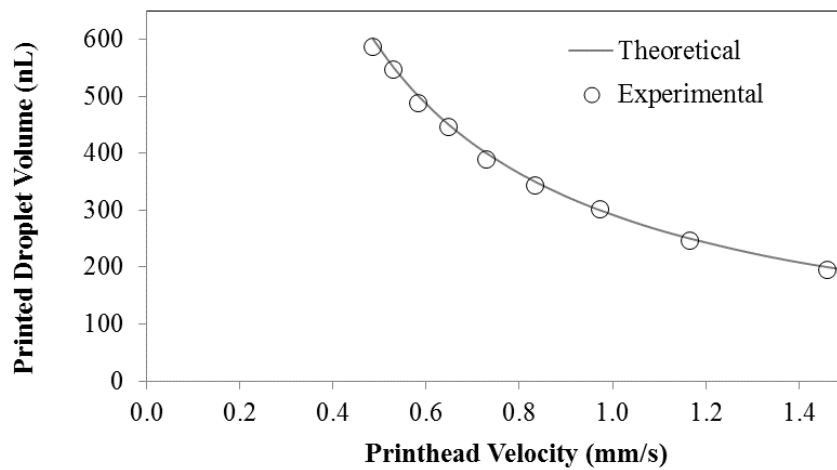
Figure 5-15: Comparison of the theoretical and experimentally measured effect of the controllable process parameter. Printhead velocity refers to speed in the z-direction. No movement occurs in the x- or y-direction for this study.

Each printed droplet volume set (200, 300, 500 and 600 nL) contains 200-300 individual droplets. The experimental printed droplet diameter is calculated from the measured droplet area, equation 5-21.

$$D_{P,experimental} = 2\sqrt{\frac{A_{measured}}{\pi}} \qquad\qquad 5\text{-}21$$

The probability distribution function of each measured printed droplet diameter is presented in figure 5-16. Distinct peaks for each droplet diameter are observed for each droplet volume set.
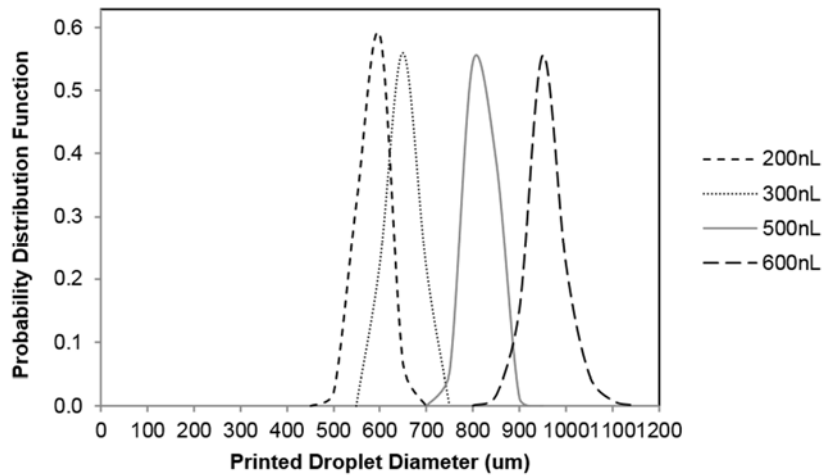
Figure 5-16: Probability distribution function of printed droplet diameter

The cumulative distribution function of the droplet circularity is directly measured from the binary photographs of fabricated result, figure 5-17. Circularity varied from 0.70 to 1.00 (fully circular) for all surveyed printed volumes. Droplets vary from 0.70-1.00 (completely circular) circularity. The probability a printed droplet will be more than 0.90 circular increases as droplet volume increases from 200 to 600 nL.
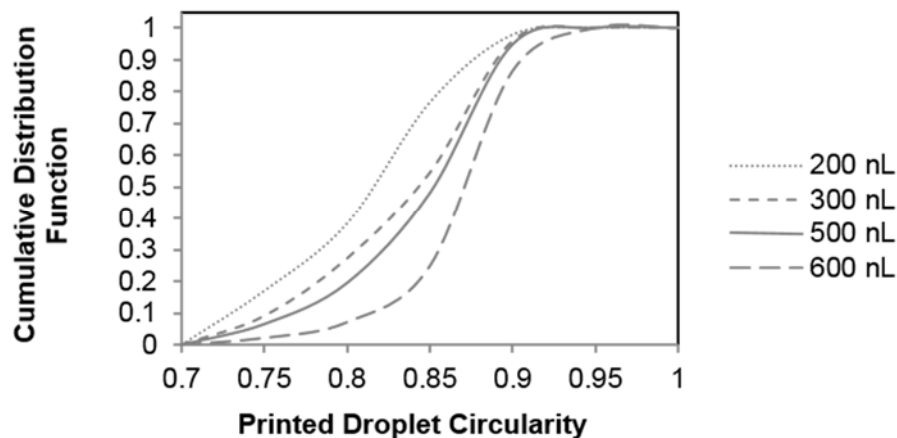
Figure 5-17: Cumulative distribution function of printed droplet circularity for 200, 300, 500, and 600 nL volumes.

5.4   *Effect of model microgravity on hetero-cellular liver model*

5.4.1   **Rationale for study**

5.4.1.1   *Objective*

Gravitational forces or the lack thereof effect dispersion of interstitial fluids in the body, cell secretion and therefore biochemistry of tissues, gene expression, and volume of individual organelles (Baqai et al., 2009b; Khaoustov et al., 2001; Talbot et al., 2010a). NASA's space life science enterprise studies cell function in microgravity to prepare clinical dosing requirements and pharmacological thresholds for long term manned space exploration. The objective of this work is to study the effect of co-culture and model microgravity using a printed hetero-cellular nano-liter droplet and rotary cell culture system. Printed hetero-cellular droplets are loaded into high aspect ratio vessels and conditioned to weightlessness using a rotary cell culture system to study drug metabolic rate in model microgravity. The effect of model microgravity on hepatocyte's organelle size (including cell cytoplasm and nucleus), metabolic rate and drug up-take rate are presented. The effect of model microgravity and co-culture condition on urea concentration, metabolic rate and cell model stiffness are presented.

5.4.1.2   *Preliminary results with mono-culture on collagen coated micro-carriers*

Preliminary work to study the effect of microgravity on human hepatic pharmacokinetics and function is conducted using a mono-culture cell model on collagen coated micro-carriers (Snyder J.E., 2012). Pharmacokinetics of the anti-nausea drug promethazine (PMZ) and the bioassay for cellular oxidation Alamar Blue are evaluated. Hepatic function is quantified by urea concentration. 3-dimensional hepatocyte aggregates experience simulated microgravity in a Synthecon Rotary Cell Culture System (RCCS). Pharmacokinetic rate and urea secretion are up-regulated in model microgravity. RCCS as a ground model of microgravity up-regulates pharmacokinetic rate of PMZ metabolism and up-regulates urea secretion. Gravity had no observed effect on the amount a cell could metabolize. The saturation concentration of both drugs was same in both gravitation conditions, RCCS as a µG ground and 1G.

Human hepatocytes of the HepG2 (ATCC) cell line are incubated with Cytodex collagen coated microcarrier beads in non-adherent plate. Average diameter of Cytodex bead is 225 µm +/- 25µm. After 24 hours in culture HepG2 adhere to microcarrier surface and begin to form aggregates. Figure 5-18 presents phase contrast images of HepG2 with microcarriers less than 1 hr and after 24 hours from cell seeding. HepG2-laden microcarriers are cultured in model µG and 1G.
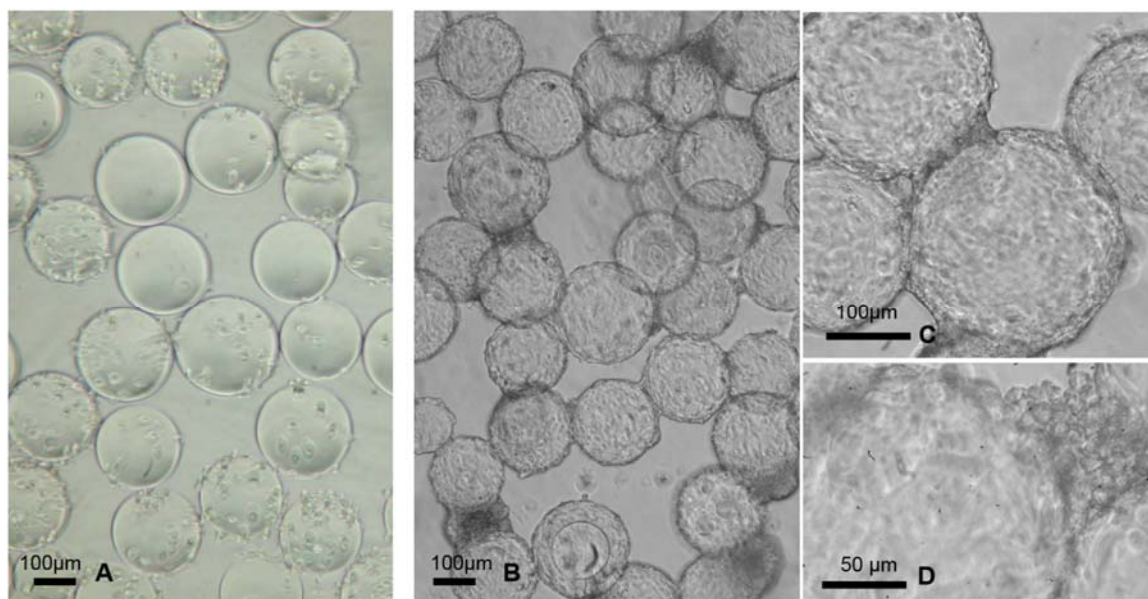
Figure 5-18: Hepatocytes attached to the surface of collagen-coated spheres. 3D aggregates of HepG2 less than 1 hour after cell seeding 10x (A) and 24 hours after cell seeding 10x (B) 20X (C) 40X(D)

The cell model is conditioned to microgravity using a ground model Synthecon rotary cell culture system (RCCS) to maintain the cell model in a state of perpetual freefall. Figure 5-19 is a schematic to introduce the operating principle of rotary cell culture as a model of microgravity. Contact forces signal the presence of a gravitational force. Perpetual freefall in a rotary cell culture system removes contact forces. Rotary cell culture is a ground model of microgravity and used to study the effect of no contact forces on cell models. Cell models are loaded into micro-spheres are loaded into high aspect ratio vessels (HARV) which are flooded with cell culture medium. Photograph of the Synthecon RCCS platform with four HARV filled with cell culture medium is presented in figure 5-20.
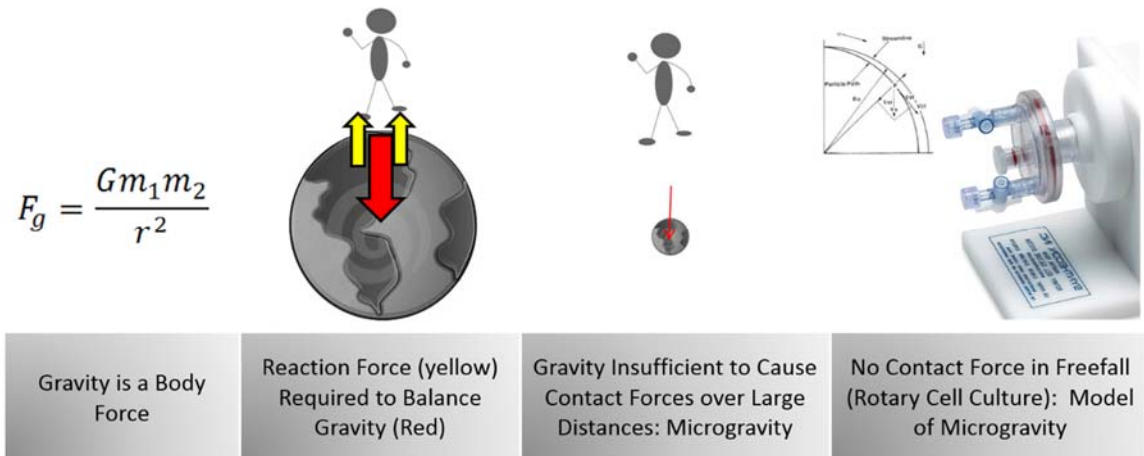
Figure 5-19: Presentation of rotary cell culture as a model of microgravity.
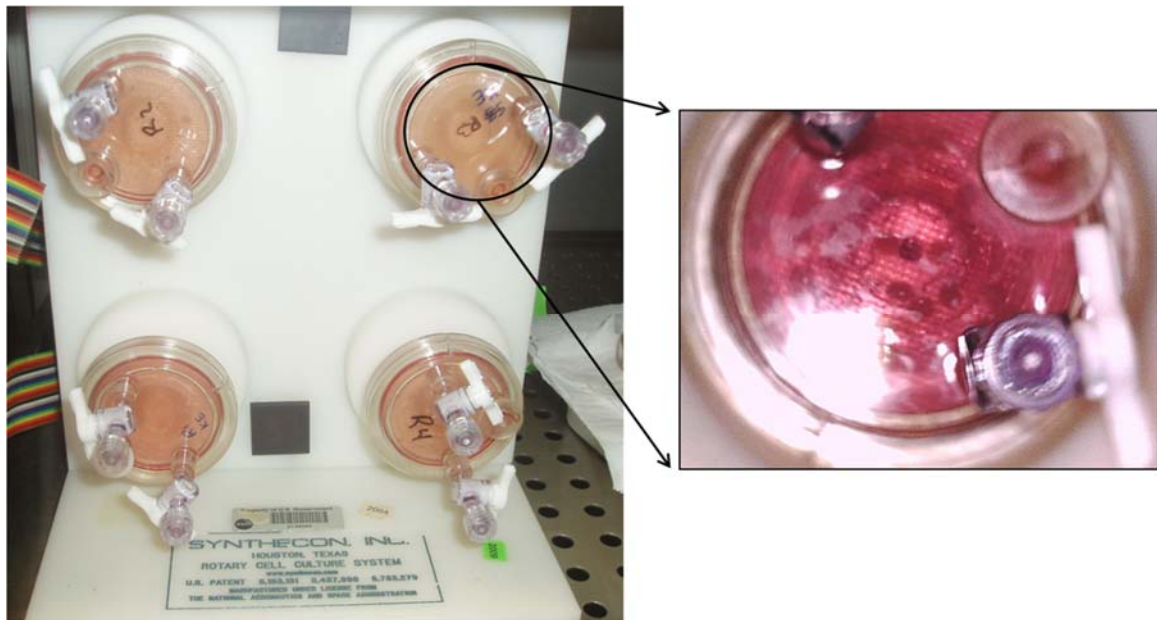
Figure 5-20: Synthecon Rotary Cell Culture System (RCCS) with High Aspect Ratio (HARV) containing cell culture medium and cell models.

RCCS rotation causes cell culture medium and the cell-laden micro-carriers to flow. Flow increases mixing and prevents local depletion of nutrients and drug and build-up of waste in the immediate vicinity of the model. 1G controls are incubated in HARV, but not rotated. To prove the results of the 1G vs. model microgravity experiment are caused by the diminished gravitational

force, and not local depletion drug, the 1G group is rotated horizontally at the same rpm as model microgravity group. In this way, both group experience mixing, but the cell model in the model microgravity group's vertical configuration experience perpetual freefall; i.e. model microgravity conditioning. A cartoon depiction of the concern of static v. rotary culture on local depeltion if nutrients and drug is presented in figure 5-21.
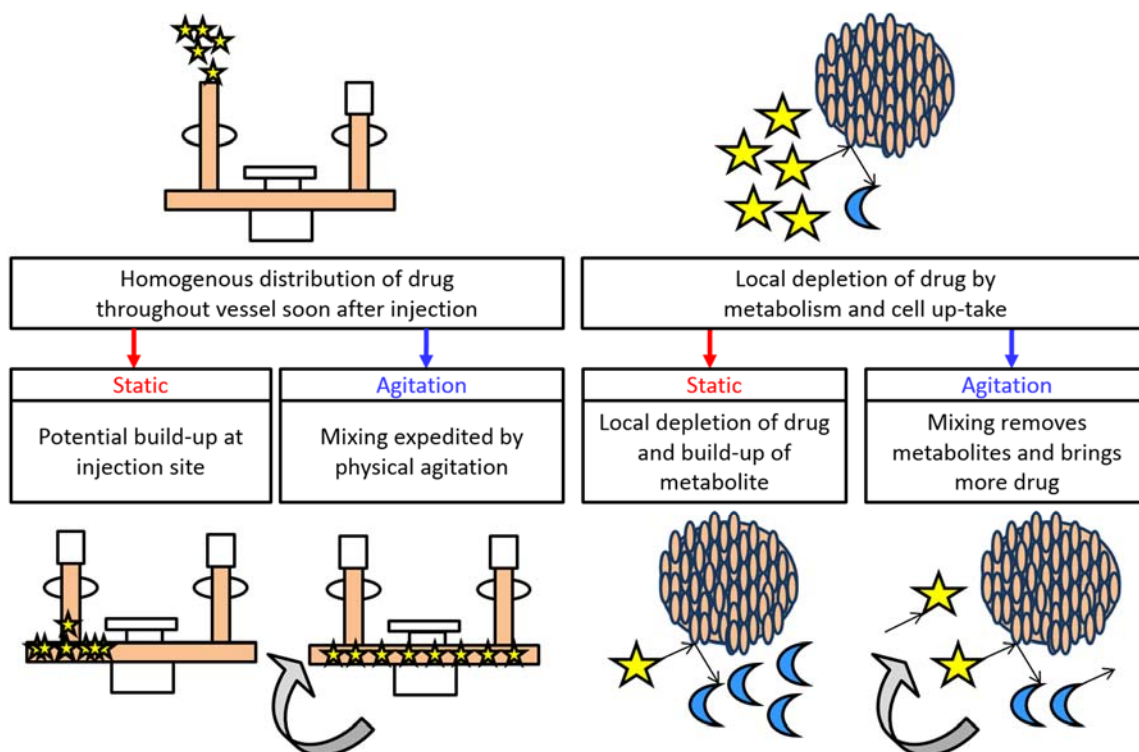
Figure 5-21: Cartoon depiction of RCCS HARV rotation to diminish the effect of local depletion of drug due to static conditions during drug-uptake study.

Pharmacokinetics of two drugs are evaluated using RCCS and HepG2-laden microspheres (1) Promethazine (PMZ) and (2) Alamar Blue. PMZ (Sigman et al.) is drug commonly prescribed to astronauts for anti-nausea. PMZ concentration is determined by high performance liquid chromatography (Waters). Alamar Blue (AbD Serotec) is an oxidation redox indicator which fluoresces after being metabolized by live cells. PMZ (0.10mg/mL) in cell culture medium is

loaded into HARV after cells have been in model microgravity for 24 hours. Cells in HARV metabolize and absorb the drug. Figure 5-22 presents pharmacokinetics of PMZ up-take in microgravity and 1G. PMZ concentration is 0.10mg/mL when loaded into the bioreactor. Cell metabolism and up-take of PMZ decreases the concentration throughout the 3 hour experiment. PMZ concentration decreases more quickly in model μG than 1G. PMZ concentration drops 7% more in model μG than 1G after 10 minutes, 22% more in model μG than 1G after 30 minutes, 23% more in model μG than 1G after 1 hour, and 18% more in model μG than 1G after 2 hours. PMZ concentration is not statistically different after 3 hours.
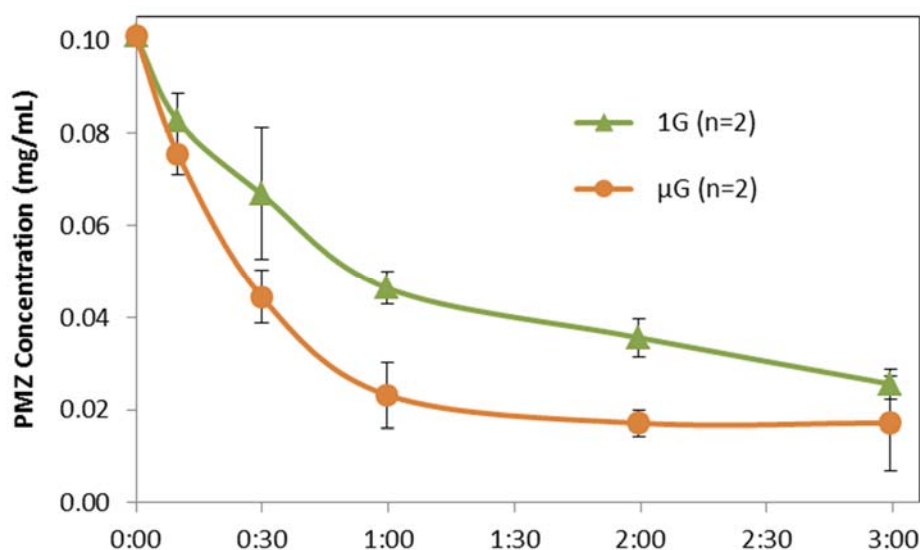
Figure 5-22: HepG2 cultured on microcarriers in RCCS after 24 hours metabolize PMZ to decrease concentration of drug.

Alamar Blue (10% v/v) in cell culture medium is loaded into HARV after cells have been in model microgravity for 24 hours. After metabolize by cells, Alamar Blue fluoresces 530-560nm excitation and 590nm emission. Fluorescence increases throughout the 3 hour experiment as cells metabolize Alamar Blue. Without metabolism by the cells the drug will be undetectable by emission/excitation spectrum sampled. Figure 5-23 presents concentration of metabolized Alamar

Blue. Alamar Blue fluorescence increases more quickly in model µG than 1G until 3 hours 30 minutes. Fluorescence is not significantly different after 6 hours.
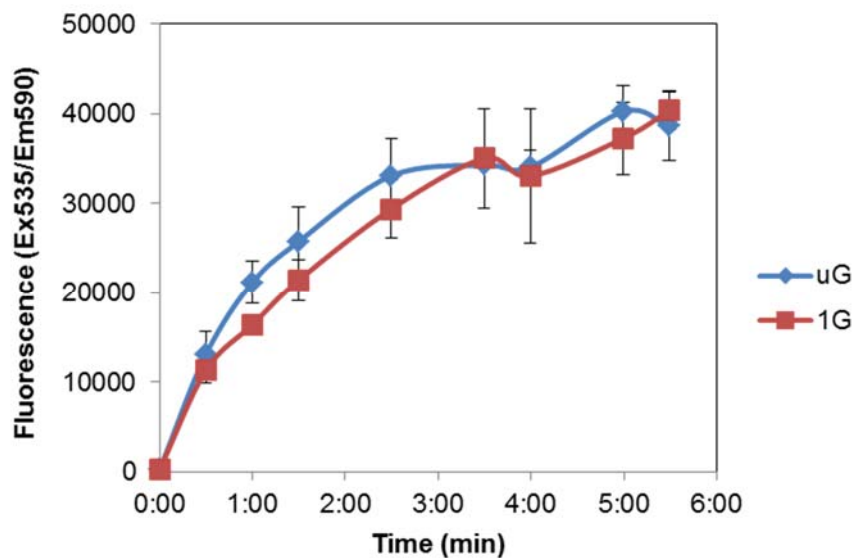
Figure 5-23: HepG2 in RCCS metabolize Alamar Blue to produce fluorescence proportional to cell number after 24 hours in RCCS.

Drug half-life is determined from experimental results. Both PMZ and Alamar Blue half-life are shorter in model µG than 1G. Figure 5-24 presents the half-life of each drug in model µG and 1G. PMZ half-life is 30.0 minutes earlier in model µG than 1G. Alamar Blue half-life is 8.4 minutes earlier in in model µG than 1G.
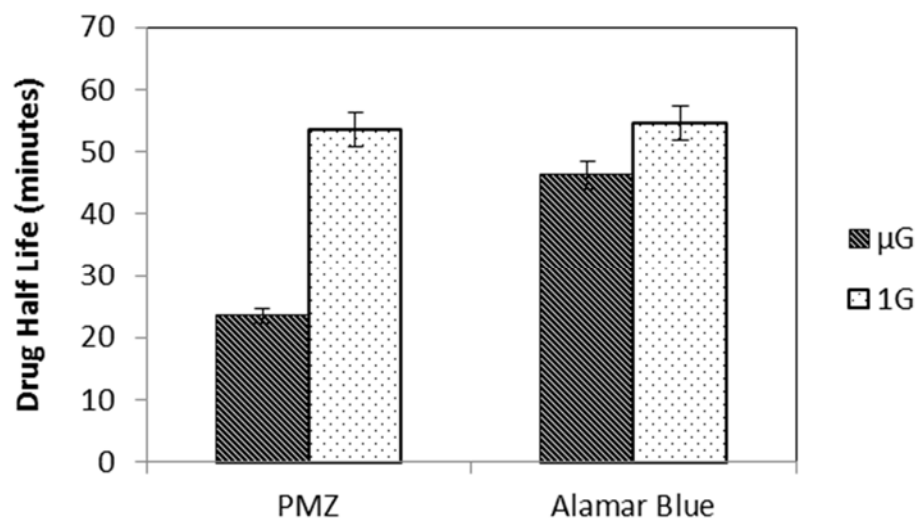
Figure 5-24: Half-life of PMZ and Alamar Blue metabolized by HepG2 cultured on microcarriers in RCCS for 24 hours.

Urea concentration is quantified after 24 hours in model µG and 1G. QuantiChrom Urea Assay Kit (BioAssay Systems, Hayward, CA) quantifies urea present in biological sample by absorbance measured at 405nm by Tecan Microplate Reader. Urea concentration in microgravity is compared to 1G controls. Figure 5-25 presents urea concentration after 24 hours in model microgravity and 1G. Urea concentration is 5.1mg/mL and 4.0mg/mL in model µG and 1G respectively. Hepatocytes secreted 22% more urea in in model µG than 1G.
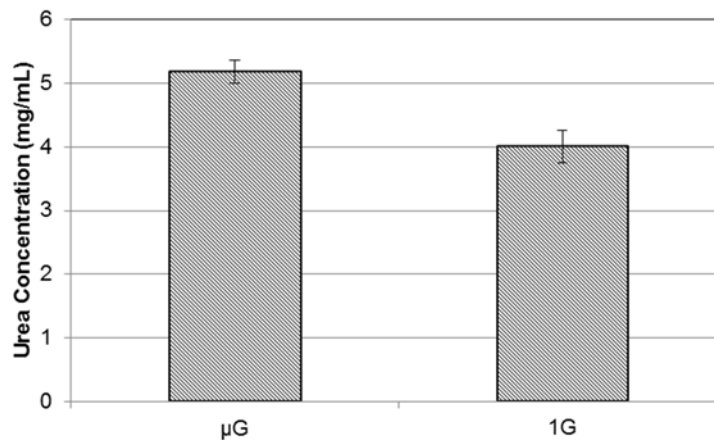
Figure 5-25: Urea concentration of HepG2 cultured on microcarriers after 24 hours in RCCS.

Ground model of microgravity up-regulates pharmacokinetic rate of PMZ metabolism and up-regulates urea secretion. Gravity had no observed effect on the amount a cell could metabolize. The saturation concentration of both drugs was same in model μG and 1G.

Pharmacokinetic rate of drug metabolism by hepatocytes is up-regulated in model μG. HepG2 up-take PMZ more quickly in model μG than 1G. Concentration difference is maintained between 18-23% for much of the first 2 hours drug is introduced. Half-life of PMZ and Alamar Blue in model μG is 30 and 8 minutes shorter respectively in model μG than 1G. Hepatocyte's capacity to metabolize drug is not effected by model μG. Saturation points for both drugs are not significantly different between model μG and 1G. No significant variance is observed after 3 hours with PMZ or after 6 hours with Alamar Blue respectively. The number of hepatocytes in model μG and 1G are not significantly different. Cell number is determined from saturation fluorescence of Alamar Blue after 6 hours. Alamar Blue is an indicator of cell viability designed to monitor kinetic cell growth. Alamar Blue fluorescence is linearly proportional to cell number with correlation coefficient of 0.92 (data not shown). No significant difference in fluorescent after 6 hours correlates to no significant difference in number of cells. Urea concentration is up-regulated in hepatocytes cultured in model μG for 24 hours. The number of cells in model μG and 1G are not

significantly different, according to Alamar Blue results. Therefore the amount of urea each cell secretes is up-regulated in model µG. Cell function and therefore biochemistry of culture and autocrine/paracrine signaling in model µG is observed to be quantitatively and temporally different than 1G.

5.4.2 Model design and fabrication

SMMB system enables fabrication of a hetero-cellular model of liver both (1) compatible with the existing RCCS platform and (2) capable of controlling the volume fraction of hepatocytes to endothelial cells. The biomimetic ratio of hepatocytes to endothelial cell in human liver sinusoid tissue is 7:1. Drag force on the droplet during RCCS culture is minimized by fabricating the minimum feasible droplet volume.

The cell model is a set of SMMB printed 200nL HepG2-laden spherical droplet. Droplets are 3.0×10^6 HepG2 cells per mL 0.5% (w/v) sodium alginate, cross-linked in 0.5% (w/v) calcium chloride. Design variables for the co-culture printed droplet presented in equation 5-22. The printing solution are chemically inert. The reaction time is unspecified.

$$\Psi_{SMMB,D} = \left[\; t_R = - \quad V_D = 200\,nL \quad \gamma_{H,E} = \frac{Hepatocyte}{Endothelial} = \frac{7}{1} \; \right] \qquad 5\text{-}22$$

The set of process parameters to produce the set of design variables presented in equation 5-23 and equation to relate the flow rate to the volume fraction, equation 4-6.

$$\Omega_{SMMB,D}(t) = \begin{bmatrix} d_x = 0 & & v_x = 0 \\ d_y = 0 & Q_H = 0.70\;mL/s & v_y = 0 \\ d_z = 1.5\;mm & Q_E = 0.10\;mL/s & v_z = 3.3\;mm/s \end{bmatrix} \qquad 5\text{-}23$$

No less than 600 droplets are printed. After printing, the cross-linking solution is aspirated from the printed droplets. Cell-laden droplets are rinsed with fresh medium, separated into two

equal volumes and loaded into HARVs. The HARVS are divided into two experimental groups: (1) model microgravity conditioning using RCCS and (2) control group under static conditions.

Model microgravity conditioning begins when HARV is secured to RCCS and the rotation rate is set to maintain cell-laden droplets in circular orbits (not sinking to the bottom of the HARV or colliding with the sides or top of the vessel). Rotation rate is adjusted between 16-18rpm. Figure 5-26 presents light microscope images of printed 200nL droplets embedded in 0.5% (w/v) sodium alginate. ImageJ analysis of fabricated droplets measured the cross-sectional area. The volume and diameter of the droplets are calculated to be 219 nL +/- 29 nL and $\emptyset$746 μm +/- 32 μm, respectively. After printing, cell-laden droplets are circular in the planar view of the light microscope. After 14 days in RCCS culture, both 1G and μG, circular droplets are found in the culture under light microscope inspection. Viable cells are present in printed droplets after 14 days. Cell-laden droplets are incubated with Live/Dead (Invitrogen) stain to fluorescently label live cells green. Figure 5-27 presents fluorescent image of live cells embedded in the droplet.
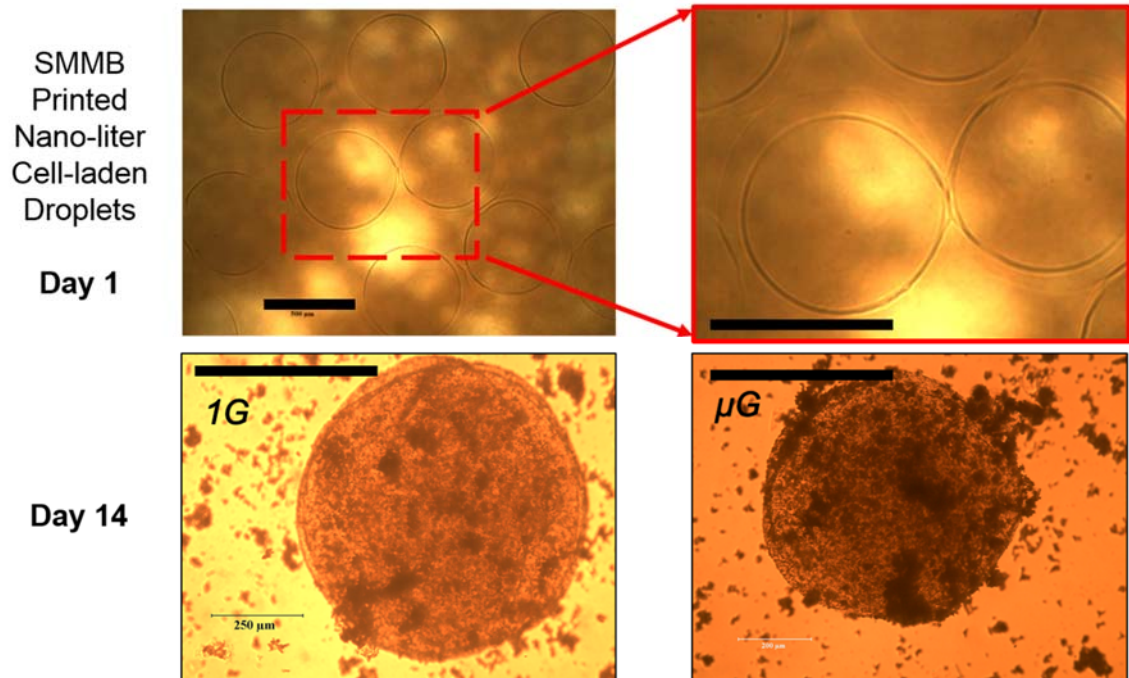
Figure 5-26: SMMB printed 200 nL cell-laden alginate droplets less than 1 day after printing (day 1) and day 14 after culture in a static (1G) and rotating (μG) high aspect rotary vessel (HARV). Calibration mark is 500μm in all images.
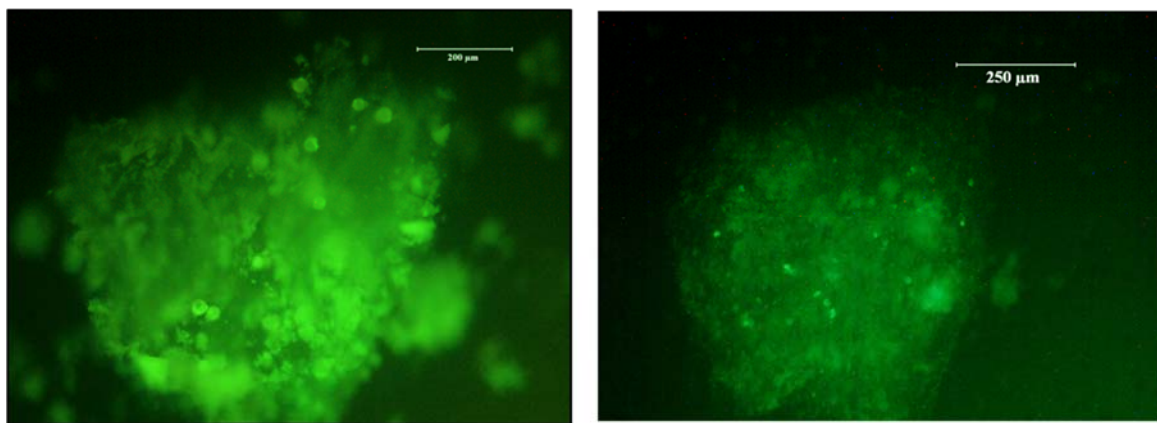
Figure 5-27: SMMB printed Hep-G2 laden droplets after 14 days in culture stained with Live/Dead fluorescent probe. Viable cells observed embedded in droplet.

5.4.3   Effect of model microgravity on printed liver model

5.4.3.1   *Hepatocyte cell area increased after 48 hrs in model microgravity*

The model microgravity environment has a significant impact on cell volume and drug up-take. Increase in cell volume in environments without a gravity vector have been well documented in literature (Kasper & Xun, 1996; Ross, 1993). It is possible the increase in cell volume causes an increased ability to up-take drug (as observed). However, increased volume alone would not increase the cell's ability to metabolize the drug.

After 48 hrs, HepG2-laden droplets are collected from the HARV for analysis. Cells are fixed and alginate is solubilized after 60 minutes 4°C incubation with 4% paraformaldehyde and gentle agitation. Cell are labeled with biz benzimide and wheat germ algumin to visualize morphological changes. The condition of the genetic material in the nucleus, chromatin, is determined by a fluorescent labeling of cell nucleus and plasma. The chromatin is labeled by biz benzimide and plasma is labeled using wheat germ algumin. The size of the cell is analyzed from the wheat germ algumin staining of the cell cytoplasm.

Cell area is measured using photographs of the fluorescently labeled cells and analysis software ImageJ (NIH). Cell solution are suspended in low density to prevent aggregation of cells in images and placed on microscope slides with cover. Using the ImageJ software, each image is calibrated to a scale watermarked during imaging, converted to 8-bit, threshold to highlight only structures relevant to imaging, and analyze particle area. Figure 5-28 presents the fluorescent image of HepG2 recovered from printed alginate droplets after 48hrs conditioning in model microgravity (A) and controls (C). Fluorescent images are converted to binary (A converted to B and C converted to D, respectively) by ImageJ for analysis. The area of each particle is calculated from pixel count and a calibration bar watermarked during imaging.
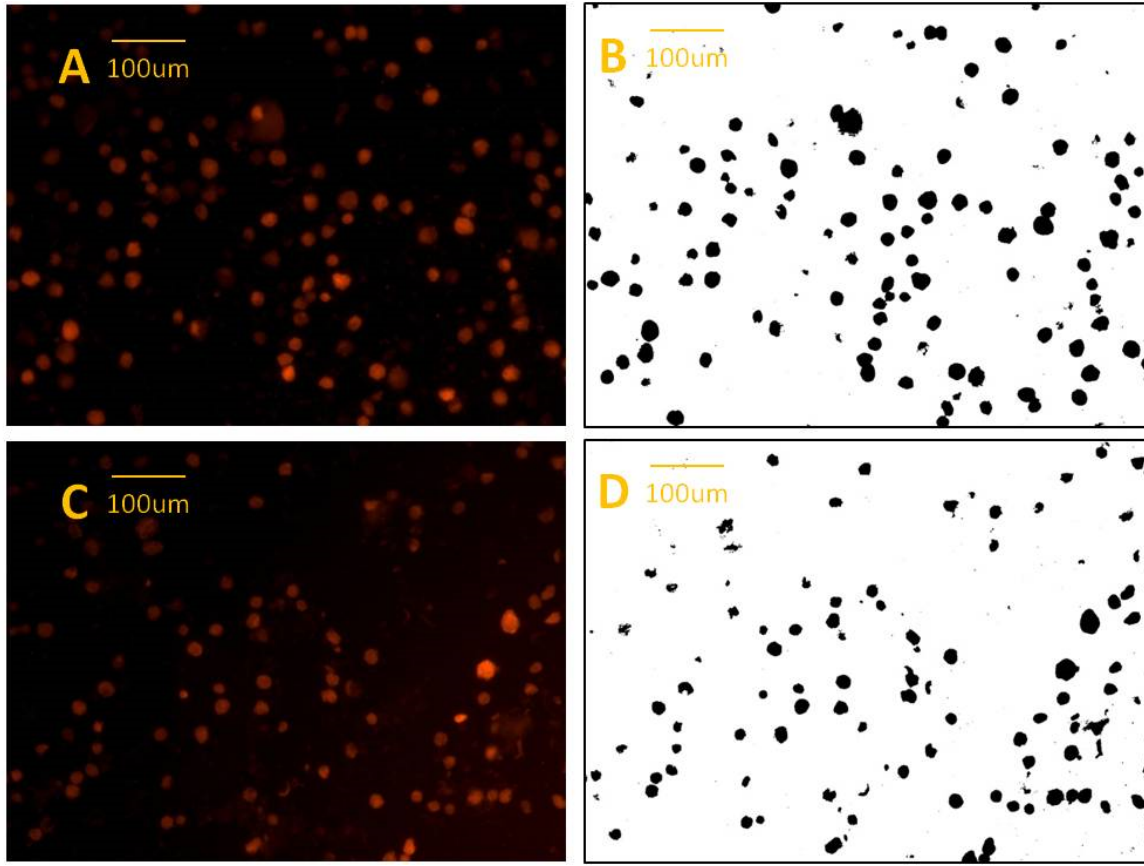
Figure 5-28: HepG2 cell cytoplasm staining by fluorescent probe after 48hrs in RCCS model microgravity (A) and static controls (C). Fluorescent images are converted to gray scale for particle count and area quantification of each cell.

The diameter of the cell (cytoplasm) and nucleus (chromatin) are calculated from the measured particles, equation 5-24 and 5-25. Size of cytoplasm and nucleus is determined for at least 300 cells. A histogram of cytoplasm and nucleus sizes (approximated as diameter) shows no significant impact on nucleus diameter, figure 5-28. Cell nucleus is not significantly affected, which remains consistent ~ ø4.8um. Cytoplasm histogram presents the different culture condition causes a shift from 7 µm for ground model to 9µm for model microgravity conditioning, figure 5-29. The spread of cytoplasm diameters around the model microgravity's 9µm mean is narrower than the spread around the control's 7µm mean diameter. The results of model microgravity vs ground

controls are summarized as follows: The mean cell cytoplasm diameter increases from ~ø7um to

~ø9um. Change in diameters produces a 60% increase in total cell volume.

$$D_{nucelus} = 2\sqrt{A_{measured,chromatin}/\pi} \qquad 5\text{-}24$$

$$D_{cytoplasm} = 2\sqrt{A_{measured,cytoplasm}/\pi} \qquad 5\text{-}25$$

Diameter of Cell Nucleus (um)	2.8	3.2	3.5	3.8	4.2	4.5	4.8	5.2	5.5	5.8	6.2
Ground Control	2.0%	4.1%	5.4%	9.5%	10.9%	12.2%	19.7%	10.2%	11.6%	7.5%	6.8%
Model Microgravity	2.6%	6.7%	9.2%	12.3%	13.8%	16.4%	13.3%	10.8%	6.7%	4.1%	4.1%
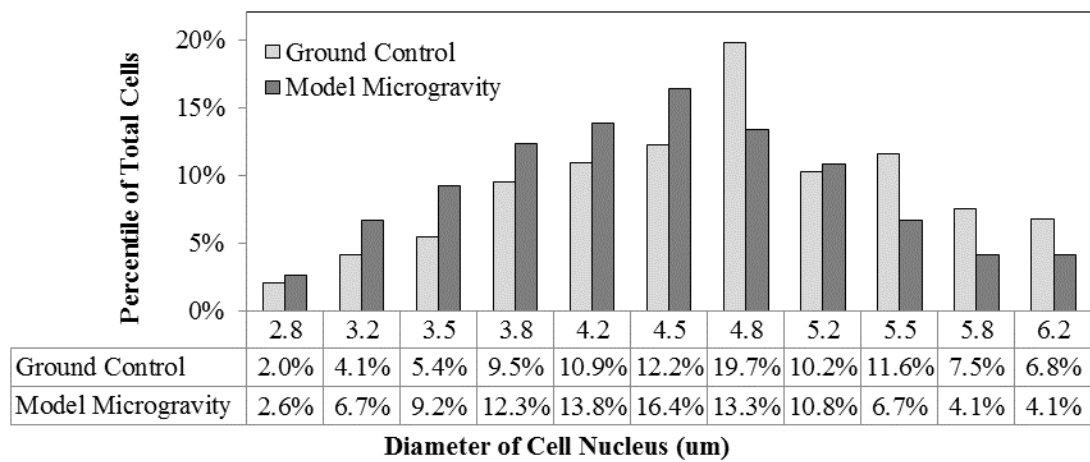
Figure 5-29: Diameter of HepG2 nucleus cell after 48hrs in model microgravity.

Diameter of Cell (um)	4.0	5.0	6.0	7.0	8.0	9.0	10.0	11.0	12.0	13.0	14.0
Ground Control	7.7%	10.0%	16.8%	24.2%	20.2%	10.5%	5.1%	2.0%	2.8%	0.0%	0.6%
Model Microgravity	3.0%	6.6%	8.4%	6.0%	11.4%	43.1%	13.8%	4.2%	2.4%	1.2%	0.0%
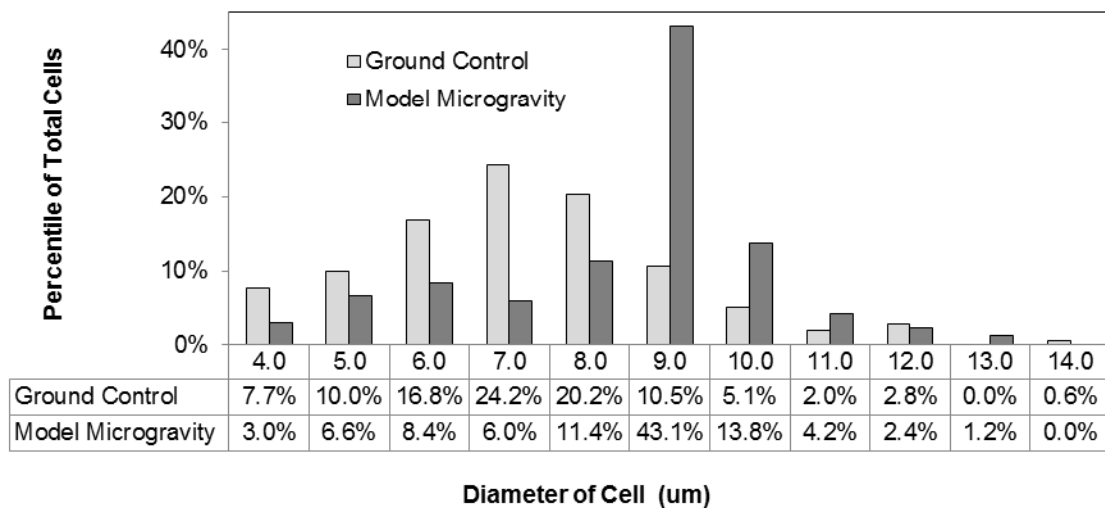
Figure 5-30: Diameter of HepG2 cell after 48hrs in model microgravity.

5.4.3.2   *Urea concentration increased in co-culture and model microgravity*

Model microgravity and co-culture both increase the concentration of urea in supernatant. Model microgravity has a stronger effect than co-culture. Effect of 48 hours model microgravity conditioning in RCCS and co-culture on urea production, as presented in figure 5-31. The concentration of urea is greater in co-culture of hepatocytes and endothelial cells than mono-cultures of hepatocytes alone. This observation is consistent with previous finding in HepG2-laden microcarriers in model microgravity presented in section 5.4.1 rationale for the study and has also been reported in literature (K. Kim, Ohashi, Utoh, Kano, & Okano, 2012). The concentration of urea is greater after 48 hours of model microgravity both mono- and co-culture cell models than 1G controls. This observation has also been reported in literature (Baqai et al., 2009a).

	1G	uG
Mono-Culture	0.26	0.28
Co-Culture	0.28	0.30
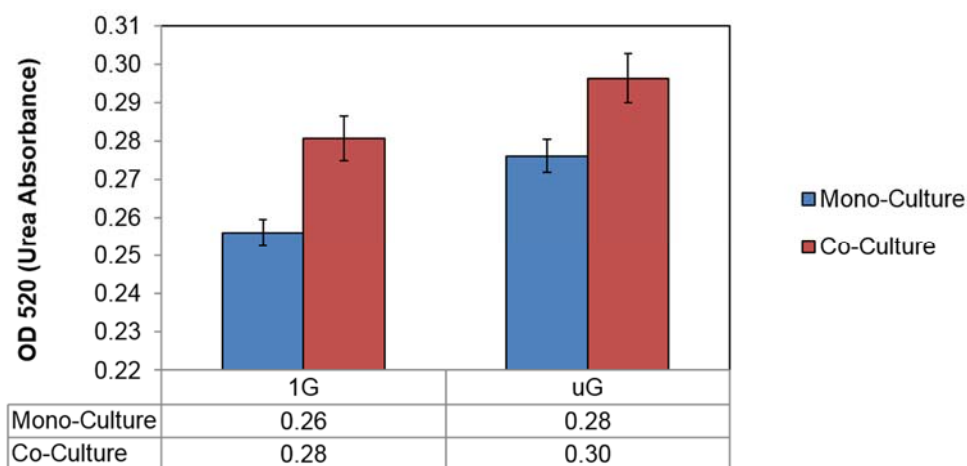
Figure 5-31: Effect of 48 hours model microgravity conditioning in RCCS and co-culture on urea production.

5.4.3.3   *Metabolic rate up-regulated in co-culture and model microgravity*

Model microgravity conditioning and co-culture with endothelial cells up-regulates hepatocytes' metabolic rate in vitro. Co-culture is a more significant factor than model microgravity to increase metabolic rate. Mono- and co-culture droplets are collected from HARV

after 14 days of either 1G (static) and model microgravity (RCCS culture) conditioning. Fresh cell culture medium with 10% (v/v) Alamar blue (Serotec) is added to the recovered cell-laden droplets. Cells metabolize Alamar blue to excitation/emission of 535/595 nm. The rate of the reaction depends on cell number and the metabolic activity of the cells. Both hepatocytes and endothelial cells convert Alamar blue to the product detected by the excitation/emission stated. Figure 5-32 presents the excitation/emission detected by fluorescence protocol of the Tecan GENios microplate reader over the reaction time. Reaction time begins when the Alamar blue is added to the cell-laden samples recovered from HARV after 14 days. Metabolism of Alamar blue is an indicator of viable cells. The rate of metabolism quantifies both (1) cell number and metabolic activity. The consequence of mono- vs. co-culture and 1G vs. model microgravity conditioning effects metabolic rate. However, this effect can be generally attributed to the experimental variable and not specifically to increased cell number or alteration in an individual cell's capacity to metabolize the Alamar blue. The results are as follows.

The experiment yielded a data set including time and excitation/emission RFU coordinates measured by the microplate reader. The measured metabolic rate (RFU/min) is determined from the experimental data and presented for comparison between experimental groups in table 5-3. Data is analyzed as a simple linear regression using least square fitting. The generalized function to corelate excitation/emission RFU of metabolized alamar Blue and time in minutes is presented in equation 5-26.

$$y(RFU) = \beta_0 + \beta_1 x \ (min) \hspace{3cm} 5\text{-}26$$

The detected fluorescent signal increases during the reaction time, as the cells metabolize the Alamar blue. The metabolism rate for mono-culture droplets in 1G and model microgravity are 38 and 44 RFU per minute, respectively. The metabolism rate for co-culture droplets in 1G and model microgravity are 330 and 530 RFU per minute, respectively. Co-culture increases the

metabolic rate of cell-laden droplet by one order of magnitude. 1G of model microgravity conditioning increases metabolic rate by less than 40% for co-culture and less than 15% for mono-culture. This effect of model microgravity and co-culture is generally attributed to increase metabolic rate. Increases in total cell number and alterations to the individual cell's capacity to metabolize Alamar blue are considered to be the causes of the observed results. However, which of the causes are specifically responsible cannot be identified based on the presented results. The observed behavior is a consequence of co-culture and model microgravity. Therefore, the presented sensitivity has applications to the design of biomimetic pharmacokinetic and space life science models.
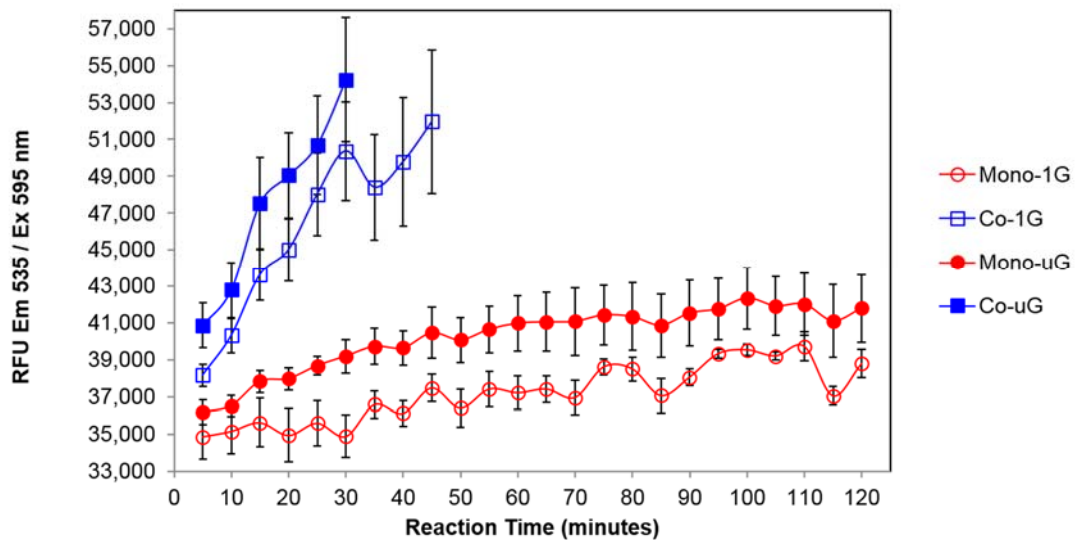
Figure 5-32: Effect of 14 day conditioning to model microgravity using RCCS and co-culture of HepG2 and endothelial cells on metabolic rate of Alamar Blue. Reaction time measured from the time Alamar Blue is added. Em/Ex detects metabolized Alamar blue.

Table 5-3. Metabolic rate to convert Alamar blue to product in mono- and co- culture and 1G and model µG gravitational conditions.

Culture Condition	Gravitational Condition	Metabolic Rate (RFU/min) (estimated by linear regression)	Linearity
Mono	1G	38	0.76
Mono	μG	44	0.81
Co	1G	330	0.90
Co	μG	530	0.98

5.4.3.4   Cell-laden droplet modulus increased after 14 days in model microgravity

Modulus of printed mono- and co-culture nano-liter droplet measured by Nanoscope atomic force microscope (AFM) analysis of force volume using contact mode. Mechanical testing for elastic modulus by AFM contact mode to measure deflection in sample (Lin, Shreiber, Dimitriadis, & Horkay, 2009). Modulus is calculated using the Hertz model of indentation and known mechanics of the cantilever. Hooke's law defines the force applied to the sample as a function of the cantilever spring constant and indentation, as presented in equation 5-27.

$$F = -k\delta \qquad\qquad 5\text{-}27$$

The Hertz model defines the force on the sample as a function of the sample's modulus and geometric parameters of the cantilever. Contact between the spherical tip cantilever and sample is modeled as shallow contact between two spherical bodies, as presented in equation 5-28 .

$$F = \frac{4}{3}\frac{E_{surface}\,\delta^{3/2}}{\left(1 - v_{surface}^2\right)}\sqrt{R_{tip}} \qquad\qquad 5\text{-}28$$

The measured indentation is the difference between the cantilever deflection and sample movement, as presented in equation 5-29.

$$\delta = z - d \qquad\qquad 5\text{-}29$$

Nanoscope analysis of the force volume from AFM contact mode generates height images and force plots of the spherical cantilever tip on the printed cell-laden nano-liter droplet, figure 5-33. The spring constant and spherical tip radius of the cantilever are 2.8 N/m and 8.0 nm respectively. Test parameters are 1000nm z-display, retract z-direction, 34.274 nm/V deflection sensitivity, 0.9965 Hz scan rate, 1.816 μm ramp scale, 0.5 Poisson's ratio and include adhesion forces. Software reports force plots of the cyclic extension-retraction of the cantilever on the printed mono- and co-culture nano-liter droplets after 14 days in model microgravity.
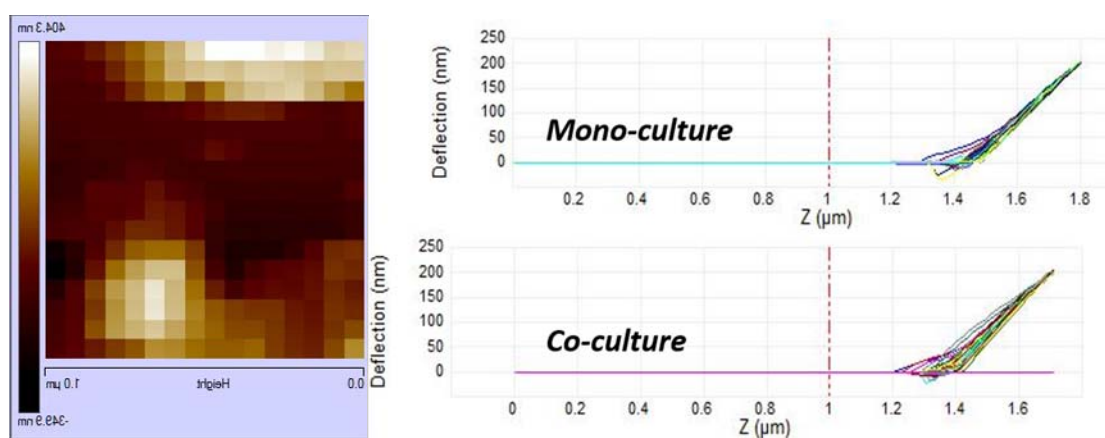
Figure 5-33: (Left) AFM contact mode height image of spherical tip cantilever on printed cell-laden nano-liter droplet. (Right) Force plot of cyclic extension-retraction of cantilever on printed mono- and co-culture nano-liter droplet using Nanoscope atomic force microscope.

Mean modulus of co- and mono-culture printed nano-liter droplet after 14 days in model microgravity are 63.4 +/- 20.5 MPa and 48.8 +/- 15.2 MPa, respectively, figure 5-34. The mean mono-culture modulus is 77% of the co-culture modulus. Hepatocyte-endothelial co-culture increases micro-organ modulus compared to mono-culture. Extracellular matrix provides mechanical support and regulatory information (Conway & Schaffer, 2012). Matrix material and cell to cell contact produce biomimetic cell junctions and barrier to mass transfer, specifically nanoparticle diffusion (Horev-Azaria et al., 2011).
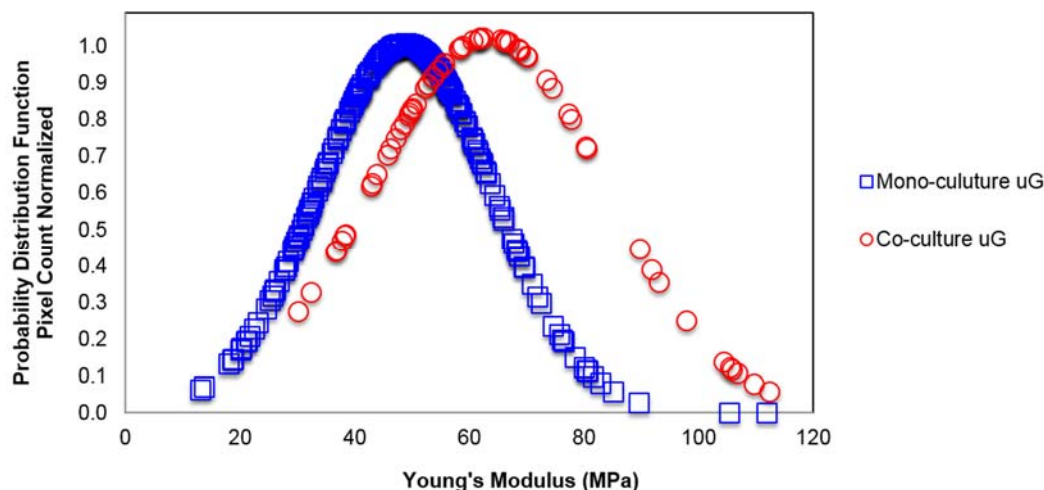
Figure 5-34: Probability distribution function of printed mono- and co-culture nano-liter droplet Young's modulus after 14 days in model microgravity.

5.4.4 Drug elimination rates and half life

The objective of the drug up-take characterization on printed co- and mono-culture cell models is to quantify drug depletion as a function of time. The study is significant to pharmacokinetic rates in model microgravity for pharmaceutical dosing during long term manned space exploration. The drug EFC (7-ethoxy-4-trifluoromethyl courmarin) is selected because EFC's fluorogenic probe properties are favorable for detection using a microplate reader. EFC is converted by protease activity inside the cell to drug product HFC (7-hydroxy-4-trifluoromethyl courmarin). EFC includes an acetone group, which allows the drug to penetrate the cell membrane for up-take. The acetone group is cleaved by protease inside either the cell's mitochondria or endoplasmic reticulum. The protease convert the EFC to the metabolized HFC form. The metabolized drug HFC resides inside the cell and is not detected in the culture's effluent without cell lysis. Therefore, the presented method is effective quantify EFC depeletion but not the synthesis of metabolized drug. The experimental plan included the following tasks: (1) fabricate 200 nL droplet laden with heaptocyte and endothelial cells with volume fraction of 7:1. (2) Culture cells in model microgravity using rotary cell culture system for 48 hours and add EFC drug. Both

model microgravity and ground 1G control groups are stored with the same volume of culture medium in high aspect ratio vessels. (3) Collect effluent over 9 hours to quantify the concentration of extracellular unbound EFC remaining in culture. (4) Empirically define the first order elimnation rate of EFC by the printed co-culture model. Equation 5-30 mathematically defines the rate constant k, as a function of the time t_i, intial concentration of drug C_0, and concentration of drug measured at time t_i to be C_i. The intial concentration of drug is 120 µM EFC concentration. The first order elimination rate is presented in equation 5-30 as a function of the rate, k, intial concentration, C_0, a second concentration, C_i, and the time lapsed between the intial and second concentration, t_i.

$$k = -\frac{1}{t_i} ln \left[\frac{C_i}{C_0}\right] \qquad \qquad 5\text{-}30$$

The EFC half life for comparison between the model microgravity and ground control (not cultured in rotary cell culture system) conditions is determined from the experimental time course data. Equation 5-31 defines the half life of the drug $t_{1/2}$ as a function of the rate constant k.

$$t_{1/2} = \frac{ln\,2}{k} \qquad \qquad 5\text{-}31$$

Figure 5-35 presents the depletion of EFC in effleunt by printed co-culture after 48 hours in high aspect vessels after 48 hours in rotary cell culture to mode microgravity or without to model ground 1G as a control. The EFC is removed from the effluent as the cells up-take drug or connvert the drug to metabolized form. The half life of EFC in model microgravity is 1.0 hour and 1.9 hours in 1G ground control, as presented in table 5-4.
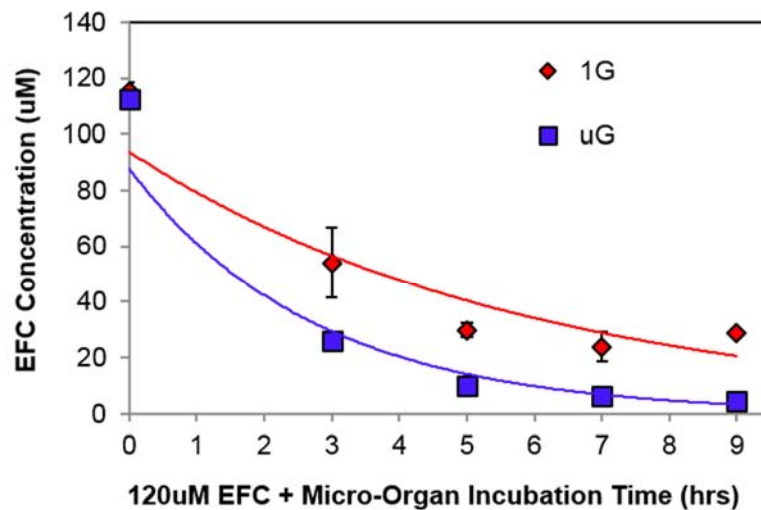
Figure 5-35: Deplation of EFC in effluent by printed co-culture in model microgravity and ground 1G conditions

Table 5-4. EFC half life with printed co-culture of hepatocytes and endothelial cells cultured in high aspect ration vessels and conditioned to model microgravity using a rotary bioreactor system of maintained as a control of 1G without the bioreactor system.

Culture Condition	Gravitational Condition	EFC Half Life (hours)
Co	1G	1.9
Co	μG	1.0

CHAPTER 6: CONCLUSION

6.1   Summary

Chapter 2 develops 3D printing and replica molding processes to fabricate interconnected and hierarchical structural environments for cell culture. Two different 3D printing and replica molding processes are introduced: (1) a precision extrusion deposition and replica molding process to produces microfluidic networks and (2) a multi-nozzle deposition and freeze casting process to produce hierarchical tissue scaffolds.   Both 3D printing processes integrate a 3D motion system with a continuous extrusion material delivery system to print patterns of the extruded filament. Internal features and external surfaces are explicitly assembled due to the layer-by-layer construction of the printed pattern. The 3D printing process parameters control the macro-scale structure of the printed pattern/void space (10^{-3}-10^{-1} m resolution) and extruded cross-section's shape and size (10^{-4}-10^{-3} m). Once fabricated, the printed pattern is embedded in a liquid-phase of a secondary material, which is subsequently cured. The composite printed pattern/ secondary material is either directly used or the printed pattern is removed, leaving a template of open channels or pores. Cell-material attachment is presented. The presented processes introduces the capability to fabricate 3D hierarchical, composite or porous/open channel architecture for scaffold guided tissue engineering.

Chapter 3 integrates the advanced biomanufacturing techniques developed in chapter 2 to fully construct a hetero-cellular microfluidic devices for drug efficacy applications. 3-dimensional open channel networks fully embedded in PDMS are fabricated by precision extrusion deposition (PED) and replica molding. Forced convection through the channels is controlled by additional hardware components and a programmable syringe pump. Cell suspension is pumped into the device, left static for 12-24 hrs for adhesion and then perfused for nutrient supply/waste removal. Alternatively, multi-nozzle deposition (MND) for hetero-cellular seeding throughout the network and in channel cross-section defines the position of cell types, support material and matrix.

Applications of the system include space life science in vitro models to study radioprotective pro-drug efficacy in co-culture. Hetero-cellular contact is controlled by forced convection through a multi-chamber co-culture microfluidic device. Cell-laden devices are stimulated with radioprotective drug and radiation exposure to study drug efficacy in co-culture compared to mono-culture microfluidic devices.

Chapter 4 develops the synchronized multi-material bioprinting (SMMB) system to package different cell types and structural matrix material in a heterogeneous array and extrude the heterogeneous array along a tool path to build 3D biology-laden structures. The fully integrated system includes a 3D motion system, multi-nozzle material delivery system with synchronized multi-material deposition head and temperature control system. The 3D motion system is a set of three linear slides, each independently controlled by automation software. The motion system is used in two ways (1) as a linear build cycle discretizes a design into a stack of 2D tool paths for layer-by-layer construction or (2) as a periodic build cycle to control the accumulation and dispensing of a predetermined material volume. The multi-nozzle material delivery system with a synchronized multi-material deposition head packages tissue matrix material-laden with cells and complementary support material in a heterogeneous array. The heterogeneous array is extruded along a tool path to produce a pattern (linear build cycle) or controlled total volume with constituent volume fractions of the component materials is dispensed (periodic build cycle). The resolution of internal features of the heterogeneous array is 10^{-5}-10^{-3} m, which improves the motion system's extruded filament patterning capability of 10^{-3}-10^{-1} m. Additional nozzles containing other heterogeneous arrangements, support material or crosslinking agents are each is independently controlled by automation software. A temperature control system expands the feasible set of tissue matrix materials to include thermally cross-linked materials such as Matrigel and collagen. The effect of the process on cell viability is presented.

Chapter 5 characterizes the synchronized multi-material bioprinting system's controllability and capability to fabricate heterogeneous nano-liter droplets and 10^4-10^{-3} m diameter printed filaments. Applications of the system include space life science in vitro models to study metabolic rate and drug efficacy in co-culture. Printed hetero-cellular droplets are loaded into high aspect ratio vessels and conditioned to weightlessness using a rotary cell culture system to study drug metabolic rate in model microgravity.

Conclusions of the conducted research and recommendations for future work are presented in Chapter 6.

6.2   *Research contributions*

The research contributions are summarized as follows:

1. Development of a combined precision extrusion deposition/ replica molding process to fabricate a 3-dimensional open network of channels embedded in a PDMS substrate for use as a cell-laden microfluidic device. To define a 3D printing and replica molding processes to fabricate microfluidic and scaffold environments with control of the macro-scale (10^{-3}-10^{-1} m) patterning of channels/structural elements and micro-scale (10^{-4}-10^{-3} m) channel cross-section of internal features.

2. Development of a novel synchronized multi-material bioprinter to package multiple solutions as a heterogeneous combined flow prior to deposition as a printed pattern or nano-liter droplet. To develop and characterize an integrated synchronized multi-material bioprinter system to produce nano-liter droplets and 10^{-4}-10^{-3} m diameter filaments with a heterogeneous packaging resolution of 10^{-5}-10^{-3} m. To characterize the integrated synchronized multi-material bioprinter system to produce nano-liter droplets and 10^{-4}-10^{-3} m diameter filaments with a heterogeneous packaging resolution of 10^{-5}-10^{-3} m.

3. For the first time, print a co-culture model of liver to study the rate of drug up-take in model microgravity using a rotary cell culture system. To apply the synchronized multi-material bioprinter system to produce hetero-cellular models to study radioprotective drug efficacy in co-culture and metabolism rates in simulated weightlessness environments.

6.3   Future research recommendations

The work presented in this thesis can be improved to include application in self-organizing architecture, built-biological system to capture infection agents and models of accelerated cell metabolism to condense the time course required to understand the effect of drug or soluble cues on in vitro cell models. Following research tasks have been outlined for future research and development.

6.3.1   Self-organizing architecture

Dormant inert materials such as metal, ceramic and plastic continuously weaken until failure during their useful life. Over time, mechanical fatigue, thermal stress and chemical erosion cause crystallographic defects to grow into cracks. Failure due to fracture occurs when cracks reach a critical length and propagate catastrophically through the structure. The cost of fracture was estimated to be $119 billion in 1982, despite evaluation and maintenance techniques to detect and repair cracks(Anderson, 1991). The estimated cost does not include injury or loss of life. In contrast to dormant inert materials, viable organisms adapt to maintain viability and structural integrity in changing physical environments. Biology has adapted to both sense and responds to the physical world. Further, organisms self-organize minimize energy spent while maintaining viability. ***The objective of the proposed future work is to blend dormant inert materials with viable organisms using advanced manufacturing techniques to produce self-organizing adaptable architecture.***

Living organism's ability to sense and respond to mechanical force and structural cues has application to adaptable building material applications. Organisms have the potential to (1) self-regenerate and proliferate to maintain the viability of a colony over time-scales longer than that of an individual constituent organism, (2) re-organize to optimize energy conservation(Nakagaki, Yamada, & Toth, 2000) and structural integrity of the collective colony, and (3) leverage a large number of individual entities over long time scales to accomplish statistically low probability events(Tarabichi et al., 2013) – one example being Darwinian evolution.

Self-organization to maintain the structural integrity of the collective colony is exemplified by the plasticity of bone and muscle tissue. Bone and muscle atrophy or increase in strength in response to environmental loading to prevent damage to the tissue itself, without unnecessarily maintaining energy-intensive structures. Wolff's Law states the bone in a healthy person remodels itself to resist applied loads. Bone is remodeled when cell secrete calcium to increase stiffness. If a bone is compressed or bent during walking or running, the mechanical vibrations applied to the bone are sensed by cells through signaling pathways connected to the nucleus. Mechanical perturbations effect the cell's gene expression and cause an increase in calcium secretion, which produces more bone. Conversely, if the cell is not stimulated, the calcium secretion lessens and the bone atrophies.

This future work has applications to NASA's ground-based research to engineer self-organizing adaptable architecture to ensure the health and security of humans beyond Earth's surface in isolated and resource-limited environments. This work is aligned with NSBRI's Human Factors and Performance science and technology team's interest to mitigate habitability and environmental risks to mission success. The deliverable countermeasure to prevent the loss of structural stability of components during extraplanetary flight is adaptable self-regenerating architecture. Architecture constructed from viable organisms has the potential to regenerate, self-organize and therefore repair after damage or fatigue. Truly adaptive self-healing built biological

systems diminish mission dependency on spare parts in the payload. Further, self-organizing architecture (such as bone or muscle tissue) is capable of automated adjustments in response to gradual alterations in load magnitude and direction without manual intervention by a human operator or crew. Automated adjustment by adaptable self-healing architecture lessen the existing dependence on non-invasive diagnostic measures to identify damaged and fatigued components prior to failure. Further, it is aligned with DOE's 2013 Report to Congress, for which Rothschild represented NASA's interests.

The highest priority is placed on safety and mission assurance, occupational health and environmental protection of the public, astronauts and NASA work force. The Human Research Roadmap's presents the following management architecture to prepare countermeasures against the effects of the space environment; evidence, risk, gap, task and deliverables. Space factors and habitability specifically solicits countermeasures to mitigate the risk of inadequate critical task design. To this end, passive adaptability and plasticity of structures and components to re-generate over the course of a mission bolster success in isolated resource-limited environments. The risk of component failing without a replacement during a mission is well recognized and increases with mission length. This proposed future research offers a countermeasure to increase the adaptability and flexibility of the built environment NASA provides astronauts during their mission. Consider the following risks to mission success:

1. *A component loses structural integrity during service due to cyclic stress from loading, temperature gradients and radiation:* Conventional inert materials weaken over time as cracks within the part grow due to environmental forces. This requires routine 3-dimensional non-invasive imaging to detect cracks before catastrophic failure. An adaptable built biological system will proliferate, migrate and secrete extracellular signals over time to maintain structural integrity by self-organizing to alleviate stress concentration within the architecture. Bone is such an example.

2. A r*eplacement component is required due to failure during an extraplanetary mission:* NASA's missions are engineered with interchangeable parts and operations defines which and how many spare components are included in the payload for such an event. However, the type and number of spare parts is limited by the risk of the failure and the expense of additional cargo. An alternative solution to redundant cargo is self-healing components. The damaged component does not have to be completely repaired or replaced. Imagine the damaged component is removed from service, a percentage of the structure is repaired and the colony of organisms replenished. The organisms recognize structural and mechanical cues from their environment and grow/align themselves to a homeostatic configuration. At which point, the component may be placed back in service.

3. *Additional or new components are required during the course of a long term manned space exploration or colonization of a non-Earth habitat:* The biomanufacturing method to assemble structural elements and organisms in 3-dimensional space is a portable technology. A reservoir colony of the organism is also a portable material with the potential for expansion. Additional or new components can be fabricated on site by printing a porous set of structural elements and allowing the organisms to grow over and through the structure as a guide. This enable modular design for large-scale construction of shielding or dwellings. The organisms are capable of integrating between fabricated components to diminish sole dependence on hardware as a fastener.

6.3.2   Built biological system to diminish the spread of infection disease

The infection disease schistosomiasis (affects 160 million people, mainly in Sub-Saharan Africa) is caused by unsanitary excreta disposal. One method to fight infection disease is to prevent the spread of the infection, or in the case of schistosomiasis, contain or dehydrate human waste. Physical barriers exist to capture infectious agents. However, species of organisms also exist which capture infectious agents; either through detainment (the capturing organisms kills or

immobilizes the infectious agent) or attraction (the infection agent prefers the environment of the capturing organism). Advanced manufacturing and biology may have a role to fight the spread of infectious disease. The density of organisms can be controlled using built biological systems. If (1) a target infectious agent and capturing organism pair can be identified (Both must be indigenous to a geographic region) and (2) the capturing agent's density can be controlled using a built biological system to a point where it significantly contains the infectious agents then (3) engineered biological systems are an enabling technology to contain (and by causality, fight) infectious disease. This work may have NASA applications to prevent the spread of biological agents between regions of space craft or more broadly between Earth to space.

6.3.3   Accelerate drug/cell interaction to condense experiment length

Cell volume and metabolic rate are related in python (Riquelme et al., 2011). University of Colorado professor Leslie Leinwand of the Molecular, Cellular and Developmental Biology Department reported to the journal Science in October of this year cardiac cells double in size (hyperrophy) during digestion in burmese pythons. Snakes require this increased cardiac capacity because they consume very large quantities. The signal for cardiac cells to double in size is a mix of three fatty acids. The University of Colorado group demonstrated the relationship between the fatty acids and heart cell doubling in size using mice. Cardiac cells are shown to physically and functionally respond to the three fatty acids identified in the study. This finding may be significant to pharmacokinetic work to drug metabolism in microgravity. Research already exists to demonstrate cell volume increases in microgravity. This recent work links cell volume increases to changes in metabolism, which supports microgravity environment alters drug metabolism. Additionally, manipulating the concentration of the presented fatty acids could speed up cell's metabolism to observe the effect of drugs or soluble cues in condensed time lines. Meaning, the effect of a drug on a cell model over years might be modeled over months or weeks using an accelerated metabolism.

6.4   Concluding remarks

The novel synchronized multi-material bioprinter integrates microfluidic techniques with cell printing to package multiple cell-laden materials and cross-linking solutions along a 3-dimensional tool path. Biomimetic assembly to support cell viability in vitro and solicit paracrine/autocrine signaling between cells presents methodological progress to guide the cell aggregate to perform tissue-level function; with application to tissue engineering and general built biological constructs. Bioprinting is an enabling technology to engineer built biological systems. Interfacing biology and architecture in built biological systems with reproducibility and engineering process control requires advanced manufacturing(W. Sun et al., 2004). Bioprinting is a computer aided manufacturing method with process control over (1) macro-scale (10^{-3}-10^{-1} m) architecture and (2) micro-scale (10^{-4}-10^{-5} m) heterogeneous packaging of components and internal features. Macro-scale architecture is critical if the built biological system is designed to physically fit into a larger system. Micro-scale heterogeneous packaging of organisms and support artifacts is critical to the function of the built biological system. Additional artifacts heterogeneously packed with the biology during printing spatial-temporally effect the built system's mechanics, physics, and chemistry. Artifact candidates include - load bearing structural elements(Hamid et al., 2011; Shor et al., 2007), open porous network for diffusion(S. Khalil & Sun, 2009b), functionalized or magnetic nanoparticles (Buyukhatipoglu et al., 2010b), and piezoelectric/conductive components.

LIST OF REFERENCES

[1]   Alini, M., Eisenstein, S. M., Ito, K., Little, C., Kettler, A. A., Masuda, K., Melrose, J., Ralphs, J., Stokes, I., & Wilke, H. J. (2008). Are animal models useful for studying human disc disorders/degeneration? *European Spine Journal, 17*(1), 2-19. doi:

[2]   Allen, J. W., Khetani, S. R., & Bhatia, S. N. (2005). In vitro zonation and toxicity in a hepatocyte bioreactor. *Toxicol Sci, 84*(1), 110-119. doi:

[3]   Anderson, T.L. (1991). *Fracture Mechanics: Fundamentals and Applications*. Boca Raton: CRC Press.

[4]   Atala, A., Bauer, S. B., Soker, S., Yoo, J. J., & Retik, A. B. (2006). Tissue-engineered autologous bladders for patients needing cystoplasty. *Lancet, 367*(9518), 1241-1246. doi:

[5]   Aydemir, N., Sevim, N., Celikler, S., Vatan, O., & Bilaloglu, R. (2009). Antimutagenicity of amifostine against the anticancer drug fotemustine in the Drosophila somatic mutation and recombination (SMART) test. *Mutat Res, 679*(1-2), 1-5. doi:

[6]   Baker, M. (2011). A Living System on a Chip. *Nature, 471*(7340), 661-665. doi:

[7]   Balaban, N. Q., Schwarz, U. S., Riveline, D., Goichberg, P., Tzur, G., Sabanay, I., Mahalu, D., Safran, S., Bershadsky, A., Addadi, L., & Geiger, B. (2001). Force and focal adhesion assembly: a close relationship studied using elastic micropatterned substrates. *Nature Cell Biology, 3*(5), 466-472. doi:

[8]   Baqai, F. P., Gridley, D. S., Slater, J. M., Luo-Owen, X., Stodieck, L. S., Ferguson, V., Chapes, S. K., & Pecaut, M. J. (2009a). Effects of spaceflight on innate immune function and antioxidant gene expression. *Journal of Applied Physiology, 106*(6), 1935-1942. doi:

[9]   Baqai, F. P., Gridley, D. S., Slater, J. M., Luo-Owen, X., Stodieck, L. S., Ferguson, V., Chapes, S. K., & Pecaut, M. J. (2009b). Effects of spaceflight on innate immune function and antioxidant gene expression. *J Appl Physiol, 106*(6), 1935-1942. doi:

[10]   Barron, J. A., Wu, P., Ladouceur, H. D., & Ringeisen, B. R. (2004). Biological laser printing: a novel technique for creating heterogeneous 3-dimensional cell patterns. *Biomed Microdevices, 6*(2), 139-147. doi:

[11]   Becker, H., Carstens, C., Elbracht, R., & Gartner, C. (2010). Opportunities and limits of cell-based assay miniaturization in drug discovery. *Expert Opinion on Drug Discovery, 5*(7), 673-679. doi:

[12]   Bhumiratana, S., Grayson, W. L., Castaneda, A., Rockwood, D. N., Gil, E. S., Kaplan, D. L., & Vunjak-Novakovic, G. (2011). Nucleation and growth of mineralized bone matrix on silk-hydroxyapatite composite scaffolds. [Research Support, N.I.H., Extramural]. *Biomaterials, 32*(11), 2812-2820. doi:

[13]   Borenstein, J. T., Weinberg, E. J., Orrick, B. K., Sundback, C., Kaazempur-Mofrad, M. R., & Vacanti, J. P. (2007). Microfabrication of three-dimensional engineered scaffolds. *Tissue Engineering, 13*(8), 1837-1844. doi:

[14]   Bornens, M., Thery, M., Racine, V., Pepin, A., Piel, M., Chen, Y., & Sibarita, J. B. (2005). The extracellular matrix guides the orientation of the cell division axis. *Nature Cell Biology, 7*(10), 947-U929. doi:

[15]   Brandon, E. F. A., Raap, C. D., Meijerman, I., Beijnen, J. H., & Schellens, J. H. M. (2003). An update on in vitro test methods in human hepatic drug biotransformation research: pros and cons. *Toxicology and Applied Pharmacology, 189*(3), 233-246. doi:

[16]   Buyukhatipoglu, K., Chang, R., Sun, W., & Clyne, A. M. (2010a). Bioprinted Nanoparticles for Tissue Engineering Applications. *Tissue Engineering Part C-Methods, 16*(4), 631-642. doi:

[17]   Buyukhatipoglu, K., Chang, R., Sun, W., & Clyne, A. M. (2010b). Bioprinted nanoparticles for tissue engineering applications. [Research Support, Non-U.S. Gov't]. *Tissue Eng Part C Methods, 16*(4), 631-642. doi:

[18]   Cao, Y., Mitchell, G., Messina, A., Price, L., Thompson, E., Penington, A., Morrison, W., O'Connor, A., Stevens, G., & Cooper-White, J. (2006). The influence of architecture on degradation and tissue ingrowth into three-dimensional poly(lactic-co-glycolic acid) scaffolds in vitro and in vivo. [Comparative Study   In Vitro Research Support, Non-U.S. Gov't]. *Biomaterials, 27*(14), 2854-2864. doi:

[19]   Chang, R., Emami, K., Wu, H. L., & Sun, W. (2010). Biofabrication of a three-dimensional liver micro-organ as an in vitro drug metabolism model. *Biofabrication, 2*(4). doi:

[20]   Chatrchyan, S., Khachatryan, V., Sirunyan, A. M., Tumasyan, A., Adam, W., Bergauer, T., Dragicevic, M., Ero, J., Fabjan, C., Friedl, M., Fruhwirth, R., Ghete, V. M., Hammer, J., Hansel, S., Hoch, M., et al. (2011). Measurement of the B0 production cross section in pp collisions at sqrt[s] = 7 TeV. *Phys Rev Lett, 106*(25), 252001. doi:

[21]   Cheng, K. C., Maguire, T. J., Novik, E., Chao, P., Barminko, J., Nahmias, Y., & Yarmush, M. L. (2009). Design and Application of Microfluidic Systems for In Vitro Pharmacokinetic Evaluation of Drug Candidates. *Current Drug Metabolism, 10*(10), 1192-1199. doi:

[22]   Cheng, K. C., Novik, E., Maguire, T. J., Chao, P. Y., & Yarmush, M. L. (2010). A microfluidic hepatic coculture platform for cell-based drug metabolism studies. *Biochemical Pharmacology, 79*(7), 1036-1044. doi:

[23]   Chu, T. M., Orton, D. G., Hollister, S. J., Feinberg, S. E., & Halloran, J. W. (2002). Mechanical and in vivo performance of hydroxyapatite implants with controlled architectures. [Research Support, Non-U.S. Gov't]. *Biomaterials, 23*(5), 1283-1293. doi:

[24]   Ciocca, L., De Crescenzio, F., Fantini, M., & Scotti, R. (2009). CAD/CAM and rapid prototyped scaffold construction for bone regenerative medicine and surgical transfer of virtual planning: a pilot study. *Comput Med Imaging Graph, 33*(1), 58-62. doi:

[25]   Conway, A., & Schaffer, D. V. (2012). Biophysical regulation of stem cell behavior within the niche. *Stem Cell Research & Therapy, 3*. doi:

[26]   Cucinotta, F. A., & Durante, M. (2006). Cancer risk from exposure to galactic cosmic rays: implications for space exploration by human beings. *Lancet Oncology, 7*(5), 431-435. doi:

[27]   Cucinotta, F. A., Kim, M. H., Willingham, V., & George, K. A. (2008a). Physical and biological organ dosimetry analysis for international space station astronauts. *Radiation Research, 170*(1), 127-138. doi:

[28] Cucinotta, F. A., Kim, M. H. Y., Willingham, V., & George, K. A. (2008b). Physical and biological organ dosimetry analysis for International Space Station astronauts. *Radiat Res, 170*(1), 127-138. doi:

[29] Cucinotta, F. A., Manuel, F. K., Jones, J., Iszard, G., Murrey, J., Djojonegro, B., & Wear, M. (2001). Space radiation and cataracts in astronauts. *Radiat Res, 156*(5), 460-466. doi:

[30] Cucinotta, F.A.; Durante, M. (2009). Risk of Radiation Carcinogenesis *Human Health and Performance Risks of Space Exploration Missions Evidence reviewed by the NASA Human Research Program* NASA.

[31] Dash, A., Inman, W., Hoffmaster, K., Sevidal, S., Kelly, J., Obach, R. S., Griffith, L. G., & Tannenbaum, S. R. (2009). Liver tissue engineering in the evaluation of drug safety. *Expert Opin Drug Metab Toxicol, 5*(10), 1159-1174. doi:

[32] Derby, B. (2012). Printing and prototyping of tissues and scaffolds. [Review]. *Science, 338*(6109), 921-926. doi:

[33] Dickson, M., & Gagnon, J. P. (2004). Key factors in the rising cost of new drug discovery and development. *Nature Reviews Drug Discovery, 3*(5), 417-429. doi:

[34] Doran, M. R., Mills, R. J., Parker, A. J., Landman, K. A., & Cooper-White, J. J. (2009). A cell migration device that maintains a defined surface with no cellular damage during wound edge generation. *Lab on a Chip, 9*(16), 2364-2369. doi:

[35] Dutta, R. C., & Dutta, A. K. (2010). Comprehension of ECM-Cell dynamics: a prerequisite for tissue regeneration. *Biotechnol Adv, 28*(6), 764-769. doi:

[36] Ebrahimkhani, Mohammad R., Neiman, Jaclyn A. Shepard, Raredon, Micha Sam B., Hughes, David J., & Griffith, Linda G. Bioreactor technologies to support liver function in vitro. *Adv Drug Deliv Rev*(0). doi:

[37] Eddings, M. A., Johnson, M. A., & Gale, B. K. (2008). Determining the optimal PDMS-PDMS bonding technique for microfluidic devices. *Journal of Micromechanics and Microengineering, 18*(6). doi:

[38]   Fischbach, C., Chen, R., Matsumoto, T., Schmelzle, T., Brugge, J. S., Polverini, P. J., & Mooney, D. J. (2007). Engineering tumors with 3D scaffolds. *Nature Methods, 4*(10), 855-860. doi:

[39]   Gabbay, J. S., Heller, J. B., Mitchell, S. A., Zuk, P. A., Spoon, D. B., Wasson, K. L., Jarrahy, R., Benhaim, P., & Bradley, J. P. (2006). Osteogenic potentiation of human adipose-derived stem cells in a 3-dimensional matrix. *Annals of Plastic Surgery, 57*(1), 89-93. doi:

[40]   Gebhardt, R., Hengstler, J. G., Muller, D., Glockner, R., Buenning, P., Laube, B., Schmelzer, E., Ullrich, M., Utesch, D., Hewitt, N., Ringel, M., Hilz, B. R., Bader, A., Langsch, A., Koose, T., et al. (2003). New hepatocyte in vitro systems for drug metabolism: metabolic capacity and recommendations for application in basic research and drug development, standard operation procedures. *Drug Metabolism Reviews, 35*(2-3), 145-213. doi:

[41]   Genes, N. G., Rowley, J. A., Mooney, D. J., & Bonassar, L. J. (2004). Effect of substrate mechanics on chondrocyte adhesion to modified alginate surfaces. [Research Support, U.S. Gov't, P.H.S.]. *Arch Biochem Biophys, 422*(2), 161-167. doi:

[42]   Gomez-Diaz, D., & Navaza, J. M. (2003). Rheology of aqueous solutions of food additives - Effect of concentration, temperature and blending. *Journal of Food Engineering, 56*(4), 387-392. doi:

[43]   Griffith, L. G., Powers, M. J., Domansky, K., Kaazempur-Mofrad, M. R., Kalezi, A., Capitano, A., Upadhyaya, A., Kurzawski, P., Wack, K. E., Stolz, D. B., & Kamm, R. (2002). A microfabricated array bioreactor for perfused 3D liver culture. *Biotechnology and Bioengineering, 78*(3), 257-269. doi:

[44]   Griffith, L. G., Sivaraman, A., Leach, J. K., Townsend, S., Iida, T., Hogan, B. J., Stolz, D. B., Fry, R., Samson, L. D., & Tannenbaum, S. R. (2005). A microscale in vitro physiological model of the liver: Predictive screens for drug metabolism and enzyme induction. *Current Drug Metabolism, 6*(6), 569-591. doi:

[45]   Griffith, Linda G., Wells, Alan, & Stolz, Donna Beer. (2014). Engineering Liver. *Hepatology*, n/a-n/a. doi:

[46]   Griffon, D. J., Sedighi, M. R., Schaeffer, D. V., Eurell, J. A., & Johnson, A. L. (2006). Chitosan scaffolds: interconnective pore size and cartilage engineering. [Research Support, Non-U.S. Gov't]. *Acta Biomater, 2*(3), 313-320. doi:

[47]   Guilak, F., Cohen, D. M., Estes, B. T., Gimble, J. M., Liedtke, W., & Chen, C. S. (2009). Control of Stem Cell Fate by Physical Interactions with the Extracellular Matrix. *Cell Stem Cell, 5*(1), 17-26. doi:

[48]   Hamid, Q., Snyder, J., Wang, C., Timmer, M., Hammer, J., Guceri, S., & Sun, W. (2011). Fabrication of three-dimensional scaffolds using precision extrusion deposition with an assisted cooling device. [Research Support, Non-U.S. Gov't]. *Biofabrication, 3*(3), 034109. doi:

[49]   Hamid, Q., Wang, C., Zhao, Y., Snyder, J., & Sun, W. (2014). A three-dimensional cell-laden microfluidic chip for in vitro drug metabolism detection. *Biofabrication, 6*(2), 025008. doi:

[50]   Harris, L. R., Jenkin, M., Jenkin, H., Dyde, R., Zacher, J., & Allison, R. S. (2010). The unassisted visual system on earth and in space. *J Vestib Res, 20*(1), 25-30. doi:

[51]   Hayflick, L. (1965). The Limited in Vitro Lifetime of Human Diploid Cell Strains. *Experimental Cell Research, 37*, 614-636. doi:

[52]   Hayward, L. N. M., & Morgan, E. F. (2009). Assessment of a mechano-regulation theory of skeletal tissue differentiation in an in vivo model of mechanically induced cartilage formation. *Biomechanics and Modeling in Mechanobiology, 8*(6), 447-455. doi:

[53]   Hellweg, C. E., & Baumstark-Khan, C. (2007). Getting ready for the manned mission to Mars: the astronauts' risk from space radiation. *Naturwissenschaften, 94*(7), 517-526. doi:

[54]   Hoganson, D. M., Pryor, H. I., Spool, I. D., Burns, O. H., Gilmore, J. R., & Vacanti, J. P. (2010). Principles of Biomimetic Vascular Network Design Applied to a Tissue-Engineered Liver Scaffold. *Tissue Engineering Part A, 16*(5), 1469-1477. doi:

[55]   Holzwarth, J. M., & Ma, P. X. (2011). Biomimetic nanofibrous scaffolds for bone tissue engineering. *Biomaterials, 32*(36), 9622-9629. doi:

[56]   Horev-Azaria, L., Kirkpatrick, C. J., Korenstein, R., Marche, P. N., Maimon, O., Ponti, J., Romano, R., Rossi, F., Golla-Schindler, U., Sommer, D., Uboldi, C., Unger, R. E., & Villiers, C. (2011). Predictive Toxicology of Cobalt

Nanoparticles and Ions: Comparative In Vitro Study of Different Cellular Models Using Methods of Knowledge Discovery from Data. *Toxicological Sciences, 122*(2), 489-501. doi:

[57]   Huh, D., Leslie, D. C., Matthews, B. D., Fraser, J. P., Jurek, S., Hamilton, G. A., Thorneloe, K. S., McAlexander, M. A., & Ingber, D. E. (2012). A Human Disease Model of Drug Toxicity-Induced Pulmonary Edema in a Lung-on-a-Chip Microdevice. *Sci Transl Med, 4*(159). doi:

[58]   Huh, D., Mammoto, A., Montoya-Zavala, M., & Ingber, D. E. (2010). A human breathing lung-on-a-chip. *Faseb Journal, 24*. doi:

[59]   Huh, D., Matthews, B. D., Mammoto, A., Montoya-Zavala, M., & Ingber, D. E. (2011). A human breathing lung-on-a-chip for drug screening and nanotoxicology applications. *Drug Metabolism Reviews, 43*, 6-6. doi:

[60]   Hunger, P. M., Donius, A. E., & Wegst, U. G. (2012). Platelets self-assemble into porous nacre during freeze casting. *J Mech Behav Biomed Mater*. doi:

[61]   Hunger, P. M., Donius, A. E., & Wegst, U. G. (2013). Structure-property-processing correlations in freeze-cast composite scaffolds. *Acta Biomaterialia*. doi:

[62]   Irimia, D., & Toner, M. (2009). Spontaneous migration of cancer cells under conditions of mechanical confinement. *Integrative Biology, 1*(8-9), 506-512. doi:

[63]   Jensen, K. F., El-Ali, J., & Sorger, P. K. (2006). Cells on chips. *Nature, 442*(7101), 403-411. doi:

[64]   Kalambur, S., & Rizvi, S. S. H. (2006). Rheological Behavior of starch-polycaprolactone (PCL) nanocomposite melts synthesized by reactive extrusion. *Polymer Engineering and Science, 46*(5), 650-658. doi:

[65]   Kamm, R. D., Sudo, R., Chung, S., Zervantonakis, I. K., Vickerman, V., Toshimitsu, Y., & Griffith, L. G. (2009). Transport-mediated angiogenesis in 3D epithelial coculture. *Faseb Journal, 23*(7), 2155-2164. doi:

[66]   Karageorgiou, V., & Kaplan, D. (2005a). Porosity of 3D biomaterial scaffolds and osteogenesis. [Research Support, N.I.H., Extramural

Research Support, U.S. Gov't, P.H.S.
Review]. *Biomaterials, 26*(27), 5474-5491. doi:

[67]   Karageorgiou, V., & Kaplan, D. (2005b). Porosity of 3D biornaterial scaffolds and osteogenesis. *Biomaterials, 26*(27), 5474-5491. doi:

[68]   Kasper, C. E., & Xun, L. (1996). Cytoplasm-to-myonucleus ratios following microgravity. [Research Support, U.S. Gov't, Non-P.H.S. Research Support, U.S. Gov't, P.H.S.]. *J Muscle Res Cell Motil, 17*(5), 595-602. doi:

[69]   Katsumi, A., Milanini, J., Kiosses, W. B., del Pozo, M. A., Kaunas, R., Chien, S., Hahn, K. M., & Schwartz, M. A. (2002). Effects of cell tension on the small GTPase Rac. *Journal of Cell Biology, 158*(1), 153-164. doi:

[70]   Khalil, S., Nam, J., & Sun, W. (2005). Multi-nozzle deposition for construction of 3D biopolymer tissue scaffolds. *Rapid Prototyping Journal, 11*(1), 9-17. doi:

[71]   Khalil, S., & Sun, W. (2009a). Bioprinting Endothelial Cells With Alginate for 3D Tissue Constructs. *Journal of Biomechanical Engineering-Transactions of the Asme, 131*(11), -. doi:

[72]   Khalil, S., & Sun, W. (2009b). Bioprinting endothelial cells with alginate for 3D tissue constructs. [Research Support, U.S. Gov't, Non-P.H.S.]. *J Biomech Eng, 131*(11), 111002. doi:

[73]   Khalil, Saif El Din. (2005). *Deposition and Structural Formation of 3D Alginate Tissue Scaffolds.* (Doctorate of Philosophy Doctoral), Drexel University, Drexel University.

[74]   Khaoustov, V. I., Risin, D., Pellis, N. R., & Yoffe, B. (2001). Microarray analysis of genes differentially expressed in HepG2 cells cultured in simulated microgravity: preliminary report. [Comparative Study Research Support, Non-U.S. Gov't Research Support, U.S. Gov't, Non-P.H.S.]. *In Vitro Cell Dev Biol Anim, 37*(2), 84-88. doi:

[75]   Kim, J. H., Cho, C. S., Choung, Y. H., Lim, K. T., Son, H. M., Seonwoo, H., Baik, S. J., Jeon, S. H., Park, J. Y., Choung, P. H., & Chung, J. H. (2009). Mechanical Stimulation of Mesenchymal Stem Cells for Tissue Engineering. *Tissue Engineering and Regenerative Medicine, 6*(1-3), 199-206. doi:

[76] Kim, K., Ohashi, K., Utoh, R., Kano, K., & Okano, T. (2012). Preserved liver-specific functions of hepatocytes in 3D co-culture with endothelial cell sheets. [Research Support, Non-U.S. Gov't]. *Biomaterials, 33*(5), 1406-1413. doi:

[77] Kim, S., & Marimuthu, M. (2011). Microfluidic cell coculture methods for understanding cell biology, analyzing bio/pharmaceuticals, and developing tissue constructs. *Analytical Biochemistry, 413*(2), 81-89. doi:

[78] Kim, Y., Larkin, A. L., Davis, R. M., & Rajagopalan, P. (2010). The Design of In Vitro Liver Sinusoid Mimics Using Chitosan-Hyaluronic Acid Polyelectrolyte Multilayers. *Tissue Engineering Part A, 16*(9), 2731-2741. doi:

[79] Kim, Y., & Rajagopalan, P. (2010). 3D Hepatic Cultures Simultaneously Maintain Primary Hepatocyte and Liver Sinusoidal Endothelial Cell Phenotypes. *PLoS One, 5*(11). doi:

[80] Kleinman, H. K., & Martin, G. R. (2005). Matrigel: basement membrane matrix with biological activity. *Semin Cancer Biol, 15*(5), 378-386. doi:

[81] Kong, B. H., Song, X. Y., & Li, D. (2008). A new tool for probing of cell-cell communication: human embryonic germ cells inducing apoptosis of SKOV3 ovarian cancer cells on a microfluidic chip. *Biotechnology Letters, 30*(9), 1537-1543. doi:

[82] Kostadinova, R., Boess, F., Applegate, D., Suter, L., Weiser, T., Singer, T., Naughton, B., & Roth, A. (2013). A long-term three dimensional liver co-culture system for improved prediction of clinically relevant drug-induced hepatotoxicity. *Toxicology and Applied Pharmacology, 268*(1), 1-16. doi:

[83] Kung, C. (2005). A possible unifying principle for mechanosensation. *Nature, 436*(7051), 647-654. doi:

[84] Lee, K. Y., & Mooney, D. J. (2012). Alginate: properties and biomedical applications. *Prog Polym Sci, 37*(1), 106-126. doi:

[85] Lee, P. J., Hung, P. J., & Lee, L. P. (2007). An artificial liver sinusoid with a microfluidic endothelial-like barrier for primary hepatocyte culture. *Biotechnology and Bioengineering, 97*(5), 1340-1346. doi:

[86]   Li, Y., Ma, T., Kniss, D. A., Lasky, L. C., & Yang, S. T. (2001). Effects of filtration seeding on cell density, spatial distribution, and proliferation in nonwoven fibrous matrices. [Research Support, Non-U.S. Gov't Research Support, U.S. Gov't, P.H.S.]. *Biotechnol Prog, 17*(5), 935-944. doi:

[87]   Liang, J. Z., Zhou, L., Tang, C. Y., & Tsui, C. P. (2013). Melt Flow Behavior in Capillary Extrusion of Nanosized Calcium Carbonate Filled PLLA/PCL Bio-Composites. *Journal of Polymers and the Environment, 21*(3), 857-863. doi:

[88]   Lin, D. C., Shreiber, D. I., Dimitriadis, E. K., & Horkay, F. (2009). Spherical indentation of soft matter beyond the Hertzian regime: numerical and experimental validation of hyperelastic models. *Biomechanics and Modeling in Mechanobiology, 8*(5), 345-358. doi:

[89]   Ling, Y., Rubin, J., Deng, Y., Huang, C., Demirci, U., Karp, J. M., & Khademhosseini, A. (2007). A cell-laden microfluidic hydrogel. *Lab Chip, 7*(6), 756-762. doi:

[90]   Lutolf, M. P., & Hubbell, J. A. (2005). Synthetic biomaterials as instructive extracellular microenvironments for morphogenesis in tissue engineering. *Nature Biotechnology, 23*(1), 47-55. doi:

[91]   Marx, U., Walles, H., Hoffmann, S., Lindner, G., Horland, R., Sonntag, F., Klotzbach, U., Sakharov, D., Tonevitsky, A., & Lauster, R. (2012). 'Human-on-a-chip' Developments: A Translational Cutting-edge Alternative to Systemic Safety Assessment and Efficiency Evaluation of Substances in Laboratory Animals and Man? *Atla-Alternatives to Laboratory Animals, 40*(5), 235-257. doi:

[92]   Mata, A., Fleischman, A. J., & Roy, S. (2005). Characterization of polydimethylsiloxane (PDMS) properties for biomedical micro/nanosystems. *Biomedical Microdevices, 7*(4), 281-293. doi:

[93]   Matthews, B. D., Overby, D. R., Mannix, R., & Ingber, D. E. (2006). Cellular adaptation to mechanical stress: role of integrins, Rho, cytoskeletal tension and mechanosensitive ion channels. *Journal of Cell Science, 119*(3), 508-518. doi:

[94]   Mazzei, D., Guzzardi, M. A., Giusti, S., & Ahluwalia, A. (2010). A low shear stress modular bioreactor for connected cell culture under high flow rates. *Biotechnology and Bioengineering, 106*(1), 127-137. doi:

[95]   Meghri, N. W., Donius, A. E., Riblett, B. W., Martin, E. J., Clyne, A. M., & Wegst, U. G. K. (2010). Directionally Solidified Biopolymer Scaffolds: Mechanical Properties and Endothelial Cell Responses. *Jom, 62*(7), 71-75. doi:

[96]   Melchels, F. P., Barradas, A. M., van Blitterswijk, C. A., de Boer, J., Feijen, J., & Grijpma, D. W. (2010a). Effects of the architecture of tissue engineering scaffolds on cell seeding and culturing. [Research Support, Non-U.S. Gov't]. *Acta Biomater, 6*(11), 4208-4217. doi:

[97]   Melchels, F. P., Barradas, A. M., van Blitterswijk, C. A., de Boer, J., Feijen, J., & Grijpma, D. W. (2010b). Effects of the architecture of tissue engineering scaffolds on cell seeding and culturing. [Research Support, Non-U.S. Gov't]. *Acta Biomaterialia, 6*(11), 4208-4217. doi:

[98]   Melchels, F. P. W., Bertoldi, K., Gabbrielli, R., Velders, A. H., Feijen, J., & Grijpma, D. W. (2010). Mathematically defined tissue engineering scaffold architectures prepared by stereolithography. *Biomaterials, 31*(27), 6909-6916. doi:

[99]   Miller, J. S., Stevens, K. R., Yang, M. T., Baker, B. M., Nguyen, D. H. T., Cohen, D. M., Toro, E., Chen, A. A., Galie, P. A., Yu, X., Chaturvedi, R., Bhatia, S. N., & Chen, C. S. (2012). Rapid casting of patterned vascular networks for perfusable engineered three-dimensional tissues. *Nature Materials, 11*(9), 768-774. doi:

[100]   Mills, R. J., Frith, J. E., Hudson, J. E., & Cooper-White, J. J. (2011). Effect of geometric challenges on cell migration. [Research Support, Non-U.S. Gov't]. *Tissue Eng Part C Methods, 17*(10), 999-1010. doi:

[101]   Moghe, P. V., Berthiaume, F., Ezzell, R. M., Toner, M., Tompkins, R. G., & Yarmush, M. L. (1996). Culture matrix configuration and composition in the maintenance of hepatocyte polarity and function. *Biomaterials, 17*(3), 373-385. doi:

[102]   Murray, P. E., Garcia-Godoy, F., & Hargreaves, K. M. (2007). Regenerative endodontics: a review of current status and a call for action. *J Endod, 33*(4), 377-390. doi:

[103]   Muschler, G. F., Nakamoto, C., & Griffith, L. G. (2004). Engineering principles of clinical cell-based tissue engineering. [Research Support, U.S. Gov't, P.H.S. Review]. *J Bone Joint Surg Am, 86-A*(7), 1541-1558. doi:

[104]   Nahmias, Y., Schwartz, R. E., Hu, W. S., Verfaillie, C. M., & Odde, D. J. (2006). Endothelium-mediated hepatocyte recruitment in the establishment of liver-like tissue in vitro. *Tissue Engineering, 12*(6), 1627-1638. doi:

[105]   Nair, K., Gandhi, M., Khalil, S., Yan, K. C., Marcolongo, M., Barbee, K., & Sun, W. (2009). Characterization of cell viability during bioprinting processes. [Research Support, Non-U.S. Gov't]. *Biotechnol J, 4*(8), 1168-1177. doi:

[106]   Nakagaki, T., Yamada, H., & Toth, A. (2000). Maze-solving by an amoeboid organism. *Nature, 407*(6803), 470. doi:

[107]   Nakamura, M., Iwanaga, S., Henmi, C., Arai, K., & Nishiyama, Y. (2010). Biomatrices and biomaterials for future developments of bioprinting and biofabrication. *Biofabrication, 2*(1). doi:

[108]   Nawroth, J. C., & Parker, K. K. (2013). Design standards for engineered tissues. [Research Support, N.I.H., Extramural]. *Biotechnology Advances, 31*(5), 632-637. doi:

[109]   Neville, C., Carraro, A., Hsu, W. M., Kulig, K. M., Cheung, W. S., Miller, M. L., Weinberg, E. J., Swart, E. F., Kaazempur-Mofrad, M., Borenstein, J. T., & Vacanti, J. P. (2008). In vitro analysis of a hepatic device with intrinsic microvascular-based channels. *Biomedical Microdevices, 10*(6), 795-805. doi:

[110]   Nikukar, H., Reid, S., Tsimbouri, P. M., Riehle, M. O., Curtis, A. S., & Dalby, M. J. (2013). Osteogenesis of mesenchymal stem cells by nanoscale mechanotransduction. [Research Support, Non-U.S. Gov't]. *ACS Nano, 7*(3), 2758-2767. doi:

[111]   Oh, S. H., Park, I. K., Kim, J. M., & Lee, J. H. (2007). In vitro and in vivo characteristics of PCL scaffolds with pore size gradient fabricated by a centrifugation method. *Biomaterials, 28*(9), 1664-1671. doi:

[112]   Omori, K., Nakamura, T., Kanemaru, S., Asato, R., Yamashita, M., Tanaka, S., Magrufov, A., Ito, J., & Shimizu, Y. (2005). Regenerative medicine of the trachea: The first human case. *Annals of Otology Rhinology and Laryngology, 114*(6), 429-433. doi:

[113]   Owen, S. C., & Shoichet, M. S. (2010). Design of three-dimensional biomimetic scaffolds. *Journal of Biomedical Materials Research Part A, 94A*(4), 1321-1331. doi:

[114]   Panoskaltsis, N., Mantalaris, A., & Wu, J. H. D. (2005). Engineering a mimicry of bone marrow tissue ex vivo. *Journal of Bioscience and Bioengineering, 100*(1), 28-35. doi:

[115]   Pek, Y. S., Wan, A. C., & Ying, J. Y. (2010). The effect of matrix stiffness on mesenchymal stem cell differentiation in a 3D thixotropic gel. [Evaluation Studies Research Support, Non-U.S. Gov't]. *Biomaterials, 31*(3), 385-391. doi:

[116]   Pelham, R. J., & Wang, Y. L. (1998). Cell locomotion and focal adhesions are regulated by substrate flexibility (vol 94, pg 13661, 1997). *Proceedings of the National Academy of Sciences of the United States of America, 95*(20), 12070-12070. doi:

[117]   Pelham, R. J., & Wang, Y. L. (1999). High resolution detection of mechanical forces exerted by locomoting fibroblasts on the substrate. *Molecular Biology of the Cell, 10*(4), 935-945. doi:

[118]   Pennella, F., Cerino, G., Massai, D., Gallo, D., Falvo D'Urso Labate, G., Schiavi, A., Deriu, M. A., Audenino, A., & Morbiducci, U. (2013). A Survey of Methods for the Evaluation of Tissue Engineering Scaffold Permeability. *Annals of Biomedical Engineering*. doi:

[119]   Ranucci, C. S., Kumar, A., Batra, S. P., & Moghe, P. V. (2000). Control of hepatocyte function on collagen foams: sizing matrix pores toward selective induction of 2-D and 3-D cellular morphogenesis. *Biomaterials, 21*(8), 783-793. doi:

[120]   Rezende, R. A., Bartolo, P. J., Mendes, A., & Maciel, R. (2009). Rheological Behavior of Alginate Solutions for Biomanufacturing. *Journal of Applied Polymer Science, 113*(6), 3866-3871. doi:

[121]   Ridley, A. J., Schwartz, M. A., Burridge, K., Firtel, R. A., Ginsberg, M. H., Borisy, G., Parsons, J. T., & Horwitz, A. R. (2003). Cell migration: Integrating signals from front to back. *Science, 302*(5651), 1704-1709. doi:

[122]   Riquelme, C. A., Magida, J. A., Harrison, B. C., Wall, C. E., Marr, T. G., Secor, S. M., & Leinwand, L. A. (2011). Fatty acids identified in the Burmese python promote beneficial cardiac growth. *Science, 334*(6055), 528-531. doi:

[123]   Ross, M. D. (1993). Morphological changes in rat vestibular system following weightlessness. [Research Support, U.S. Gov't, Non-P.H.S. Research Support, U.S. Gov't, P.H.S.]. *J Vestib Res, 3*(3), 241-251. doi:

[124]   Rott, N. (1990). Note on the History of the Reynolds-Number. *Annual Review of Fluid Mechanics, 22*, 1-11. doi:

[125]   Ruys, A. J., Wei, M., Sorrell, C. C., Dickson, M. R., Brandwood, A., & Milthorpe, B. K. (1995). Sintering effects on the strength of hydroxyapatite. [Comparative Study]. *Biomaterials, 16*(5), 409-415. doi:

[126]   Sachlos, E., & Czernuszka, J. T. (2003). Making tissue engineering scaffolds work. Review: the application of solid freeform fabrication technology to the production of tissue engineering scaffolds. [Review]. *Eur Cell Mater, 5*, 29-39; discussion 39-40. doi:

[127]   Sant, S., Hancock, M. J., Donnelly, J. P., Iyer, D., & Khademhosseini, A. (2010). Biomimetic Gradient Hydrogels for Tissue Engineering. *Canadian Journal of Chemical Engineering, 88*(6), 899-911. doi:

[128]   Sarasa-Renedo, A., Tunc-Civelek, V., & Chiquet, M. (2006). Role of RhoA/ROCK-dependent actin contractility in the induction of tenascin-C by cyclic tensile strain. *Experimental Cell Research, 312*(8), 1361-1370. doi:

[129]   Sato, T., & Clevers, H. (2013). Growing Self-Organizing Mini-Guts from a Single Intestinal Stem Cell: Mechanism and Applications. *Science, 340*(6137), 1190-1194. doi:

[130]   Sato, T., Vries, R. G., Snippert, H. J., van de Wetering, M., Barker, N., Stange, D. E., van Es, J. H., Abo, A., Kujala, P., Peters, P. J., & Clevers, H. (2009). Single Lgr5 stem cells build crypt-villus structures in vitro without a mesenchymal niche. *Nature, 459*(7244), 262-U147. doi:

[131]   Satyanarayana, S., Karnik, R. N., & Majumdar, A. (2005). Stamp-and-stick room-temperature bonding technique for microdevices. *Journal of Microelectromechanical Systems, 14*(2), 392-399. doi:

[132]   Shachar, M., Benishti, N., & Cohen, S. (2012). Effects of mechanical stimulation induced by compression and medium perfusion on cardiac tissue engineering. [Research Support, Non-U.S. Gov't]. *Biotechnol Prog, 28*(6), 1551-1559. doi:

[133]   Shajii, A., & Freidberg, J. P. (1996). Theory of low Mach number compressible flow in a channel. *Journal of Fluid Mechanics, 313*, 131-145. doi:

[134]   Shiu, Y. T., Li, S., Marganski, W. A., Usami, S., Schwartz, M. A., Wang, Y. L., Dembo, M., & Chien, S. (2004). Rho mediates the shear-enhancement of endothelial cell migration and traction force generation. *Biophysical Journal, 86*(4), 2558-2565. doi:

[135]   Shor, L., Guceri, S., Wen, X., Gandhi, M., & Sun, W. (2007). Fabrication of three-dimensional polycaprolactone/hydroxyapatite tissue scaffolds and osteoblast-scaffold interactions in vitro. [Research Support, U.S. Gov't, Non-P.H.S.]. *Biomaterials, 28*(35), 5291-5297. doi:

[136]   Shuler, M. L., Viravaidya, K., & Sin, A. (2004). Development of a microscale cell culture analog to probe naphthalene toxicity. *Biotechnology Progress, 20*(1), 316-323. doi:

[137]   Sigman, K., Ghibu, F., Sommerville, W., Toledano, B. J., Bastein, Y., Cameron, L., Hamid, Q. A., & Mazer, B. (1998). Intravenous immunoglobulin inhibits IgE production in human B lymphocytes. *Journal of Allergy and Clinical Immunology, 102*(3), 421-427. doi:

[138]   Silva, M. M. C. G., Cyster, L. A., Barry, J. J. A., Yang, X. B., Oreffo, R. O. C., Grant, D. M., Scotchford, C. A., Howdle, S. M., Shakesheff, K. M., & Rose, F. R. A. J. (2006). The effect of anisotropic architecture on cell and tissue infiltration into tissue engineering scaffolds. *Biomaterials, 27*(35), 5909-5917. doi:

[139]   Snyder, J. E., Hamid, Q., Wang, C., Chang, R., Emami, K., Wu, H., & Sun, W. (2011). Bioprinting cell-laden matrigel for radioprotection study of liver by pro-drug conversion in a dual-tissue microfluidic chip. *Biofabrication, 3*(3). doi:

[140]   Snyder J.E., Zhang Y., Emami K., Wu H., Sun W., . (2012). In Vitro Disease Model of Microgravity Conditioning on Human Energy Metabolism. *In proceeding of: Bioengineering Conference (NEBEC), 38th Annual Northeast Bioengineering Conference*. doi:

[141]   Sobral, J. M., Caridade, S. G., Sousa, R. A., Mano, J. F., & Reis, R. L. (2011). Three-dimensional plotted scaffolds with controlled pore size gradients: Effect of scaffold geometry on mechanical performance and cell seeding efficiency. *Acta Biomaterialia, 7*(3), 1009-1018. doi:

[142]   Song, J. W., Cavnar, S. P., Walker, A. C., Luker, K. E., Gupta, M., Tung, Y. C., Luker, G. D., & Takayama, S. (2009). Microfluidic Endothelium for Studying the Intravascular Adhesion of Metastatic Breast Cancer Cells. *Plos One, 4*(6). doi:

[143]   Song, Y. S., Lin, R. L., Montesano, G., Durmus, N. G., Lee, G., Yoo, S. S., Kayaalp, E., Haeggstrom, E., Khademhosseini, A., & Demirci, U. (2009). Engineered 3D tissue models for cell-laden microfluidic channels. *Anal Bioanal Chem, 395*(1), 185-193. doi:

[144]   Spiteri, C. G., Pilliar, R. M., & Kandel, R. A. (2006). Substrate porosity enhances chondrocyte attachment, spreading, and cartilage tissue formation in vitro. [In Vitro
Research Support, Non-U.S. Gov't]. *J Biomed Mater Res A, 78*(4), 676-683. doi:

[145]   Sun, G. M., & Gerecht, S. (2009). Vascular regeneration: engineering the stem cell microenvironment. *Regenerative Medicine, 4*(3), 435-447. doi:

[146]   Sun, W., & Chang, R. (2008). Effects of dispensing pressure and nozzle diameter on cell survival from solid freeform fabrication-based direct cell writing. *Tissue Engineering Part A, 14*(1), 41-48. doi:

[147]   Sun, W., Chang, R., Emami, K., & Wu, H. L. (2010). Biofabrication of a three-dimensional liver micro-organ as an in vitro drug metabolism model. *Biofabrication, 2*(4), 1-11. doi:

[148]   Sun, W., Chang, R., & Nam, Y. (2008). Direct cell writing of 3D microorgan for in vitro pharmacokinetic model. *Tissue Engineering Part C-Methods, 14*(2), 157-166. doi:

[149]   Sun, W., Starly, B., Darling, A., & Gomez, C. (2004). Computer-aided tissue engineering: application to biomimetic modelling and design of tissue scaffolds. [Research Support, Non-U.S. Gov't

[150]   Takayama, S., Hsiao, A. Y., Torisawa, Y. S., Tung, Y. C., Sud, S., Taichman, R. S., & Pienta, K. J. (2009). Microfluidic system for formation of PC-3 prostate cancer co-culture spheroids. *Biomaterials, 30*(16), 3020-3027. doi:

[151]   Talbot, N. C., Caperna, T. J., Blomberg, L., Graninger, P. G., & Stodieck, L. S. (2010a). The effects of space flight and microgravity on the growth and differentiation of PICM-19 pig liver stem cells. *In Vitro Cellular & Developmental Biology-Animal, 46*(6), 502-515. doi:

[152]   Talbot, N. C., Caperna, T. J., Blomberg, L., Graninger, P. G., & Stodieck, L. S. (2010b). The effects of space flight and microgravity on the growth and differentiation of PICM-19 pig liver stem cells. *In Vitro Cell Dev Biol Anim, 46*(6), 502-515. doi:

[153]   Tamma, R., Colaianni, G., Camerino, C., Di Benedetto, A., Greco, G., Strippoli, M., Vergari, R., Grano, A., Mancini, L., Mori, G., Colucci, S., Grano, M., & Zallone, A. (2009). Microgravity during spaceflight directly affects in vitro osteoclastogenesis and bone resorption.

[154]   Tan, C. G., Stronach, B., & Perrimon, N. (2003). Roles of myosin phosphatase during Drosophila development. *Development, 130*(4), 671-681. doi:

[155]   Tarabichi, M., Antoniou, A., Saiselet, M., Pita, J. M., Andry, G., Dumont, J. E., Detours, V., & Maenhaut, C. (2013). Systems biology of cancer: entropy, disorder, and selection-driven evolution to independence, invasion and "swarm intelligence". *Cancer Metastasis Rev*. doi:

[156]   Torsoni, A. S., Marin, T. M., Velloso, L. A., & Franchini, K. G. (2005). RhoA/ROCK signaling is critical to FAK activation by cyclic stretch in cardiac myocytes. *American Journal of Physiology-Heart and Circulatory Physiology, 289*(4), H1488-H1496. doi:

[157]   Tourovskaia, A., Figueroa-Masot, X., & Folch, A. (2005). Differentiation-on-a-chip: a microfluidic platform for long-term cell culture studies. *Lab Chip, 5*(1), 14-19. doi:

[158]   Trepat, X., & Fredberg, J. J. (2007). Remodeling of the cytoskeleton by a single transient stretch. *Biophysical Journal*, 632a-632a. doi:

[159]   Tsuruga, E., Takita, H., Itoh, H., Wakisaka, Y., & Kuboki, Y. (1997). Pore size of porous hydroxyapatite as the cell-substratum controls BMP-induced osteogenesis. *Journal of Biochemistry, 121*(2), 317-324. doi:

[160] Turner, C. H., & Burr, D. B. (1993). Basic Biomechanical Measurements of Bone - a Tutorial. *Bone, 14*(4), 595-608. doi:

[161] UK: 3Rs Prize awarded to Donald Ingber for lung-on-a-chip device. (2013). *Altex-Alternatives to Animal Experimentation, 30*(2), 272-272. doi:

[162] van der Meer, A. D., & van den Berg, A. (2012). Organs-on-chips: breaking the in vitro impasse. *Integrative Biology, 4*(5), 461-470. doi:

[163] van Midwoud, P. M., Verpoorte, E., & Groothuis, G. M. M. (2011). Microfluidic devices for in vitro studies on liver drug metabolism and toxicity. *Integrative Biology, 3*(5), 509-521. doi:

[164] Vazquez, A., Luduena, L. N., & Alvarez, V. A. (2007). Processing and microstructure of PCL/clay nanocomposites. *Materials Science and Engineering a-Structural Materials Properties Microstructure and Processing, 460*, 121-129. doi:

[165] Vernikos, J., & Schneider, V. S. (2010). Space, gravity and the physiology of aging: parallel or convergent disciplines? A mini-review. *Gerontology, 56*(2), 157-166. doi:

[166] Walker, G. M., Zeringue, H. C., & Beebe, D. J. (2004). Microenvironment design considerations for cellular scale studies. *Lab on a Chip, 4*(2), 91-97. doi:

[167] Wang, F., Shor, L., Darling, A., Khalil, S., Sun, W., Guceri, S., & Lau, A. (2004). Precision extruding deposition and characterization of cellular poly-epsilon-caprolactone tissue scaffolds. *Rapid Prototyping Journal, 10*(1), 42-49. doi:

[168] Wegst, U. G. K., Schecter, M., Donius, A. E., & Hunger, P. M. (2010). Biomaterials by freeze casting. *Philosophical Transactions of the Royal Society a-Mathematical Physical and Engineering Sciences, 368*(1917), 2099-2121. doi:

[169] Wei, G., & Ma, P. X. (2004). Structure and properties of nano-hydroxyapatite/polymer composite scaffolds for bone tissue engineering. [Comparative Study Evaluation Studies]. *Biomaterials, 25*(19), 4749-4757. doi:

[170] Whitesides, G. M., Ng, J. M. K., Gitlin, I., & Stroock, A. D. (2002). Components for integrated poly(dimethylsiloxane) microfluidic systems. *Electrophoresis, 23*(20), 3461-3473. doi:

[171] Whitesides, G. M., Siegel, A. C., Tang, S. K. Y., Nijhuis, C. A., Hashimoto, M., Phillips, S. T., & Dickey, M. D. (2010). Cofabrication: A Strategy for Building Multicomponent Microsystems. *Accounts of Chemical Research, 43*(4), 518-528. doi:

[172] Williams, D., Kuipers, A., Mukai, C., & Thirsk, R. (2009). Acclimation during space flight: effects on human physiology. *CMAJ, 180*(13), 1317-1323. doi:

[173] Wu, M. H., Huang, S. B., & Lee, G. B. (2010). Microfluidic cell culture systems for drug research. *Lab on a Chip, 10*(8), 939-956. doi:

[174] Yamada, M., Utoh, R., Ohashi, K., Tatsumi, K., Yamato, M., Okano, T., & Seki, M. (2012). Controlled formation of heterotypic hepatic micro-organoids in anisotropic hydrogel microfibers for long-term preservation of liver-specific functions. *Biomaterials, 33*(33), 8304-8315. doi:

[175] Yang, Y., Beqaj, S., Kemp, P., Ariel, I., & Schuger, L. (2000). Stretch-induced alternative splicing of serum response factor promotes bronchial myogenesis and is defective in lung hypoplasia. *Journal of Clinical Investigation, 106*(11), 1321-1330. doi:

[176] Yeo, L. Y., Chang, H. C., Chan, P. P., & Friend, J. R. (2011). Microfluidic devices for bioapplications. *Small, 7*(1), 12-48. doi:

[177] Yeung, T., Georges, P. C., Flanagan, L. A., Marg, B., Ortiz, M., Funaki, M., Zahir, N., Ming, W. Y., Weaver, V., & Janmey, P. A. (2005). Effects of substrate stiffness on cell morphology, cytoskeletal structure, and adhesion. *Cell Motility and the Cytoskeleton, 60*(1), 24-34. doi:

[178] Yildirim, E. D., Yin, X., Nair, K., & Sun, W. (2008). Fabrication, Characterization, and Biocompatibility of Single-Walled Carbon Nanotube-Reinforced Alginate Composite Scaffolds Manufactured Using Freeform Fabrication Technique. *Journal of Biomedical Materials Research Part B-Applied Biomaterials, 87B*(2), 406-414. doi:

[179] Yoo, D. (2012). New paradigms in internal architecture design and freeform fabrication of tissue engineering porous scaffolds. [Research Support, Non-U.S. Gov't]. *Med Eng Phys, 34*(6), 762-776. doi:

[180] Yung, C. W., Fiering, J., Mueller, A. J., & Ingber, D. E. (2009). Micromagnetic-microfluidic blood cleansing device. *Lab on a Chip, 9*(9), 1171-1177. doi:

[181] Zhao, Q., Du, J., Gu, H., Teng, X. L., Zhang, Q., Qin, H., & Liu, N. Z. (2007). Effects of YC-1 on hypoxia-inducible factor 1-driven transcription activity, cell proliferative vitality, and apoptosis in hypoxic human pancreatic cancer cells. *Pancreas, 34*(2), 242-247. doi:

[182] Zmora, S., Glicklis, R., & Cohen, S. (2002). Tailoring the pore architecture in 3-D alginate scaffolds by controlling the freezing regime during fabrication. *Biomaterials, 23*(20), 4087-4094. doi:

VITA

Education	o PhD, Mechanical Engineering (2014), Drexel University, Philadelphia Pa
	o BS, Mechanical Engineering (2009), Drexel University, Philadelphia, Pa
Honors and Awards	o Drexel University Graduate Student Association (GSA) President (2012-2013)
	o Drexel University Lee Smith Traveling Fellowship (2012)
	o NSF Student Conference Fellowship for Civil, Mechanical, Manufacturing, and Industrial Engineering Research and Innovation Conference (2012)
	o 18th IAA Humans in Space Symposium Outstanding Poster Award (2011)
	o National Space Biomedical Research Institute (NSBRI) Summer Internship (2010)
Selected Journal Publications	o Snyder JE, Hunger PM, Wang C, Hamid Q, Wegst UG, Sun W. Combined multi-nozzle deposition and freeze casting process to superimpose two porous networks for hierarchical three-dimensional microenvironment. Biofabrication 2014;6(1):015007..
	o Snyder JE, Emami K, Du B, Zhang Y, Wu H, Sun W. Effect of model microgravity on human hepatic pharmacokinetics and urea secretion. Bioengineering Conference (NEBEC), Annual Northeast. 2012, 171-172
	o Snyder JE, Hamid Q, Wang C, Chang R, Emami K, Wu H, Sun W. Bioprinting cell-laden matrigel for radioprotection study of liver by pro-drug conversion in a dual-tissue microfluidic chip. Biofabrication 2011;3(3).
	o Hamid Q, Snyder JE, Wang C, Timmer M, Hammer J, Guceri S, Sun W. Fabrication of threedimensional scaffolds using precision extrusion deposition with an assisted cooling device. *Biofabrication* 2011;3(3).
Patents	o **US20110136162 A1** Wei Sun, Robert Chang, Eda Yildirim, Halim Ayan, Jessica Snyder. "Compositionsand Methods for Functionalized Patterning of Tissue Engineering Substrates Including Bioprinting Cell-Laden Constructs for Multicompartment Tissue Chambers" Filed 8/31/2010.